

**Results of a Large Airplane Impact into a Field of
Holtec HI-STORM Spent Nuclear Fuel Storage Casks,
with Appendices A-C**

REDACTED

02/12/2008

The Nuclear Regulatory Commission does not support many of the assumptions and/or information contained in this report. This report cannot be used independently to develop any conclusions regarding security or protective measures. This report should not be shared with industry and should not be released to anyone outside the agency.

Results of a Large Airplane Impact into a Field of Holtec HI-STORM Spent Nuclear Fuel Storage Casks (U)

Final Draft Submitted to the Office of Nuclear Material Safety
and Safeguards, U.S. Nuclear Regulatory Commission (U)

By

The Transportation Risk & Packaging Department

Department 6141

Sandia National Laboratories

Albuquerque, NM

August 20, 2004

**J.A. Smith, J.L. Sprung, D.J. Ammerman, G. Bessette, R.
Dykhuisen, V. Figueroa, R.J. Kalan, K. Gwinn, C. Lopez, R.
Oneto, C. Morrow, J. Mould, K.B. Sorenson, W.D. Sundberg,
and D. Tennant (U).**

NATIONAL SECURITY INFORMATION

CLASSIFIED BY:	Ken B. Sorenson
TITLE/ORG:	Manager 6141/August 18, 2004
DERIVED FROM:	CG-RDM-1, June 1996 and CG-NMF-2, Dec 1991
DECLASSIFY ON:	X4

This page intentionally left blank

Table of Contents (U)

Executive Summary (U)	6
1 Introduction (U)	15
1.1 The Threat (U)	15
1.2 The HI-STORM Storage Cask (U)	16
1.3 The Analysis Methodology (U)	17
1.3.1 Examining the Structural Response to the Impact (U)	17
1.3.2 Examining the Response to a Subsequent Fire (U)	18
1.3.3 Examining the Source Term and Consequences (U)	19
1.4 Roadmap to an Exploration of the Cask Vulnerabilities (U)	19
2 Field of HI-STORM Storage Casks (U)	20
2.1 Complexity of Scenarios (U)	20
2.1.1 Analyses Performed (U)	22
2.1.2 Selected Scenario (U)	25
2.2 Analysis of the Field of Storage Casks for the Selected Scenario (U)	25
2.2.1 Structural Analysis of the Selected Scenario (U)	26
2.2.2 Thermal Analysis for the Selected Scenario (U)	56
3 Conclusions (U)	92
4 References (U)	93
Appendix A: Structural Analysis (U)	A-1
Appendix B: HI-STORM Storage Cask Engine Impact Analyses (U)	B-1
Appendix C: Effect of Pool Fires on a Dry Storage Cask (U)	C-1

P39 ovs-sk1
EX2

List of Figures (U)

Figure Ex-1. Typical HI-STORM Cask Layout with Scale Airplane (U).....	6
Figure Ex-2. Cask-to-Cask Impact with Jetliner Impact Loading (U).....	8
Figure 1-1. The HI-STORM Storage Cask (U).....	17
Figure 2-2. Scale Views of the Jetliner and the Field of Storage Casks (U).....	21
Figure 2-3. Full Jetliner Model used in CTH Analysis (U).....	27
Figure 2-4. Simplified CTH Jetliner Model Impacting a Single Cask (U).....	27
Figure 2-6. Total Force on the HI-STORM Cask (1 N = 0.22 lbs) (U).....	29
Figure 2-7. Cask Horizontal Velocity as a Function of Time (1 mph = 0.447 m/s) (U).....	30
Figure 2-8. Cask Horizontal Velocity as a Function of Displacement (1 mph = 0.447 m/s; 1 m = 3.28 ft) (U).....	31
Figure 2-9. Clear Spacing Distances between the Casks on a Typical Pad Layout (U).....	32
Figure 2-10. Loading Zones for Force Time-History of Jetliner (U).....	34
Figure 2-11. Cask-to-Cask FE Model with Jetliner Pressure Force Time-History (U).....	35
Figure 2-12. Selected Deformed Images of Whole Jetliner Loading of the Cask-to-Cask Impact: VonMises Stress Contours for the Steel and Damage Parameter for the Concrete Portions of the Model (1 MPa = 145 psi) (U).....	37
Figure 2-13. Resulting Velocity and Acceleration of the Two Casks in the Cask-to-Cask Impact with the Jetliner Pressure (1 m/s = 2.24 mph) (U).....	38
Figure 2-17. Force versus Time Data Developed for the Jet Engine Using J79 Impact Data (1 N = 0.22 lbs) (U).....	41
Figure 2-25. Schematic of Gap Between MPC and the Overpack (U).....	47
Figure 2-26. Schematic Drawing of the MPC (U).....	48
Figure 2-27. Canister FE Model (U).....	49
Figure 2-28. A Detailed View of Canister Lid Weld Region (U).....	50

ex. 2

p. 4.6

ex 2

4b

Ex 2 4c

Ex 2

Ex 2

Ex. 2

ex. 2

ex. 2

ex. 2 4d

ex. 2

ex. 2

ex. 2

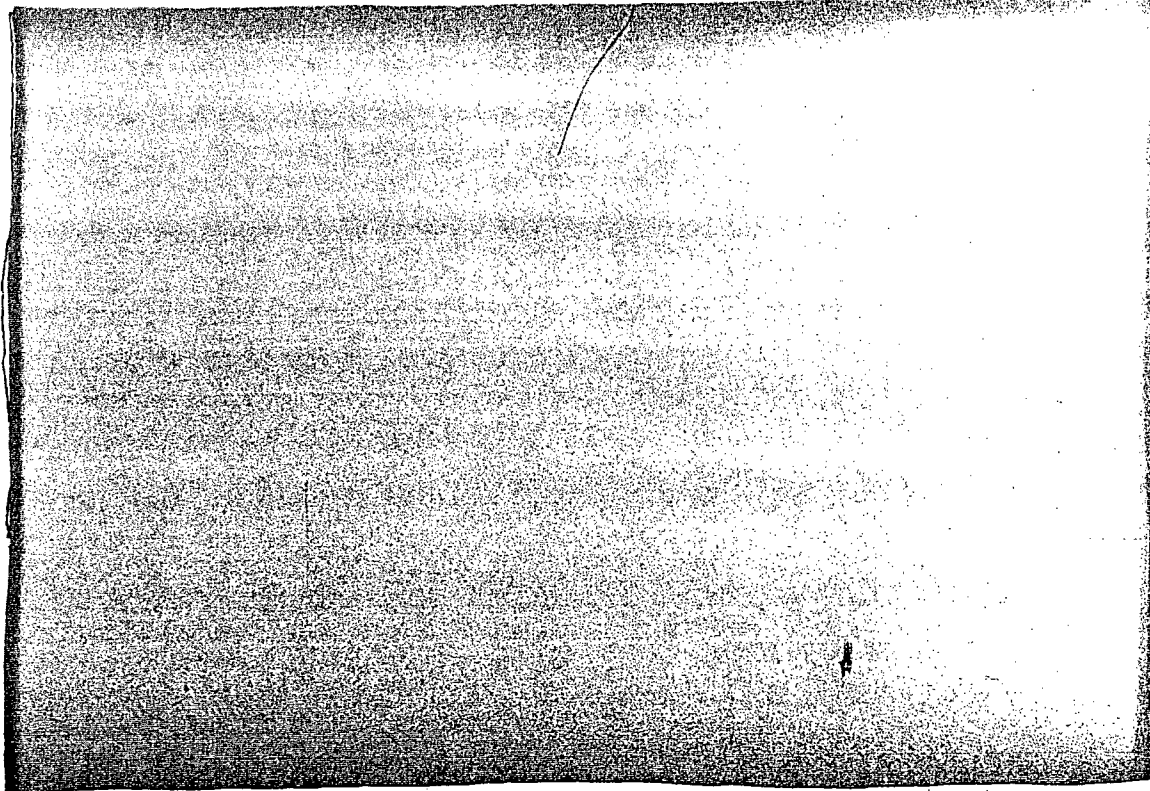
ex 2

ex 2

ex 2

ex 2 4e

ex 2



Ex. 2
p. 5a

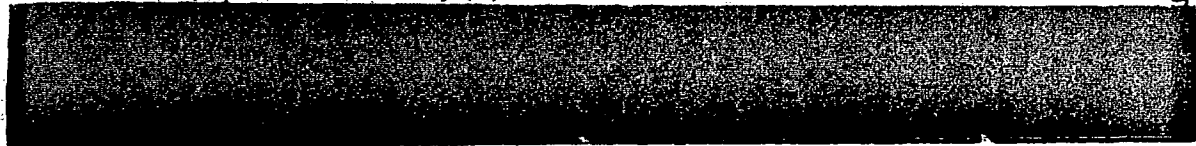
Ex. 3
p. 5b

List of Tables (U)



Ex. 3
p. 5c

Table 2.2. Radionuclide Inventory (Bq) of One High-Burnup, BWR/6, 8x8, Ten-Year
Cooled, Spent Fuel Assembly (U)59



Ex. 3
p. 5d

Results of a Large Airplane Impact into a Field of Holtec HI-STORM Spent Nuclear Fuel Storage Casks (U)

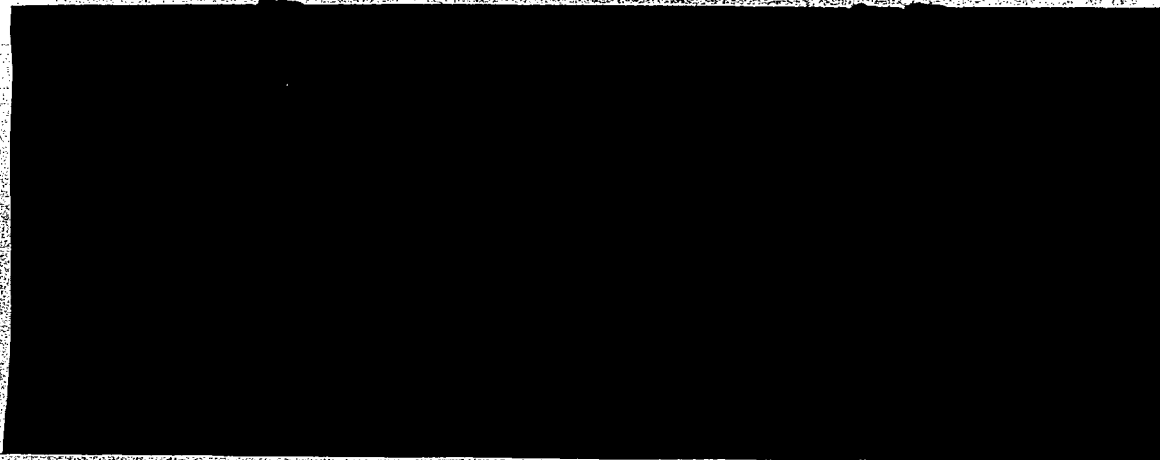
Executive Summary (U)

Introduction (U)

(U) The terrorist events of September 11th, 2001 exposed U.S. infrastructure facilities to attack scenarios that had not heretofore been assessed from a vulnerability standpoint. This Executive Summary describes the vulnerabilities and consequences of a large airplane attack on a nuclear site with an array of licensed Holtec HI-STORM-100 Cask System commercial spent nuclear fuel storage casks (hereafter referred to as HI-STORM). The results of this work are based on a two-year study that comprehensively addressed many technical and engineering aspects of analyzing such an attack on a variety of packages and casks.

Purpose (U)

(U) As a direct result of the September 11th, 2001 large airplane attacks on the World Trade Center and the Pentagon, the U.S. Nuclear Regulatory Commission (NRC) contracted with Sandia National Laboratories (SNL) to conduct a vulnerability and consequence assessment of such attacks on an array of HI-STORM storage casks. Figure Ex-1 provides a measure of scale for this particular attack scenario against a typical cask array configuration.



Ex. 3
p. 6a

(U) In the early part of the investigation, attack parameters were studied and defined to represent a realistic attack scenario. Parameters that were considered included airplane type, speed of impact, angle of impact, location of impact on the cask, and orientation of impact relative to the cask array. For the plane (i.e., the attack weapon), parameters were defined that were consistent

with the September 11th, 2001 attacks (i.e., a realistic scenario). For the cask, parameters (e.g., orientation and location of impact on the cask) were defined for a realistic impact scenario with due consideration to potential cask damage.

Cask Description (U)

(U) The HI-STORM storage cask contents include 24 or 32 pressurized water reactor (PWR) or 68 boiling water reactor (BWR) assemblies.

The maximum weight of a fully loaded cask is 163,296 kg (360,000 lbs).

Ex. 2
p. 7a

Ex. 2
p. 7b

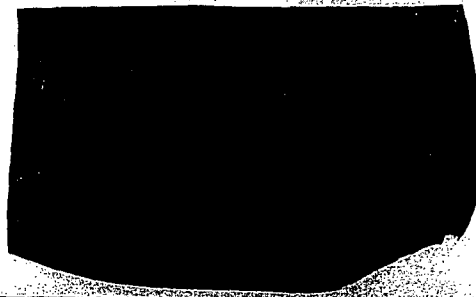
Airplane Description (U)

(U) Airplane models were developed to best capture loadings that would result from impacts to casks in a real event. The airplane mass is representative of the class of airplanes involved in the September 11th, 2001 terrorist events. A full center fuel tank mass was included, as well as "hard" parts of the airplane (the front landing gear and the engines). Discussions were held with the plane manufacturer to verify mass distributions, stiffness, and front landing gear characteristics. Field investigations of a representative airplane were also conducted to verify dimensions and locations of specific components that were modeled.

Structural Analysis (U)

(U) Due to the complex nature of the airplane impacting the cask, two separate types of analyses were conducted. The first type evaluated the impact of the entire airplane into a cask and the second type of analysis reviewed the cask integrity due to impacts by hard components of the jetliner. The airplane was modeled using a hydrodynamic analysis code in the first type of analyses. The main phenomenon evaluated in these analyses was the transfer of momentum from the airplane to the impacted cask. This momentum could then be related to the force that the airplane imparts to the stationary cask and the subsequent velocity achieved by the impacted cask(s). This was then followed by a detailed cask-to-cask impact analysis with the force of the impacting jetliner applied to the initially impacted cask.

Ex. 2
p. 7c



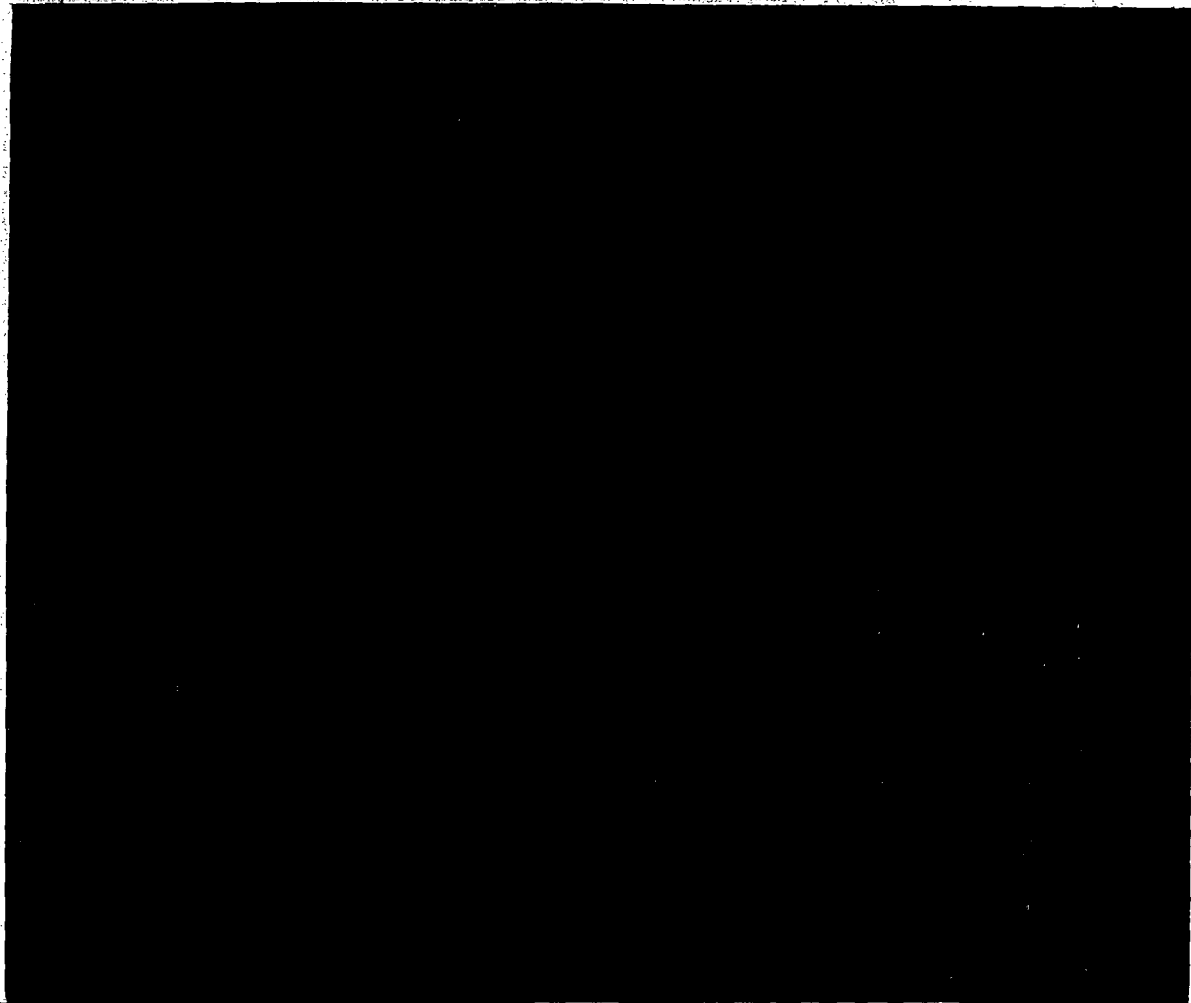
SGI
-I

EX 3
p. 5a



SGI

EX 3
p. 8b



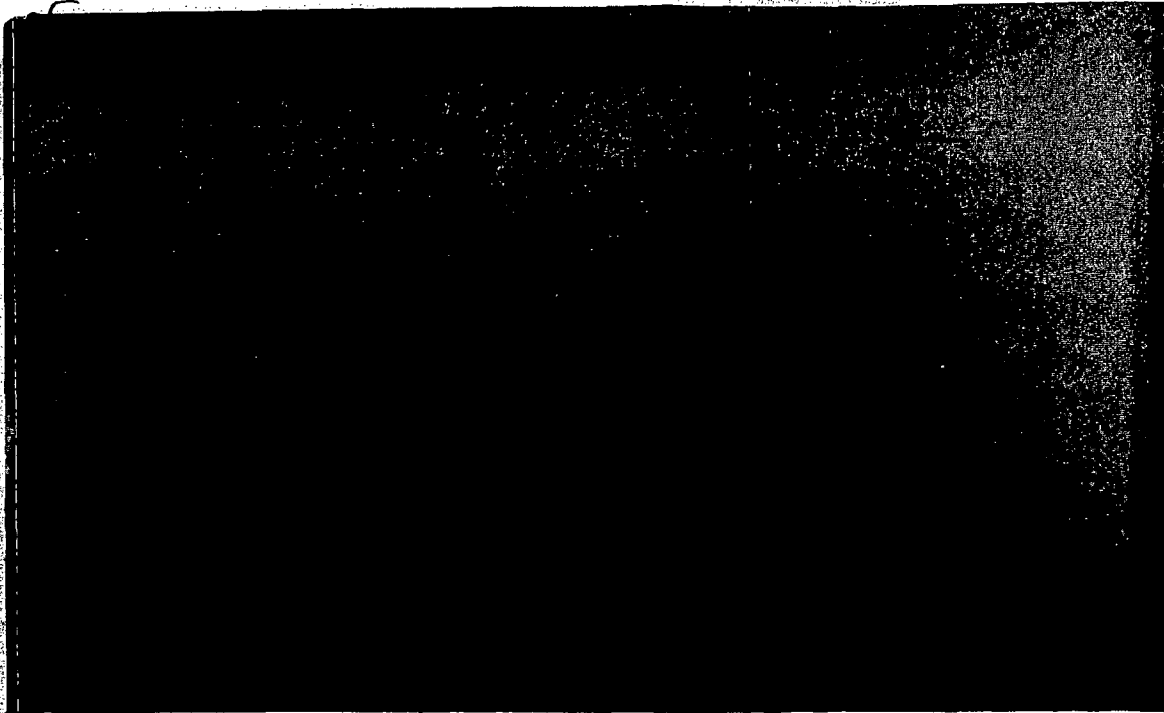
EX # 2
p. B. C

EX 2

EX # 2

EX 2

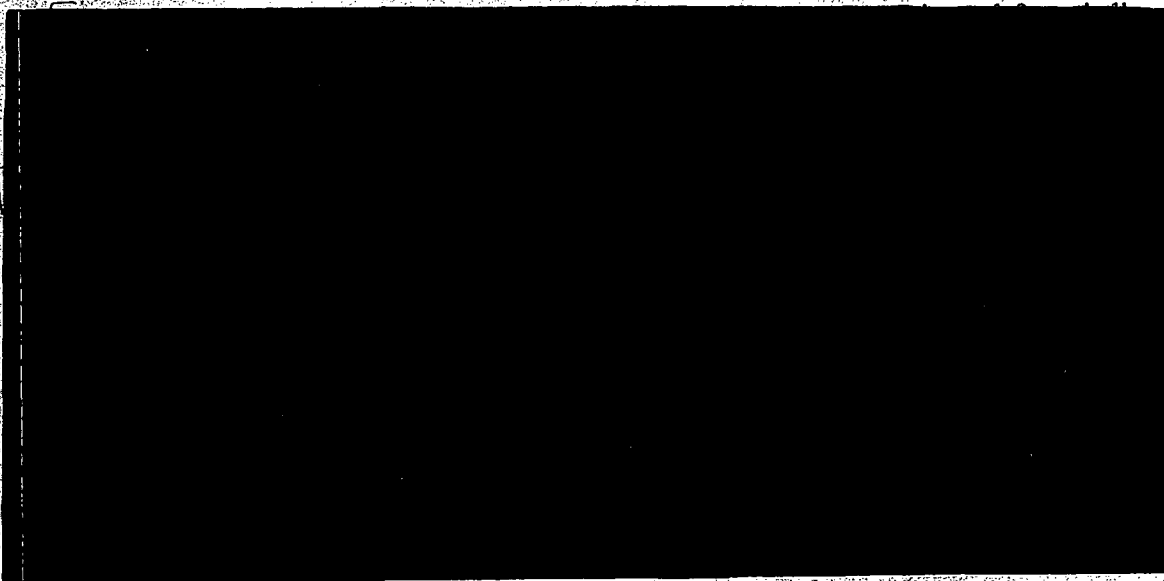
Thermal Analysis (U)



Ex. # 2
p. 9. b

Ex. # 2

Source Term Estimate (U)



Ex 3

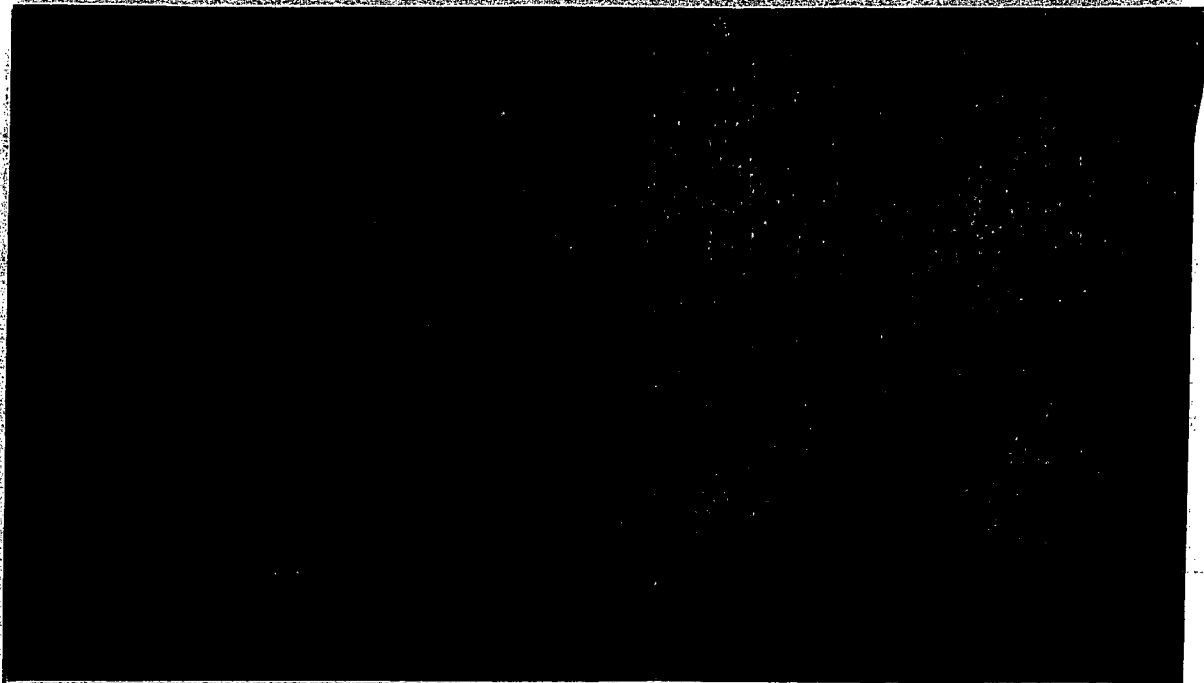
SGI
p. 9. c

Ex 3

SGI EX3
p. 9d

Ex 3

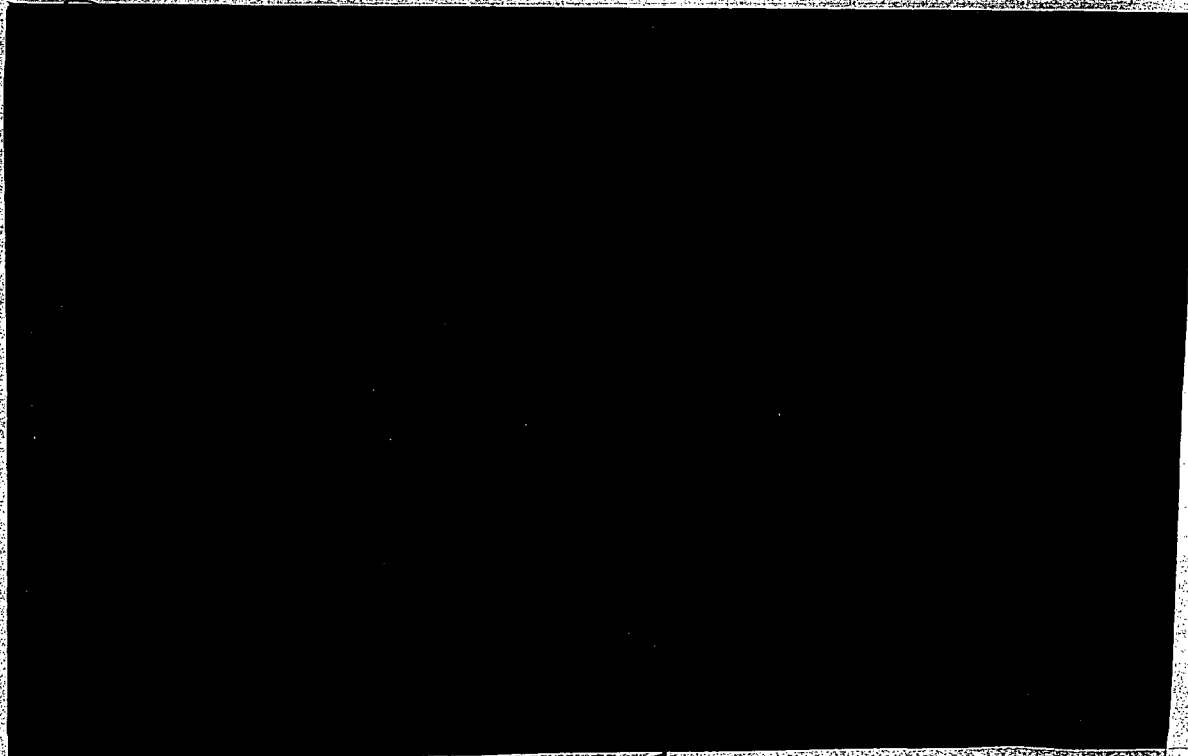
Ex 3
p. 9e



Ex 3
SGT
p.10a

Ex 3
p.10b

Consequence Estimate (U)



Ex. 3
p.10.c

SGT

Conclusion (U)



SGT

p. 11a

Ex. 3

This page intentionally left blank.

Acknowledgements (U)

(U) The following report documents a portion of the results of a more than two-year effort to understand the issues related to the intentional attack by a large airplane on transportation packages and storage casks conducted at Sandia National Laboratories for the U.S. Nuclear Regulatory Commission Office of Nuclear Materials Safety and Safeguards (NMSS). The HI-STORM cask investigated in this study that is documented in this report and its associated appendices was the initial cask reviewed in response to the September 11th 2001 attacks on the World Trade Center towers and the Pentagon. The study required the help of many people (as the long list of authors demonstrates). The authors gratefully acknowledge the additional contributions of Mona Aragon for her support in presenting some of the information graphically and our co-authors at Weidinger Associates, Inc, Los Altos, Ca and their support staff. In addition, the authors gratefully acknowledge the staff at the NRC whose guidance and support were invaluable. This included; C. Bajwa, S.P. Bush-Goddard, D.T. Huang, C.G. Interrante, R. Parkhill, B. Schlapper, M.J. Shah, R.E. Shewmaker, A. Snyder, and B. White.

Preface

(U) The following report is the first of a series of eleven reports documenting the work conducted to review the consequences of a terrorist attack on storage and transportation casks/packages by Sandia National Laboratories (SNL) Department of Transportation Risk & Packaging Department (6141) for the Nuclear Regulatory Commission (NRC) office of Nuclear Materials Safety and Safeguards (NMSS) in response to the September 11th 2001 attacks on the WTC and Pentagon. The magnitude of the events of September 11th resulted in the need to re-evaluate these packages for severe events such as these. This resulted in analyses that have stretched the bounds of previous studies and the capabilities of computation techniques. There is very little experience or data for these types of events. The resulting analyses of these events can result in non-intuitive results. Therefore, initially many analyses were conducted to help develop a knowledge base and experience in analyzing these types of events.

(U) The following report has been divided into a main body and three appendices to help provide clarity. The main body of the report discusses the methodology and generally discusses the main analyses conducted as part of this study. In addition, it narrows the possible scenarios reviewed down to one "selected scenario" that is discussed in detail and evaluated in the main body. All of the structural and thermal analyses conducted for this study are discussed in detail in the appendices.

Results of a Large Airplane Impact into a Field of Holtec HI-STORM Spent Nuclear Fuel Storage Casks (U)

1 Introduction (U)

Classified
Ex 1
p. 15a

(U) This report should not be considered a Safety Analysis of the casks to this threat. Traditionally, a safety analysis would assume the worst conditions and examine the safety of the system to this worst case, whereas this study examines a credible scenario that was chosen based on the September 11th, 2001 attacks on the Pentagon and the World Trade Centers (WTC). Nor is this study a complete vulnerability assessment, which would examine all the vulnerability to this threat and their likelihood of occurring during an attack. All possible scenarios are not examined in this study and the likelihood of the events was not evaluated. A wide range of scenarios was considered and one scenario was evaluated in detail. Calculations were performed that support the examination of other scenarios, but these scenarios were not examined in detail. The study discusses the complexity of the many possible scenarios that might occur under such an attack, and guidance on what would happen under this credible scenario. Especially for an array of storage casks, it is not practical to assess and quantitatively determine the results of all possible scenarios involving the jetliner impacts. Therefore, an attempt was made to overview the broad possibilities and vulnerabilities of the systems and emphasize one particular scenario with associated results.

(U) The body of this report summarizes the analyses performed and looks in detail at one particular scenario. However, for a complete description of all of the analyses and technical description of the computer codes that were used, the reader should consult the appendices. The main body of this report examines the vulnerability of a field of storage casks to one of many potential intentional impact scenarios by a jetliner. The appendices discuss other possible scenarios.

1.1 The Threat (U)

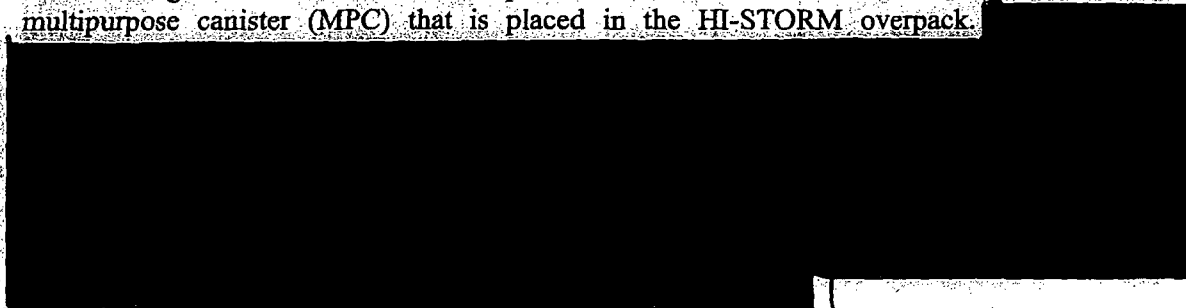
Classified
Ex 1
p. 15b

Ex.
p. 16a

1.2 The HI-STORM Storage Cask (U)

(U) This report examines the vulnerabilities of the Holtec HI-STORM 100 Cask System commercial spent nuclear fuel dry storage casks (hereafter referred to as HI-STORM) (Holtec International, 2000). Subsequent reports will examine additional spent fuel storage casks and radioactive material packages and threats.

(U) The HI-STORM storage cask (Shown in Figure 1-1) contents include up to 32 pressurized water reactor (PWR) or up to 68 boiling water reactor (BWR) assemblies. For these analyses, the PWR configuration was used. The spent fuel assemblies are sealed in a stainless steel multipurpose canister (MPC) that is placed in the HI-STORM overpack.

Ex. 2
p. 16b

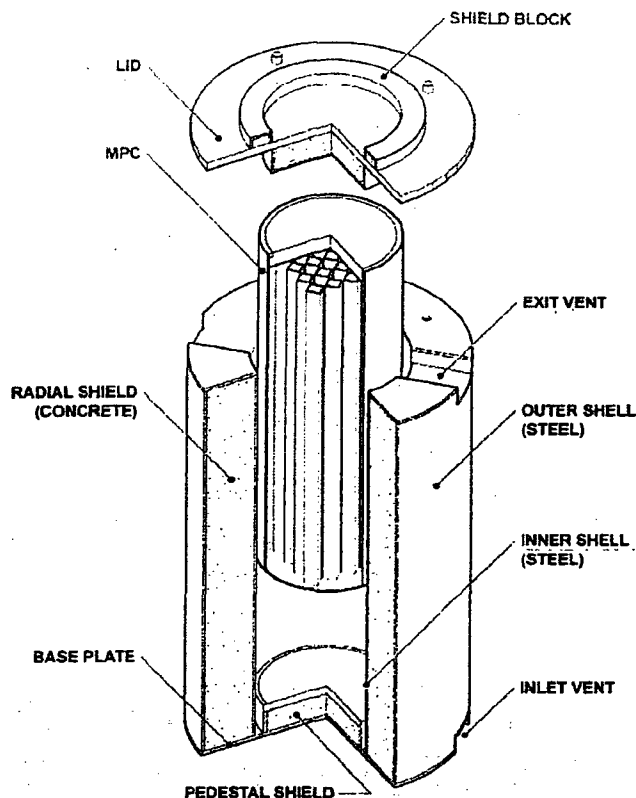


Figure 1-1. The HI-STORM Storage Cask (U).

The contents of the figure are unclassified.

1.3 The Analysis Methodology (U)

(U) Analyzing the intentional impact of a large commercial jetliner into either a field of storage casks is a very complex problem with a limited number of previous studies to build upon. The problem required bringing together a large group of analysts and integrating results from many different resources to estimate the cask or package vulnerabilities and consequences.

1.3.1 Examining the Structural Response to the Impact (U)

(U) As described in more detail in Section 2 and Appendix A, the structural response of the cask was divided into the global and local responses to the jetliner impact. The global response examines the kinetics of the cask/jetliner impact. For the analyses discussed in this report, the global analysis results in an exit velocity of the cask after impact. Exit velocity refers to the residual velocity after the cask "exits" the initial jetliner impact event. The global analyses were performed using an Eulerian computer analysis code. The spacing between the casks is known and a determination of the cask velocity as a function of time and distance was necessary to assess cask-to-cask impacts.

Ex 3
p. 181Ex #2
p. 186Ex 3
p. 182Ex #2
p. 18d

Finite element (FE)

analyses were performed for these tasks.

(U) Once the jetliner impacts the field of casks, it is very difficult to determine which of the many possible resulting scenarios may occur. Modeling the complete jetliner and cask (or casks) in detail is not practical with current technology. Therefore, in many instances, different aspects of the problem were decoupled by performing individual, independent analyses to evaluate the cask systems vulnerabilities. The field of storage casks has the potential of subsequent cask-to-cask impacts, with the secondary impacts becoming a largely chaotic problem.

(U) These analyses for a single representative scenario will be discussed in more detail in Sections 2 and 3. Appendix A and B give the complete results for all of the analyses performed for this study.

1.3.2 Examining the Response to a Subsequent Fire (U)

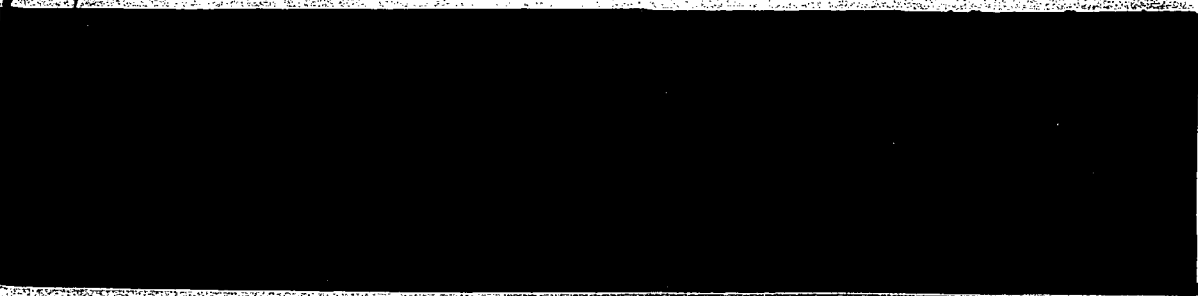
(U) The attacks on the WTC and the Pentagon clearly demonstrate the potential seriousness of ensuing fires from large jetliner crashes (ASCE, 2002; FEMA, 2002)



Ex #2 p. 18e

SGI Ex 3
p. 18f

A survey of previous jetliner crashes was used to establish the potential fire duration.

Ex #2
p. 18g

1.3.3 Examining the Source Term and Consequences (U)

(U) Source term estimates were developed based on the structural response of cask system. Earlier work (Sprung et al., 1990) relates individual fuel rod failure to a failure strain level. A failure strain criterion of 1% (Sanders et al., 1990) is used to represent rod failure.

[REDACTED]

[REDACTED]

[REDACTED]

[REDACTED]

Ex # 2
p. 19a

Ex # 2
p. 19b
Ex 3 p. 19c
Ex # 2
p. 19d

Ex # 3
p. 19e

1.4 Roadmap to an Exploration of the Cask Vulnerabilities (U)

(U) This report consists of four sections. Following this introduction, Section 2 covers the scenario selection for the attack, as well as the associated structural and consequence analysis for the selected scenario. For a field of storage casks, there are many possible scenarios of the jetliner impacting the cask and the subsequent events. Section 2 is an examination of details of a realistic sequence of events that could likely happen. This realistic set of events is termed the 'selected scenario' that is analyzed in detail in the main body of this report. The selected scenario is both credible and realistic, based on the September 11 attacks. Detailed evaluations of the selected and other scenarios are given in Appendix A and B for impacts and Appendix C for fires. Additional analyses detailed in the appendices provided a comprehensive assessment of cask performance under a wide range of attack scenarios. A brief summary is given in Section 3. The references for the body of the report are listed in Section 4.

2 Field of HI-STORM Storage Casks (U)

(U) The increasing number of storage cask facilities used for the storage of spent fuel provides a potential target for terrorist attacks like those of September 11th, 2001. This study examines the potential vulnerabilities of such an attack on a facility containing a field of HI-STORM storage casks. Future reports will document similar examinations of other storage casks and transportations packages.

2.1 Complexity of Scenarios (U)

(U) When considering a single cask, there are a large number of potential impact locations and orientations on the cask that could be examined. If a field of casks is considered, the geometric possibilities become overwhelming. A crash into a field of casks results in a chaotic event, during which many secondary cask-on-cask impacts may occur. Cask layout, approach direction and speed of the airplane, and how accurately a pilot could direct the airplane all influence the geometric possibilities. A realistic threat must be considered, but dismissing scenarios as unrealistic is difficult.

The cask is approximately 1/3rd the height of the Pentagon and 1/67th the height of the World Trade Center towers.

Figure 2-1.

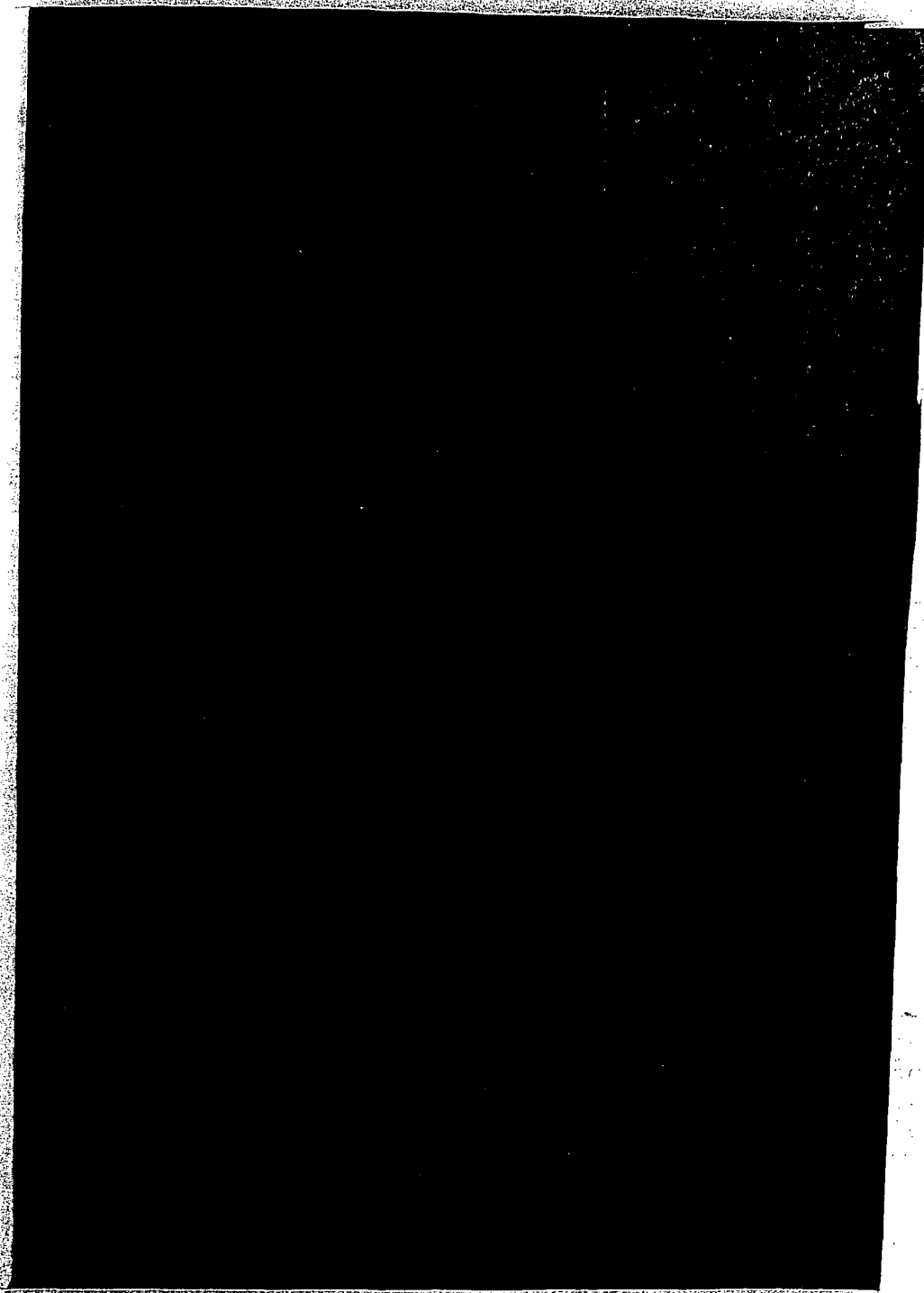
The contents of this figure are unclassified.

Ex. 2
p. 20a

Ex. 2
p. 20b

Ex. 3
p. 20c

Ex. 2
p. 20d



p. 21a
Ex. 3

Figure 2-2. Scale Views of the Jetliner and the Field of Storage Casks (U).
The contents of this figure are unclassified.

(U) As seen in Figure 2-2, the possibilities for the impact analysis are numerous. The horizontal angle of approach (θ) can vary from perpendicular to the long axis of an individual pad to parallel to this axis. The impact position along the pad (x) can vary from the first cask to the fourth cask. The vertical angle of approach (α) can vary from horizontal to vertical. The vertical position (h) of impact can vary from the bottom of the cask to above the top (initial impact on the top surface rather than the side). Within the scope of this study, it is not possible to assess the vulnerability of the storage cask array to all possible impacts (in a complete vulnerability assessment all possible impacts and variations in the airplane and impact speed would be considered). Multiple analyses were performed in this study to evaluate a broad range of possibilities. Despite all the geometric possibilities discussed above, the post-impact thermal environment is nearly independent of the impact scenarios reviewed in this report.

(U) In the main body of this report, only one reasonable scenario is discussed in detail. The reasoning for choosing the scenario and relationships between the chosen scenario and other possible scenarios are also given. The detailed results for the structural and thermal analyses are given in the Appendices. In addition, the appendices discuss other analyses that support the review of other scenarios and the codes and material models used.

2.1.1 Analyses Performed (U)

(U) Numerous analyses were performed for this study. Parametric studies helped finalize parameters used in the study, analyses were performed to understand how the results would change with varying impact orientations, and some analyses were performed to support model development. Details of most of these analyses are provided in the appendices. All of these analyses helped establish the final realistic scenario to examine the potential vulnerabilities of a field of storage casks.

2.1.1.1 Global and Local Structural Analyses (U)

(U) Global analyses were performed to determine the resulting force on individual casks in the impacted field and the exit velocities of impacted casks. This was important in understanding the jetliner-to-cask momentum transfer required to evaluate cask-to-cask impacts. Approximately 15 analyses were performed using the Eulerian shock physics code, CTH, to model the jetliner and impacted casks. Parametric studies were performed to verify material property parameters, modeling techniques, and impact orientation issues (see Appendix A).

(U) Eulerian codes model material flowing through the model mesh. Therefore, a mesh that encompasses the whole jetliner model becomes an extremely large and time-consuming analysis to complete. Since only a portion of the jetliner's mass can interact with a single cask during impact (because the jetliner is much larger than the cask), an evaluation was conducted to explore the possibility of using a reduced jetliner model to evaluate the jetliner impacts.

[REDACTED] The resulting average force on the cask calculated from each analysis was compared, along with the cask velocity as a function of time. [REDACTED]

Therefore, for subsequent analyses,

Ex 2
p. 22a

Ex 2
p. 22b

the simplified jetliner model was used for the global analyses. Material parameters for both the airplane and the HI-STORM cask are provided in Appendices A and B.

(U) Since there is some uncertainty involved in determining the material properties of the casks and the jetliner, a small number of parametric analyses were performed to determine the influence that the cask's concrete and steel properties and the jetliner's fuselage properties had on the resulting force and velocities of the casks.

[REDACTED] This type of analyses can be a challenge using CTH. Therefore, a parametric study was performed to evaluate the best method of incorporating the pad beneath the cask.

(U) The various analyses performed as part of the global analysis for this study are discussed in more detail in Appendix A. The analyses discussed above resulted in the finalizing of the global analyses parameters used in the final global analyses, discussed below. These analyses provided the resulting average force as a function of time on the cask and the cask velocity as a function of time and displacement used for detailed local analyses of the cask integrity.

(U) Local analyses were then conducted to examine vulnerabilities of the cask system (the overpack and the MPC) in detail. These analyses were used to determine the cask integrity and can be divided into three categories:

1. Hard component impact,
2. Cask-to-Cask impact, and
3. MPC evaluation.

[REDACTED] A variety of impact orientations were examined for each component. The engine impacts were examined using an engine force time history loading function developed from test data of jet engine impacts into concrete wall panels (see Appendix A) and additionally examined using an FE model of the engine.

(U) An impact by the jetliner into the field of casks results in subsequent cask-to-cask impacts during the impact event (i.e., while the jetliner is still interacting with the field of casks) and from the residual velocity of the casks afterwards. In this report, this residual velocity is termed "exit" velocity since it is the velocity from which the cask exits the initial jetliner impact event.

(U) To explore the vulnerability of the cask, numerous cask-to-cask impacts at different velocities and orientations were examined.

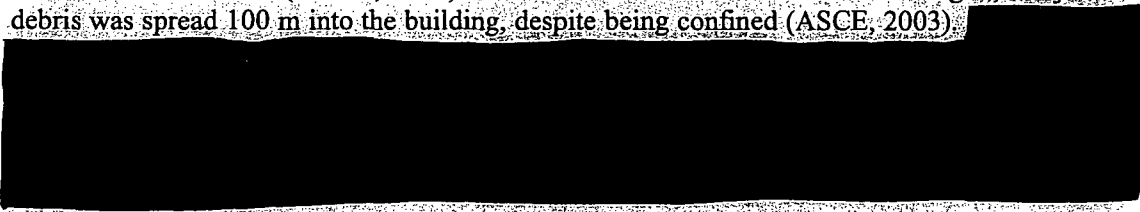


Ex. 3
p. 24a

(U) Details of all the calculations are provided in the appendices and, for those calculations that support the selected scenario, are provided in the body of this report.


2.1.1.2 Thermal Analyses (U)

(U) The attacks on the World Trade Center (WTC), Pentagon, and the crash in Pennsylvania on September 11, 2001, did not result in long duration jet fuel fires. For the World Trade Center attacks, it is estimated that the jetliner fuel that did not burn in the initial fireball was consumed in less than 5 minutes (FEMA, 2002). If one considers the attack on the Pentagon, the jetliner debris was spread 100 m into the building, despite being confined (ASCE, 2003).



Ex. 2
p. 24b

(U) In addition to the experiences from the September 11th attacks, other studies support the conclusion that long duration fires from this type of event are unlikely. Fisher et al. (1990) presented data that suggest that long duration fires do not result from high-speed airplane impacts.



Ex. 2
p. 24c

(U) As stated above, the experiences of the September 11th attacks and previous studies suggest that the pooling of fuel for the scenario considered is very unlikely. In addition, the casks and any jet fuel not burned in the initial fireball will have a velocity due to the jetliner impact. The casks and the fuel will come to rest at some location. However, it is unlikely that a pool of fuel and a cask will end up co-located. Thus, a long-duration, co-located pool fire is deemed not a

credible event for a jetliner impact into an open field of storage casks.



Ex. 3
p. 25a

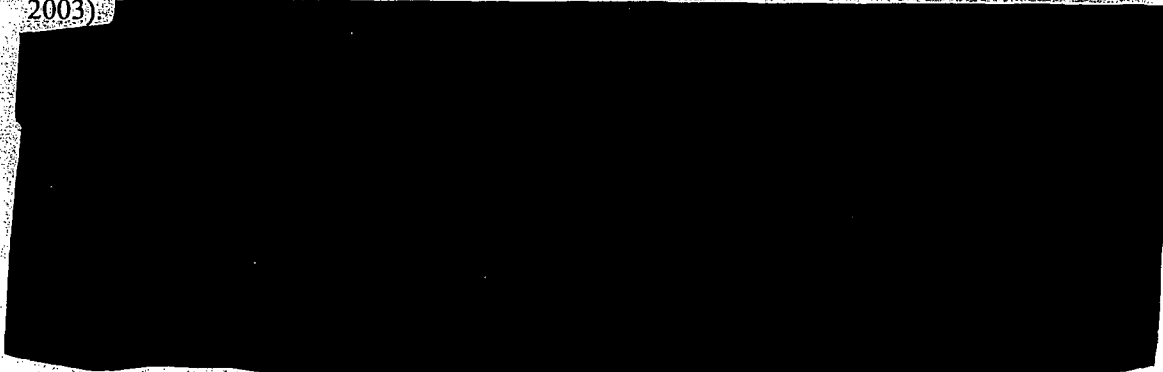
Ex. 2
p. 25b

2.1.2 Selected Scenario (U)



Ex. 1
p. 25c

(U) A report by Tieszen (1995) states that the potential of a pool fire resulting from a high-speed impact of a plane on a hard surface is very low. Anecdotal evidence from historical accidents (Kimura, 2003) also suggests that the probability of pool fires occurring due to the jetliner's remaining fuel after impact is very low. If one considers the September 11th, 2001 attack on the Pentagon, the jetliner debris was spread 100 m into the building, despite being confined (ASCE, 2003).



Ex. 2
p. 25d

Ex. 1
p. 25e

2.2 Analysis of the Field of Storage Casks for the Selected Scenario (U)

(U) With the scenario established, the following sections discuss in detail the analyses that evaluate the vulnerability of a field of HI-STORM casks to this scenario. The analysis methodology follows what was discussed previously in Section 1.3.

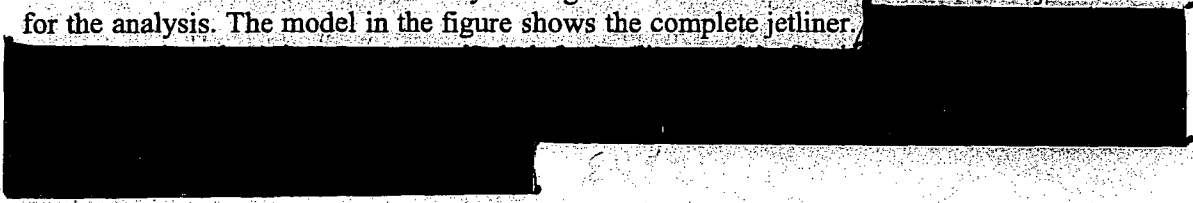
2.2.1 Structural Analysis of the Selected Scenario (U)

(U) As discussed in Section 1.3 and in detail in Appendix A, the structural analyses were decoupled (global and local analyses) to evaluate the response of the cask array to an impact by a jetliner. The global analysis evaluated the momentum transfer of the jetliner to the cask. This was followed by a local analysis that evaluated the containment of the cask system.

2.2.1.1 Global Analyses for the Selected Scenario (U)

(U) The goal of this global analysis was to determine the following: (1) the momentum imparted to a single cask by the impacting jetliner, (2) the cask velocity as a function of time during the event, and (3) the load history on the cask. The CTH Eulerian shock physics code was used to conduct the analysis. The CTH family of codes encompasses the mesh generation, analysis modules, and post-processing software for the analysis of transient, large deformation, and/or problems involving strong shocks. CTH is a well-established code used for numerous defense-related applications. Of interest here are impact applications. CTH has been used extensively for anti-armor and hypervelocity impact applications, where impact velocities are typically greater than 1 km/s (e.g., see Hertel, 1992; Kmetyk and Yarrington, 1994; and Wilson, et al., 1998). There has been limited extension of CTH to lower impact velocity regimes (e.g., see Silling, 1992). A more thorough discussion of CTH and how it was used for this problem is given in Appendix A.

(U) Given the size and complexity of the problem being modeled, simplified representations of the airplane and cask were considered to approximate the momentum transfer and resultant cask velocity. When considering large cask arrays, the initial airplane impact can lead to subsequent cask-to-cask interaction. The outcome of the global analysis was used to provide a set of initial conditions for the detailed local analyses. Figure 2-3 shows the CTH model of the jetliner used for the analysis. The model in the figure shows the complete jetliner.



Ex 2
p 26a

SGI
p. 27a
Ex. 3

Figure 2-3. Full Jetliner Model used in CTH Analysis (U).
The contents of this figure are unclassified.

SGI
p. 27b
Ex. 3

Figure 2-4. Simplified CTH Jetliner Model Impacting a Single Cask (U).
The contents of this figure are unclassified.

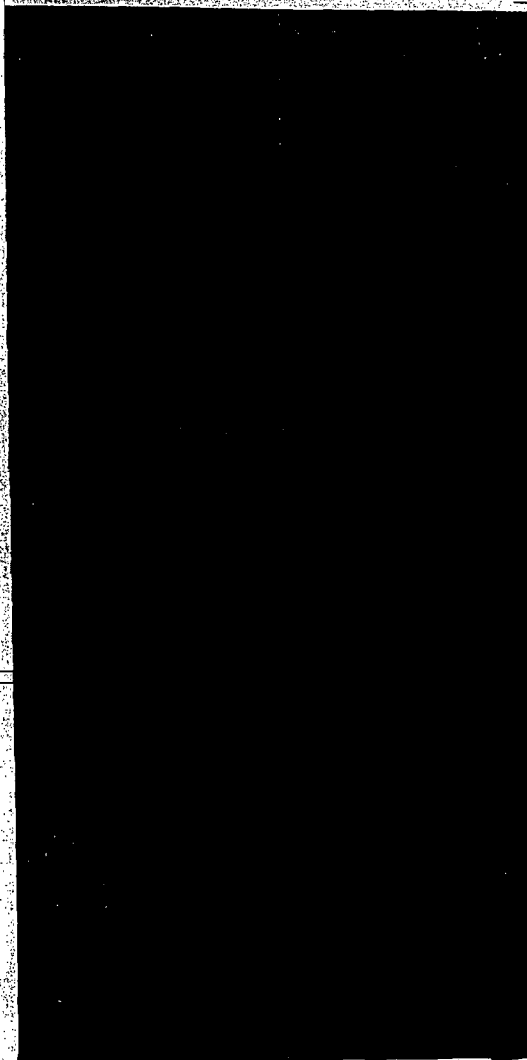
(U) The CTH analysis of a horizontal impact into a single HI-STORM cask was performed to determine the average force as a function of time on the cask and the velocity of the cask as a function of time. This analysis also enabled determining of the cask velocity as a function of its translation. Figure 2-5 shows results of the CTH analysis of the jetliner impacting the casks.

Ex. 2
p. 27c

EX 1
p. 27d



Ex 1
p. 28a



SGI
p. 28b
Ex. 3

Figure 2-5.

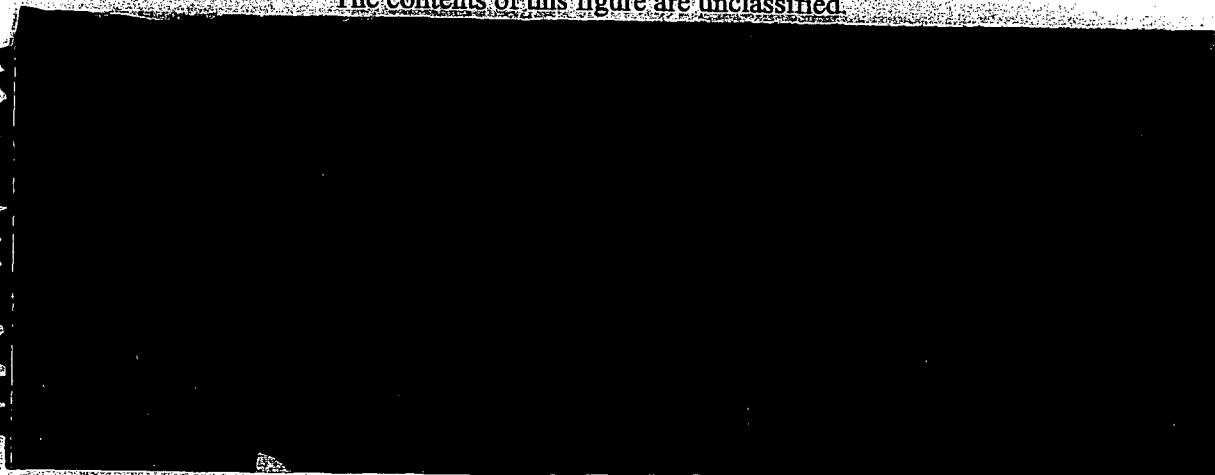
The contents of this figure are unclassified.

ex. 2
p. 28c



SGI
p. 29a
EX 3

Figure 2-6. Total Force on the HI-STORM Cask (1 N = 0.22 lbs) (U).
The contents of this figure are unclassified.



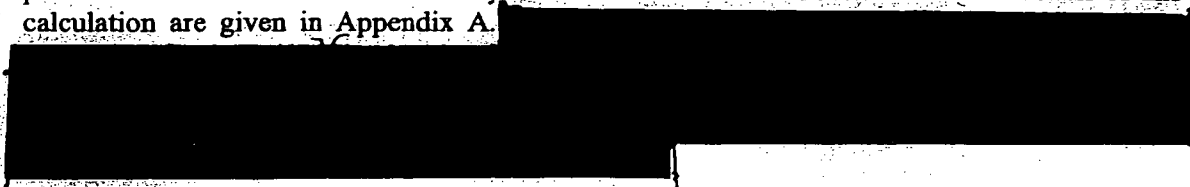
EX 1
p. 29b

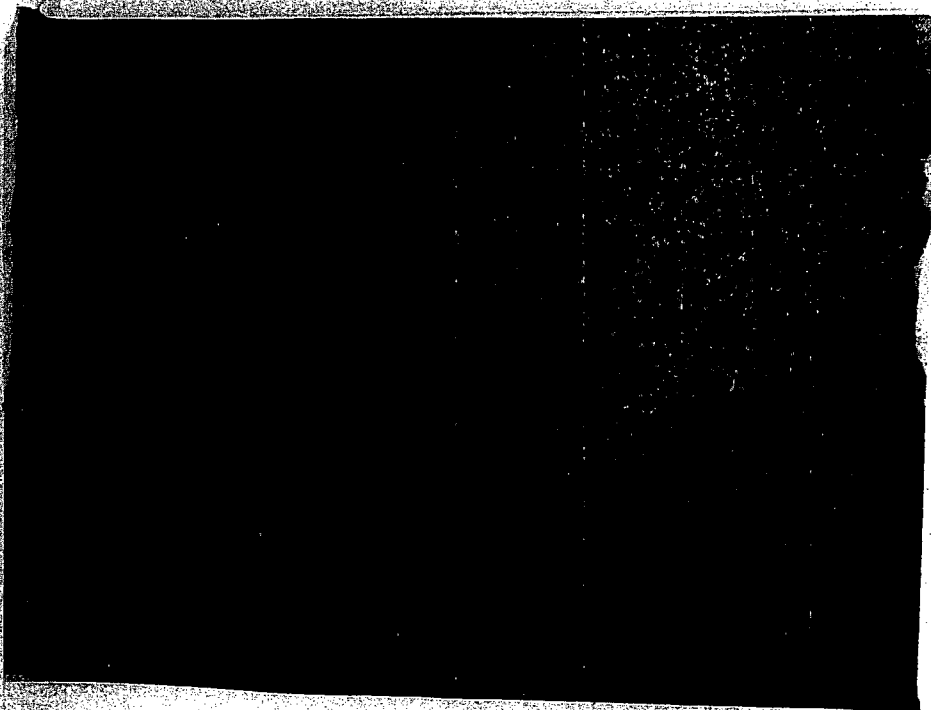
Ex 1
p. 30c

Figure 2-7. Cask Horizontal Velocity as a Function of Time (1 mph = 0.447 m/s)
(U).

The contents of this figure are classified C.

(U) To verify the exit velocity calculated using the CTH code, a simple calculation was performed to calculate the exit velocity based on conservation of momentum. The details of this calculation are given in Appendix A.

Ex 3
SGI
p. 30b
Ex. 2
p. 30c



EX 1
p. 31a

Classified

Figure 2-8. Cask Horizontal Velocity as a Function of Displacement (1 mph = 0.447 m/s; 1 m = 3.28 ft) (U).

The contents of this figure are classified C.

[Redacted]

The schematic in Figure 2-9 shows a typical pad layout. The figure shows the clear spacing between the casks.

[Redacted]

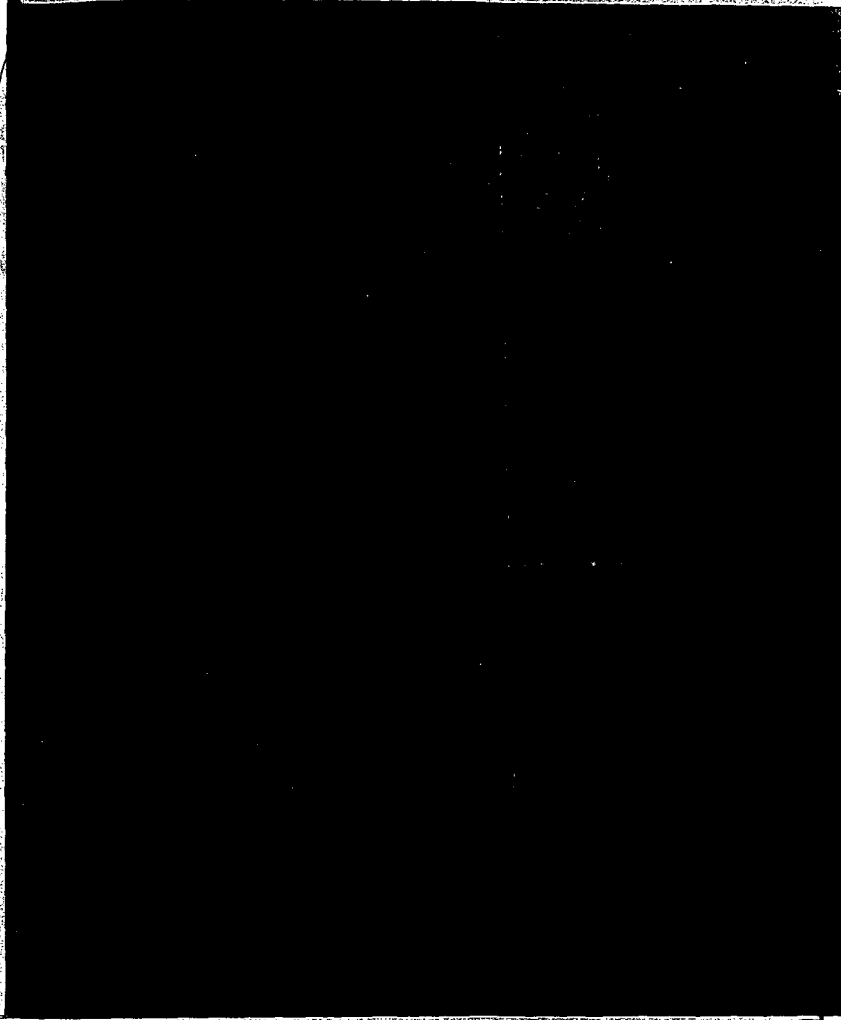
Ex. 2
p. 31b

Ex. 2
p. 31c

The third case requires some additional explanation. It is possible for the casks to be placed on the pad in varying order.

[Redacted]

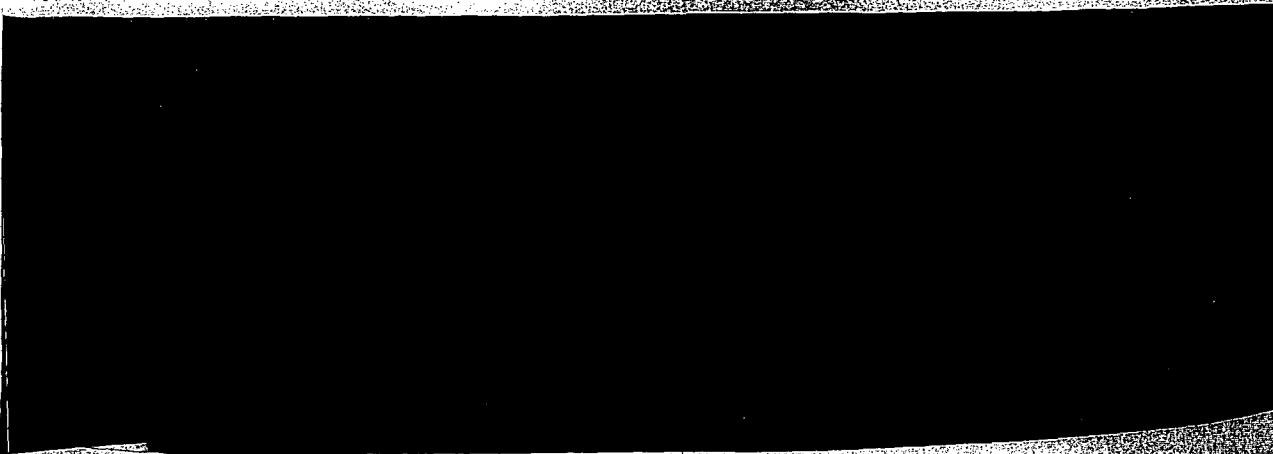
Ex. 2
p. 31d



Ex # 2
p 32^a

Figure 2-9. Clear Spacing Distances between the Casks on a Typical Pad Layout (U).

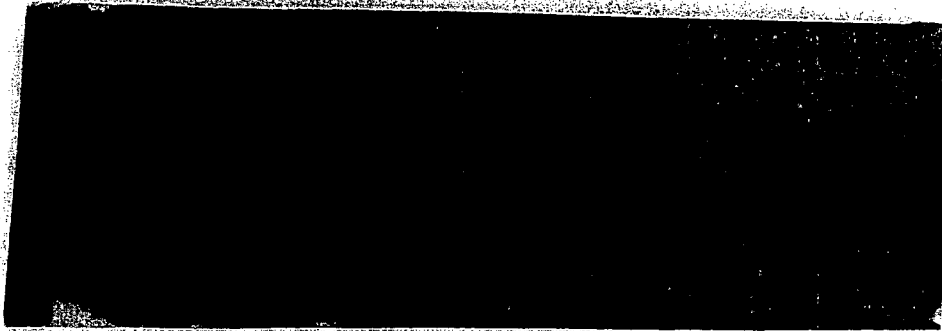
The contents of this figure are unclassified.



EX 1
p. 32b

Table 2-1. Cask Velocity as a Function of Separation Distance (U).
The contents of this table are classified C.

Classified



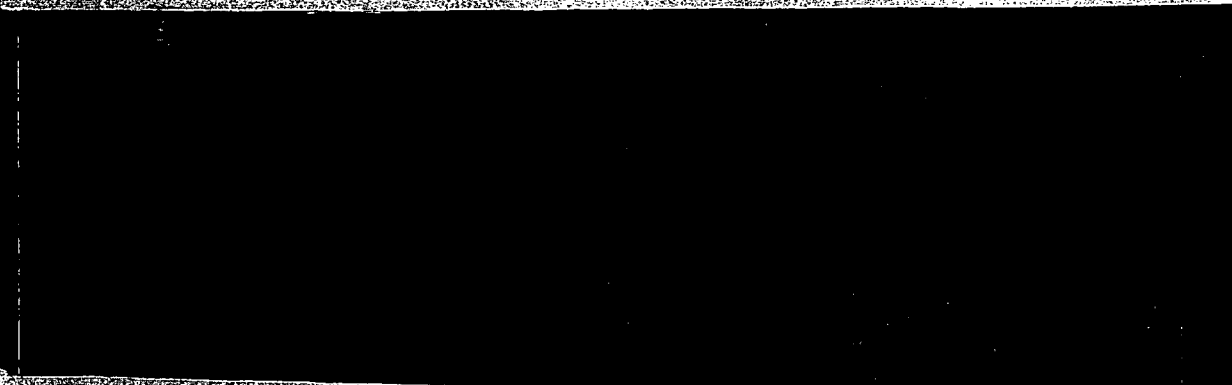
EX 1
p. 33a

2.2.1.2 Local Analyses for the Selected Scenario (U)

(U) Detailed FE analyses were performed to evaluate the cask overpack and MPC response to determine if there would be a release caused by the loadings imparted to the cask from a jetliner impact into the field of storage casks. Complete details of the analysis results are provided in the appendices. Material properties were based on values from the Safety Analysis Report (SAR) (Holtec International, 2000), and where actual test data for material properties was found, this was used. Parameters like force and velocity were taken from the global analysis discussed in the previous section and applied in these local analyses of the cask. Presented below are the analyses that were performed in support of the scenario discussed in Section 2.1.2. Other analyses were performed that could be applied to other possible scenarios. These other analyses helped verify the appropriateness of the FE model, bound potential vulnerabilities, and provide insight into the behavior of the cask under different scenarios.

Classified
EX 1
p. 33b

2.2.1.2.1 Cask-to-Cask Impact for the Selected Scenario (U)



Classified
EX 1
p. 33c

Ex. 1
p. 34aEx. 2
34b

Therefore, an analysis was conducted of the jetliner impacting one cask that translates and impacts a second cask using the force time-history developed from the global analyses discussed in Section 2.2.1.1.

(U) The force time-history applied to the cask impacted by the jetliner is shown in Figure 2-6. The loading is applied to the FE model in the form of pressure, to the zones shown in Figure 2-10.

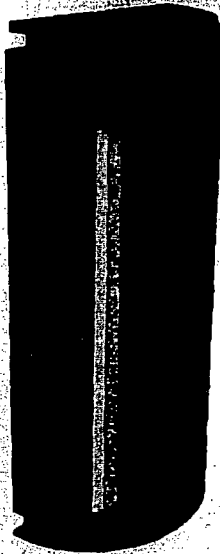
Ex. #2
p. 34c

Figure 2-10. Loading Zones for Force Time-History of Jetliner (U).

The contents of this figure are unclassified.

(U) To produce the pressure necessary to represent the net total CTH loading shown in Figure 2-6, the total force was corrected to account for the overall cosine distribution shown in Figure 2-10, and the area of jetliner projection loading.

Ex. #2
p. 34d

[REDACTED]

(U) The analysis of cask-to-cask impact while the jetliner loads the front cask was the most detailed and complex FE analysis performed. [REDACTED]

[REDACTED] All HI-STORM components are modeled to achieve the correct kinematics during the scenario. This included the total mass of the MPC, shown in Figure 2-11. [REDACTED]

Ex. 2

p35

Ex. 2
p35bEx. 2
p35cSGI
p35d
Ex. 3

Figure 2-11. Cask-to-Cask FE Model with Jetliner Pressure Force Time-History (U).

The contents of this figure are unclassified.

(U) Also included in this model is element death for the main bolts. [REDACTED]

[REDACTED] A complete description of the FE model is provided in Appendix A.

(U) Several images of the deformed model at different times are shown in Figure 2-12 (VonMises stress is shown distributed on the steel components, and damage is distributed on the concrete portions of the model). [REDACTED]

Ex. 2
p35eEx. 2
p35f

Ex. 2
p. 369Ex. 1
p. 365

(U) Also shown in Figure 2-13 is the acceleration time-history of the MPCs for both casks.

Ex. 3
p. 366

Therefore, the MPC's had to be evaluated for such impacts. These analyses are discussed below in Section 2.2.1.2.3.

Ex. #2
p. 364

2.2.1.2.2 Hard Component Impact Analysis for the Selected Scenario (U)

Landing gear and engines from the jetliners that attacked the WTC buildings proceeded through the widths of the buildings and fell 4 to 6 city blocks from the buildings (FEMA, 2002).

Ex. #2
p. 366

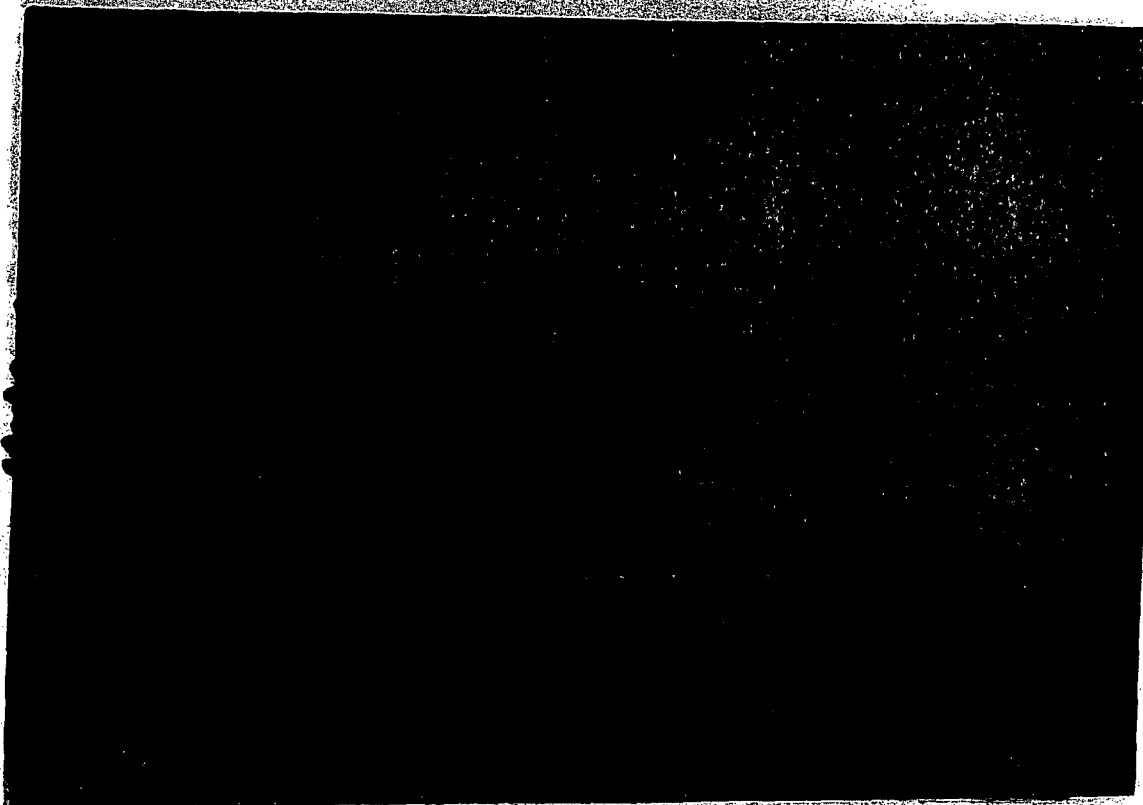
In addition, the black box from the jetliner (which is housed in the tail of the jetliner) was found near the nose landing gear in the wreckage, indicating that the jetliner continued to break up and crush, with the mass coming to a rest near the farthest point of penetration (ASCE, 2003). National Transportation and Safety Board (NTSB) reports of airplane crashes also cite the hard components of the airplane as being found separated from the wreckage and penetrating significantly into soil (e.g., NTSB, 2000).

Ex. 2
p. 364

SGI
p-37a-Ex.3

Figure 2-12. Selected Deformed Images of Whole Jetliner Loading of the Cask-to-Cask Impact: VonMises Stress Contours for the Steel and Damage Parameter for the Concrete Portions of the Model (1 MPa = 145 psi) (U).

The contents of this figure are unclassified.

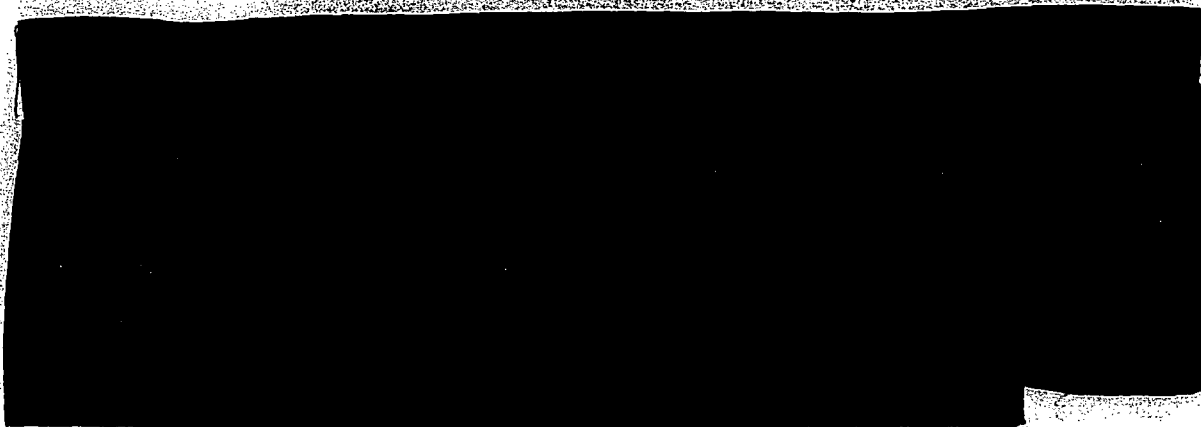


Classified

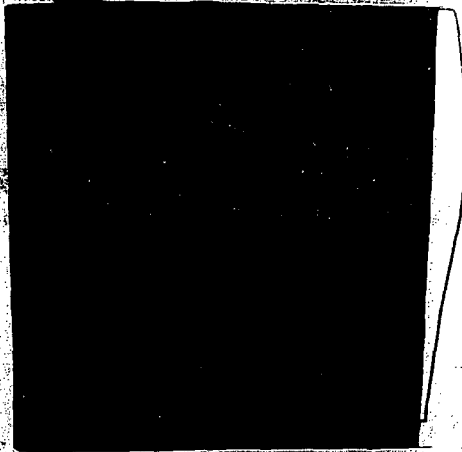
Ex 1
38a

Figure 2-13. Resulting Velocity and Acceleration of the Two Casks in the Cask-to-Cask Impact with the Jetliner Pressure (1 m/s = 2.24 mph) (U).

The contents of this figure are classified C.



Ex. 2
p. 38b



Ex #2
p39a

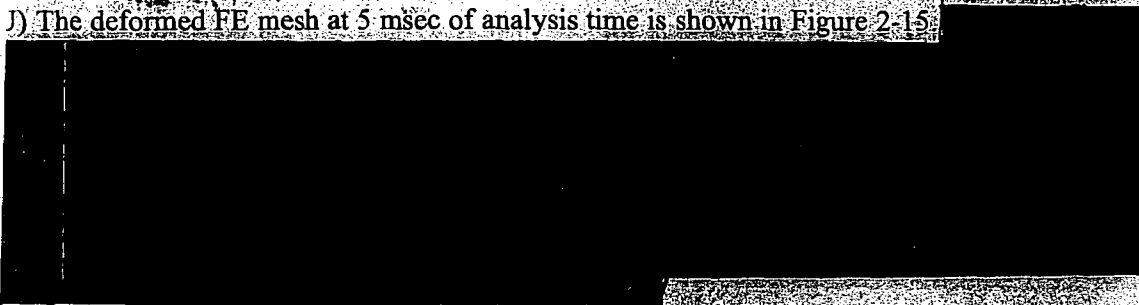
Figure 2-14.



The contents of this figure are unclassified.

Ex 3
p39b

J) The deformed FE mesh at 5 msec of analysis time is shown in Figure 2-15.



Ex #2
p39c



Ex #2
p39d

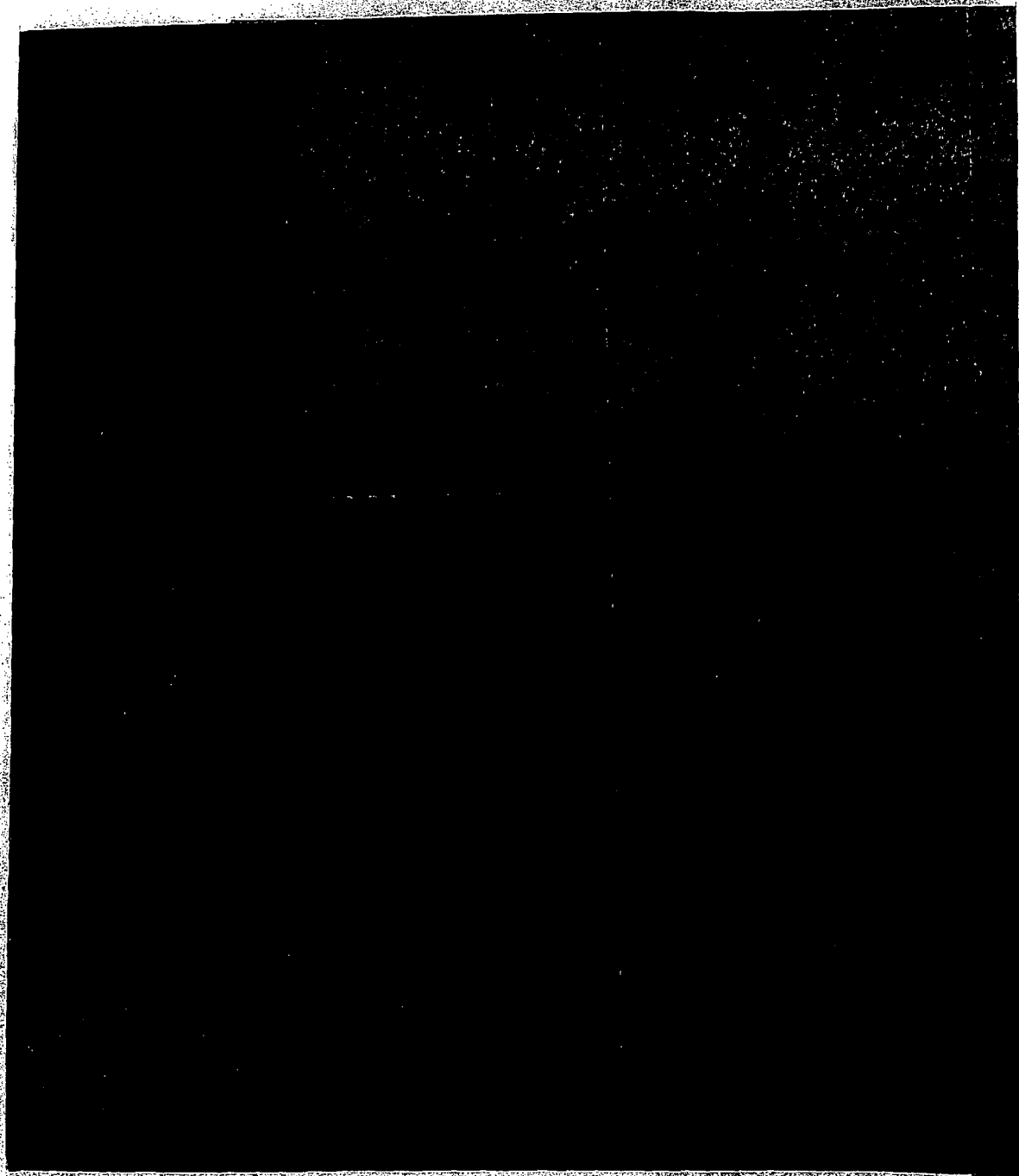
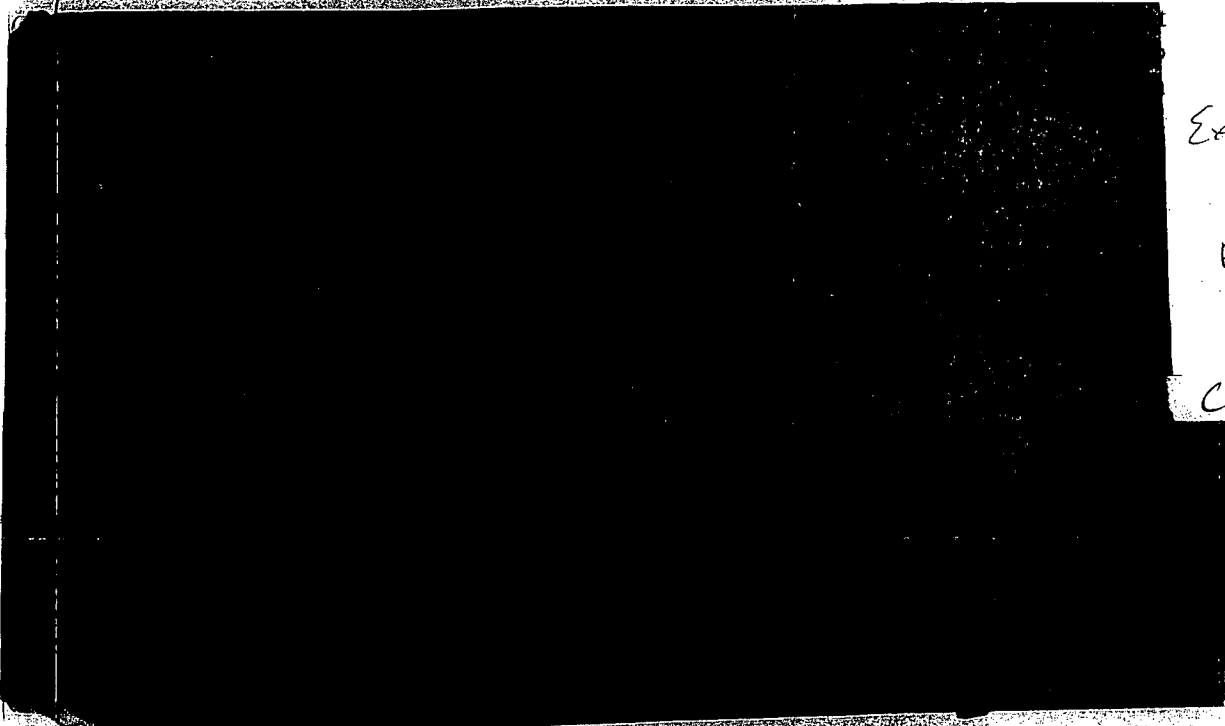


Figure 2-16.

The contents of this figure are unclassified.



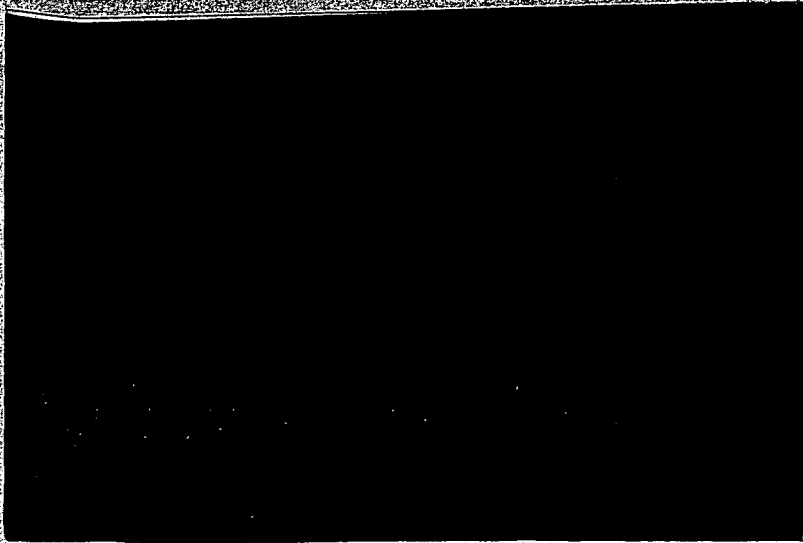
Ex #2
p41a

Ex.3 p41b

Ex.2 p41c

Classified

Ex1
p41d



Ex.3
p41e

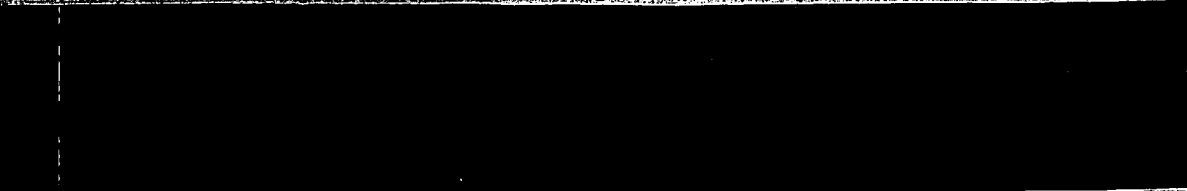
Ex.2
p41f

Figure 2-17



The contents of this figure are unclassified.

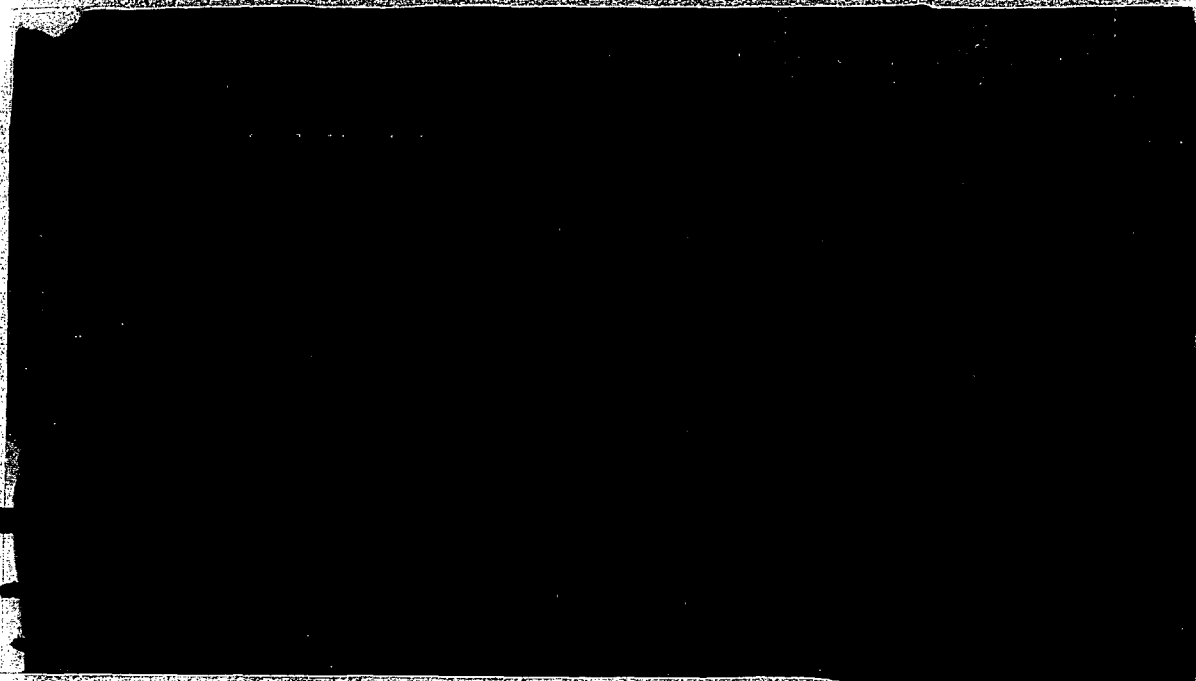
Classified



Ex.1
p41g



Ex 1
p. 42a

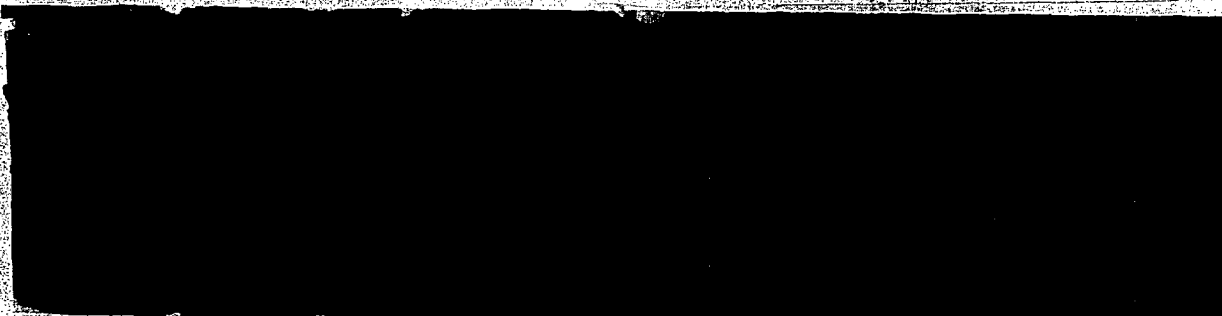


Ex 1
p. 42b

Figure 2-18.

The contents of this figure are classified C

Ex 3
p. 42c

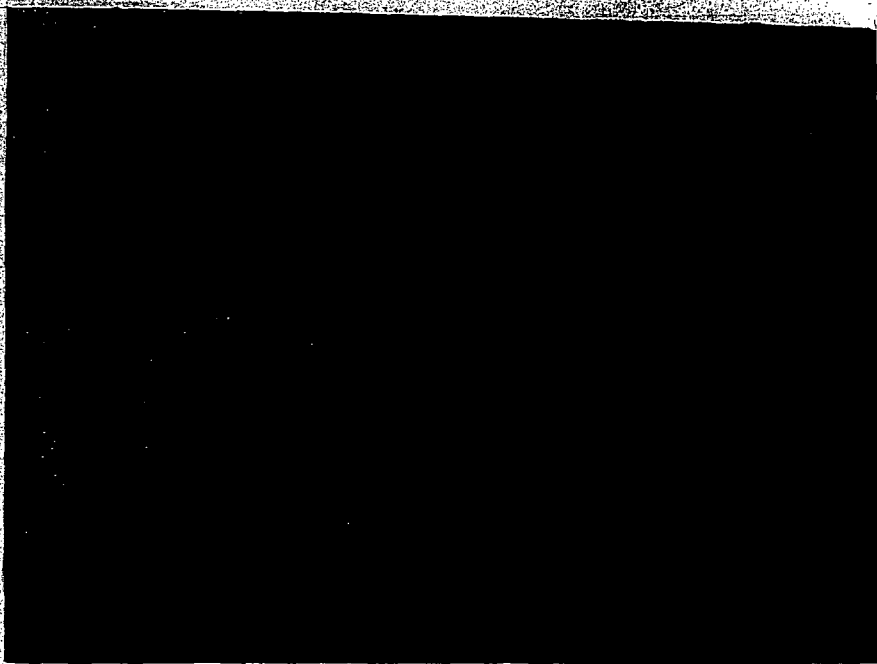


Ex 1
p. 42d



Ex. 2
p43a

The contents of this figure are unclassified.



p43b
Ex. 3

Figure 2-20.

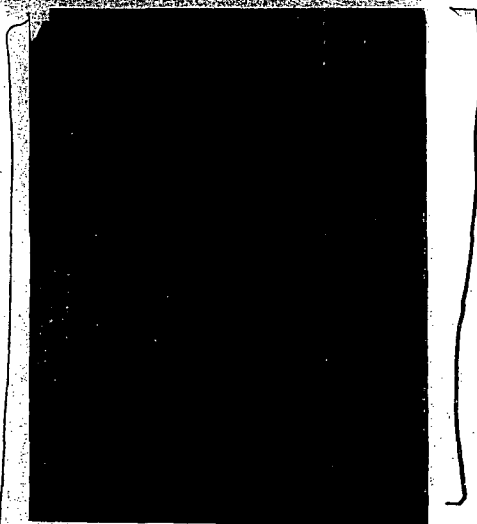
The contents of this figure are unclassified.

Ex. 2

p. 43c



Ex 1
p 44a



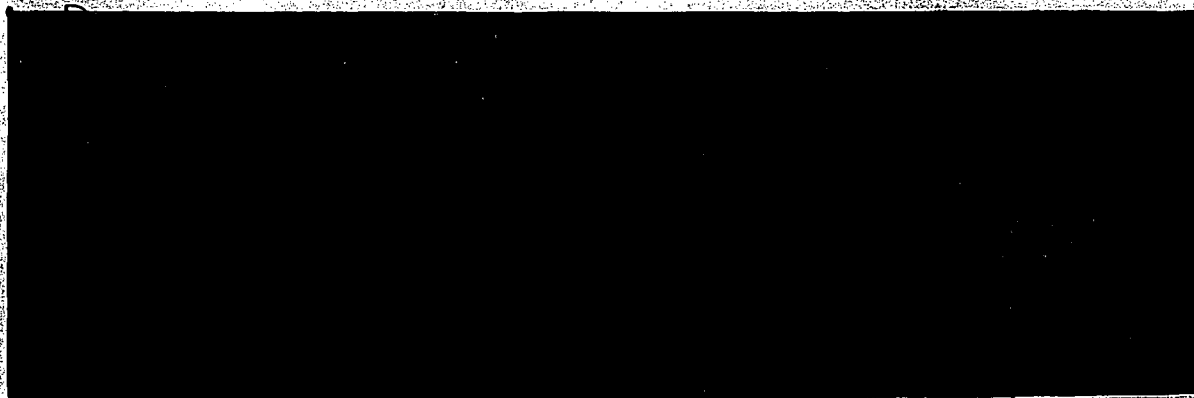
SGI-EX. 3
p. 44b

Figure 2-21.

The contents of this figure are unclassified.

Ex # 2
p. 44c

2.2.1.2.3 MPC Integrity Analysis (U)



Ex # 2
p. 44d

Class. free

~~CONFIDENTIAL~~ - NSI

Final Draft



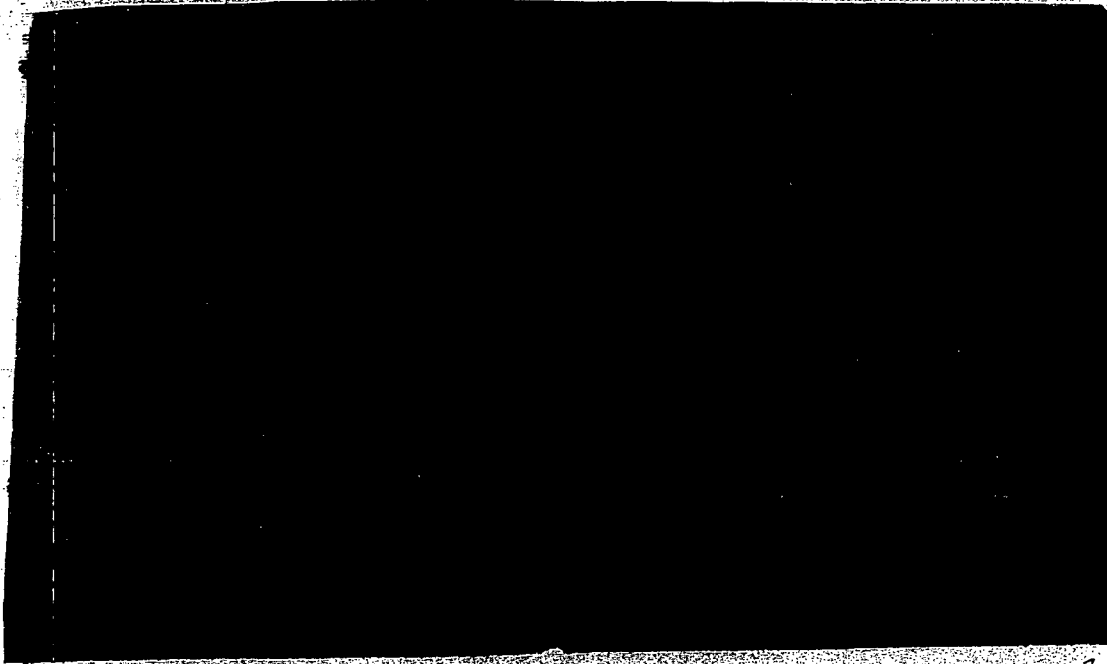
Ex 1
p. 45a

figure 2-22.



The contents of this figure are classified C

Ex 2 — P. 45b



Classified

Ex 1
p. 45c

figure 2-23.



The contents of this figure are classified C.

Ex 2
p. 45d

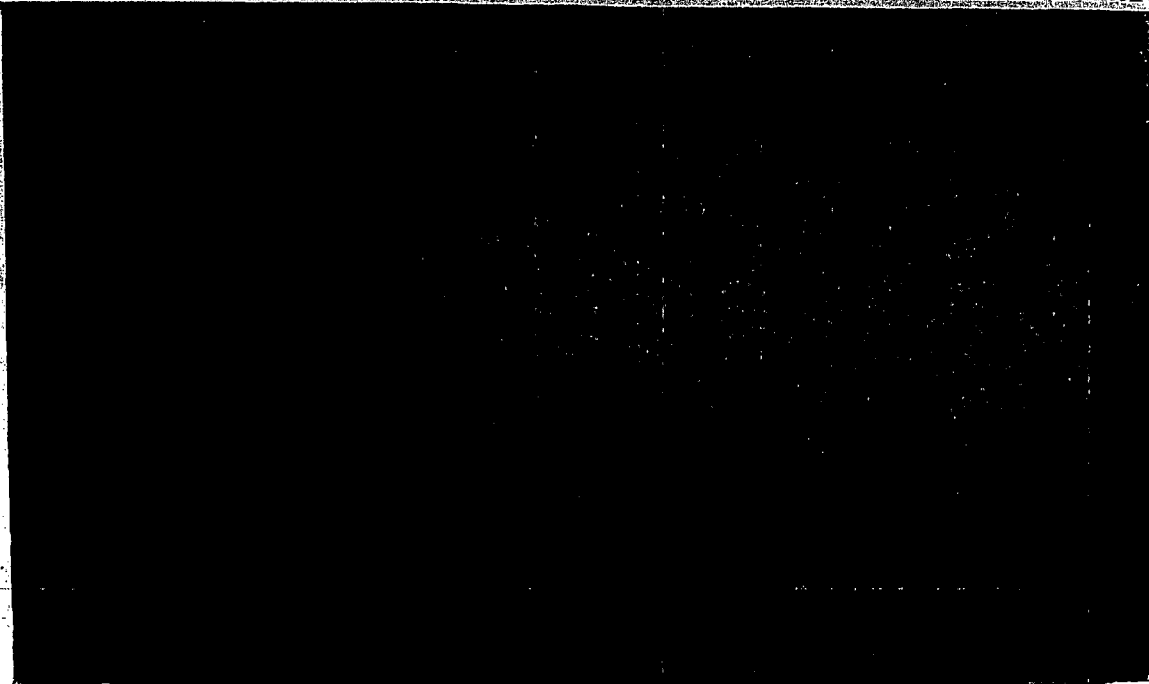
Ex 1
p. 46a

Figure 2-24.

The contents of this figure are classified C.

] Ex #2 p. 46b

Ex. 2
p. 46c

Decoupling the analysis of the MPC and the overpack saved considerable computation time. The analyses were performed for the MPC impacting a rigid surface that represents the overpack or a hard surface in the jetliner impact zone. The results of these analyses were used to determine if the MPC would fail during some of the jetliner impact scenarios examined in this study.

Ex #2
p. 46d

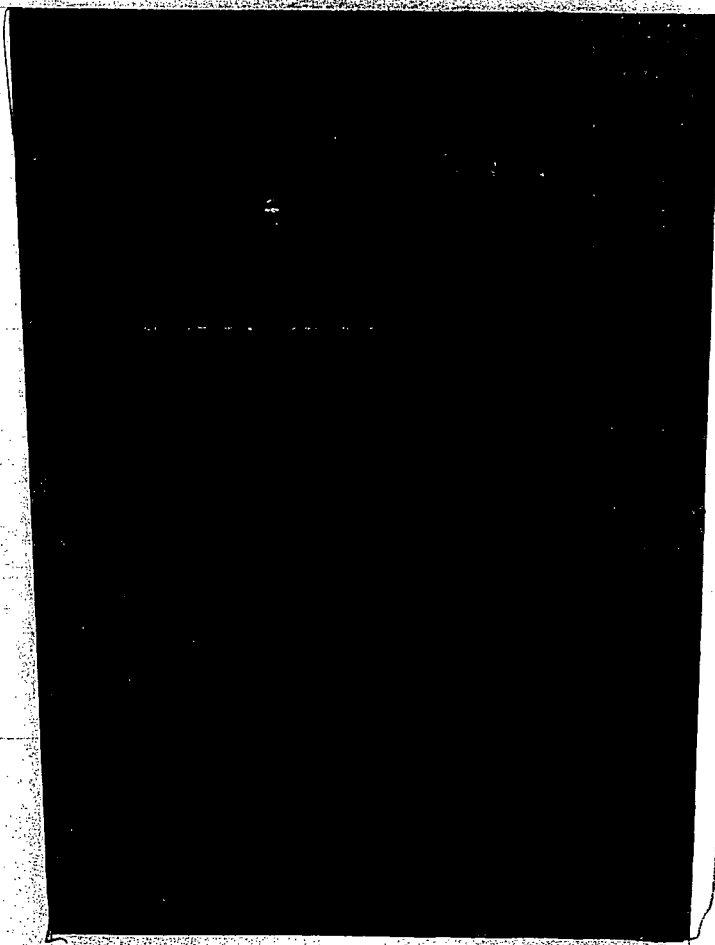
(U) A schematic drawing of the MPC is shown in Figure 2-26.

Ex #2
p. 46e

The density of the material was adjusted so that the total weight of the canister is equal to the specified design weight. Modeling the fuel assemblies in this manner does not allow

Ex #2
p. 46f

direct determination of the fuel rod behavior, but assesses the loads that the assemblies apply to the canister. Modeling the MPC internals in this manner was considered representative of either PWR or BWR fuel. This analysis does not provide enough detail to determine the loads the fuel rods or basket would apply to the MPC canister. Analysis with detail such as this is beyond the resolution of this study.



Ex 2

p47 a

Figure 2-25. Schematic of Gap Between MPC and the Overpack (U).

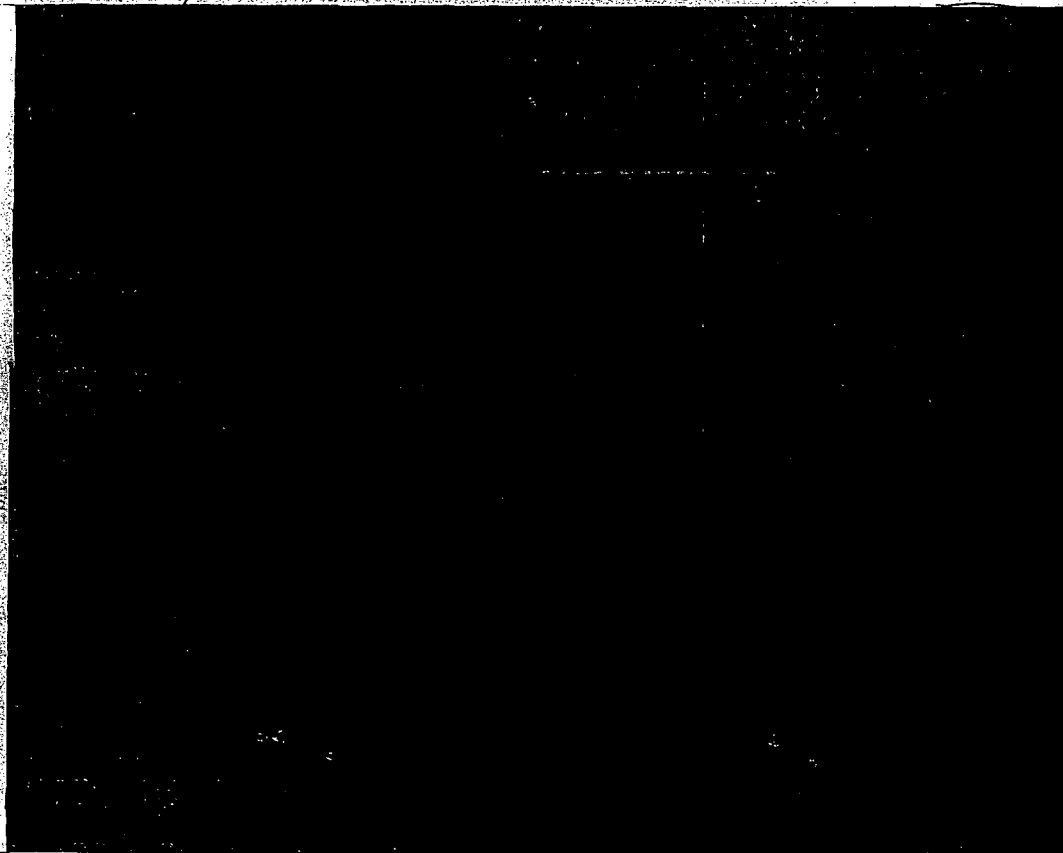
The contents of this figure are unclassified.

(U) The material of the canister body is modeled using the ductile tearing model in PRONTO3D (Wellman and Salzbrenner, 1992; Wellman et al, 1993; Stone and Wellman, 1993). This is a power-law-hardening model with a ductile failure criterion. The ductile failure criterion is based on an evolution equation in which the plastic strain increment, scaled by the stress ratio, accumulates until a critical value is reached, at which point the ductile tearing is initiated. This scalar parameter is the ductile Tearing Parameter (TP). The evolution equation for this parameter is as follows:

$$TP = \int_0^{\bar{\epsilon}_p} \left(\frac{2\langle \sigma_{\max} \rangle}{3(\sigma_{\max} - \sigma_m)} \right)^4 d\epsilon_p$$

where $\bar{\epsilon}_p$ is the plastic strain, σ_{\max} is the maximum principal stress, and σ_m is the mean (hydrostatic) stress

$$\sigma_m = \frac{(\sigma_{11} + \sigma_{22} + \sigma_{33})}{3}$$



Ex #2
p48.1

(U) The integral accumulates plastic strain only when the maximum principal stress is positive, as indicated by the Heavieside function brackets, $\langle \rangle$. Thus, plastic strain with a negative maximum principal stress causes no change in the values of TP.

(U) The critical value of TP for a particular material is established by analyzing a tensile test specimen. The TP for the specimen is then calculated using the computed stress state from the FE model and substituting the strain-to-failure, $\bar{\epsilon}_f$, as the upper integration limit. This provides a critical value of TP, which can be used to predict failure in other analyses. The strain-to-fail is

puted from the reduction in area of the tensile specimen in the actual tensile test.

Ex #2

The FE model of the MPC is presented in Figure 2-27, with a detailed view of the canister wall and lid weld region presented in Figure 2-28. There is a plane of symmetry through the center axis of the cask body, so only half of the canister is modeled.

Ex. 2

p. 49b

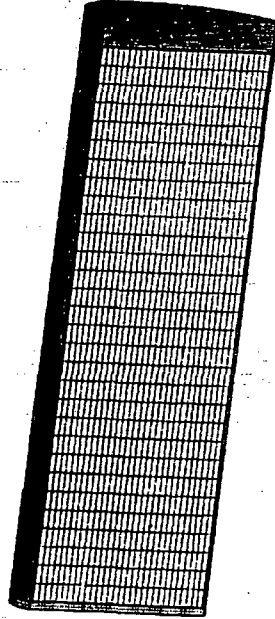


Figure 2-27. Canister FE Model (U).

The contents of this figure are unclassified.

Figure 2-30

Figure 2-31 show the equivalent plastic strain in the canister wall and end plates.

Ex. 2
p. 49cEx. 2
p. 49dSGI
p. 49e

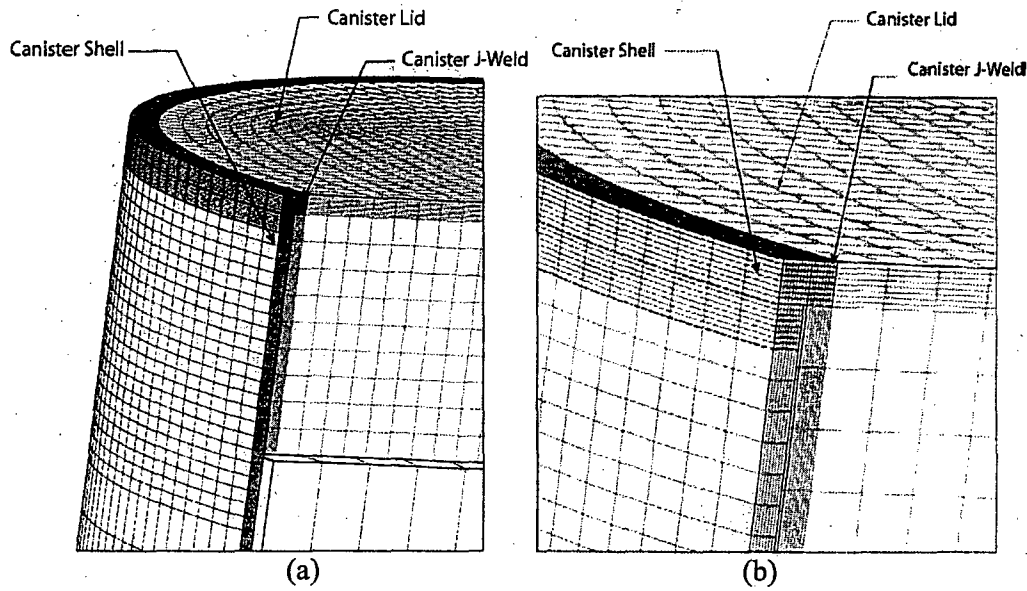
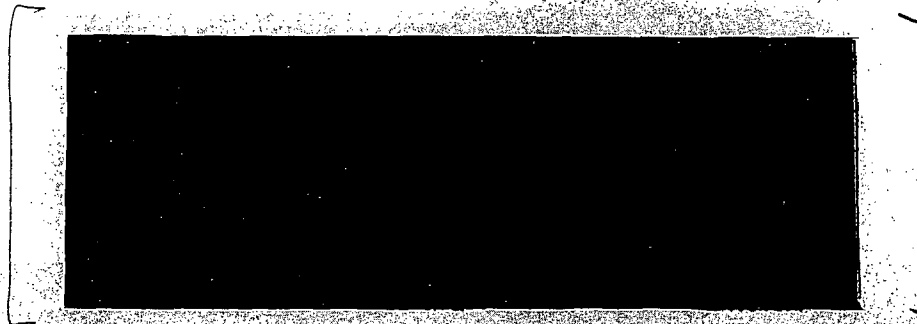


Figure 2-28. A Detailed View of Canister Lid Weld Region (U).

The contents of this figure are unclassified.



Ex 3
p. 50a

Figure 2-29.

The contents of this figure are unclassified.

Ex #2
p. 50b

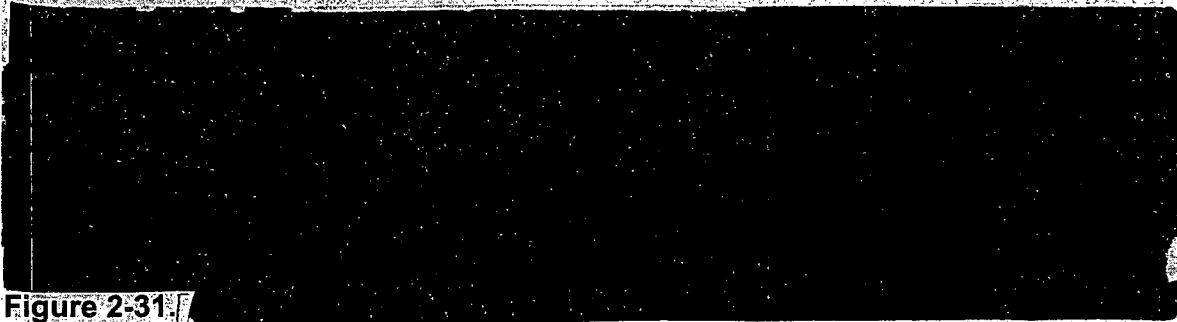


Ex 1
p. 50c

Figure 2-30.
(U)

The contents of this figure are classified C.

Ex #2
p. 50d



Ex. 1
p51a

Figure 2-31.

Ex. #2
p51b

The contents of this figure are classified C.

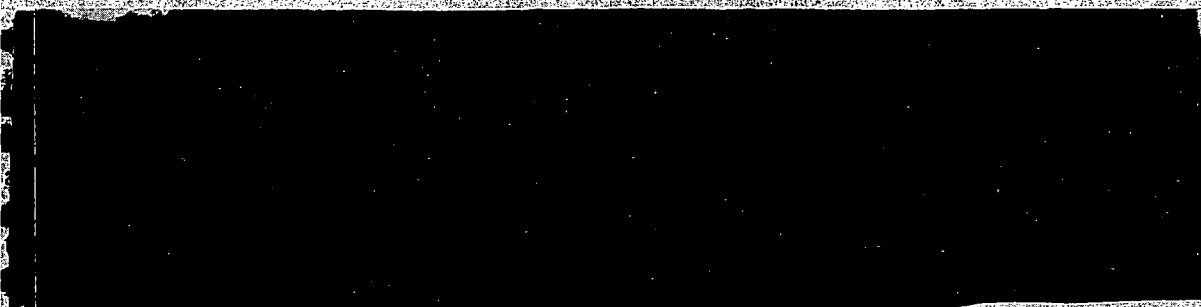


Ex. #2
p51c

Figure 2-32.

The contents of this figure are unclassified.

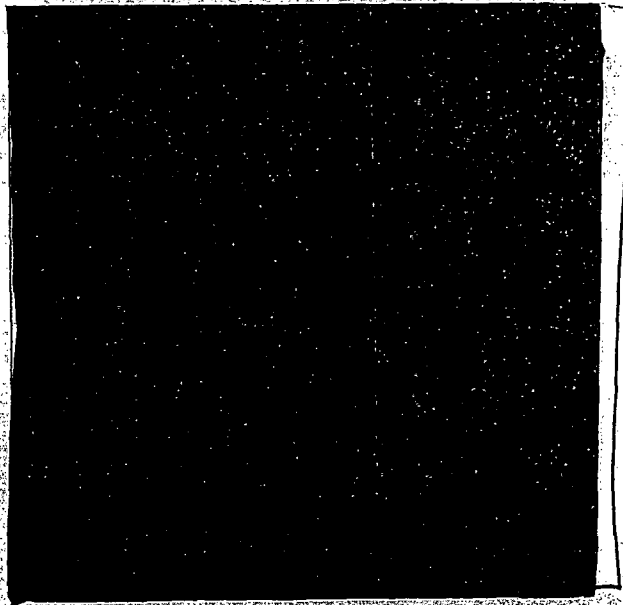
Ex. #2
p51d



Ex. 1
p51e



Ex. 3 p51f
Ex. 2 p51g
Ex. 3 p51h



S6I Ex. 3
p52.9

Figure 2-33.

The contents of this figure are unclassified.

Ex #2
p52.4

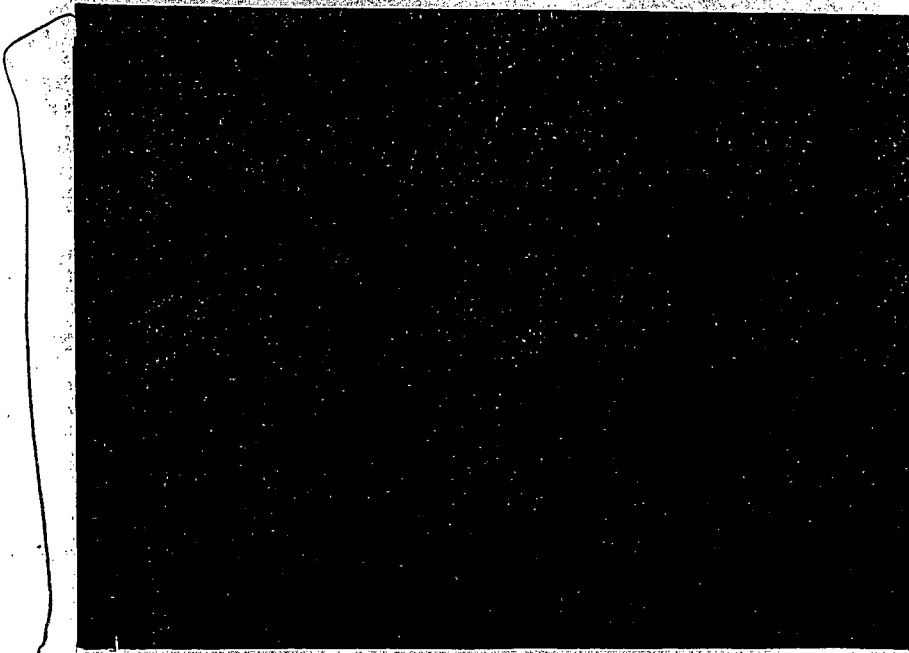


Classified Ex. 1
p52.6

Figure 2-34.

The contents of this figure are classified C.

Ex #2
p52.2



SGR

p. 53a Ex. 3

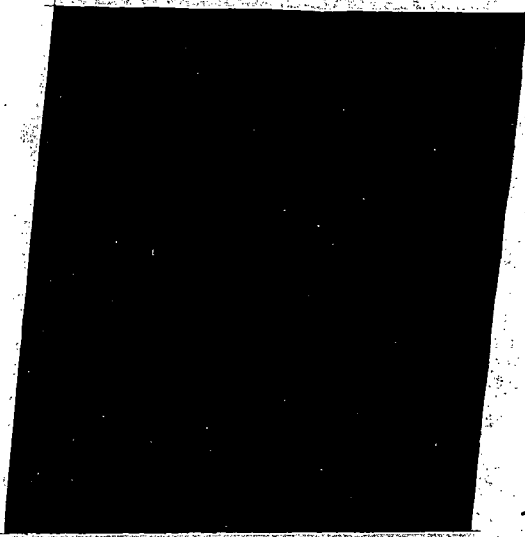
Figure 2-35.



Ex. 2

The contents of this figure are unclassified.

p. 53b, Ex. 2



SGR p. 53c Ex. 3

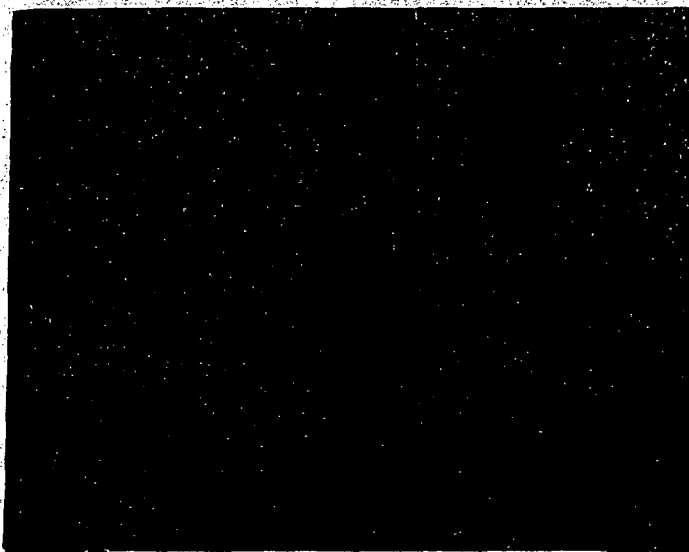
Figure 2-36.



The contents of this figure are unclassified.

Ex. 2

p. 53d



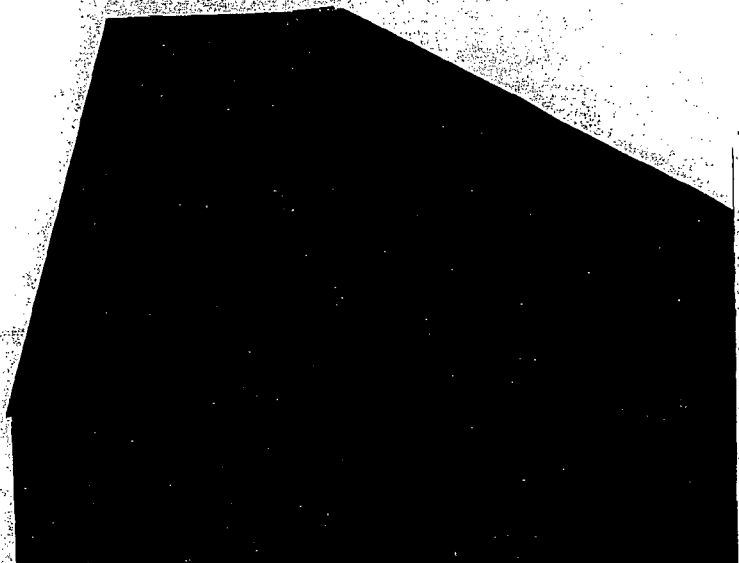
SGT Ex. 3
p54a

Figure 2-37.



The contents of this figure are unclassified.

Ex. 2
p54b



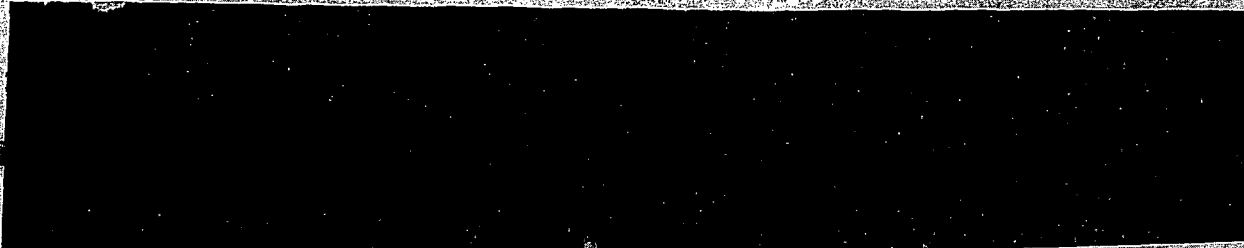
SGT Ex. 3
p54c

Figure 2-38.

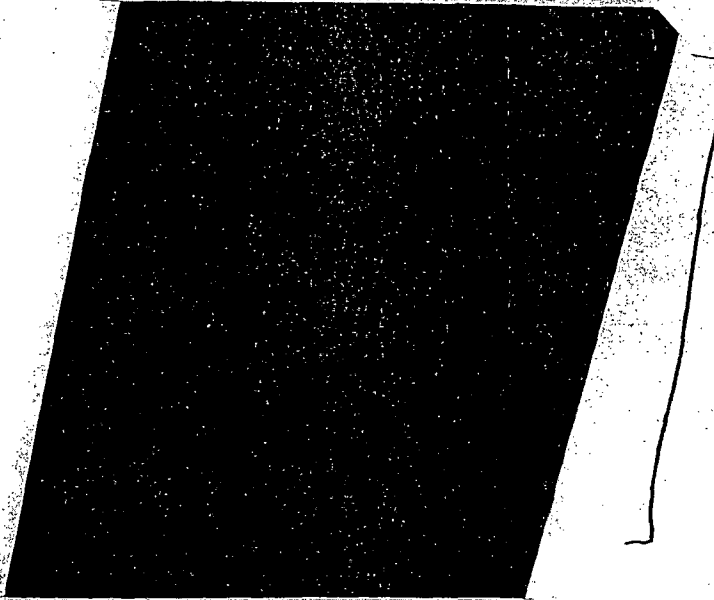


The contents of this figure are unclassified.

Ex. 2
p54d



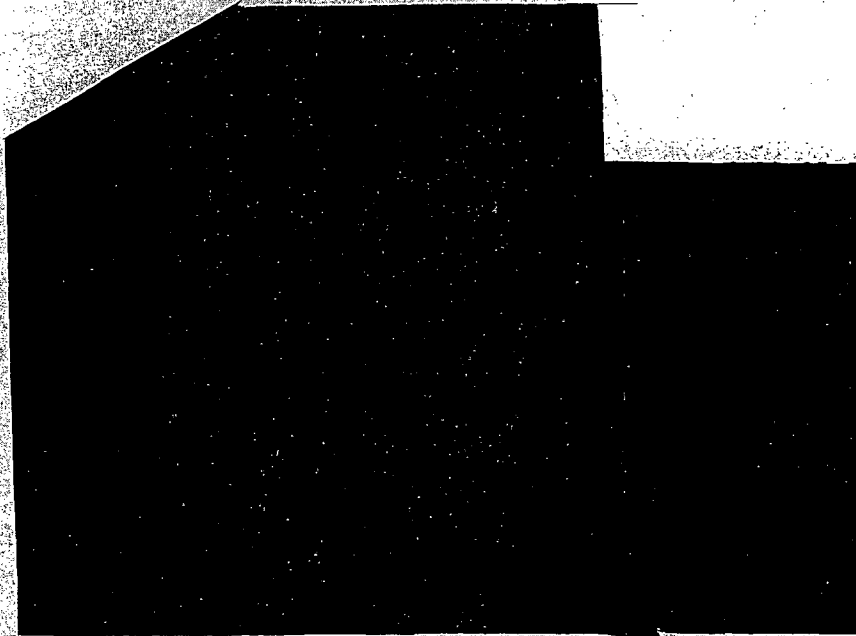
Ex. 1
p54e



SGI, Ex. 3
PSS.a

Figure 2-39.

The contents of this figure are unclassified.



Ex #3
SGI
PSS.c

Figure 2-40.

The contents of this figure are unclassified.

Ex #2
PSS.d

Ex1
p569

2.2.2 Thermal Analysis for the Selected Scenario (U)

(U) Based on the previous discussion in Section 2.1.1.2, a long-duration, fully engulfing, colocated fire following impact is not deemed a credible event for the selected scenario.

OWD-SRI
p564
Ex2

Classified

p560
Ex1

Classified

~~CONFIDENTIAL~~ ~~NSI~~

Final Draft

Ex1
p.57a

Ex #3
p.57b

Classified

p.57c
Ex1

p.57d
Ex.3

out-spl
p.57e
Ex2

SG1 Ex3
p.57f

~~CONFIDENTIAL~~ ~~NSI~~

P58a
Ex 3
561

P58c

2.2.3.2.1 Cask Inventory (U)

Ex 1
P58b

(U) Because an ORIGEN calculation provides output for over 800 radionuclides, the number of radionuclides in the ORIGEN output was reduced by dividing the 10-year cooled amount of each radionuclide by its A_2 value (IAEA, 1987; CFR) and then selecting the smallest set of these normalized curie amounts that yielded a sum greater than 99.9 percent of the sum of all of these normalized curie amounts. This procedure reduced the ORIGEN output set of over 800 radionuclides to a much smaller set of 12 radionuclides that are important for the estimation of radiological health effects.

(U) Seven radionuclides were added to this initial reduced set of 12 radionuclides. Five radionuclides, Ru-106, Cs-134, Ce-144, Pm-147, and Eu-154, were added so that all of the inventories used in this study contained the same set of radionuclides. Next, in order to have a noble gas in the inventory, although eliminated by the A_2 screen, Kr-85, the noble gas with the largest curie amount in the ORIGEN inventory for 10-year cooled high burnup spent BWR fuel, was added to the reduced set of radionuclides using the Ci amount calculated by ORIGEN. Finally, Co-60 was added to the reduced set of radionuclides so that release of Co-60 due to the spallation of CRUD (Hazelton, 1987) from rod surfaces could be addressed.

(U) Co-60 is formed by activation of Ni-60. Ni-60 is a constituent of Zircaloy, the alloy from which fuel rod cladding is fabricated, and also of the CRUD (Hazelton, 1987) deposits that form on fuel rod cladding surfaces during reactor operation. Because Co-60 that is formed by activation of the Ni-60 constituent of the alloy from which fuel rod cladding is manufactured cannot escape from the cladding matrix, while Co-60 that is formed by activation of Ni-60 in CRUD can be released by spallation of these deposits from cladding surfaces, the Co-60

inventory calculated by ORIGEN for activation of constituent Ni in cladding was replaced by an estimate of the amount of Co-60 in CRUD. This estimate was developed as follows. If the peak surface concentration at discharge of $595 \mu\text{Ci}/\text{cm}^2$ for Co-60 in CRUD on average burnup BWR spent fuel rods (Sandoval, 1991b) is assumed to apply to the total surface area of all of the rods in one GE 8x8 fuel assembly, then the Co-60 discharge inventory for that assembly will be about 60.6 Ci. Then, if high-burnup fuel is in the reactor for 5 cycles and average burnup for 3 cycles, at discharge there will be 5/3 more CRUD on high-burnup rods than on average burnup rods. Further, decay will reduce Co-60 amounts by 0.5 during each successive 5-yr period. Lastly, measurements of the variation of CRUD layer thickness with position on spent fuel rods (Lukic, 2003) indicate that $d_{\text{CRUD,Av}}/d_{\text{CRUD,Max}} = 0.3$. Thus,

$$\begin{aligned}\text{Co-60} &= I_{\text{discharge}}(d_{\text{CRUD,Av}}/d_{\text{CRUD,Max}})(\text{burnup factor})(\text{decay factor}) \\ &= (60.6 \text{ Ci})(0.3)(5/3)(0.5)^2(3.7 \times 10^{10} \text{ Bq/Ci}) = 2.80 \times 10^{11} \text{ Bq}\end{aligned}$$

(U) Table 2.2 lists the final reduced set of 19 radionuclides and gives the amount of each nuclide in Becquerels in one high-burnup, General Electric, 8x8, ten-year cooled, spent fuel assembly.

SG1
Ex 3
P59a

Table 2.2. Radionuclide Inventory (Bq) of One High-Burnup, BWR/6, 8x8, Ten-Year Cooled, Spent Fuel Assembly (U).

The contents of this table are unclassified.

Nuclide	Amount (Bq)	Nuclide	Amount (Bq)	Nuclide	Amount (Bq)
Co-60	2.80E+11	Ce-144	7.47E+11	Pu-241	7.70E+14
Kr-85	4.07E+13	Pm-147	4.96E+13	Am-241	1.77E+13
Sr-90	5.00E+14	Eu-154	6.11E+13	Am-242m	2.90E+11
Y-90	5.00E+14	Pu-238	5.85E+13	Am-243	4.51E+11
Ru-106	4.29E+12	Pu-239	2.75E+12	Cm-243	4.44E+11
Cs-134	7.55E+13	Pu-240	5.11E+12	Cm-244	8.33E+13
Cs-137	8.14E+14				

where

P59b
Ex 2
040-SR1

P60a
SG1
EX3

P60b
EX2
and SR1



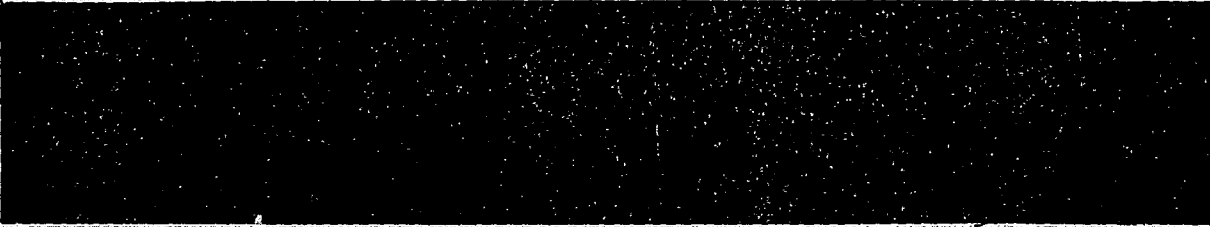
Figure 2-41. Peak Tensile Strains and Rod-to-Rod Pinch Forces for a 13.4 m/s (30 mph) Side Impact of a Model of One Half of One 15x1 Slice of a B&W 15x15 PWR Fuel Assembly (U).

The contents of this figure are unclassified.




Ex1
P60C

¹ C. Beyer, 2003, Personal communication.



(U) **BWR Spent Fuel.** For a GE 8x8 fuel assembly that contains 63 fuel rods and one water rod, reasonable values (Transnuclear, 2000a; Holtec, June 2000c; Holtec, April 2000; Sanders, 1992b) for the length, o.d. cladding thickness, and pitch of these fuel rods; the diameter and the active fuel length of the fuel pellets in one of these rods; and the height and number of fuel rod spacers are $L_{\text{rod}} = 405$ cm, outer $d_{\text{rod}} = 1.25$ cm, $t_{\text{cladding}} = 0.085$ cm (and thus inner $d_{\text{rod}} = 1.08$ cm), $\ell_{\text{pitch}} = 1.626$ cm, $d_{\text{pellet}} = 1.06$ cm, $L_{\text{pellets}} = 366$ cm, $h_{\text{spacer}} = 4.13$ cm, and $n_{\text{spacers}} = 7$ (and thus the distance between spacers, $L_{\text{spacer}} = 58$ cm $= 405$ cm/7).

Ex1
Pg 1aPg 1b
Ex1

(U) **Spent Fuel Pellet Properties.** During reactor operation, compression of fuel cladding and swelling and cracking of the fuel pellets in a fuel rod largely eliminates the rod's fuel-cladding gap and creates an internal network of cracks inside of the pellets that has a free volume about equal to the volume of the fuel-cladding gap in fresh fuel. Abrasion during insertion of the pellets into the rod and vibration during reactor operation causes fuel fines to form on pellet external surfaces and also on pellet crack surfaces. In high-burnup spent fuel pellets, capture of epithermal neutrons by Uranium atoms in the pellet rim produces a friable layer of fuel fines on the outer surface of each pellet. Measurements indicate that the thickness of this friable rim layer (t_{rim}) in high burnup BWR spent fuel is about 150 μm (Manzel, 2002; Einziger, 2004; Manzel, 2000).

(U) Because the body and the rim of high burnup spent fuel pellets have quite different morphologies (Manzel, 2002; Thomas, 1992; Spino, 1996), release of noble gases and of fuel fines from these two regions of a high burnup pellet will be quite different. Like fresh UO_2 pellets, the body regions of high burnup spent fuel pellets consist of sintered 10 μm UO_2

particles. The voids and the internal crack network that form in pellet bodies cause these body regions to have porosities of 5 to 10 percent (Einziger, 2004; Manzel, 2000; Spino, 1996). For spent fuel pellets with burnups of 55 to 60 GWd/MTU, during reactor operation, about 8 percent of the noble gas atoms generated by the decay of fission products diffuse to particle grain boundaries and then escape to the rod free volume through the pellet's internal crack network (Einziger, 2004; Manzel, 2000).

P620
EX 2
DUO
SR1

(U) In the rim layer, 0.1 to 0.3 μm subgrains are generated by the recrystallization of UO_2 and gas atoms in subgrain interiors migrate to subgrain boundaries, where they accumulate in micropores that were formed by clustering of lattice vacancies (Manzel, 2002; Thomas, 1992; Spino, 1996). Increase of gas pressure with time in these micropores is relieved by growth of micropore volumes (Manzel, 2002) (release of the energy stored in the pressurized gas in the micropore creates additional micropore surface by breaking U-O bonds at subgrain boundaries and by plastic deformation of subgrain boundary surface). Measurements (Manzel, 2000; Spino, 1996) show that the porosity of the rim layer ranges from about 10 to 20 percent with 15 percent being typical of fuel with burnups of 60 to 70 MWd/kgU (Einziger, 2004; Manzel, 2000; Spino, 1996). Therefore, $F_{\text{pores,rim}} = 0.15$.

(U) Because distances to grain boundaries are so short in rim layer subgrains, noble gas atoms formed by fission product decay migrate efficiently to rim layer subgrain boundaries. Consequently, 90 percent of the noble gas atoms formed in the pellet rim layer are contained in the micropores that have formed on subgrain boundaries (Manzel, 2000;). Because the impact forces caused by the jetliner/cask and cask/cask impacts will fracture only a small portion of the grain boundaries associated with the UO_2 subgrains that comprise the rim layer, release of noble gases from the rim layer due to impact fracturing should not be substantial.

(U) The volume of fuel pellets in a single BWR rod and the volume of the rim layer on these pellets are given by $V_{\text{pellets}} = \pi(d_{\text{pellet}}/2)^2 L_{\text{active}}$ and $V_{\text{rim}} = \pi d_{\text{pellet}} t_{\text{rim}} L_{\text{active}}$, and thus $V_{\text{rim}}/V_{\text{pellets}} = 4t_{\text{rim}}/d_{\text{pellet}} = 4(150 \mu\text{m}/1.057 \text{ cm}) = 0.057$. But the capture of epithermal neutrons, that causes the rim layer to form, doubles the concentration of radionuclides in the rim layer compared to their concentration in the pellet body (Einziger, 2004). Thus, about 11.3 percent of the total radionuclide inventory in the pellets in a rod resides in the friable rim layer of these pellets and the remaining 88.7 percent of the total inventory is contained in the body of the pellets. Accordingly,

$$F_{\text{RC,k}} = (0.113)(\text{rim release k}) + (0.887)(\text{body release k})$$

P620
EX 2

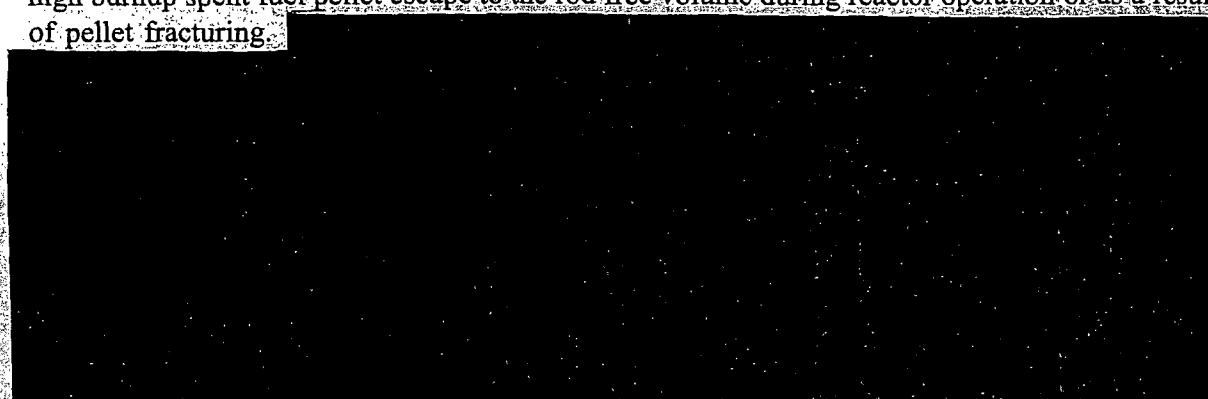
P63a
EX1

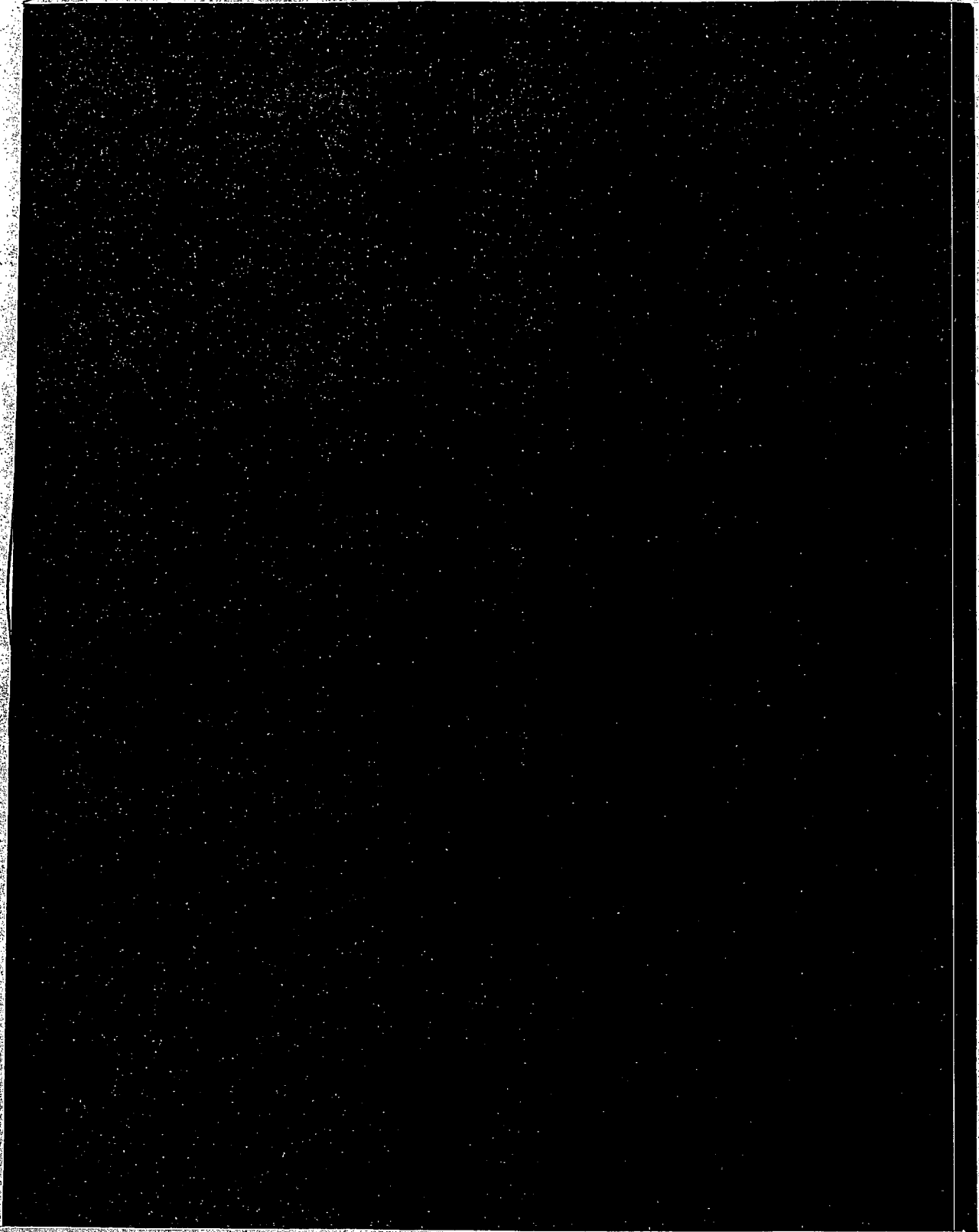
(U) Averaging these two values for P_{He} yields $P_{He} = 11.0 \text{ atm} = (10.5 \text{ atm} + 11.6 \text{ atm})/2$.

(U) The ORIGEN calculation described above shows that one GE, 8x8, 10-year cooled, high burnup BWR spent fuel assembly contains 90 g of Kr and 1436 g of Xe. Therefore, n_{total} , the number of moles of fission product noble gases in a single BWR rod, is

$$n_{total} = [(90 \text{ g}/83 \text{ g mole}^{-1}) + (1436 \text{ g}/131 \text{ g mole}^{-1})]/(63 \text{ fuel rods per assembly}) = 0.191 \text{ moles}$$

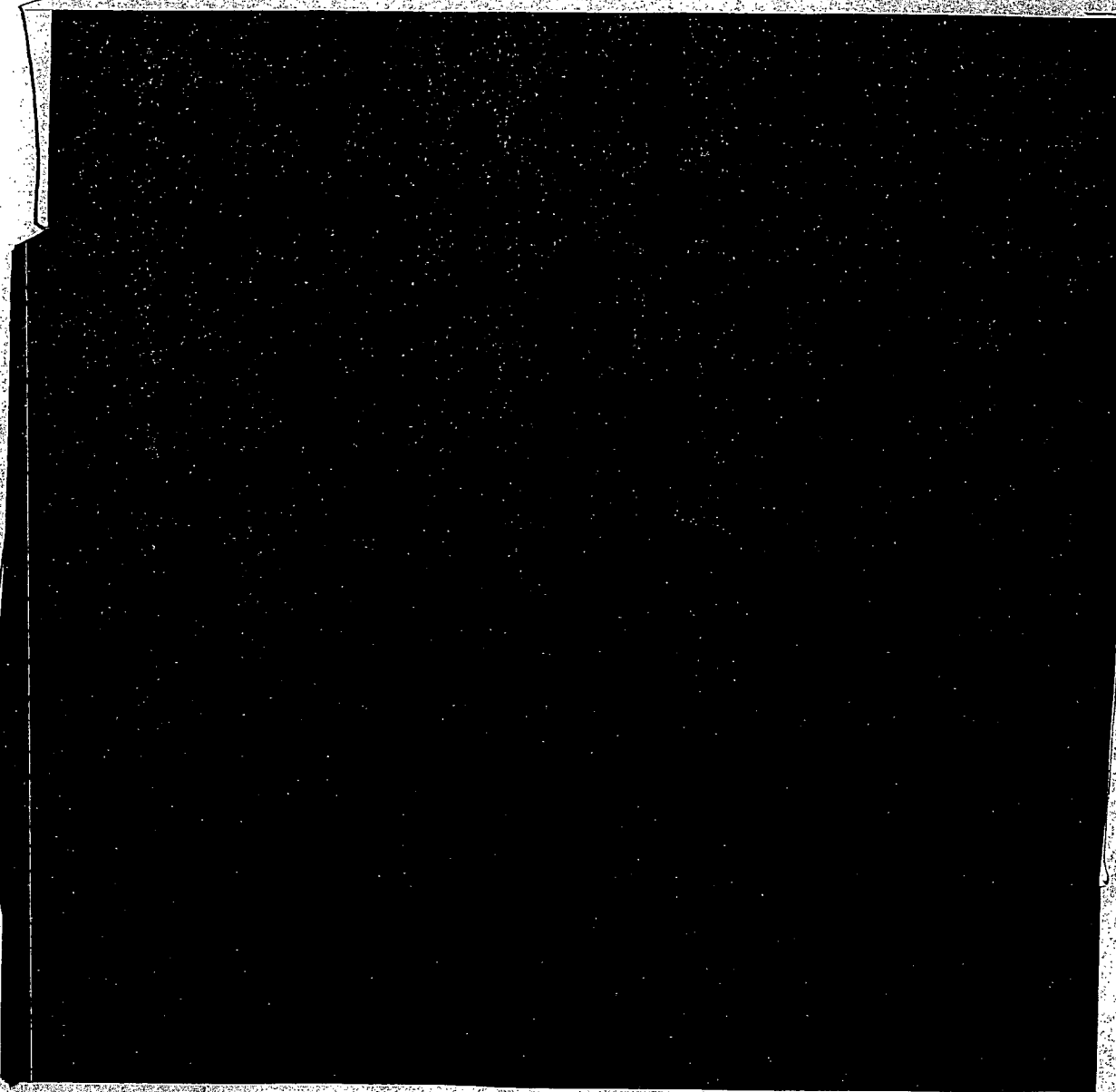
(U) As noted above, about 10 percent of the fission product noble gas atoms in the body of a high burnup spent fuel pellet escape to the rod free volume during reactor operation or as a result of pellet fracturing.

P63b
EX2
000
SR1



P649
Ex2
ovo
SR1

P659
EX2
DUO SRI



² P. C. Reardon, January 2004, Personal communication.

P66a
Ex 3
SG1



Figure 2-42.

Ex2
P66b

The contents of this figure are unclassified.

(U)



P66C
Ex2
OW-SR1

EX2
P67a
OUO-SRI

(U) Therefore, when applied to the rim layer of high burnup spent fuel pellets, the DOE Handbook equation was modified by letting

$$E = E_{\text{Imp}} + \alpha U_{\text{Pores}}$$

P67b
EX2
OUO-SRIP67c
EX1

(U) **Estimation of U_{Pores} .** The stored energy U released by depressurization of a gas is given by the following equation (Chung, 2003)

$$U = \frac{P_i V}{\gamma - 1} \left[1 - \frac{P_f}{P_i} \right]^{\frac{\gamma - 1}{\gamma}}$$

where P_i and P_f are the initial pressure of the gas and the pressure after depressurization, V is the volume of the gas vessel, and $\gamma = C_p/C_v = 1.65$ for Xe.

(U) Pore pressure can be calculated using the ideal gas law by setting V equal to the rim layer volume times the porosity of the rim layer and letting n equal the number of moles of fission product noble gases in the rim layer. Thus,

$$P_{\text{pore}} = n_{\text{rim}} \frac{RT}{F_{\text{pores,rim}} V_{\text{rim}}}$$

P68a
Ex 2
OVO-
SRI

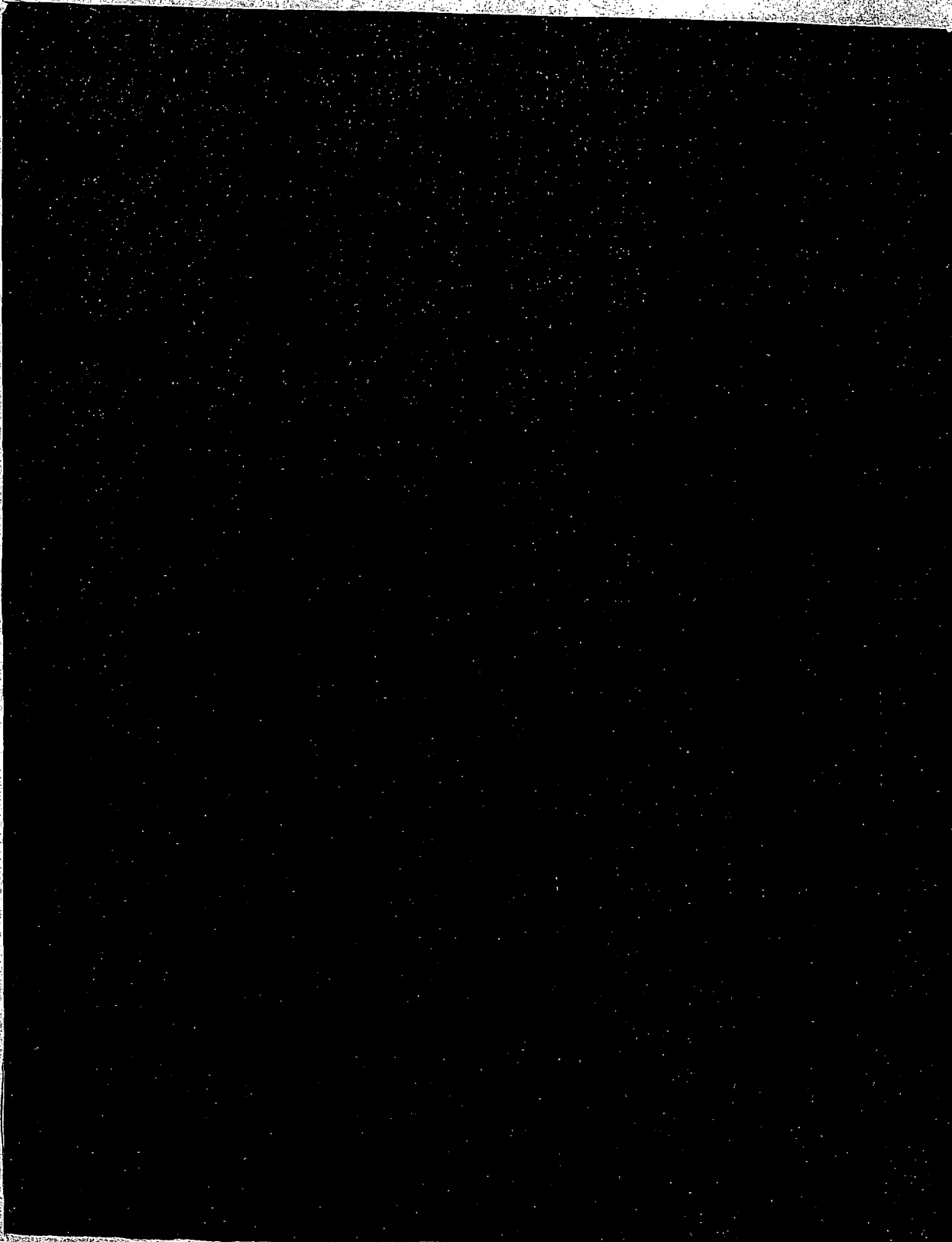
000-SR1
P69a
Ex 2

(U) Third, because the noble gas filled pores in the rim are located on subgrain boundaries, an alternative value for the number of pores per cm^3 in the rim layer can be estimated as the product of the two dimensional pore density and the subgrain surface area per cm^3 of rim layer. Because the rim subgrains are cubes with an average side length of about $0.2 \mu\text{m}$, the volume of a subgrain is $0.008 \mu\text{m}^3 = 8 \times 10^{-15} \text{cm}^3$, the number of subgrains per cm^3 of rim layer is $1 \text{cm}^3 / (8 \times 10^{-15} \text{cm}^3) = 1.25 \times 10^{14}$, and $A_{\text{subgrains}}$, the subgrain surface area per cm^3 , is the number of subgrains per cm^3 times the surface area of one subgrain divided by two, since each subgrain face is shared by another subgrain. Thus, $A_{\text{subgrains}} = [1.25 \times 10^{14} \text{ subgrains/mm}^3][6(0.2 \mu\text{m})^2]/2 = 1.5 \times 10^{13} \mu\text{m}^2/\text{cm}^3$, and the number of pores per cm^3 is the number of pores per μm^2 times the subgrain surface area per $\text{cm}^3 = (0.1 \text{ pores}/\mu\text{m}^2)(1.5 \times 10^{13} \mu\text{m}^2/\text{cm}^3) = 1.5 \times 10^{12} \text{ pores}/\text{cm}^3$, which is about a factor of 15 larger than the value of $9.12 \times 10^{10} \text{ pores per cm}^3$ developed by Spino et al. (Spino, 1996).

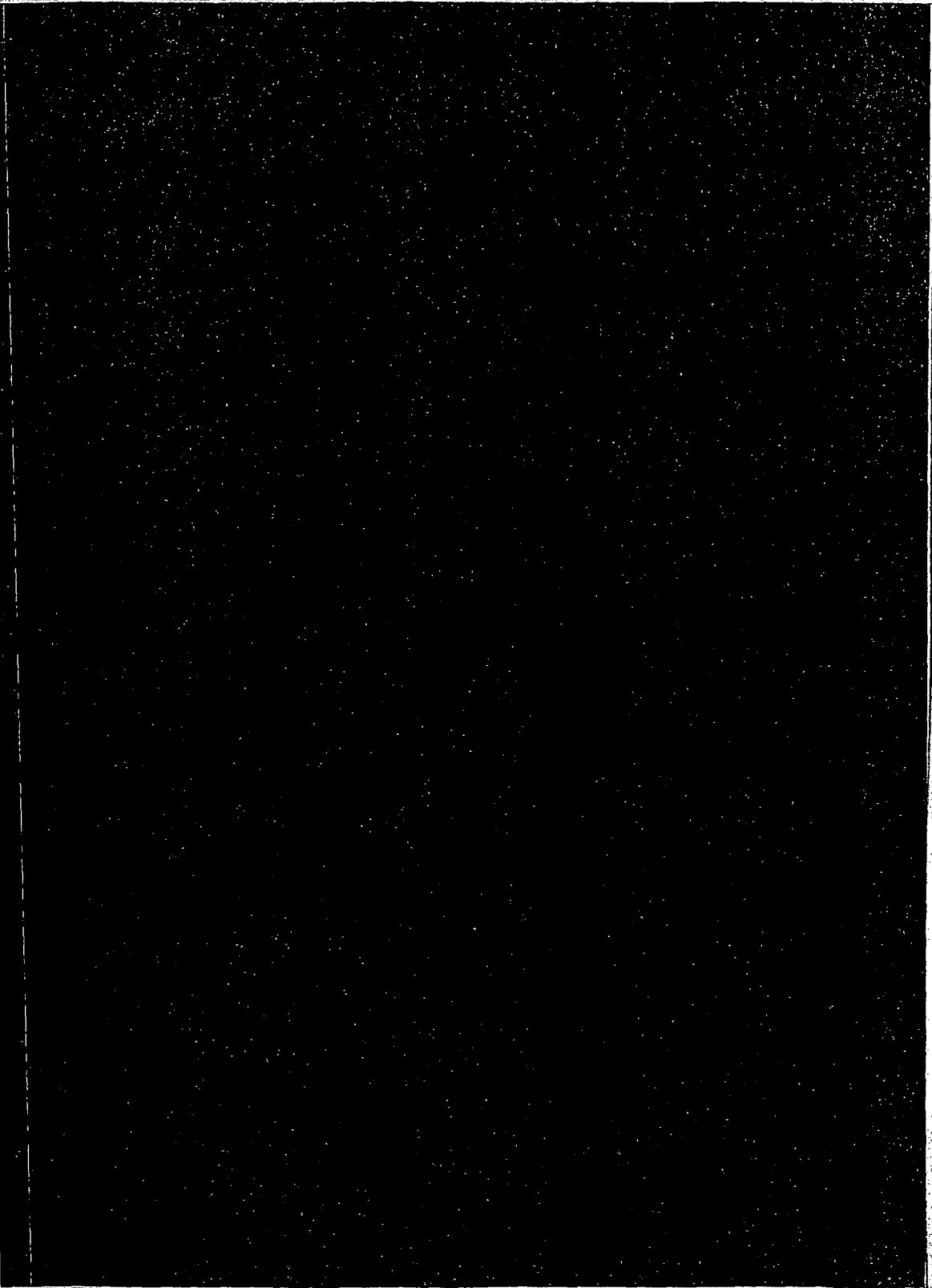
(U)

P69b
Ex 2
000-SR1

(U)

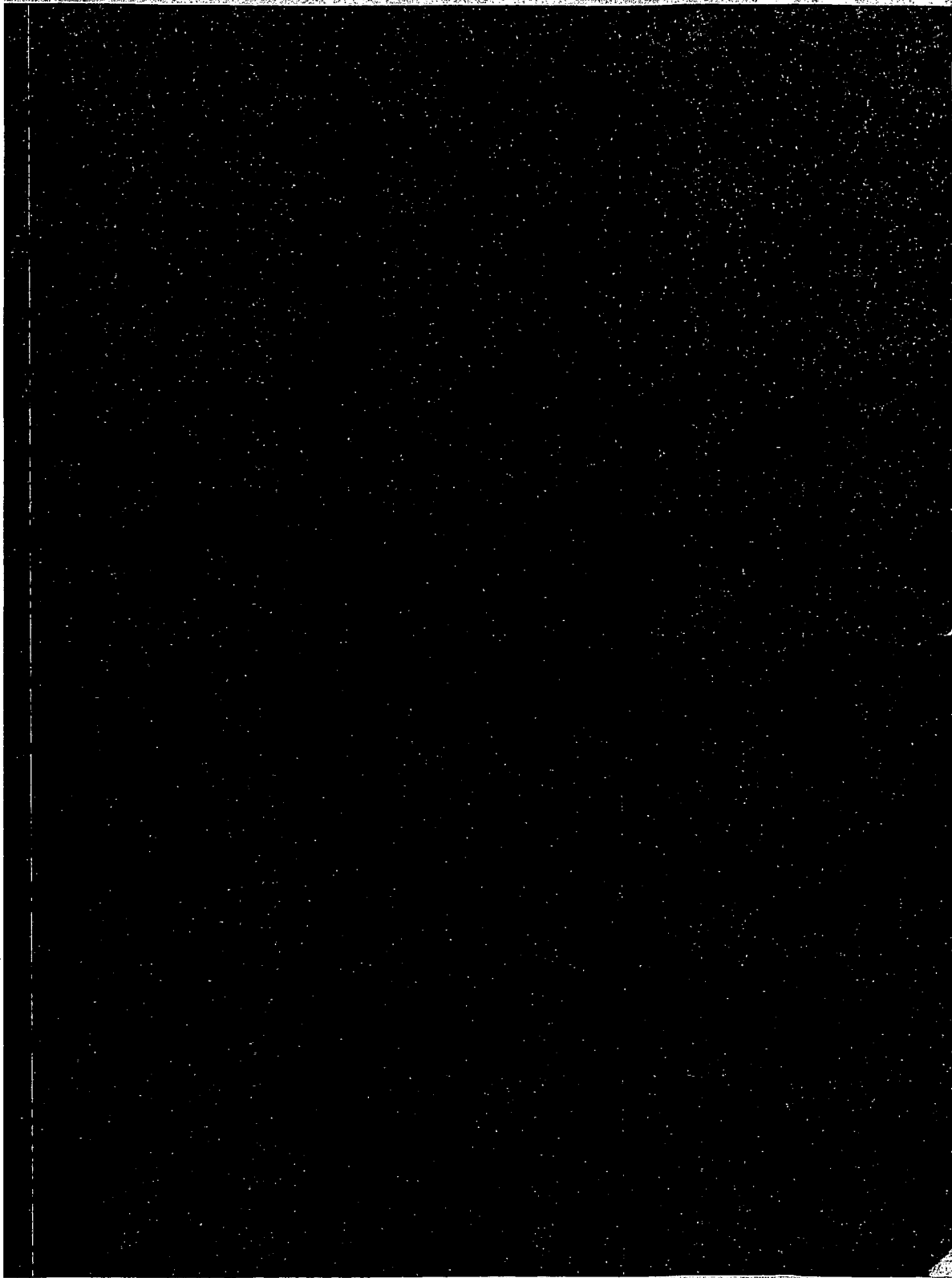


#2
Ex 000-SR1
p70a



#2
Ex 040-54
p7/g

Ex. 2
DUU-
SRI
P. 729



#2
EX
OW-SRI
P739

EX3

P 74a

P75a
EX2
OVD-
SG1

P75b
EX3
SG1

P75c
EX1

Classified

~~CONFIDENTIAL~~ - NSI

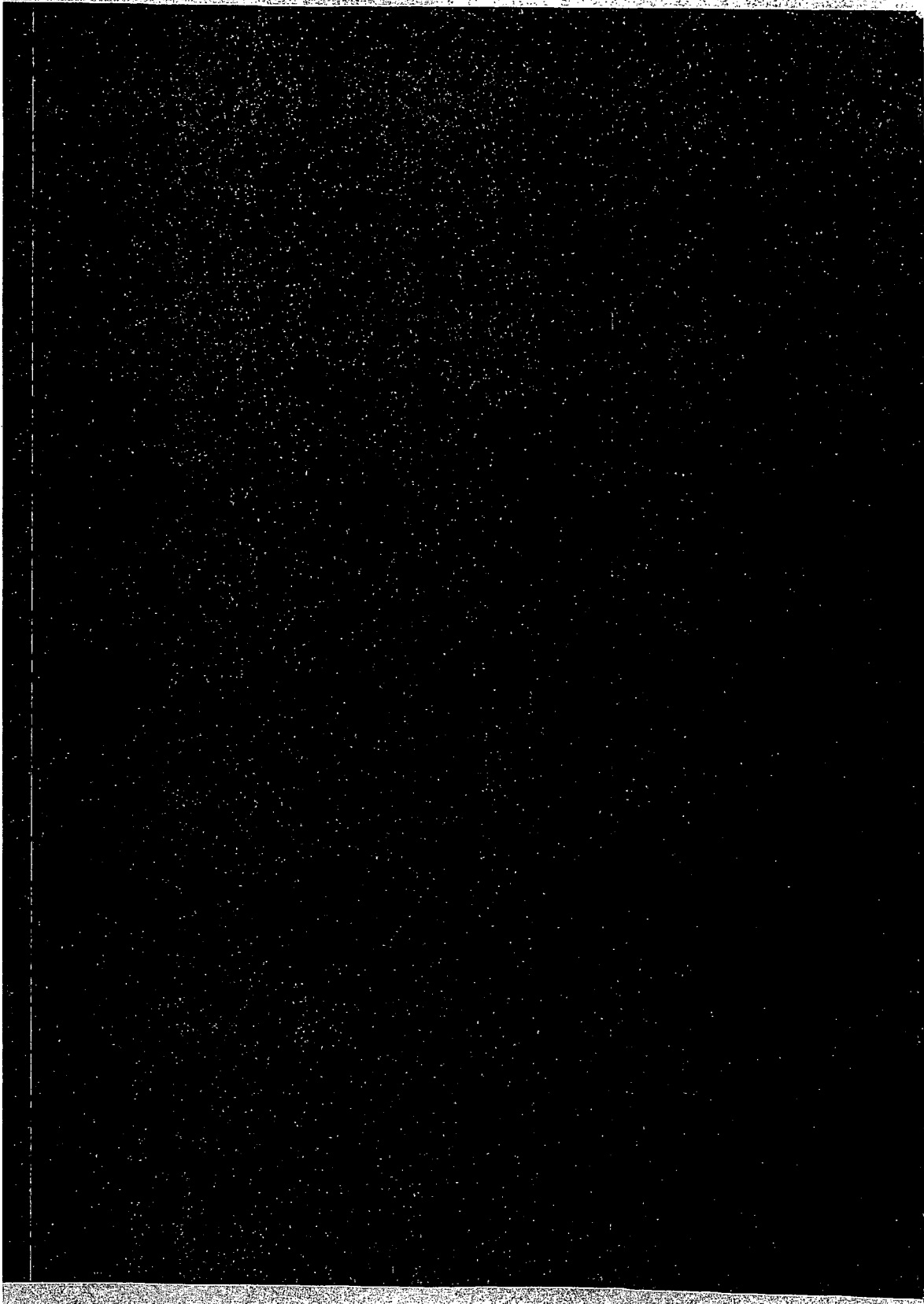
Final Draft

Ex. 1

P769

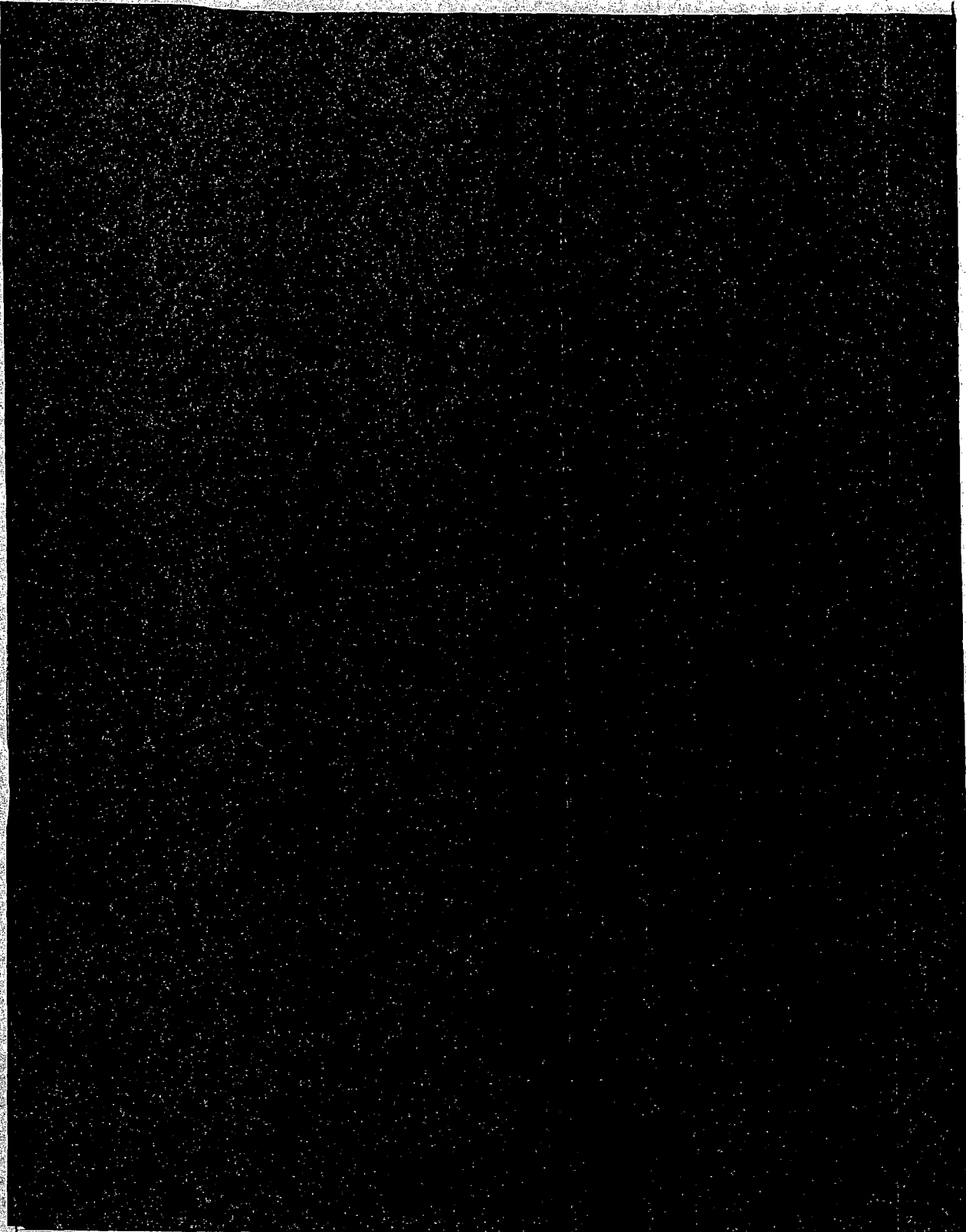
Ex 3
P76b

~~CONFIDENTIAL~~ - NSI



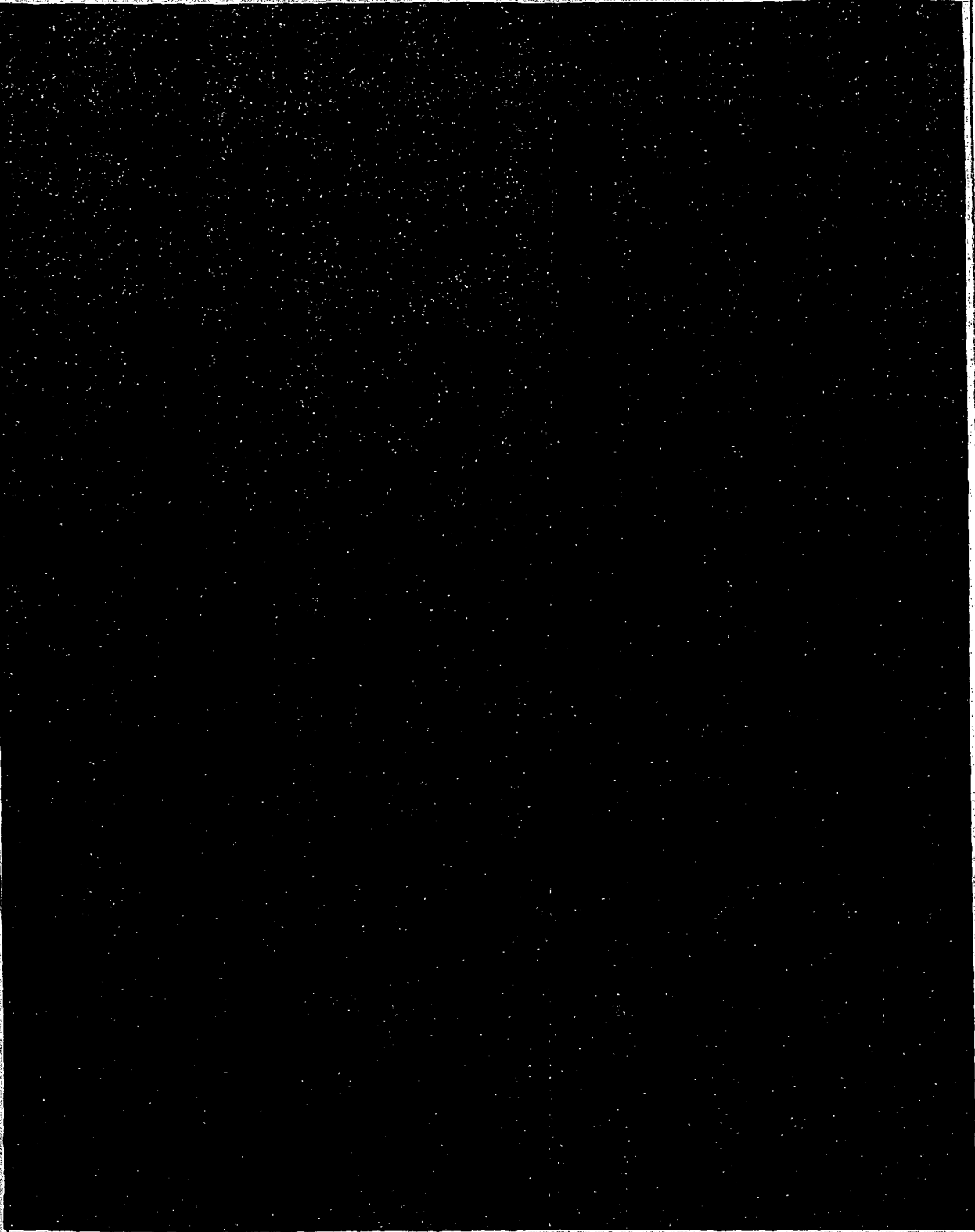
Ex #3

877a



43
Ex
P 78a

Am
Ex
p79a



#3
Ex
P 80a

Ex 3
pg 1a

Ex 3
pg 1b

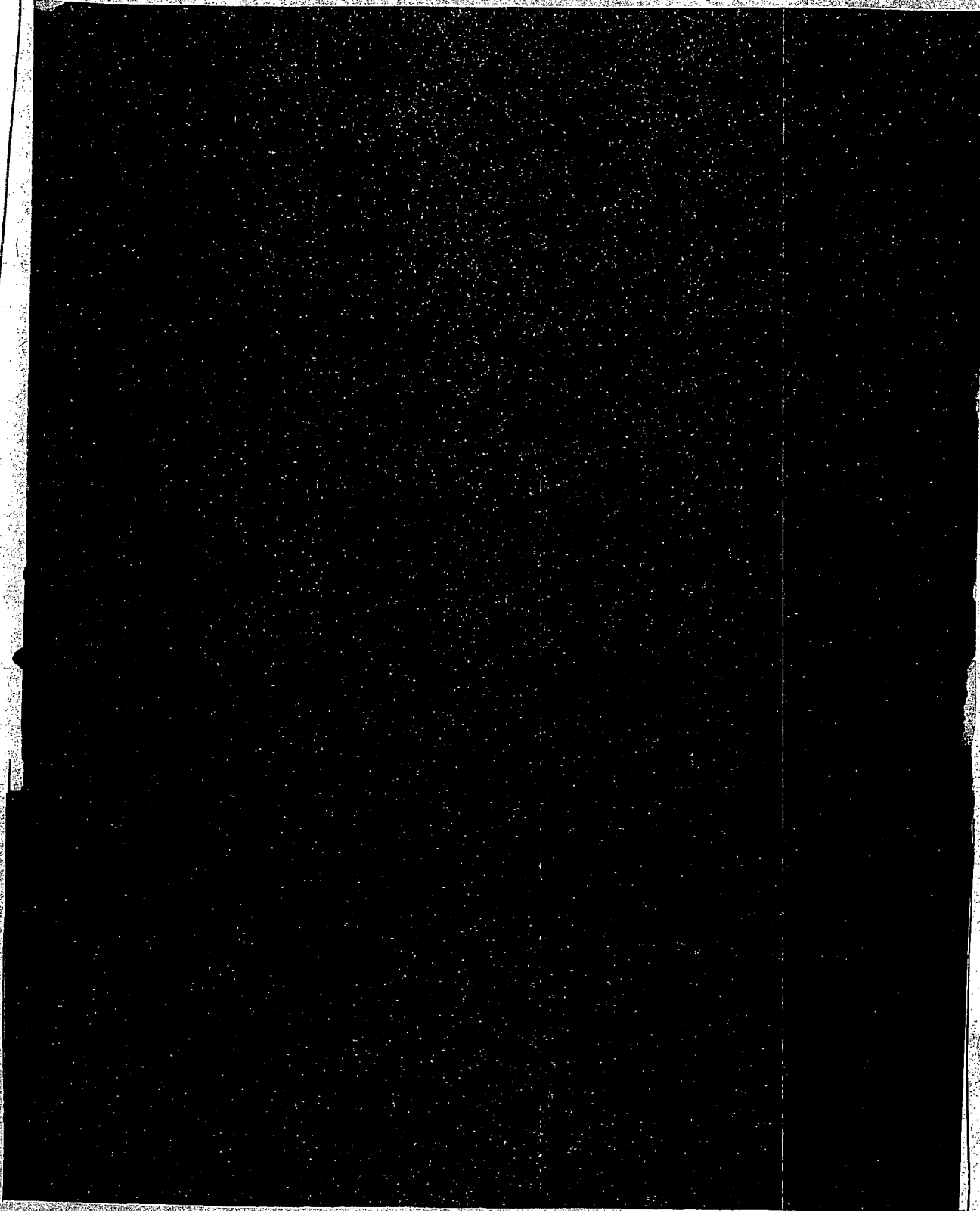
Ex 1
pg 1c

Ex 1
pg 1d

Classified

~~CONFIDENTIAL~~ - NSI

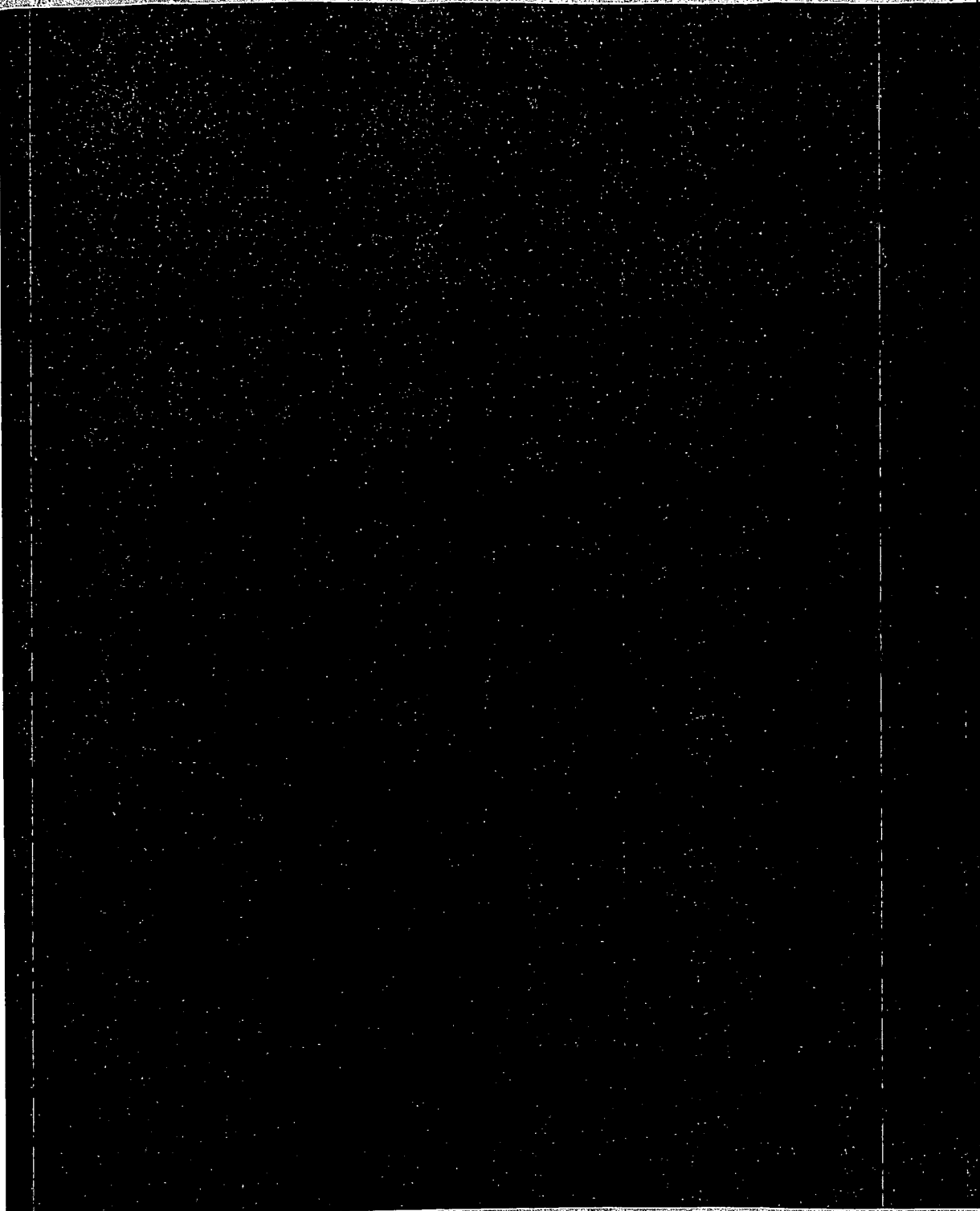
Final Draft



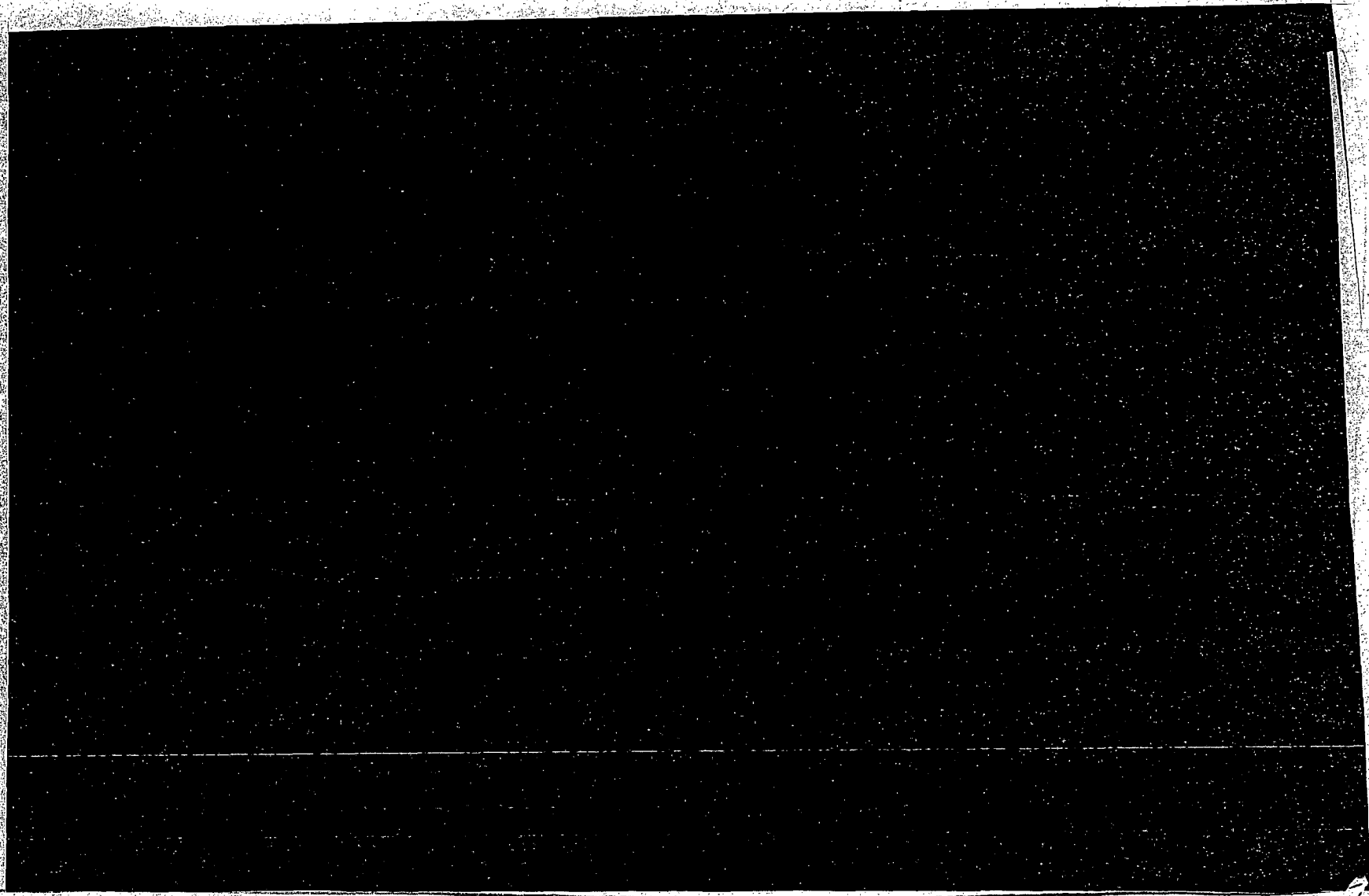
*Ex 1
Ex 2
p.829*

*Ex. 3
p.826*

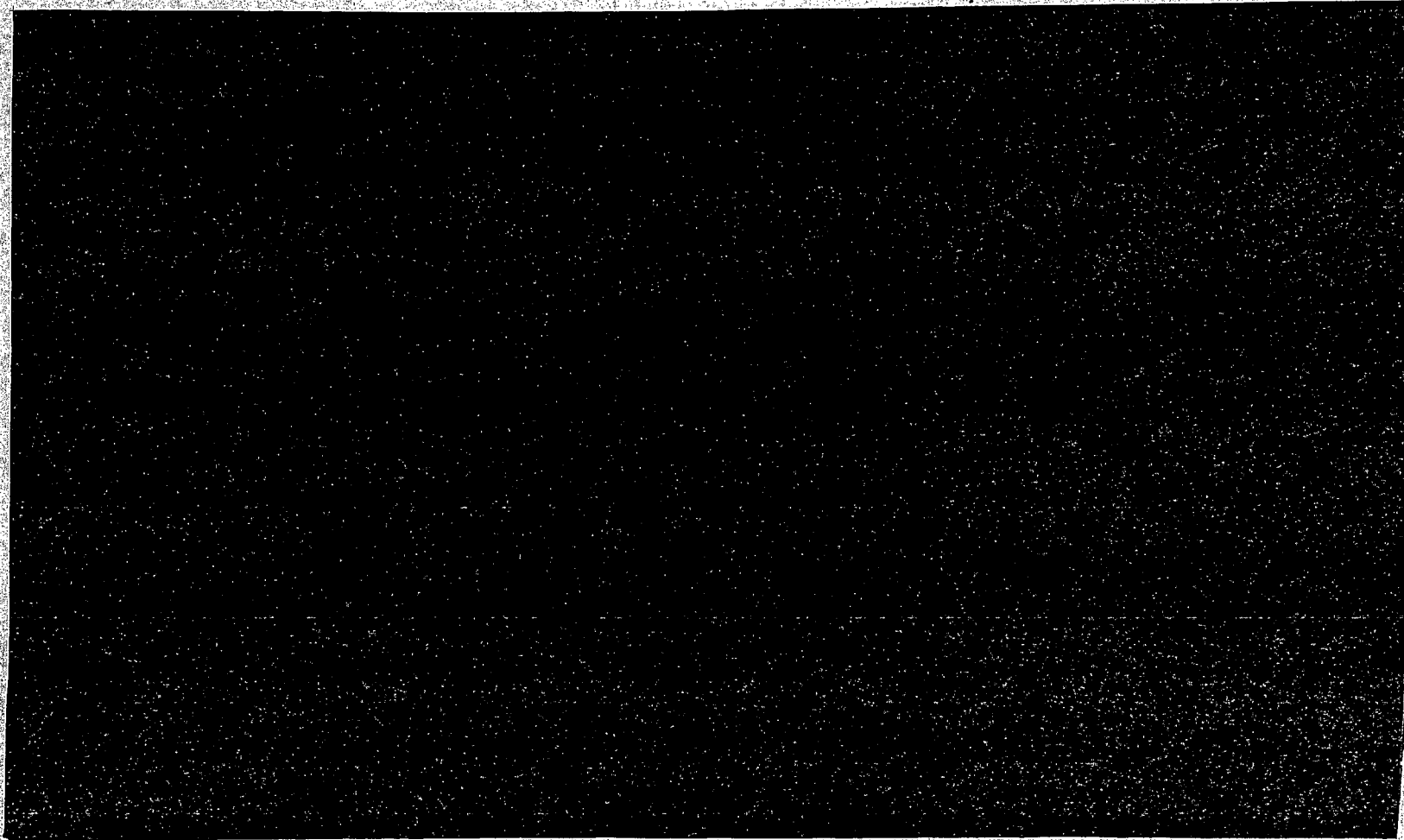
2.2.3.5 Consequence Calculations Performed (U)



#3
St
P 030



10/12/2003



Ex. 3
p. 85c

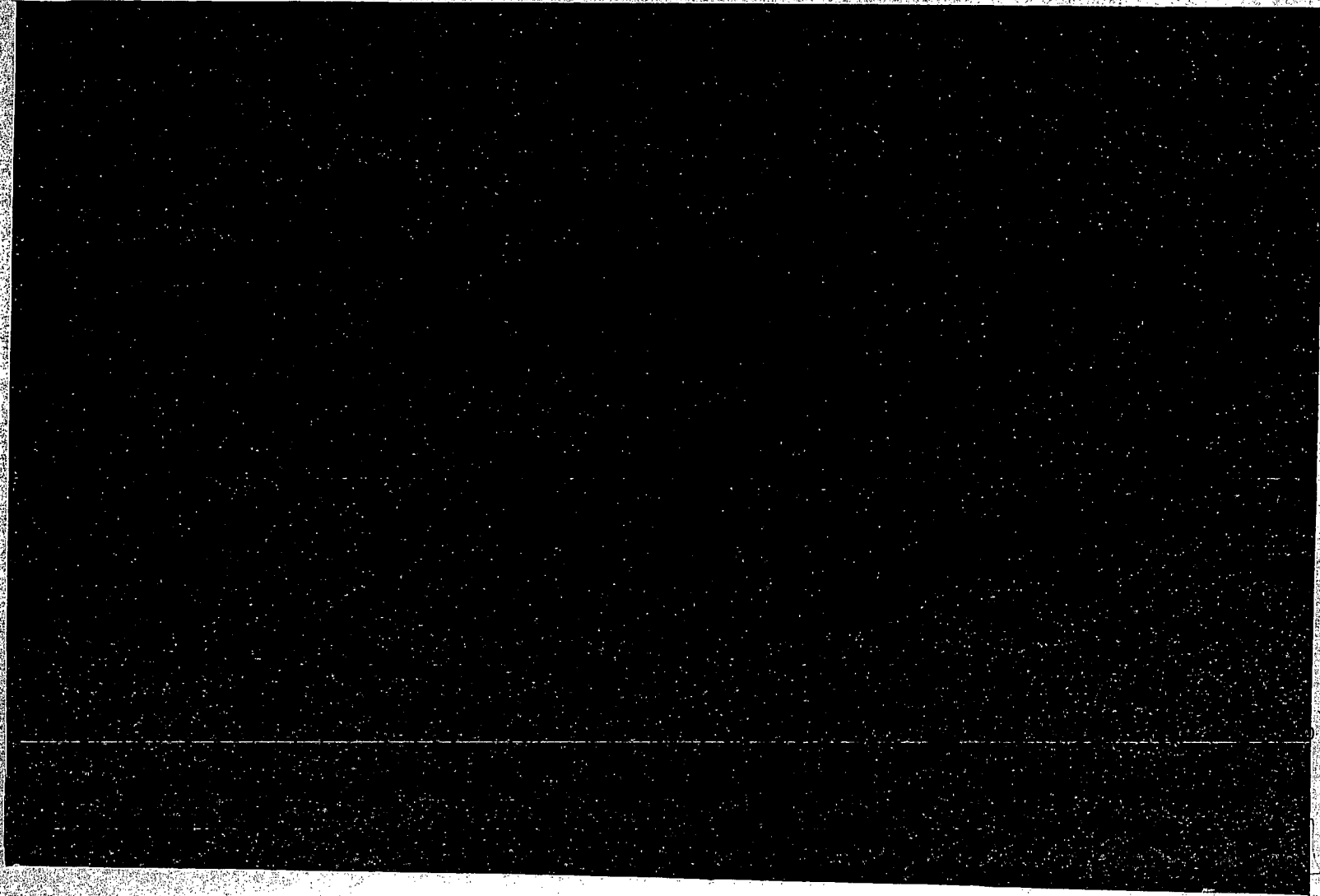
Figure 2-44.



Ex. 3
p. 85b

~~CONFIDENTIAL~~ - NSI

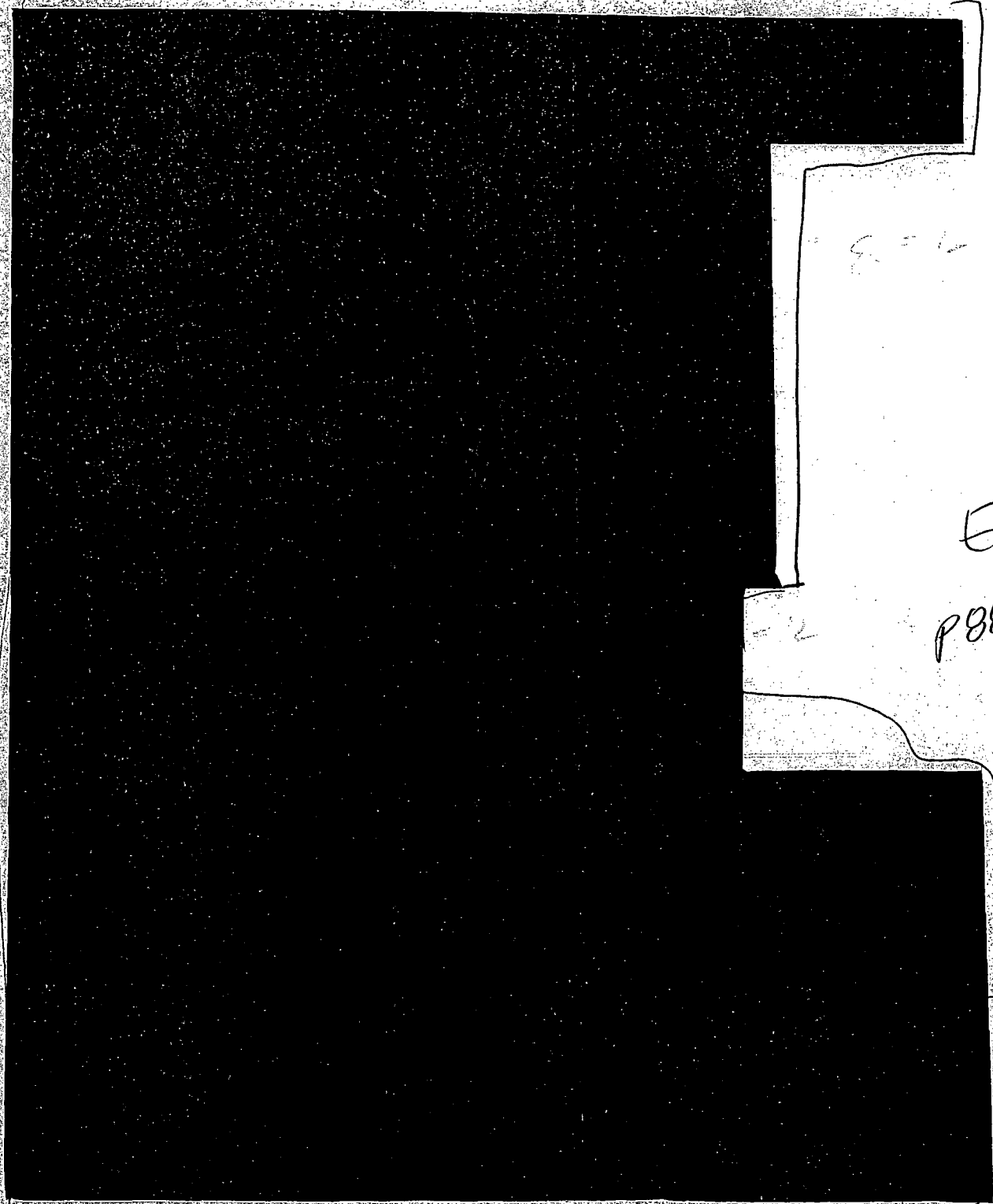
Final Draft

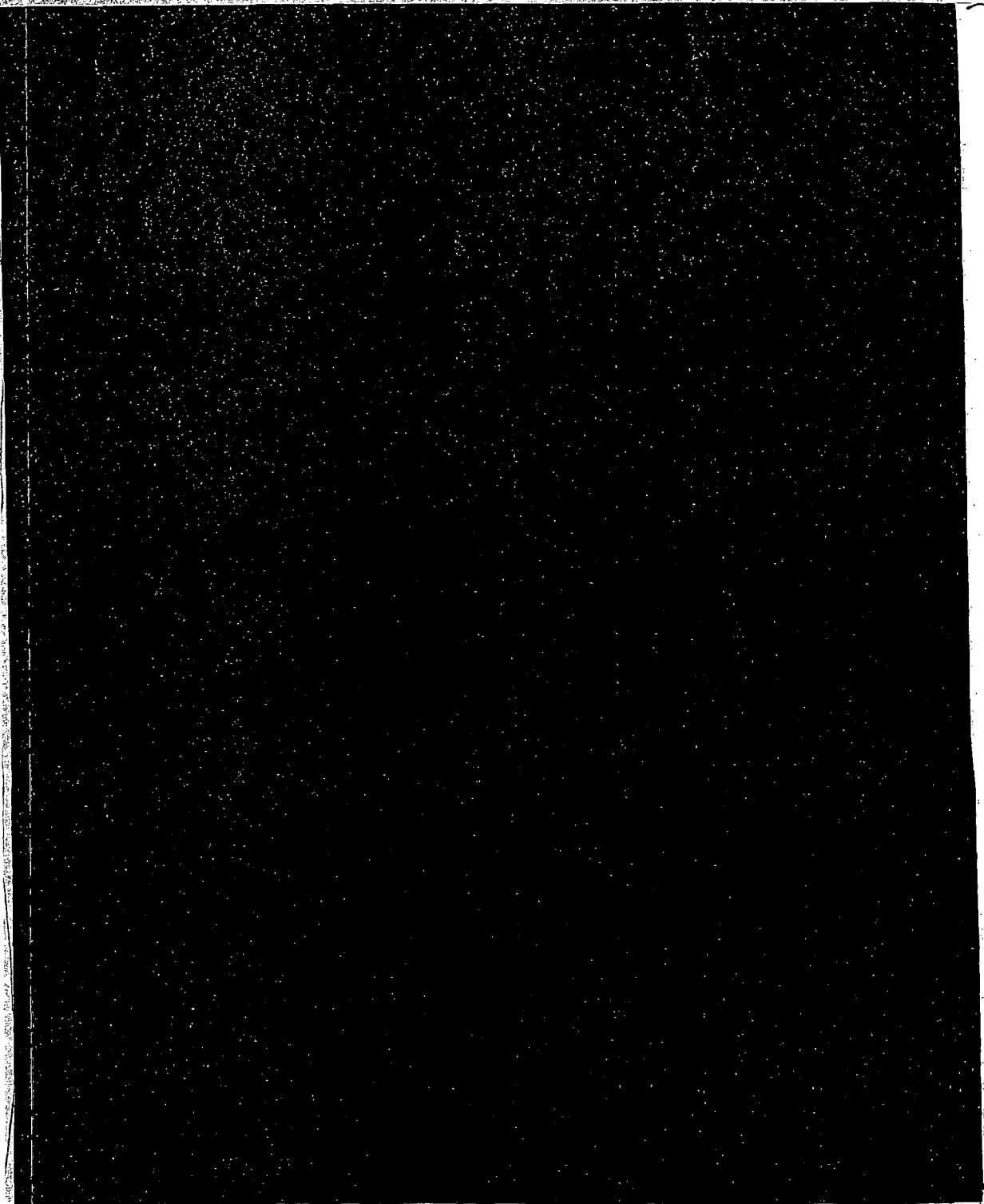


Ex #3
peba

Σ + #3

p 879





Ex. 3
p 89.9

Ex-3
p90a

Ex 1
p90b

Ex-3
p90c

Ex 1
p90d

Ex.3
p90e

Ex.1
p90f

~~CONFIDENTIAL - NSI~~

Final Draft

~~CONFIDENTIAL - NSI~~

Ex #3
p91a

3 Conclusions (U)

(U) A large airplane attack on a field of dry spent nuclear fuel casks was evaluated. A range of airplane attack speeds was considered, as well as angle of attack and location of attack on the specific targets. Although numerous attack scenarios were considered, a single attack scenario was selected as being realistic and representative of different attack scenarios for comprehensive evaluation. Parameters for the selected attack scenario were defined based on previous work done for the reactor vulnerability study, evidence from the September 11, 2001 attacks, and surveys of historical plane accidents.

[REDACTED]

Ex #3
1929

(U) The selected scenario for the storage casks bounded a wide range of attack parameters. Supporting analyses in Appendix A show that cask response results are relatively insensitive to the attack scenario. Various angles of attack and locations of attack on the target were analyzed. Resultant cask and fuel responses were similar to the selected scenario case.

[REDACTED] However, the parameter values used in the equations have mixed pedigrees. [REDACTED]

Ex 3
p92b

Ex 2
p92c

4 References (U)

(U) American Society of Civil Engineers (ASCE). 2003. *The Pentagon Building Performance Report*, Renton, Virginia.

(U) Beal, S.K. 1978. "Correlations for the Sticking Probability and Erosion of Particles," J. Aerosol Sci., 9, 455.

[REDACTED]

(U) Chung, J., Ed. 2003. *Health and Safety Manual*, Chap. 7, App. E, "Stored Energy of a Pressurized Gas Vessel", LBNL/PUB-3000, Lawrence Berkeley National Laboratory, Berkeley CA, available at <http://www.lbl.gov/ehs/pub3000/>.

(U) Code of Federal Regulations (CFR). Volume 49, Part 173.435 (49 CFR 173.435).

[REDACTED]

(U) Federal Emergency Management Agency (FEMA). 2002. *World Trade Center Building Performance Study: Data Collection, Preliminary Observations, and Recommendations*, FEMA 403, Washington, D.C.

SGI

p939
Ex. 3

Ex. 3
p93b

(U) Fischer, L.E., J. H. Van Sant, and C. K. Chou. 1990. *Draft Criteria for Controlled Tests for Air Transport Packages*, UCRL-ID-103684, Lawrence Livermore National Laboratory, Livermore CA.

(U) Fromentin, A. 1989. *Particle Resuspension from a Multilayer Deposit by Turbulent Flow*, PSI-Bericht Nr. 38, Programm LWR-Sicherheit, Paul Scherrer Institute.

(U) Geelhood, K and C. Beyer. 2003. *Examination of Strain to Failure Data from Irradiated Zircaloy*, white paper prepared for the NRC spent fuel package vulnerability study, copy available on request from Jeremy -, (505) 844-0134.

(U) Golubev, I.F. 1970. *Viscosity of Gases and Gas Mixtures, A Handbook*, Israel Program for Scientific Translations, Jerusalem, Table 4, p. 62.

(U) Hazelton, R. F. 198., *Characteristics of Fuel Crud and Its Impact on Storage, Handling, and Shipment of Spent Fuel*, PNL-6273, Pacific Northwest Laboratory, Richland WA 99352.

(U) Hertel, E.S. 1992. *A Comparison of the CTH Hydrodynamics Code with Experimental Data*, SAND92-1879, Sandia National Laboratories, Albuquerque, NM.

(U) HOLTEC International. 2000. *HI-STORM Topical Safety Analysis Report*, Revision 10, Holtec International Report No. HI-951312, Holtec International, Marlton, NJ (available from NRC document room).

(U) HOLTEC International. 2000. *Safety Analysis Report for the Holtec International Storage, Transport, and Repository Cask System (HI-STAR 100 Cask System)*, Revision 9, Holtec Report HI-951251, April 20, 2000, Table A.3, p. A-21.

(U) HOLTEC International. 2000. *Topical Safety Analysis Report (Rev. 10) with Certificate of Compliance No., 1014 for the HI-STORM 100 Cask System*, Holtec Report HI-951312, June 2000:

- a. Table 1.2.2, p. 1.2-26 and Table 5.2.29, p. 5.2-38
- b. Table 2.0.2, p. 2.0-26 and Table 3.A3, p. 3.A-14
- c. Table 2.1.4, p. 2.1-14; Table 3.5.1, p. 3.5-5; Table 4.3.5, p. 4.2-14; and Table 5.2.26, p. 5.2-35
- d. Table 4.3.5, p. 4.3-14
- e. Table 4.4.14, p. 4.4-45
- f. Table 4.4.13, p. 4.4-44
- g. Table 2.2.3, p. 2.2-23

SGI
p940
Ex. 3

h. Figure 5.3.6, p. 5.3-17

(U) Hossain, Q.A., Kennedy, R.P., Murray, R.C., Mutreja, K., and Tripathi, B.P. 1997. *Structures, Systems, and Components Evaluation Technical Support Document, DOE Standard, Accident Analysis for Aircraft Crash into Hazardous Facilities*, UCRL-ID-123577, Lawrence Livermore National Laboratories, Livermore, CA.

(U) International Atomic Energy Agency (IAEA). 1987. *Safety Series No. 7, IAEA Safety Guides, Explanatory Material for the IAEA Regulations for the Safe Transport of Radioactive Material (1985 Edition)*, 2nd Edition, Vienna.

[REDACTED]

56I
p95a
Ex 3

(U) Kimura, C. 2003. *Historical Commercial Airplane Crash Database*, submitted to Sandia National Laboratories. Can be obtained from Carlos Lopez, (505) 845-9545.

(U) Kmetyk, L.N., and Yarrington, P. 1994. *CTH Analyses of Steel Rod Penetration into Aluminum and Concrete Targets with Comparisons to Experimental Data*, SAND94-1498, Sandia National Laboratories, Albuquerque, NM.

(U) Lorenz, R. A. et al. 1980. *Fission Product Release from Highly Irradiated LWR Fuel*, NUREG/CR-0722, Oak Ridge National Laboratory, Oak Ridge TN, pps 48-80.

(U) Manzel, R. and C.T. Walker. 2000. "High Burnup Fuel Microstructure and its Effect on Fuel Rod Performance," *Proc. Intl. Topical Meeting on LWR Fuel Performance*, Park City Utah.

(U) R. Manzel and C. T. Walker, 2002, EPMA and SEM of fuel Samples from PWR Rods with an Average Burn-up of Around 100 MWd/kgHM, *Journal of Nuclear Materials*, 301, 170 (2002).

[REDACTED]

56I
p95b
Ex 3

(U) National Transportation Safety Board (NTSB). 2000. *Aircraft Accident Report Controlled Flight into Terrain Korean Air Flight 801 Boeing 747-300, HL7468 Nimitz Hill, Guam August 6, 1997 DCA97MA058, NTSB/AAR-00/01*, Washington, D.C.

(U) Ranz, W. E. 1958. *Principles of Inertial Impaction*, Bulletin No. 66, Department of Engineering Research, Pennsylvania State University, University Park, PA, Fig. 8, P. 21

[REDACTED]

56I
p95c
Ex 3

(U) Riera, J.D. 1968. "On the Stress Analysis of Structures Subjected to Aircraft Impact Forces," *Nuclear Engineering and Design*, Vol. 8, pp. 415-426.

(U) Silling, S.A. 1992. *Eulerian Simulation of the Perforation of Aluminum Plates by Nondeforming Projectiles*, SAND92-0493, Sandia National Laboratories, Albuquerque, NM.

(U) Sanders, T.L., Seager, K.D., Rashid, Y.R., Barrett, P.R., Malinauskas, A.P., Winziger, R.E., Jordan, H., Tomas, A.D., Sutherland, S.H., and Reardon, P.C. 1992. *A Method for Determining the Spent-Fuel Contribution to Transport Cask Containment Requirements*, SAND90-2406, Sandia National Laboratories, Albuquerque, NM:

- a. Figure III-60, p. III-107
- b. Table I-3, p. I-11 and Table I-5, p. I-19
- c. Table I-3, p. I-10, Table I-4, p. I-15, and Table I-6, p. I-25
- d. Table I-5, p. I-19
- e. Table I-4, p. I-16
- f. Figure IV-1, p. IV-12

(U) Sandoval, R. P. et al. 1991. *Estimate of CRUD Contribution to Shipping Cask Containment Requirements*, SAND88-1358, Sandia National Laboratories, Albuquerque, NM:

- a. p. 13
- b. Table 1, p. 15
- c. Figure I-13, p. I-40



SGI
pg 6a
ex 3

(U) Spino, J., K. Vennix, and M. Coquerelle. 1996." Detailed Characterization of the Rim Microstructure in PWR Fuels in the Burn-up Range 40-67 GWd/tM," *Journal of Nuclear Materials*, 231, 179 (1996).

(U) Sprung, J.L. et al. 1990. *Evaluation of Severe Accident Risks: Quantification of Major Input Parameters*, NUREG/CR-4551, U.S. Nuclear Regulatory Commission, Washington DC 20555.

(U) Sprung, J. L. et al. 1998. *Data and Methods for the Assessment of the Risks Associated with the Maritime Transport of Radioactive Materials: Results of the SeaRAM Program, Vol. 2, Appendix IV, Cask-to-Environment Release Fractions*, SAND98-1171, Sandia National Laboratories, Albuquerque, NM:

- a. Table 4-1, p. 4-3 and Figures 4-1a and 4-1b, p. 4-5

- b. Figure 6-1, p. 6-6
- c. Appendix IV, p. 2-1

(U) Sprung, J. L., D.J. Ammerman, N.L. Breivik, R.J. Dukart, F.L. Kanipe, J.A. Koski, G.S. Mills, K.S. Neuhauser, H.D. Radloff, R.F. Weiner, H.R. Yoshimura. 2000. *Reexamination of Spent Fuel Shipment Risk Estimates*, NUREG/CR-6672, U.S. Nuclear Regulatory Commission, Washington, DC (available at ttd.sandia.gov/nrc/modal.htm):

- a. pps. 7-35 thru 7-48
- b. Section 7.2.2, Accident Source Terms, p. 7-13
- c. Section 5.4.1, Rod Failure Strain Criterion, p 5-28
- d. Section 7.3.3, Particles, p 7-30
- e. Section 7.3.6, CRUD, p. 7-48
- f. p.7-21
- g. Section 8.12 Loss of Shielding Accidents, p. 8-47.

(U) Stone, C.M. and Wellman, G.W. 1993. "Implementation of Ductile Failure in Pronto2d and Pronto3D," Memo to Distribution, Sandia National Laboratories, Albuquerque, NM.

(U) Sugano, T., Tsubota, H., Kasai, Y., Koshika, N., Ohnuma, H., Von Riesemann, W.A., Bickel, D.C., and Parks, M.B. 1993. "Local Damage to Reinforced Concrete Structures Caused by Impact of Aircraft Engine Missiles, Part 1. Test Program, Method and Results," *Nuclear Engineering and Design*, Vol. 140, pp. 387-405.

(U) Sugano, T., Tsubota, H., Kasai, Y., Koshika, N., Orui, S., Von Riesemann, W.A., Bickel, D.C., and Parks, M.B. 1993. "Full-Scale Aircraft Impact Test for Evaluations of Impact Force," *Nuclear Engineering and Design*, Vol. 140, pp. 373-385.

(U) Talyor, L.M., and Flanagan, D.P. 1989. *PRONTO3D A Three-Dimensional Transient Solid Dynamics Program*, SAND87-1912, Sandia National Laboratories, Albuquerque, NM.

(U) Tieszen, S.R. 1995. *Fuel Dispersal Modeling for Aircraft-Runway Impact Scenarios*, SAND95-2529, Sandia National Laboratories, Albuquerque, NM.

(U) Thomas, L. E. C. E. Beyer, and L. A. Charlot. 1992. "Microstructural Analysis of LWR Spent Fuel at High Burnup," *Journal of Nuclear Materials*, 188, 80 (1992).

(U) Transnuclear, Inc.. 2000. *TN-68 Dry Storage Cask Final Safety Analysis Report*, Revision 0, Transnuclear, Inc., Hawthorne, NY (available from NRC document room):

- a. Table 5.2-1, p. 5.6-2 and Table 6A-1, p. 6A-6
- b. Table 5.2-2, p. 5.6-7

(U) Vankeerberghen, M. 1995. *Recent Gas Flow Measurements in IFA-504 Rods*, HWR-433, Halden Reactor Project, Halden, Norway.

(U) Weast, R. C., Ed. 1966. *Handbook of Chem. and Phys.*, 47th Edition, R. C. Weast, Ed., The Chemical Rubber Co., Cleveland OH 44114, 1966, p. F-40.

(U) Wilson, L.T., Hertel, E.S., Schwalbe, L.A., and Wingate, C. 1998. "Benchmarking the Sphinx and CTH Shock Physics Code for Three Problems in Ballistics," *Proceedings of the Seventh International Symposium on Ballistics*, Johannesburg, South Africa.

(U) Wellman, G.W. and Salzbreinner, R. 1992. *Quasistatic Modeling and Testing of Exclusion Region Barrier Mock-Ups*, SAND92-0024, Sandia National Laboratories, Albuquerque, NM.

(U) Wellman, G.W., Diegert, K.V., and Salzbreinner, D.R. 1993. *Two-Dimensional Quasistatic Modeling of Exclusion Region Barriers in Support of Design Guide Development*, SAND93-0905, Sandia National Laboratories, Albuquerque, NM.

(U) Wright, A. L. and W. L. Pattison. 1985. "Results from Simulated Upper-Plenum Aerosol Transport and Aerosol Resuspension Experiments," *Proceedings of the CSNI Specialists Meeting on Nuclear Aerosols in Reactor Safety*, 4th to 6th September, 1984, Karlsruhe, FRG, ed. W. O. Schikarski and W. Schock, Printed Feb., CSNI 95, KfK 3800, 1985.

Appendices (U)

(U) Appendix A: Structural Analysis

**(U) Appendix B: HI-STORM Storage Cask
Impact Analyses**

**(U) Appendix C: Effect of Pool Fires on a Dry
Storage Cask**

Appendix A: Structural Analysis (U)

A.1 Introduction (U)

(U) The following appendix discusses most of the structural analyses performed for the review of the HI-STORM dry storage cask (Holtec International, 2000). Appendix B discusses some additional structural analyses performed in support of the HI-STORM cask review. The analysis methodology, threat, and a brief explanation of some of the tools are discussed in this section. The details of the analyses are discussed in the remainder of this appendix.

A.1.1 Structural Analysis Methodology (U)

(U) The structural analysis for this study was performed in a two-stage effort that included global analyses of a jetliner impacting the cask and local analyses of hard jetliner components impacting specific locations on the cask overpacks. This methodology is shown schematically in Figure A-1 for a field of storage casks. Due to the complicated nature of the jetliner/cask interactions involved in the impact scenarios, this was considered the only feasible approach. Even using massively parallel computers associated with state-of-the-art methodology, these analyses test the limits of computing resources and methodology. The computer code used to perform the global analyses was originally developed for hypervelocity impacts (1 km/s (3200 ft/s) or greater) of relatively hard missiles into relatively soft targets. The application discussed in this appendix involves the impact of relatively soft missiles (the jetliner) into relatively hard targets (the spent fuel casks) at lower velocities than the code was originally developed to examine. The application of the codes to problems such as these is expected to provide reasonable global estimates of damage to the cask and the jetliner.

(U) The decoupling of the analyses into the global and local analyses is consistent with the methodology outlined in the Department of Energy (DOE) standard, *Accident Analysis for Aircraft Crash into Hazardous Facilities*, (DOE, 1996) and with the methodology outlined in the American Society of Civil Engineers (ASCE) manual, *Structural Analysis and Design of Nuclear Plant Facilities* (ASCE, 1980). There are numerous references in both of these sources that support this methodology. A critical review of this approach as applied to nuclear power plants (NPPs) can be found in Kot et al. (1982).

(U) The global analyses were performed to gain insight into issues such as the maximum exit velocity, tipping, sliding, and deformation/damage to the cask due to the total impacting mass of the jetliner. The exit velocity gives the speed of the cask after the impact of the jetliner.

(U) In general, previous studies of airplane impacts into targets like buildings were performed using force time histories. These force time-histories were developed for deformable missiles (jetliner, in this case) impacting rigid surfaces. The force time history can be divided into two components. A portion of the forcing function is due to the crushing strength of the airplane and the other portion is due to the rate of change of the airplane momentum is (the inertial force). Previous studies have shown that for the global response of an airplane impact into a structure, the inertial force is the most significant portion of the loading (Riera, 1968, 1980; ASCE, 1980; Kot et al, 1982; Wolf et al, 1978). This is demonstrated clearly in ASCE (1980), where the force

SGT
A-2a
Ex. 3

a) The Problem: A large jetliner impact into a field of casks.

SGT
A-2b
Ex. 3

b) The Solution, Step 1 – Global Analysis: Analysis of the jetliner and its associated hard components impacting a single cask. Examine global effects of the impact and determine the velocity of the cask.

Ex. B
SGT
A-2c

c) The Solution, Step 2 – Local Analysis: Analysis of jetliner hard component impacts into a cask. Examine cask integrity.

Figure A-1. Structural Analysis Methodology (U).

The contents of this figure are unclassified.

time history function was developed for a specific airplane.

This resulted in "little effect on the final results" ASCE (1980).

(U) The computational power to model the airplane and structure has only recently become feasible. Analyses such as those described in Section A.2.1, where the airplane is modeled, are more sophisticated methods to apply force to the structure.

both the stiffness and the mass of the jetliner.

The model incorporates

(U) The global analysis is then followed by local analyses of the impact of jetliner hard components into the spent fuel cask.

airplane parts in a crush zone.

(U) This local analysis methodology is described in (DOE, 1996; ASCE, 1980; Kot et al., 1982).

Landing gear and engines from the jetliners that attacked the World Trade Center (WTC) buildings preceded though the widths of the buildings and fell four to six city blocks from the buildings (FEMA, 2002). The nose landing gear of the jetliner that attacked the Pentagon was found to have penetrated as far as the third ring of the Pentagon (91 m (300 ft) into the building, the furthest extent of the damage). In addition, the black box from the jetliner (which is housed in the tail) was found near the nose landing gear in the wreckage, indicating that the jetliner continued to break up and crush with the mass coming to rest near the farthest point of penetration (ASCE, 2003). National Transportation and Safety Board (NTSB) reports of airplane crashes also cite the hard components of the airplane as being found separated from the wreckage and penetrating significantly into soil (e.g., NTSB, 2000).

A.1.2 Structural Impact Threat (U)

ex. 2
A-3a

ex. 2
A-3b

ex. 2
A-3c

ex. 2
A-3d

ex. 2
A-3e

ex. 1
A-3f

Ex 1

A-4a

(U) The specific layout for a field of storage casks can result in many possible impact orientations and cask-to-cask impacts. Section A.2 discuss analyses of many possibilities. The analyses were conducted to explore the possible vulnerabilities to different impact scenarios. As discussed in the main body of this report, analyses described in this and the other appendices have been applied to explore a realistic scenario.

A.1.3 Analysis Tools (U)

(U) Two types of computer codes are used for the structural analysis of a large jetliner impacting the nuclear spent fuel dry storage casks. For the global analysis discussed in Section A.2.1, the Eulerian shock physics code CTH is employed. CTH was developed to examine complex phenomena surrounding shock physics. It can analyze penetration and perforation, compression, high explosive detonation and initiation phenomena, hypervelocity impacts, and model complex large-deformation plastic flow phenomena. It uses an Eulerian mesh to solve the conservation equations. Finite-volume approximations are used to solve the governing equations of conservation of mass, momentum, and energy. It runs in a massively parallel environment and has been used extensively at SNL and at other institutions. Although the code was developed for higher velocity applications, there has been some benchmarking for velocities in the range of the current scenarios (Silling, 1992). A more detailed description of CTH can be found in Section A.2.1.3.

(U) Most of the detailed local analyses, discussed in Section A.2.2, were conducted using the explicit finite element (FE) code Pronto3D (Taylor, 1989). This is a 3D, solid dynamics FE code that uses a Lagrangian formulation with explicit time integration. It was developed to analyze large deformations of highly nonlinear materials subjected to extremely high strain rates. The code was developed at SNL and has been used extensively at SNL for a large variety of applications. One set of FE calculations discussed in Section A.2.2.5.2 used the Presto FE code (Koterak, 2003). This is a new SNL FE code for the same applications as Pronto3D, but it developed specifically for a parallel computing framework.

(U) Detailed structural information on commercial jetliners is difficult to obtain. There is a continual effort at SNL to improve these models. The current model of the jetliner was developed by a review of the open literature. Although some improvements could potentially be made, it is believed that this model is representative of a jetliner and has been used extensively for many of the current vulnerability studies being conducted at SNL.

(U) Model for the casks was derived from the certification Safety Analysis Report (SAR) (Holtec International, 2000). The SAR provided both the correct geometry and material descriptions of the casks.

A.2 Structural Analysis of a Jetliner Impacting a Field of Storage Casks (U)

(U) A jetliner intentionally impacting a field of HI-STORM dry storage casks results in many possible scenarios of a hard component impacting a cask and subsequent cask-to-cask impacts. In addition, the total momentum imparted onto a cask or casks must be analyzed. The global and local analyses conducted on the HI-STORM storage cask are covered in Sections A.2.1 and A.2.2, respectively. Many scenarios were examined in order to explore the vulnerabilities of these casks. The likelihood of particular scenarios examined varies. The global and local analyses combined examine many potential vulnerabilities of the dry storage cask field to an impact from a large commercial jetliner.

A.2.1 Global Analysis of a Jetliner Impacting a Field of Storage Casks (U)

A.2.1.1 Introduction (U)

(U) An analysis was conducted to assess the vulnerability of the storage cask to jetliner impact. The goal of this global analysis was to determine the following: (1) the momentum imparted to a single cask by the impacting jetliner, (2) the cask exit velocity, and (3) the load history on the cask. The CTH Eulerian shock physics code was used to conduct the analysis. Given the size and complexity of the problem being modeled, simplified representations of the jetliner and cask were considered to approximate the momentum transfer and resultant cask velocity. When considering large cask arrays, the initial jetliner impact can lead to subsequent cask-to-cask interaction. The outcome of the global analysis will provide a set of initial conditions for the

detailed local analyses. These initial conditions include the cask exit velocity for a cask-to-cask impact, as well as the angular velocity when cask tip-over occurs.

(U) The CTH analysis is composed of two portions: an initial study and the final analysis. The purpose of the initial study was to scope out the jetliner impact problem and outline a reasonable approach for analyzing it. A parameter study was conducted as part of this initial work to address various modeling issues (e.g., uncertainties associated with modeling jetliner and cask materials). The conclusions from the initial study helped determine model inputs for the final analysis. The remainder of this section is devoted to documenting the threat definition, the CTH analysis methodology, and the results from both the initial parameter study and final analysis.

Ex. 1
p. A-6a

Table A-1. Initial Global Jetliner Impact Analyses (U).

The contents of this table are unclassified.

Ex3
SGI
A-6b
SGI
A-6C
Ex3

Table A-1. Initial Global Jetliner Impact Analyses (Continued) (U).
The contents of this table are unclassified.

SGI
P.A-7a
Ex.3

Table A-2. Final Global Analyses (U).
The contents of this table are unclassified.

--

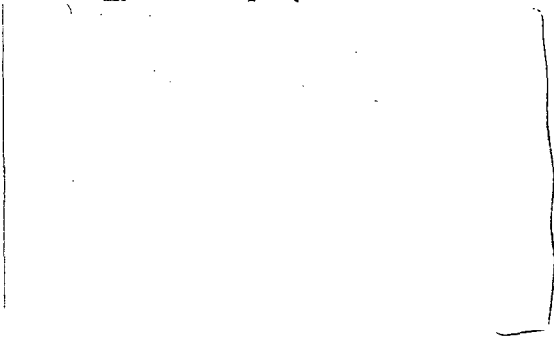
Ex 3
SGL
A-8a

A.2.1.2 Threat Scenario (U)

--

Ex. 1
A-8b

(U) The jetliner model was composed of nine major components:



ex. 2
p. A-9a

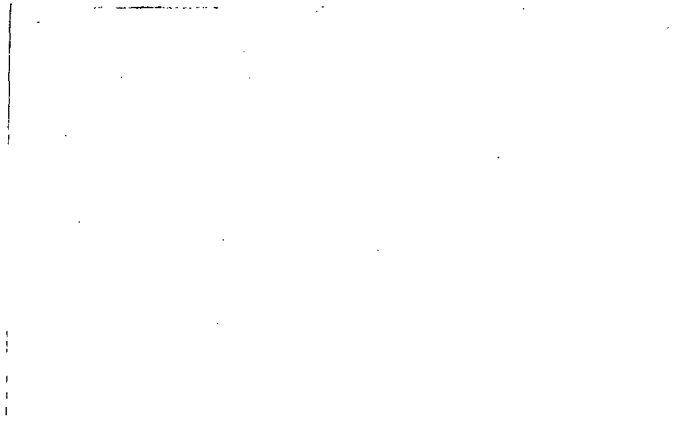
The masses of these nine major jetliner components are provided in Table A-3. For purposes of comparison, the weight for the jetliner ranges between 142,420 and 152,410 kg (314,000 and 336,000 lbs) (depending on the model configuration) for Boeing these jetliners at 60% maximum structural payload and 80% usable fuel (Boeing, 1989).

ex 3
SGT
A-9b

Figure A-2. FE Model of Jetliner (U).

The contents of this figure are unclassified.

Table A-3. Mass of Jetliner Components (U).
The contents of this table are unclassified.



Ex 3
SGI
A-10a

A.2.1.3 CTH Analysis (U)

A.2.1.3.1 Background – CTH Methodology (U)

(U) The CTH Eulerian shock physics code (McGlaun et al., 1990; Hertel et al.; 1993, and Bell et al., 2000) was used to perform this global analysis. The CTH family of codes encompasses the mesh generation, analysis modules, and post-processing software for the analysis of transient, large deformation, and/or problems involving strong shocks. CTH is a well-established code that has been used for numerous defense-related applications. Of interest here are impact applications. CTH has been used extensively for anti-armor and hypervelocity impact applications, where impact velocities are typically greater than 1 km/s (3200 ft/s) (e.g., Hertel, 1992; Kmetyk and Yarrington, 1994; and Wilson et al., 1998). There has been limited extension of CTH to lower impact velocity regimes (e.g., Silling, 1992). A brief overview of the CTH methodology is provided herein. The reader is directed to McGlaun et al. (1990) and Hertel et al., (1993) for a more thorough discussion of the CTH methodology.

(U) CTH is an explicit Eulerian code, meaning that the time marching scheme is conditionally stable with the stable time step determined by the Courant condition. For a given time step, CTH utilizes a two-step approach for the solution of conservation equations. The two-step solution approach first involves a Lagrangian step, where the CTH mesh is allowed to deform. This deformation provides an indication of material motion through the fixed, CTH reference mesh. The Lagrangian step is followed by a remap step. The remap algorithm advects material quantities (i.e., the volume fluxes, mass, momentum, and energy) from the deformed Lagrangian configuration back into the fixed, CTH reference mesh.

(U) The CTH reference mesh is a rectilinear mesh, which is subdivided into cells. For 3-D applications, the cells are modeled as rectangular parallelepipeds, with the cell faces aligned with the global Cartesian coordinate system. Over the course of a calculation, material moves through the fixed, CTH mesh. The Eulerian solution approach does not allow explicit tracking of

material interfaces. Specialized interface tracking algorithms have been developed to reconstruct the material interfaces. The algorithm utilized by CTH is the Sandia Modified Young's Reconstruction Algorithm (SMYRA) (Bell, 1992). With this algorithm, material interfaces are reconstructed based on the volume fraction of material in the cell of interest and its neighboring cells. The volume fractions indicate the presence or absence of materials in these cells. SMYRA provides a planar representation of the material interface within a cell.

(U) Impact applications are characterized by transient wave propagation, nonlinear material response, and large material deformations. In an Eulerian approach, material moves through the fixed mesh. This is advantageous for modeling large material deformations and it avoids mesh entanglement issues typically encountered with Lagrangian methods. However, since the mesh is fixed, there typically exists cell containing multiple materials or material and void. These are referred to as mixed cells.

Ex #2
A-11a

Ex #2
A-11b

A.2.1.3.2 CTH Problem Setup (U)

Ex. 1
A-11c

SG1
PA-12a
Ex3**Figure A-3. Initial Problem Geometry (U).**

The contents of this figure are unclassified.

(U) CTH allows a wide variety of options for controlling the calculation. For this analysis, the multimaterial temperature and pressure model option (mmp, frac=1) was specified. This allows each material to have its own temperature and pressure in a mixed material cell. As momentum and energy cannot both be conserved during the material advection step, the user must choose the advection scheme for the energy (momentum is always conserve within CTH). The default scheme was chosen, which advects the internal energy, but discards any discrepancies in the kinetic energy.

OUO-SRI
PA-12b
Ex 2

(U) The CTH mesh was sized to meet the requirements for each calculation.

OUO-SRI
PA-12C
Ex. 2

(U) Materials are inserted into the CTH mesh at startup of the calculation. Material insertion usually involves defining a body as a set of geometric objects, which are then assigned unique material identification numbers. A simplified representation of the cask was developed, which included the overpack steel shells, top lid, base plate, and concrete.

PA-12d
Ex2
OUO-SRI

The simplified model was thought sufficient for the goals of this analysis, which were to assess the global response of the cask. CTH also provides a capability for inserting a hex-meshed FE model into the CTH mesh at startup of the calculation. This provides a convenient means to insert bodies with complex geometries into the CTH mesh and was used for inserting the jetliner model.

(U) Typically, the resolution of the CTH mesh is derived from the minimum dimension of an inserted material. In general, one would like to have several cells across the thickness of an inserted material.

[A much finer mesh is required to accurately resolve the cask detail. One must trade-off the cost and accuracy of a calculation. A finer mesh was desired, but was impractical due to increased analysis turnaround times and limited computational resources.

(U) Before discussing the material modeling, it is useful to outline the evolution of the calculations described in Table A-4. The initial calculations, CTH-SA and CTH-SA-V1, consider a simplified jetliner (SA) impacting the cask without any underlying concrete pad or soil. Essentially, the cask is free-floating in space.

[The purpose of calculations CTH-SA and CTH-SA-V1 was to scope out the level of difficulty of the calculation and provide some comparison of results based on available concrete model data. As previously mentioned, the concrete pad under the cask was not modeled. Consequently, the impact scenario can be roughly equated with assuming frictionless contact between the cask and the underlying concrete pad. In turn, this provides an estimate of the cask exit velocity that can be achieved following initial impact (the exit velocity serves as an initial condition in more detailed analyses addressing cask-to-cask impact presented in Section A.2.2).

(U) During the course of the initial study, questions arose regarding the adequacy of considering an SA.

[A problem was set up to answer this question. This calculation, CTH-FA, modeled the impact of the full airplane (FA) against the cask and allowed for direct comparison with the previous calculations.

(U) In summary, very little difference was noted between the momentum imparted to the cask for the SA and FA models.

ex. 2
A-13a

ex. 2
A-13b

ex. 2
A-13c

ex. 2
A-13d

ex. 2
A-13e

ex. 2
A-14a

Section A.2.1.4.2 discusses the significance of the participating and non-participating mass in more detail.

(U) Further excursion calculations were considered, all using the SA model.

ex. 2
A-14b

The excursion calculations, CTH-SA-V2 through CTH-SA-MIX3-V2, are summarized in Table A-4 and discussed in more detail in Section A.2.1.3.4.

Table A-4. Description of CTH Calculations (U).

The contents of this table are unclassified.

Calculation	Calculation Description
CTH-SA	
CTH-SA-V1	Same as CTH-SA, except cask concrete modeled with "tuned" concrete model (see Section A.2.1.3.3 for description of tuned model).
CTH-FA	Same as CTH-SA, except using FA.
CTH-SA-V2	
CTH-SA-REV	Same as CTH-SA, except using corrected cask steel material properties.
CTH-SA-MIX3	Same as CTH-SA, with addition of underlying concrete pad and soil.
CTH-SA-MIX5	
CTH-SA-MIX3-V1	Variant of CTH-SA-MIX3.
CTH-SA-MIX3-V2	

ex. 2
A-14c] ex 2
A-14dex 2
A-14e] ex 2
A-14f

A.2.1.3.3 CTH Material Modeling (U)

Background – CTH Material Models (U)

(U) The CTH material model inputs for the cask and jetliner are provided in Tables A-5 and A-6. The nomenclature in the tables follows the keyword inputs for CTH, which are defined in Table A-7. CTH model inputs are in cm-g-sec-eV units. The units in the tables have been converted to SI, as these are widely accepted by the engineering community.

(U) CTH decouples the material behavior into the dilatational and deviatoric response. The dilatational response is described by an EOS, while a strength model describes the deviatoric response. In the CTH terminology, the strength model is referred to as an elastic-plastic (EP) model. An EOS expresses a relationship between the thermodynamic pressure, density, and internal energy in a state of equilibrium. An EP model is a plasticity model, designed to capture the shear-induced response of the material.

(U) CTH supports a wide range of EOS and EP models. The choice of model depends on the problem and materials involved. The EOS and EP models used in this analysis are defined in Tables A-5 and A-6. The Mie-Gruneisen EOS is commonly used in shock physics applications, and describes the pressure response in the material as a linear function of the internal energy. Porous materials are best represented by a P- α model. The state variable α relates the porous material density to the density of the matrix material. It is used to track the crushing behavior of the material. The geologic yield surface allows a pressure-dependent yield surface. The Von Mises yield surface models a rigid, perfectly plastic yield surface. These models are described in more detail in Bell et al. (2000) and Hertel and Kerley (1998).

(U) Typically, a fracture model supplements the EOS and EP models. For this analysis, a PMIN model based on a minimum principal stress criterion was considered. With this model, the material pressure is relaxed to a state prior to fracture whenever the prescribed fracture criterion is exceeded. This is done with an iterative algorithm that increases the material density until a consistent relaxed pressure state is achieved, while holding the energy constant. Void is then inserted into the cell to account for the change in material volume resulting from increasing the density. The PMIN fracture model is really a spall model, designed to replicate spallation occurring along free surfaces.

Table A-5. CTH Material Parameters for Cask (U).

The contents of this table are unclassified.

ex. 2
A-16a

Ex 2
A-16b
Ex 2
A-16c
Ex 2
A-16d

³ — Material data corrected in CTH-SA-REV using CTH library data (Mie-Gruneisen EOS for iron and Johnson-Cook strength model for carpenter electric iron)

Table A-6. CTH Material Parameters for Jetliner (U).

The contents of this table are unclassified.

ex. 2
A-17a

Ex 2
A-17b

Table A-7. CTH Material Parameter Definitions (U).

The contents of this table are unclassified.

Material Model	Parameter Definitions
Mie-Gruneisen EOS	r0 – Initial material density cs – Initial sound speed of material s1 – Linear coefficient in us-up Hugoniot curve s2 – Quadratic coefficient in us-up Hugoniot curve g0 – Gruneisen parameter cv – Specific heat
P- α EOS	r0 – Void-free density for porous materials rp – Initial density of porous material ps – Compaction pressure; pressure at which compaction of porous material is complete pe – Elastic pressure; Used to include an elastic region in pore compaction model, where pe is the minimum pressure at which pore compaction begins ce – Sound speed in elastic pore compaction region cs, s1, s2, g0, cv – same as Mie-Gruneisen EOS model
Geological Yield Surface Strength Model	yield – The yield strength as the pressure becomes very large yield0 – Yield strength at zero pressure dydp – The initial slope of the yield surface as a function of pressure at zero pressure poisson – Poisson's ratio
Von Mises Yield Surface Strength Model	yield – Yield strength in tension poisson – Poisson's ratio
Fracture Model	PMIN, stress – Material fracture with subsequent void insertion based upon a minimum principal stress criterion pfrac – fracture stress of material

Cask Materials (U)

(U) Given the time constraints associated with this analysis, heavy reliance was made on “off-the-shelf” material inputs that would provide a reasonable approximation of the material response. Kipp¹ provided the baseline material inputs for the cask concrete. This data represents a fit to multiaxis specimen tests of a conventional strength Portland cement (CSPC) concrete (Frew, 2001).

develop material model inputs.

(Typically, multiaxis specimen test data is required to

¹ Personal Communication with Marlin Kipp, Sandia National Laboratories, June 2002.

ex. 2
A-18a

ex. 2
A-18b

1 ex. 2
A-18c

ex. 2
A-19a

A-5.

] The adjusted model inputs are shown in Table

Ex 2
A-19bex. 2
A-19cex. 2
A-19dex. 2
A-19e

] Note that the goal is to obtain global estimates of the cask response. These will serve as initial conditions for more detailed studies seeking to answer the question of cask damage and potential rupture.

] At the onset of this analysis, material specifications were unavailable. Unfortunately, when they did become available, the yield strength of the steel was not corrected. The SA516, Grade 70 steel used in the cask has a static yield strength of 262 MPa (38 ksi) and an ultimate strength of 483 MPa (70 ksi) at ambient conditions. The material model inputs were revised in a later calculation, CTH-SA-REV, to better match the actual steel and assess the implications of using the higher-strength steel. Material input data was readily available for a carpenter electric iron (Johnson and Holmquist, 1989), which appeared to exhibit a comparable hardening response as the SA516, Grade 70 steel. The steel behavior was modeled using a Mie-Gruneisen EOS for iron and the Johnson-Cook strength model. The Johnson-Cook model (Johnson and Cook, 1983) is a phenomenological model; i.e., an isotropic power-law plasticity model for large deformations. It takes into account both rate and thermal effects. Material parameters for both the EOS and strength model were taken from the CTH material library.

ex 2
A-19f

] As discussed later, the use of the revised steel properties had little effect on the results. This should not be surprising, given the coarse mesh resolution and lack of detail in the cask model.

Ex 2
A-19g

Ex 2
A-20a**Jetliner Materials (U)**

(U) The jetliner model is a simplified representation of a jetliner. The model developed represents a current best estimate of the mass distribution and key hard components within the jetliner. The stiffness of the jetliner structure affects the loading on the cask. The material model inputs in Table A-6 were developed to replicate the stiffness of the actual jetliner within the context of its simplified representation.

(U) Considerable effort was expended to replicate the stiffness of the fuselage skin, as it directly affects the resulting force on a cask.

Ex 2
A-20b

modified jetliner material can be described as a porous aluminum material.

The

Ex 2
A-20c

(U) There was one modification to the porous aluminum material model data used in this study as compared to previous studies using this model.

Ex 2
A-20d

This fracture stress is only valid for tensile stress. There is no compression fracture limit in the CTH model.

Once again, the goal of this analysis is to assess the global cask response. Here it is important to match the mass of the jetliner components, which, in turn, will provide a more realistic assessment of the momentum transfer between the jetliner and cask.

Ex 2

A-21a

Ex 2
A-21bEx 2
A-21c

Materials Modeling Summary (U)

(U) Uncertainty in material properties and how these materials are modeled are intrinsic to this type of analysis. For this study, the cask SAR (Holtec International, 2000) provided guidance for cask properties. The cask material properties listed in the SAR are typically minimum specified properties, and do not take into account rate effects for dynamic events such as those examined in this study. Although jetliner manufacturers have a detailed understanding of the material properties for their jetliners, these properties are not readily accessible. It is also not clear how jetliner materials behave under these types of scenarios. It is a relatively new endeavor to attempt to model jetliner in these types of scenarios. Given these uncertainties, every attempt has been made to use realistic values for the material properties to provide the most realistic behavior of the jetliner and cask in these types of scenarios.

A.2.1.3.4 CTH Analysis Results (U)

Impact Phenomenology (U)

Ex. 1
A-21d

Ex 2
A-22a

Ex 2
A-22b

Ex 2
A-22c

Ex 2
A-22d

Ex 2
A-22e

Ex 2
A-22f

This analysis looks at the global response, with its results feeding more detailed analyses that will make the damage assessment (see Section A.2.2).

Ex 1
A-22g

Side-On Cask Velocity (U)

Ex. 1
A-22h

Ex 2
A-23a

Ex 2
A-23b

Ex 2
A-23c

Ex 2
A-23d

Ex 2
A-23e

Figure A-4. CTH-FA Calculation (initial analysis velocity), Material Plots at Selected Times (U).

The contents of this figure are unclassified.

Ex 3
A-24a

Ex 3
A-24b

Ex 3
A-24c

(e) CTH-SA-REV

Figure A-5. Material Plots at 60 msec for Calculations CTH-FA Through CTH-SA-REV, Initial Study (initial analysis velocity) (U).

The contents of this figure are unclassified.

Ex 3
A-25a

Ex 3
A-25b

Ex 3
A-25c

Figure A-6. Material Plots at 100 msec for Calculations CTH-FA Through CTH-SA-REV, Initial Study (initial analysis velocity) (U).

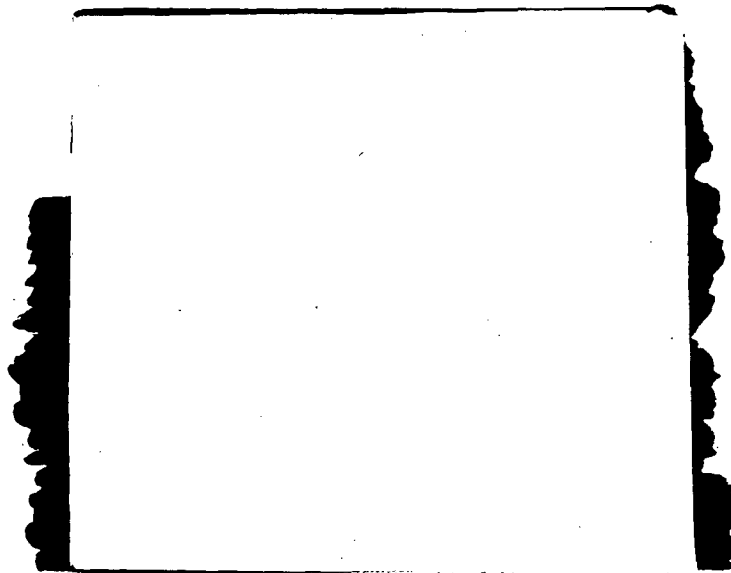
The contents of this figure are unclassified.

(U) It is interesting to note the similarity of results in Figure A-7. The differences are small compared SA calculations. However, there is a small but noticeable difference compared to the SA and FA calculations. The final cask velocity is slightly less for the FA impact. This is nonintuitive and likely the result of numerical artifacts in the problem development.

Ex 2
A-25d

Ex 2
A-26a
Apparently, this effect propagates upstream, causing minor changes in the velocity field for material in the impact region.

Ex 2
A-26b
From an analysis standpoint, this is significant because it allows a much-reduced problem to be calculated.



Ex 1
A-26c
Figure A-7. Cask Side-On Velocity as a Function of Time for Calculations CTH-FA Through CTH-SA-REV, Initial Study (initial analysis velocity) (1 m/s = 2.24 mph) (U).

The contents of this figure are classified C.

(U) Calculations CTH-SA and SA-V1 considered the impact of the SA against the cask; however, the cask concrete material differed for the two calculations.

(U) Calculation CTH-SA-V2 sought to address issues of modeling the fuselage material. In this calculation, a standard Mie-Gruneisen EOS was used to model the dilatational response using the same properties for the porous aluminum material (i.e., parameters r_p and p_s were not defined). The difference in cask velocity history compared with other SA calculations is small.

The cask velocity history is essentially the same as that in the CTH-SA and CTH-SA-V1 calculations.

Ex 2
A-27a

Ex 2
A-27b

Ex 1
A-27c

Figure A-8. Cask Side-On Velocity as a Function of Displacement for Calculations CTH-FA Through CTH-SA-REV, Initial Study (initial analysis velocity) (1 m/s = 2.24 mph) (U).

The contents of this figure are classified C.

Computed Force on Cask (U)

(U) The total force exerted on the cask was also of interest. By virtue of the Principle of Virtual Work, the forces calculated from the rate of change in momentum of the cask can be equated to the applied loads. This provides an estimate of the total applied force (f) on the cask, which is readily computed by

$$f = d(m v_x) / dt.$$

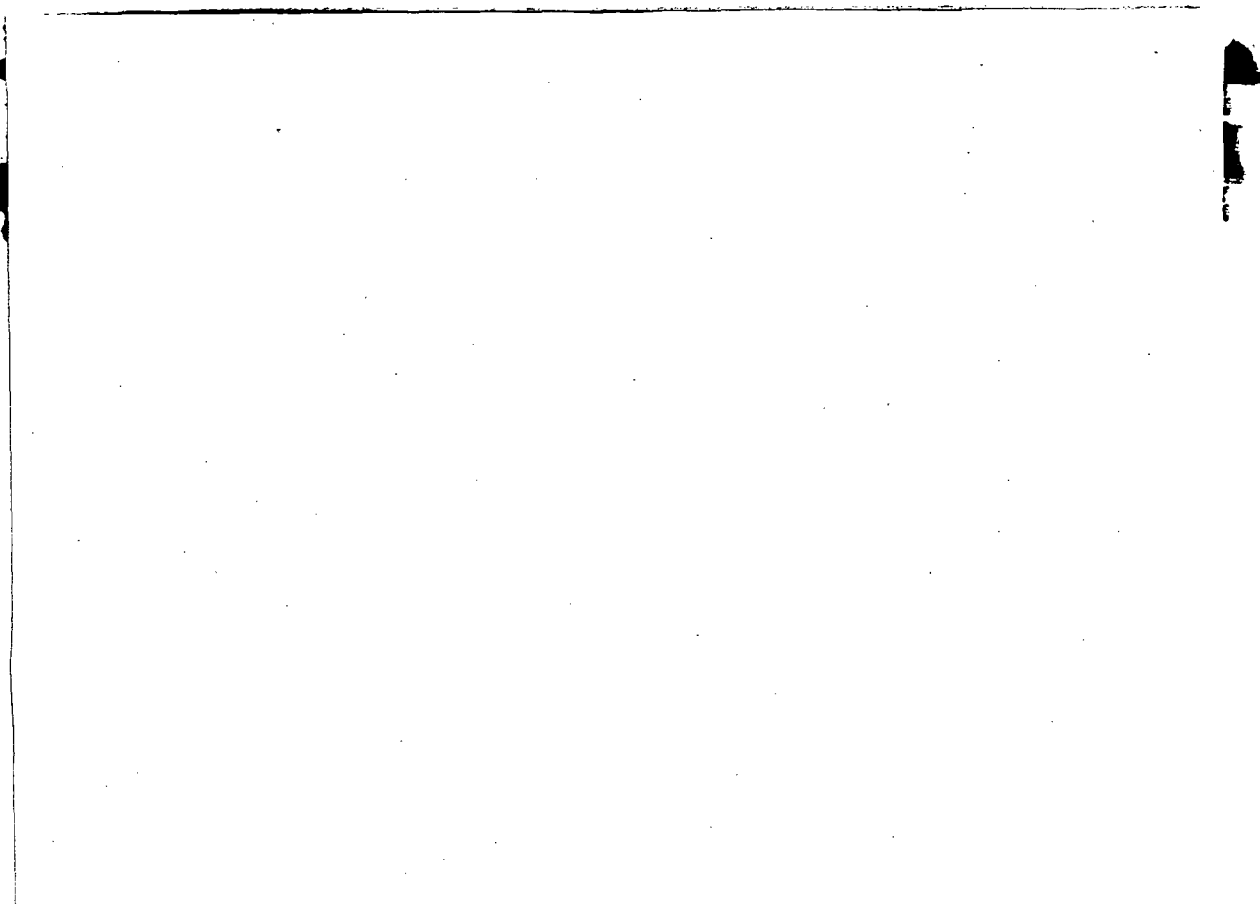


Figure A-9. Total Force on Cask for Calculations CTH-FA Through CTH-SA-REV, Initial Study (initial analysis velocity) (1 N = 0.22 lb) (U).

The contents of this figure are classified C.

(U) CTH tracers were embedded along the outer cask surface to estimate the localized loading. Pressure histories at selected locations on the outer cask surface are provided in Figure A-10 for calculation CTH-SA. These results are representative of pressure histories obtained in the other calculations. The pressures provide some indication of the interface loading on the cask surface (a true measure would be given by the normal stress, which cannot be derived from the available CTH tracer data). The pressures exhibit considerable variability and are difficult to interpret!

Ex 2
A-29aEx. 1
A-29b

Figure A-10. Pressures at Selected CTH Tracer Locations, CTH-SA Calculation, Initial Study (initial analysis velocity) (1 MPa = 145.0 psi) (U).

The contents of this figure are classified C.

(U) A load distribution can be derived from the total force in Figure A-9. Using a Riera approach (Riera, 1968), the total force could be represented as a uniform pressure across a patch on the target. The assumed load distribution could be improved upon by developing a set of superimposed force-time histories from the total force (e.g., identify separate force histories associated with each component). These superimposed loadings could then be applied to different pressure patches, each representing regions impacted by individual jetliner components. From a vulnerability standpoint, either approach is sufficient as long as the prescribed loading results in a realistic representation of the threat-target interaction.

(U) Note the differences between a Riera force function and the one derived in this analysis. A Riera approach assumes a normal impact against a rigid surface. Riera derives a force function that is dependent on the jetliner impact velocity, the jetliner mass distribution per unit length, and the load required to crush the fuselage (often referred to as the crush force or buckling load). The contribution of individual jetliner components to the total force is implicitly derived from the mass distribution, which is approximated as a line distribution. Simplifying assumptions are made in the determination of the crush force and mass distribution (see Riera (1968) or Sugano et al. (1993a) for details). The major difference between a Riera force and that derived here is the conservatism associated with impacting a rigid surface.

Ex 2 A-29c
Ex 2 A-29d

Effects of Underlying Concrete Pad (U)

(U) The concrete pad underlying the cask will affect the nature of the momentum transfer between the threat and target. Jetliner debris will be restrained from flowing underneath the cask, as depicted in Figure A-3.

Translational (slip) velocities of the cask are also of interest.

The lack of resolution is also responsible for the non-physical slip behavior noted between the cask concrete and base plate.

Figure A-11. Material Plots at 60 msec, Initial Study (initial analysis velocity) (U).

The contents of this figure are classified C.

However, it is not perfect. This option creates a sticky interface between materials, with slip controlled by the volume-averaged shear strength of the materials residing in the mixed cell. The treatment of mixed cells along the pad surface is problematic. In this region, mixed cells are composed of the cask concrete, steel base plate, and concrete pad. The coarseness of the mesh causes these materials to stick together. In turn, the concrete pad rotates with the cask.

Ex 2
A-30aEx 2
A-30bEx 1
A-30cEx 2
A-30dEx 2
A-30e

Cask Rotational Velocity (U)

The rotation angle is measured from the vertical and was computed from tracers embedded at the top and base of the cask. The rotation angle was differentiated using a central difference scheme to obtain the instantaneous angular velocity. Tracers were also embedded at the rear corner of the cask to monitor the cask motion relative to the underlying pad.

Ex 2
A-31g

Ex 2
A-31b

A-31c
Ex 2000-SKI

A-31d
Ex 1

Figure A-12. Cask Rotation Angle and Angular Velocity, CTH-SA-MIX3, Initial Study (initial analysis velocity) (U).

The contents of this figure are classified C.

(U) The angular velocity varies considerably with time. Any estimates of the angular velocity for a cask-to-cask impact problem will depend upon the cask spacing and jetliner impact location along the height of the cask. For a cask array, it is customary to specify the center-to-center cask spacing. The spacing can be used to determine the separation distance D between casks as follows:

$$D = S - d_{\text{cask}},$$

where S is the center-to-center spacing and d_{cask} is the cask diameter. The tip-over angle at which one cask will impact another, θ_{contact} , can then be derived as follows:

$$\theta_{\text{contact}} = \tan^{-1}(D / h_{\text{cask}}),$$

where h_{cask} is the height of the cask. For a given jetliner impact location, the tip-over angle can be compared with the rotation angle in Figure A-12 to find the time at which contact occurs, t_{contact} . This can be cross-referenced with the angular velocity plot to find the angular velocity at initial contact, ω_{contact} . It is assumed that the cask rotates about a fixed point.

The slip velocity V_{slip} is the translational velocity at the corner of the cask, which is obtained from CTH tracers embedded near the base of the cask.

Ex 2
A-32a
Ex 2
A-32b
Ex 2
A-32c

Table A-8. Estimates of Cask Angular Velocity as a Function of Cask Separation Distance for the Initial Set of Analyses (U).

The contents of this table are unclassified.

The fracture stress of the base material was set artificially low to preclude any rotation of the underlying base material with the cask.

Ex 2
A-32d

Other than this change, all other CTH inputs were the same as in CTH-SA-MIX3.

Ex 2
A-32e

Ex 2
A-32f

(U) The angular velocity depends on the jetliner's impact location along the height of the cask. Intuitively, the higher the impact point on the cask, the greater the angular velocity of the cask.

Ex 2
A-32g

EX #3
SG1
A-33a

Figure A-13.

The contents of this figure are unclassified.

EX #2
A-33b

(U) Material plots at 60 msec for the two calculations are provided in Figure A-14. The dense, base material coupled with its low fracture stress allows the cask to rotate freely. The calculated rotation angle and angular velocity for the two calculations are provided in Figure A-15.

EX #2
A-33c

EX2
A-33d

SG1
A-33e
EX3

Figure A-14. Material Plots at 60 msec, Initial Study (initial analysis velocity) (U).

The contents of this figure are unclassified.

EX.1

A-34a

EX #2
A-34b

The contents of this figure are classified C. —

A.2.1.3.5 Uncertainties in the CTH Analysis (U)

(U) The goal of the CTH vulnerability analysis is to estimate the global response of the cask, thus providing initial conditions for more detailed analyses modeling cask-to-cask interaction. The initial study sought to scope out the problem, and outlines a reasonable approach for analyzing jetliner impact. The initial study also exposed a number of uncertainties in the CTH analysis.

(U) Given the size and complexity of the problem being modeled, simplified representations of the jetliner and cask were considered to approximate of the momentum transfer. The size of the problem also made it necessary to rely on a fairly coarse mesh. A finer mesh was desired, but was impractical due to increased analysis turnaround times and limited computational resources. The coarse mesh will affect the accuracy of the solution; however, it is not expected to drastically affect quantities in the global response calculations, such as the total momentum. The loss of accuracy associated with using the coarse mesh is expected to affect localized response calculations, such as determination of cask damage and breach. These determinations are best made using a structural analysis code, with the results of the present CTH analysis providing the initial and/or boundary conditions.

(U) Aside from meshing issues, there are other sources of uncertainty in this analysis. These uncertainties include (1) geometric errors associated with the simplified cask and jetliner models, (2) material response modeling, and (3) impact conditions. The jetliner modeling is believed to present the greatest source of uncertainty in the analysis. Errors associated with modeling jetliner component location and geometry are believed to be the primary source of uncertainty in this analysis. This statement is substantiated by the calculated force history, where there is a direct correlation between the load history and the time at which jetliner components impact the cask.

EX2

A-34c

Ex 2
A-35g

(U) In contrast to the jetliner, there are detailed descriptions available for the cask. However, only a simplified representation was considered in the global analysis.

Ex 2
A-35h

There is obviously room for improvement in the cask model, particularly in the representation of the MPC.

Ex 2
A-35c

(U) Variations associated with the material modeling appear to be a second-order effect in this analysis. Calculations CTH-SA-V1, CTH-SA-V2, and CTH-SA-REV support this conclusion, as these were run specifically to address variations in material modeling. With the level of refinement used in this study, there is no apparent effect on the global behavior of the cask due to small variations in the material properties.

Ex 2
A-35dEx 2
A-35e

Section A.2.1.3.1 discusses the different options CTH provides to address this issue, and parametric runs to examine these options are presented in Section A.2.1.3.4. A verification of the maximum side-on velocity is presented in Section A.2.1.4.2 and provides some insight into the degree of conservatism introduced by this issue.

(U) Modeling such a jetliner impact problem would substantially increase the size and complexity of the analysis. For a CTH analysis, the mesh would have to encompass the entire jetliner and target as a bounding box. This is a substantially larger problem than that modeled in the present analysis. Parametric analyses are impractical for these large problems.

Ex 2
A-35fEx 2
A-35g

A.2.1.4 Finalized CTH Analysis Results (U)**A.2.1.4.1 Problem Definition (U)**EX. 1
A-36a**A.2.1.4.2 Maximum Velocity Estimates (U)**EX. 1
A-36b**Jetliner Impact at Cask Mid-Height (U)**EX. 1
A-36c

(U) The frictional force between the pad and cask is minimal and will not significantly affect the results. If one assumes a friction coefficient of 0.3 and uses the nominal cask weight of 163300 kg (360000 lbs), the frictional force is approximately 481000 N (108000 lbs).

EX. 2
A-36d

EX 1
A-37g

Figure A-16. Cask Side-On Velocity as a Function of Time (1 m/s = 2.24 mph) (U).
The contents of this figure are classified C.

EX 1
A-37b

Figure A-17. Cask Side-On Velocity as a Function of Displacement (1 m/s = 2.24 mph;
1 m = 0.3048 ft) (U).

The contents of this figure are classified C.

EX 1
A-38a

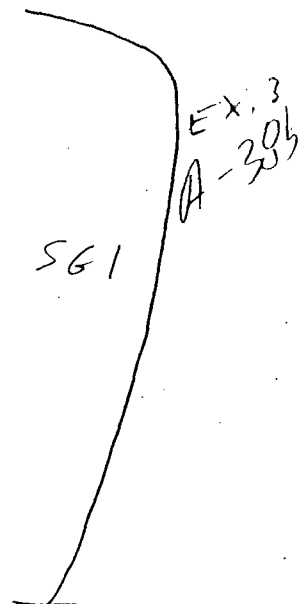


Figure A-18. Total Force on Cask (1 N = 0.224 lb) (U).

The contents of this figure are unclassified.

Jetliner Impact at Cask Top Edge (U)

EX 2
A-38c

(U) Figure A-19 shows the velocity as a function of time.

For cask-to-cask impacts in the local analyses discussed in Section A.2.2, the velocity as a function of translational distance is plotted in Figure A-20.

SG1
A-38d
EX 3

EX 1
A-39a

Figure A-19 Velocity vs. Time for the Jetliner Impact at the Top Edge of Cask
(1 m/s = 2.24 mph) (U).

The contents of this figure are classified C.

EX 1
A-39b

Figure A-20 Velocity vs. Displacement for Jetliner Impact at the Top Edge of the Cask
(1 m/s = 2.24 mph; 1 m = 0.3048 ft) (U).

The contents of this figure are classified C.

Summary of Cask-to-Cask Velocities for the Local Analyses (U)

(U) The global analyses discussed in the previous two sections are used to establish velocities in the local analysis, discussed in Section A.2.2. Since the exit velocity of the cask is a function of translational distance (as shown in Figures A-17 and A-20), an examination of the pad layout is required. The schematic in Figure A-21 shows a typical pad layout. The figure shows the clear spacing between the casks.

400
Ex 2
Ex 2 400
Ex 2 400
} Ex 2 400
Ex 2 400

(U) The third case requires some additional explanation.



Ex 2
A-419

Figure A-21 Clear Spacing Distances Between the Casks on a Typical Pad Layout (U).

The contents of this figure are unclassified.

The table includes the velocity at the corresponding distance and the time required to reach this distance.

Ex 2 A-41b

Ex 2 A-41c

These values are important for cask impacts beyond the single-pad scenarios.

Table A-9: Cask Velocity as a Function of Separation Distance (U).
The contents of this table are classified C.

EX. 1
A-429

Verification of Maximum Side-On Velocity Estimates (U)

(U) To verify the exit velocity being calculated using the CTH code, a simple calculation was performed to determine the exit velocity based on transfer of momentum.

Therefore, to verify the exit velocity CTH calculated, a similar approach has been used here.

EX 2
A-42b

EX 2
A-42c

Participating Jetliner Mass (U)

(U) Figure A-22 shows a cross section of the jetliner fuselage with the outline of the HI-STORM cask in red.

EX 2
A-42d

Therefore, the total mass of the jetliner impacting the cask is summarized in Table A-10.

Table A-10 Total Mass of Jetliner Impacting Cask (U).

The contents of this table are unclassified.

Ex 2
A-43A

Ex 2
A-43b

Figure A-22. Fuselage with HI-STORM Cask Overlay (U).

The contents of this figure are unclassified.

(U) Because the cask is not flat, not all of the impacting mass effectively imparts its momentum to the cask (the mass near the edge of the cask strikes a glancing blow). Figure A-23 shows how the relative effective impacting mass is calculated.

Ex 2 A-43C

~~CONFIDENTIAL - NSI~~

Final Draft

Ex 2

A-44g

Ex 2

A-44b

Figure A-23. Determination of Relative Effective Mass (U).

The contents of this figure are unclassified.

Ex 2 A 44c

EX 1
A 44d

Conservation of Momentum of Participating Mass (U)

EX 1
A-44e

~~CONFIDENTIAL - NSI~~

Significance of Non-Participating Mass (U)

(U)

To clarify this, a brief review of the methodology originally developed by Riera (1968) and studied further by many others (ASCE, 1980; Attaway, 2003; Wolf et al., 1978) is necessary. The force applied to a structure by the impact of a deformable object into a rigid structure can be divided into two terms. One term is that due to the crushing strength of the impacting object, and the other is due to the change in the object's momentum. The standard format for the equation describing this is as follows:

$$F = P_c + \alpha \mu v^2,$$

where

 P_c = The crush strength of the impacting object. α = constant μ = mass per unit length of the uncrushed portion of the impacting object. v = the velocity of the uncrushed portion of the impacting object

Research has shown that the portion of the loading from crushing the impacting object is low (Wolf et al., 1978; ASCE, 1980; Attaway, 2003).

From testing conducted at SNL on a fuselage section of a C-141 military jetliner (designed to carry cargo), it was found that crush strength of the fuselage was approximately 4,410,000 N (991,457 lb) (Uncapher et al., 1994; Attaway, 2003).

(U)

EX 2
A-459
EX 2
A-456EX 2
A-45CEX 2
A-45d

A-45e EX3

A-45f EX1

EX 2
A-45g

(U) As the Riera description of the force suggests, at the velocity under consideration, the majority of the force applied to the cask is due to the change in the jetliner's momentum. For this momentum to be imparted to a cask, it must interact with the cask.

EX 2
A-469

Comparison to CTH Results (U)

EX 1
A-465

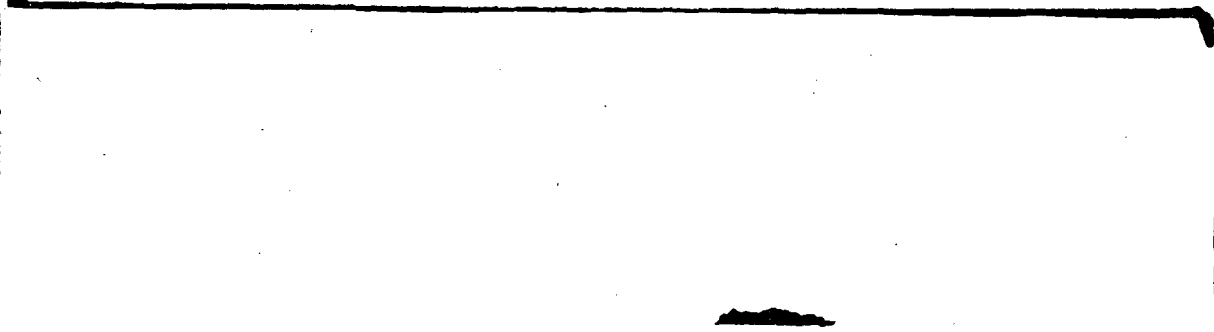
Speed Variability With Respect to Number of Casks (U)

EX 1
A-460

EX-1
A-47a

Figure A-24. Cask Exit Velocity as a Function of the Number of Interacting Casks (U).
The contents of this figure are classified C.

A.2.1.4.3 Rotational Velocity Estimates (U)



EX-1
A-47b



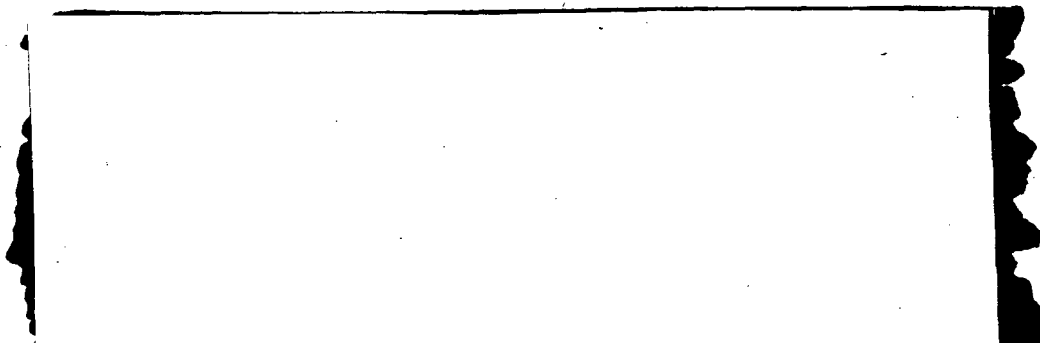
EX. 1
A-48a

Figure A-25. Cask Rotation Angle, CTH-SA-REV (U).

The contents of this figure are classified C.

Table A-11. Estimates of Cask Angular Velocity as a Function of Cask Separation Distance (U).

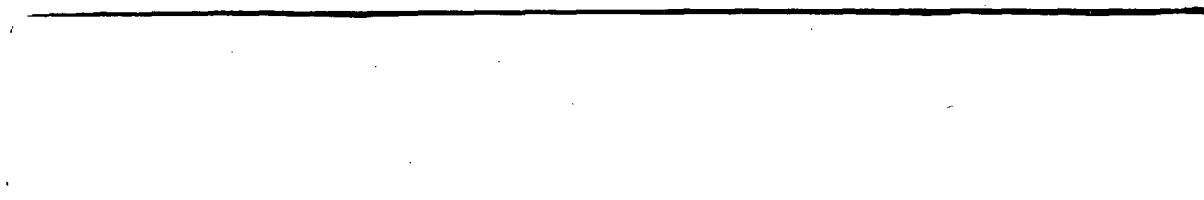
The contents of this table are classified C.



EX. 1
A-49b

A.2.2 Local Analysis of a Jetliner Impacting a Field of Storage Casks (U)

A.2.2.1 Introduction (U)



EX. 1
A-49c

Ex 1
A-49a

(U) The impact scenarios require the use of three-dimensional, nonlinear, transient dynamic, FE capability; Pronto3D (Taylor, 1989) was used for most of the analyses in this study.

Ex 2
A-49b

All these behaviors are required to judge the containment function from the various local scenarios studied.

(U) The threat to the dry storage cask, which is a relatively large, stiff structure, must focus the energy of impact to cause a loss of containment. This focusing of energy can be either in a time or surface area sense. Otherwise, the very size and strength of the cask will distribute the energy throughout its components without causing a loss of containment.

Ex 2
A-49c

Both of these components are considered in this study. Also, the global momentum of the jetliner will be analyzed to study the response of the structure to the overall threat.

(U) These threat scenarios were substantiated by evidence at the Pentagon during a terrorist attack. The front landing gear set was found largely intact at the forward point of damage in the debris. The remaining portions of the jetliner were mostly unrecognizable shards of aluminum.

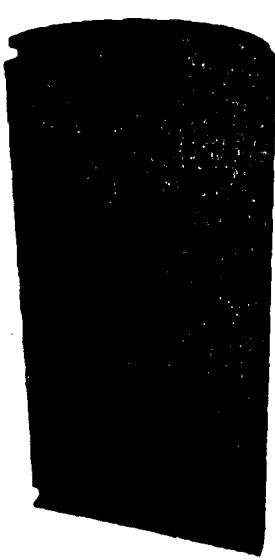
A.2.2.2 Analysis Model (U)

(U) The complicated interaction of materials response and nonlinear geometric contact resulting from this attack requires an explicitly integrated transient dynamics FE analysis code. Pronto3d was used for this purpose. The FE model of the HI-STORM overpack (i.e., the model does not include a model of the MPC that contains the fuel) used ~274,000 elements for the smallest half-symmetry meshes, and were completed on the 3 teraflop massively parallel computer at SNL. This allowed a number of scenarios to be examined in this study. The larger cask-to-cask analyses totaled ~676,000 elements.

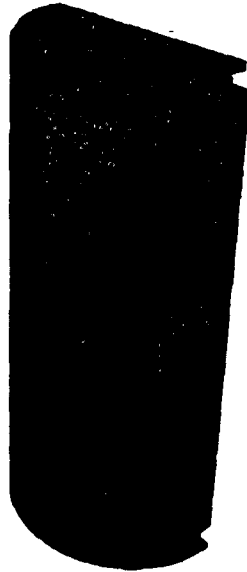
(U) The FE mesh used for most of the analyses is shown in Figure A-26. All dimensions of this HI-STORM storage cask were obtained from the SAR (Holtec International, 2000).

Ex 2
A-49d

Several views are shown in Figure A-26 of the interior detail. Reference to these views during the results discussions will aid in understanding the various components.



Total Model

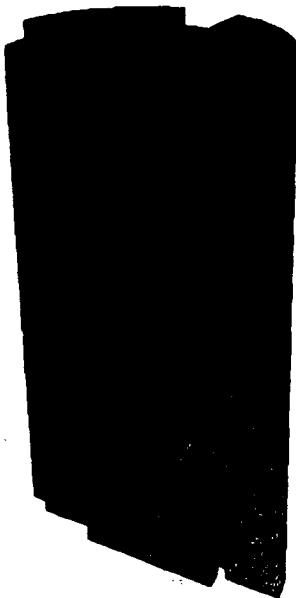


Backside of Model
showing vents

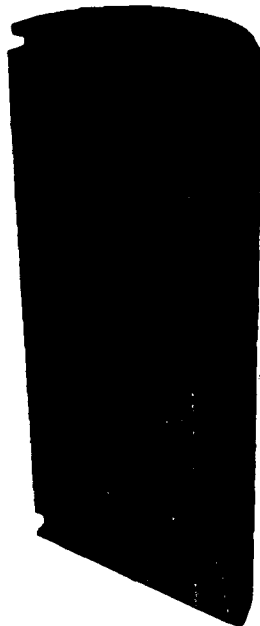


Close-Up of Corner Showing Mesh

UNC



Concrete Portion of Model



Steel Portion of Model



Cross-Section Through Model

UNC

Figure A-26. FE Model for the HI-STORM Cask (U).

The contents of this figure are unclassified.

(U) Also shown in Figure A-26 is a close-up view of the mesh density used in the analyses.

The steel and concrete were modeled without surface traction, i.e., without friction or continuity between these parts, due to this construction detail.

Ex 2
A-515

Ex 2
A-516

Ex 2
A51C

(U) In each of the analyses discussed in this section, the casks were free to displace when impacted. The pad beneath the casks was not modeled. The frictional force due to the pad beneath the casks is small compared to the force of the jetliner impacting the cask.

A.2.2.3 Material Behavior (U)

(U) The steel forming the shell of the HI-STORM is A516 Grade 70. Properties for this material are listed in Table A-12, and were obtained from uniaxial tensile data (Cherry and Smith, 2001). Test data provides a more accurate measure of the casks performance than the minimum specified properties in the SAR. The steel material properties used in the FE analyses are listed in Table A-12 and the concrete properties are listed in Table A-13.

Ex 2
A-516

Table A-12. Material Behavior Definitions for Structural Impact Analyses (U).

The contents of this table are unclassified.

Ex 2
A-524

(U) The concrete material behavior uses the model developed by Karagozian and Case (K&C), which is implemented in Pronto3d (Taylor, 1989). Development of this model was sponsored by the Defense Threat Reduction Agency, and accounts for the complex behavior of concrete. This concrete model decouples the volumetric and deviatoric response, with user-defined functions describing the pressures, unloading bulk moduli, and volumetric strains. Strain-rate dependency is included with this model as well.

Ex 2
A524

(U) The input parameters for the K&C concrete model have been automated, so the typical user only specifies the concrete strength (Attaway, 2000). This program determines the input parameters based on information from a series of test data.

Ex 2
A524

Table A-13. K-C Concrete Model Behavior Data (U).

The contents of this table are unclassified.

--	--

Ex 2
A-535

A.2.2.3.1

(U) [] Although it is much more rigid than the jetliner fuselage, it does not behave as a rigid structure.

Ex2 - A-533
Ex2 - A53C
Ex2 - A53D
Ex2 A53E

A.2.2.4 Threat Definition (U)

Ex 2 - A53 F2

~~CONFIDENTIAL - NSI~~

Final Draft

P.A-54a
Ex 1

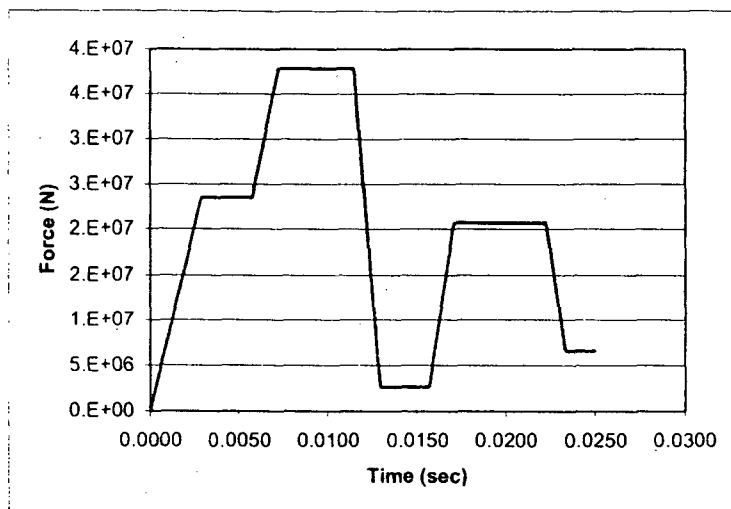
P.A-54b
Ex 1

] Ex 2
A54C

The contents of this figure are classified C.

A-54

~~CONFIDENTIAL - NSI~~



The contents of this figure are unclassified.

] Ex 2 A-55a

Ex 1 PA-55b

A.2.2.4.1

]

Ex 2 A-55c

Ex. 1
A-55d

A-55

Ex.3
SG1
A569

The contents of this figure are unclassified.

Ex2
A56b

Ex.3
SG1
A56c

The contents of this figure are unclassified.

Ex #2 A56d

A.2.2.4.2 Jetliner Momentum Area Loading (U)

Analyses were conducted using the force time-history developed from the global analyses discussed in Section A.2.1 for a jetliner impacting a single cask.

(U) The force time-history applied to the cask impacted by the jetliner is shown in Figure A-18.

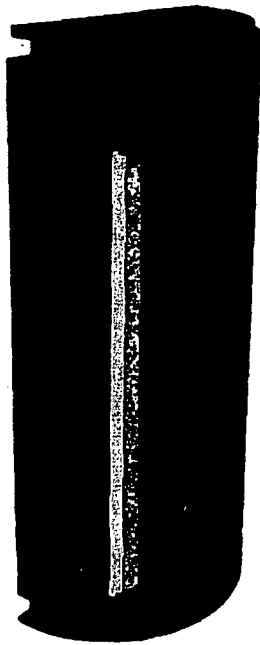


Figure A-31. Pressure Loading Surfaces for the Side Impact of Jetliner Pressure Loading (U).

The contents of this figure are unclassified.

For this analysis, the pressure loading shown in Figure A-18 was applied to the front cask.

EX 2
A589

The total components of the HI-STORM are necessary to achieve the correct kinematics during the scenario, and the total mass of the MPC is included in the analysis model, shown in Figure A-32. A symmetry boundary accounts for the other half of the model.

EX 2
A586

EX 2
A58C

A.2.2.4.3 Cask-To-Cask Impact (U)

Therefore, for a field of casks, the variation of possibilities for cask-to-cask impacts is substantial. Analyses were conducted to examine the many possible cask-to-cask impact scenarios. Four different impact orientations were evaluated at various cask velocities. The analyses conducted are summarized in Table A-14.

EX 2
A58d

EX 2
A58e

SG1 A58f
EX 3

A58g
EX 2

The contents of this figure are unclassified.

A-58

Table A-14. Cask-To-Cask Impact Orientations (U).

The contents of this table are classified C.

EX: 1
A-599

and only half the casks were modeled.

] In these cases, symmetry was taken advantage of

EX: 3
SG1 A596
EX: 3
SG1 A596

~~CONFIDENTIAL - NSI~~

Final Draft



Σx^2
A-604

Σx^2 A-604
The contents of this figure are unclassified.

Σx^2 A600

Σx^2 A602
The contents of this figure are unclassified.

A-60

~~CONFIDENTIAL - NSI~~

(u) For these analyses, no symmetry boundary was appropriate. The models shown above were mirrored to allow complete three-dimensional motion. This model becomes very large (1.2 million elements for this case) and the impacting cask was translated to produce contact on a vertical line 45 degrees from the initial velocity vector. These analyses assess if off-angle, i.e., not perfectly lined-up impacts, are of concern, as these impact orientations are much more likely to occur.

Ex 2
A-61aEx 2
A-61b

Ex #2 A-61c

Ex 2
A-61d

Ex #2 A-61e

The contents of this figure are unclassified.

A.2.2.5 Analyses Results (U)

A.2.2.5.1

Ex # 2 A-629

Ex # 2
A-629

Ex # 1
A-629

Ex # 2 A-629

The contents of this figure are classified C.

~~CONFIDENTIAL-NSI~~

Final Draft

A.2.2.5.2 [

7 Ex #2 A-639

EX 1
A-63b

A.2.2.5.3 [

Ex #2 A-63c

EX.1
A-63d

EX3
SGT
A-63e

Ex #2 A-63f

A-63

~~CONFIDENTIAL-NSI~~

~~CONFIDENTIAL - NSI~~

Final Draft

Ex #2
A-64g

Figure A-37.

The contents of this figure are unclassified.

#2 A-64b

EX.1
A-64c

The contents of this figure are classified C.

Ex #2
A-64d

A-64

~~CONFIDENTIAL - NSI~~

Classified ✓

~~CONFIDENTIAL - NSI~~

Final Draft

EX. 1
A-65a

Figure A-39. Side Impact Sectioned View of VonMises and Concrete Damage
(1 MPa = 145 psi) (U).

The contents of this figure are classified C.

A.2.2.5.4

EX 2
A-65b

A.2.2.5.5

EX. 1
A-65c

EX 2
A-65d

EX. 1
A-65e

~~CONFIDENTIAL - NSI~~

Ex. 1
A-66a

Figure A-40.

The contents of this figure are classified C.

Ex. 2 A-66b

Ex. 1
A-66c

Figure A-41.
(U).

The contents of this figure are classified C.

Ex 2
A-66d

(U)

Ex 2
A-66e

~~CONFIDENTIAL - NSI~~

Final Draft

A.2.2.5.6

EX 2
A-679

EX 1
PA-67b

A.2.2.5.7

(U)

DUO-SR1
P.A-67c
EX 2

A-67

~~CONFIDENTIAL - NSI~~

EX-1
A-68a

[Figure A-42.

The contents of this figure are classified C.

EX2
A-68b

EX. 1
A-69a

Figure A-43.

The contents of this figure are classified C.

(U) Ex # 2

EX 2000-SM
A-69b

PA-69C
Ex 2

PA-69d
Ex 1

EX1
A-70d

Figure A-44.

The contents of this figure are classified C.

EX2 DW
p A-70b

EX1
A-70c

Figure A-45.

The contents of this figure are classified C.

EX. 2 DW-S
A-70d

EX 1
A-71a

Figure A-46. Equivalent Plastic Strain for a Cask-to-Cask Impact (U).

The contents of this figure are classified C.

EX. 1
A-71b

EX. 2
A-71c

(U)

EX. 2
A-72a

Figure A-47. Cask-To-Cask Impact Results at 30 msec (1 MPa = 145 psi) (U).
The contents of this figure are unclassified.

EX. 1
A-72b

Figure A-48. VonMises Stress in Steel Only, for a Cask-To-Cask Impact (1 MPa = 145 psi) (U).

The contents of this figure are classified C.

Excl
A-73a

[Figure A-49. Cask-To-Cask Impact - Equivalent Plastic Strain Distribution (U).
The contents of this figure are classified C.

EX1
A-74B

Figure A-50. Results from a cask-to-cask Side Impact (U).
The contents of this figure are classified C.

Inclined Cask-To-Cask Impact (U)

SG1 EX3 A-74B

EX1
A-74C

Ex 1
A-75a

Figure A-51. Inclined Cask-To-Cask Impact for Analysis Times of 10, 30, 50 and 100 msec
(1 MPa = 145 psi) (U).

The contents of this figure are classified C.

5 4 2

(U)

Ex
#2
A-75b

Ex. 1
A-75c

PA-76a
Ex1

Figure A-52. Cask-To-Cask, CG Over-Corner Impact: Undeformed and Deformed Shape (U).

The contents of this figure are classified C.

Oblique Cask-To-Cask Impact (U)

PA-76b
Ex1

55 m/s Oblique Impact Results (C)

PA-76c
Ex1

SG1
PA-76d
Ex3

EX.1
A -77a

Figure A-53. Equivalent Plastic Strain and Concrete Damage for Cask-To-Cask CG-Over-Corner Impact (U).

The contents of this figure are classified C.

EX 1
A-78a

A.2.2.5.8 [Multi-Purpose Canister Analysis (U)

(U) Most of the local analyses results presented previously do not include the MPC, which is the final barrier to release of radioactive materials from the spent fuel stored.

EX 2
A-78b

EX. 1
A-78c

~~CONFIDENTIAL~~ ~~NSI~~

Final Draft

Ex. 1
A-79a

[Figure A-54a. Oblique Impact Results from Cask-To-Cask Collision (1 MPa = 145 psi) (U).
The contents of this figure are classified C.]

A-79

~~CONFIDENTIAL~~ ~~NSI~~

~~CONFIDENTIAL - NSI~~

Final Draft

EX.1
A-80a

Figure A-54b. Oblique Impact Results from Cask-To-Cask Collision (1 MPa = 145 psi) (U).
The contents of this figure are classified C.

A-80

~~CONFIDENTIAL - NSI~~

EXI
A-81a

Figure A-55. Oblique Impact Results from a Cask-To-Cask Collision (1 MPa = 145 psi) (U).
The contents of this figure are classified C.

~~CONFIDENTIAL - NSI~~

Final Draft

Ex #2

Ex #2

Ex 2
A-82a

Figure A-56. Schematic of Gap Between MPC and the Overpack (U).

The contents of this figure are unclassified.

(U) A schematic drawing of the shipping/storage canister is shown in Figure A-57. (T)

Ex #2
A-82b

The density of the material was adjusted so that the total weight of the canister was equal to the specified design weight. Modeling the fuel assemblies in this manner does not allow direct determination of the behavior of the fuel rods, but assesses the loads that the assemblies apply to the canister.

~~CONFIDENTIAL - NSI~~

PA-83a
Ex 2

Figure A-57. Schematic Drawing of the Shipping/Storage Canister (U).

The contents of this figure are unclassified.

(U) The material of the canister body was modeled using the SPL Strength material model in PRONTO3D (Wellman and Salzbrenner, 1992; Wellman et al., 1993; Stone and Wellman, 1993). This is a power-law-hardening model with a ductile failure criterion. The ductile failure criterion is based on an evolution equation in which the plastic strain increment, scaled by the stress ratio, is accumulated until a critical value is reached, at which point the ductile tearing is initiated. This scalar parameter is the ductile Tearing Parameter (TP). The evolution equation for this parameter is as follows:

$$TP = \int_0^{\bar{\epsilon}_p} \left(\frac{2\langle \sigma_{max} \rangle}{3(\sigma_{max} - \sigma_m)} \right)^4 d\bar{\epsilon}_p$$

where $\bar{\epsilon}_p$ is the plastic strain, σ_{max} is the maximum principal stress, and σ_m is the mean (hydrostatic) stress

$$\sigma_m = \frac{(\sigma_{11} + \sigma_{22} + \sigma_{33})}{3}$$

(U) The integral accumulates plastic strain only when the maximum principal stress is positive, as indicated by the Heavyside function brackets, $\langle \rangle$. Thus, plastic strain with a negative maximum principal stress causes no change in the values of TP.

(U) The critical value of TP for a particular material is established by analyzing a tensile test specimen. The TP for the specimen is then calculated using the computed stress state from the FE model and substituting the strain-to-failure, $\bar{\epsilon}_f$, as the upper integration limit. This provides a critical value of TP, which can be used to predict failure in other analyses. The strain-to-fail is computed from the reduced area of the tensile specimen in the actual tensile test. A TP value of 2.6 was developed for 304 stainless steel using thin plate tensile specimens.

(U) The FE model of the shipping canister is presented in Figure A-58, with a detailed view of the canister shell and lid weld region presented in Figure A-59. There is a plane of symmetry through the center axis of the cask body, so only half of the canister is modeled.

SG 1
A-84a
Ex 3

(U) The resulting deformation from the side-on impact is presented in Figure A-60. Figure A-61 and Figure A-62 show the equivalent plastic strain in the canister wall and end plates.

Ex 3
A-84b

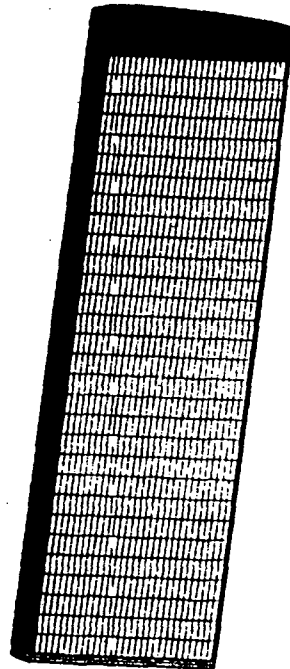


Figure A-58. Canister FE Model (U).
The contents of this figure are unclassified

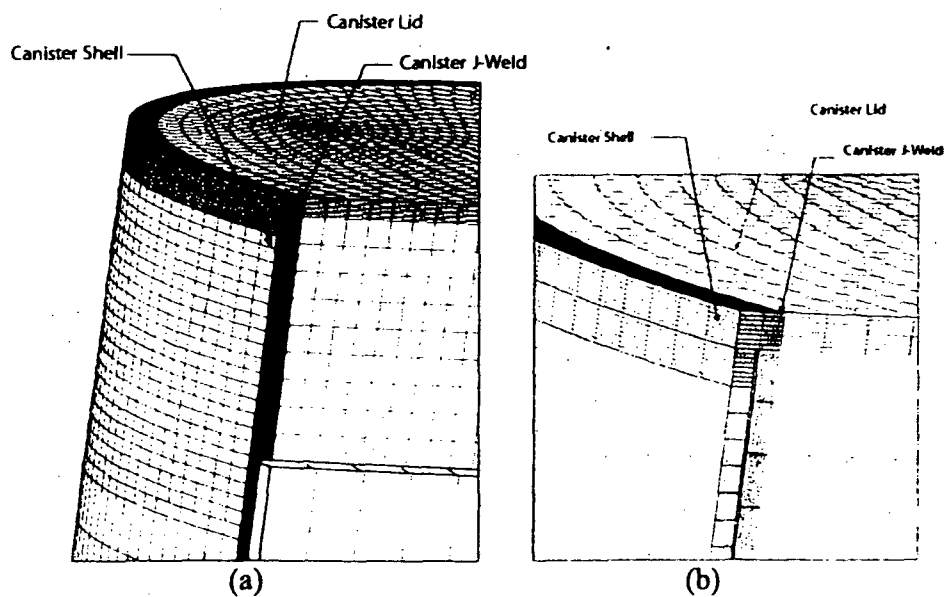


Figure A-59. A Detailed View of Canister Lid Weld Region (U).
The contents of this figure are unclassified.

Figure A-60.

The contents of this figure are unclassified.

Ex 2
A-86a

Ex 2
A-86b

Ex 1
A-86c

Figure A-61.

The contents of this figure are classified C.

Ex 2
A-86d

Ex 1
A-86e

Figure A-62.
(U).

The contents of this figure are classified C.

Ex 2
A-86f

~~CONFIDENTIAL~~ ~~NSI~~

Final Draft

EX.1
A-87a

Figure A-63.

(U.)
The contents of this figure are classified C.

EX #2 A-87b

EX.1
A-87c

A-87

~~CONFIDENTIAL~~ ~~NSI~~

EX^{II} 2
A-88a

Figure A-64.

(U).

The contents of this figure are unclassified.

EX^{II} 2
A-88b

EX. 1
A-88c

Figure A-65.

(U).

The contents of this figure are classified C.

EX^{II} 2
A-88d

EX. 1
A-89a

[Figure A-66.

(U).

The contents of this figure are classified C.]

EX 2 A-89b

EX 2 A-89c

[Figure A-67.

The contents of this figure are unclassified.]

(U.) EX 2 A-89d

2
EX
A-90a

Figure A-68.

The contents of this figure are unclassified.

(U.) EX 2
A-90b

EX 1
A-90c

Figure A-69.

(U).

The contents of this figure are classified C.

EX # 2
A-90d

Σ[#] 2
Ex
A-91a

Σ[#] 2
Ex
A-91b

The contents of this figure are unclassified.

Ex. 1
A-91c

The contents of this figure are classified C.

Σ[#] 2
Ex
A-91d

A.2.3 Structural Analysis of a Jetliner Impacting a Field of Storage Casks: Summary and Discussion (U)

(U) Approximately 40 analyses were performed to examine the vulnerability of a field of storage casks to an intentional impact from a jetliner. Some of the analyses directly evaluated the cask vulnerability, while others were parametric runs to support the methodology development, and others required additional reasoning to evaluate cask vulnerabilities to some local scenarios that develop as the jetliner impacts and creates a chaotic environment of cask-to-cask impacts. The following section summarizes the results of the analyses and addresses some of the issues that could not be directly evaluated by the global CTH or local FE analyses.

A.2.3.1 Global Analysis Summary and Discussion (U)

(U) The purpose of the global analyses was to determine the global behavior of casks subjected to the impact of a jetliner. These analyses resulted in two sets of data for use with the local analyses.

These global analyses provided the only way to determine the transient behavior of the cask velocity to impacts at different locations on the cask.

A.2.3.2 Local Analysis Summary and Discussion (U)

(U)

EX. 2 A-92C

EX. 1
92d

~~CONFIDENTIAL - NSI~~

Final Draft

Ex #1
A-93a

ite

Ex #2
A-93b

] The analyses discussed in this section address many possible structural scenarios. Some of these scenarios are more likely than others.

Geometric aspects of the pad layout and jetliner approach have been combined with these structural analyses results to examine the realistic scenario described in depth in the main body of this report.

Ex 2
A-93c

EX1
A-93d

(U) This value of exit velocity is expected to be an upper bound value for a number of reasons:

A-93

~~CONFIDENTIAL - NSI~~

Ex 2 A-94a
Ex 2 A-94b
Ex 2 A-94c
Ex 2 A-94d

For each Ex 2 A-94e

subsequent impact, the resulting velocities will decrease.

Therefore, it is these initial impacts that have been investigated more fully.

Ex 2 A-94f

Ex 1
A-94g

A.2.3.3 Possible Mitigation Strategies (U)

Ex 3
CGV
PA-94h

Table A-15. Local Analyses of Cask-To-Cask Impacts (U).

The contents of this table are classified C

Ex. 1
A-95a

Table A-15. Local Analyses of Cask-To-Cask Impacts (Continued) (U).
The contents of this table are classified C

EX 1
A-96a

Table A-16. Analyses of Hard Component Cask Impacts (U).
The contents of this table are unclassified.

SGI
EX. 3
A-97a

~~CONFIDENTIAL~~ - NSI

Final Draft

[Table A-17. Other Cask Calculations (U).

The contents of this table are classified C

EX1
A-98
a

A-98

~~CONFIDENTIAL~~ - NSI

A.3 References (U)

- (U) American Society of Civil Engineers (ASCE). 1980. *Structural Analysis and Design of Nuclear Plant Facilities*, Manuals and Reports on Engineering Practice, No. 58, Reston, Virginia.
- (U) American Society of Civil Engineers (ASCE). 2003. *The Pentagon Building Performance Report*, Renton, Virginia.
- (U) American Society for Metals (ASM), ed. 1982. *Engineering Properties of Steel*, Harvey, P.D., American Society for Metals, Metals Park, Ohio.
- (U) Attaway, et al., 2000. *Enhancements to PRONTO3D to Predict Structural Response to Blast*, SAND2000-1017, Sandia National Laboratories, Albuquerque, NM.
- (U) Attaway, S.W., Arguello, J.G., Bessette, G., Schmitt, B., Gwinn, K., Crawford, D., Tieszen, S., Baer, M. 2003. *Technology Overview for Analysis of Aircraft Impact*, SAND2003-1952, Sandia National Laboratories, Albuquerque NM.
- (U) 767-Airplane Characteristics for Airport Planning, D6-58328, Revision F, February 1989 (Obtained from Boeing Website, www.boeing.com).
- (U) Bell, R.L. 1992. *An Improved Material Interface Reconstruction Algorithm for Eulerian Codes*, SAND92-1716, Sandia National Laboratories, Albuquerque, NM.
- (U) Bell, R.L., Baer, M.R., Brannon, R.M., Crawford, D.A., Elrick, M.G., Hertel, E.S., Silling, S.A., and Taylor, P.A. 2000. *CTH User's Manual and Input Instructions, Version 6.0*, Sandia National Laboratories, Albuquerque, NM.
- (U) Cherry, J.L., and Smith, J.S. 2001. *Capacity of Steel and Concrete Containment Vessels with Corrosion Damage*, NUREG/CR-6706, SAND2000-1735, Sandia National Laboratories, Albuquerque, NM.
- (U) Crawford, D.A. 2002. Personal Communication.
- (U) Department of Energy. 1996. *Accident Analysis for Aircraft Crash Into Hazardous Facilities*, DOE-STD-3014-96, Washington, D.C.
- (U) Federal Emergency Management Agency (FEMA). 2002. *World Trade Center Building Performance Study: Data Collection, Preliminary Observations, and Recommendations*, FEMA 403, Washington, D.C.
- (U) Frew, D.J. 2001. *Results of Instrumented Penetration Experiments into Concrete Targets; Low-Strength (23 MPa) and High-Strength (38 MPa) Concrete*, US Army Engineer Research and Development Center and Sandia National Laboratories, June 2001.

Ex 2
PA-100a
DUU-SRI

(U) Hertel, E.S. 1992. *A Comparison of the CTH Hydrodynamics Code with Experimental Data*, SAND92-1879, Sandia National Laboratories, Albuquerque, NM.

(U) Hertel, E.S., Bell, R.L., Elrick, M.G., Farnsworth, A.V., Kerley, G.I., McGlaun, J.M., Petney, S.V., Silling, S.A., Taylor, P.A., and Yarrington, L. 1993. *CTH: A Software Family for Multi-Dimensional Shock Physics Analysis*, SAND92-2089C, Sandia National Laboratories, Albuquerque, NM.

(U) Hertel, E.S., and Kerley, G.I. 1998. *CTH Reference Manual: The Equation of State Package*, SAND98-0947, Sandia National Laboratories, Albuquerque, NM.

(U) HOLTEC International. 2000. *HI-STORM Topical Safety Analysis Report*, Revision 10, Holtec International Report No. HI-951312, Holtec International, Marlton, NJ, 2000 (available from NRC document room).

(U) Hossain, Q.A., Kennedy, R.P., Murray, R.C., Mutreja, K., and Tripathi, B.P. 1997. *Structures, Systems, and Components Evaluation Technical Support Document, DOE Standard, Accident Analysis for Aircraft Crash into Hazardous Facilities*, UCRL-ID-123577, Lawrence Livermore National Laboratories, Livermore, CA.

(U) Johnson, G.R., and Cook, W.H. 1983. "A Constitutive Model for Metals Subjected to Large Strains, High Strain Rates, and High Temperatures," *Proceedings of the Seventh International Symposium on Ballistics*, The Hague, The Netherlands.

(U) Johnson, G.R., and Holmquist, T.J. 1989. *Test Data and Computational Strength and Fracture Model Constants for 23 Materials Subjected to Large Strains, High Strain Rates, and High Temperatures*, LA-11463-MS, Los Alamos National Laboratory, New Mexico.

(U) Kipp, M.E. June 2002. Personal Communication.

Ex 2
A-100b
DUU-SRI

(U) Kot, C.A., Lin, H.C., van Erp, J.B., Eichler, T.V., and Wiedermann, A.H. 1982. *Evaluation of Aircraft-Crash-Hazards Analyses for Nuclear Power Plants*, NUREG/CR-2859, ANL-CT-81-32, Argonne National Laboratory, Argonne, Illinois.

(U) Koteras, J.R., et al. 2003. *PRESTO Users Manual*, SAND-2003-?????, Sandia National Laboratories, Albuquerque, NM, ??????

(U) McGlaun, J.M., Thompson, S.L., and Elrick, M.G. 1990. "CTH: A Three-Dimensional Shock Wave Physics Code," *International Journal of Impact Engineering*, Vol. 10, pp. 351-360.

(U) National Transportation Safety Board (NTSB). 2000. *Aircraft Accident Report Controlled Flight into Terrain Korean Air Flight 801 Boeing 747-300, HL7468 Nimitz Hill, Guam August 6, 1997 DCA97MA058*, NTSB/AAR-00/01, Washington, D.C.

(U) Noble, C.R. 2000. *Damage Estimation of a Concrete Wall Panel Subjected to Aircraft Impact*, UCRL-ID-141941, Lawrence Livermore National Laboratory, Livermore, CA.

(U) Riera, J.D. 1968. "On the Stress Analysis of Structures Subjected to Aircraft Impact Forces," *Nuclear Engineering and Design*, Vol. 8, pp. 415-426.

(U) Riera, J.D. 1980. *A Critical Reappraisal of Nuclear Power Plant Safety Against Accidental Aircraft Impact*, Nuc. Eng. Des., No. 57, pp. 193-206.

(U) Sprung, J. L., D.J. Ammerman, N.L. Breivik, R.J. Dukart, F.L. Kanipe, J.A. Koski, G.S. Mills, K.S. Neuhauser, H.D. Radloff, R.F. Weiner, H.R. Yoshimura. 2000. *Reexamination of Spent Fuel Shipment Risk Estimates*, NUREG/CR-6672, U.S. Nuclear Regulatory Commission, Washington, DC, (available at ttd.sandia.gov/nrc/modal.htm).

(U) Sugano, T., Tsubota, H., Kasai, Y., Koshika, N., Orui, S., Von Riesemann, W.A., Bickel, D.C., and Parks, M.B. 1993. "Full-Scale Aircraft Impact Test for Evaluations of Impact Force," *Nuclear Engineering and Design*, Vol. 140, pp. 373-385.

(U) Talyor, L.M., and Flanagan, D.P. 1989. *PRONTO3D: A Three-Dimensional Transient Solid Dynamics Program*, SAND87-1912, Sandia National Laboratories, Albuquerque, NM.

(U) Uncapher, W.L., Harding, D.C., Pierce, J.D., Arviso, M., Bobbe, J.G., Bolton, D.L., and Steinberg, D.R. 1994. *Axial Impact Testing of a C-141B Aircraft Fuselage Section with Shipping Containers*, SAND94-2739, Sandia National Laboratories, Albuquerque NM, December 1994.

(U) Wilson, L.T., Hertel, E.S., Schwalbe, L.A., and Wingate, C. 1998. "Benchmarking the Sphinx and CTH Shock Physics Code for Three Problems in Ballistics," *Proceedings of the Seventh International Symposium on Ballistics*, Johannesburg, South Africa, March 1998.

(U) Wellman, G.W. and Salzbrenner, R. 1992. *Quasistatic Modeling and Testing of Exclusion Region Barrier Mock-Ups*, SAND92-0024.

(U) Wellman, G.W., Diegert, K.V., and Salzbrenner, D.R. 1993. *Two-Dimensional Quasistatic Modeling of Exclusion Region Barriers in Support of Design Guide Development*, SAND93-0905.

(U) Wolf, J.P., Bucher, K.M., and Skrikerud, P.E. 1978. "Response of Equipment to Aircraft Impact," *Nuc. Eng. Des.*, No. 47, pp. 169-193.

Appendix B: HI-STORM Storage Cask Engine Impact Analyses (U)

B.1 Background and Scope (U)

B.2 Cases Analyzed (U)

(U)

Ex 1 p. B-1a

Ex 2 p. B-1b

Ex 3 p. B-1c

B.3 FLEX Finite Element Software (U)

(U) The simulations were conducted with FLEX (Vaughan and Mould, 2000), a three-dimensional, nonlinear, large deformation, explicit, transient analysis finite element code. The FLEX code implements a wide variety of constitutive models and has been extensively used to simulate impact, blast, and nonlinear responses of structures through failure. Details of the software and validation for impact and blast environments are given below.

(U) A large variety of extensively tested elements, including plates, shells, hexahedra, beams and bars, are available to model the geometric details of the structures of interest. In addition, the code contains nonlinear generalized spring/dashpot elements that are useful for lumped parameter representation of joints and connections.

(U) WAI has been at the forefront of developing nonlinear material models for a wide variety of materials, including metals, concrete, rock, soils, and composites (Mould and Levine, 1993; DiMaggio and Sandler, 1971; Tennant et al., 1997; Mould et al., 1994; Mould and Levine, 1987; Levine, 1982). Slide-line capability with friction is available for modeling contact and separation with impacting surfaces. FLEX also includes rate-dependent failure models available for modeling the material response in highly dynamic failure environments. Steel reinforcement of concrete may be simulated explicitly. Code features are summarized in Table B-1.

Ex 3
p. B-2a

The contents of this figure are unclassified

Ex 2 p. B-2b

(U) FLEX targets dynamic analysis, but several static solution options are also available for combined gravitational, impact, and blast loading of structures. It is written in standard Fortran 77 and is operational on Microsoft WindowsTM-based personal computers. On these machines it is capable of solving blast, fragment, impact, progressive collapse, and ground shock problems with millions of degrees of freedom. This allows higher fidelity solutions within a specified parameter space to be generated rapidly to compare with engineering tools and/or to develop refined tools. The code is also operational on HP, IBM, SGI, and Sun workstations and supercomputers. FLEX is written to take full advantage of vectorization on systems that support it. The code has been parallelized using the symmetric multiprocessing (SMP) paradigm for shared memory machines, such as the SGI Origin 3000 and multiprocessor PC hardware.

(U) Output from the program includes time histories and/or snapshots of field variables such as displacement, velocity, stress, and strain. These data are saved during an analysis for post-processing. The data structures of the various output files are purposefully kept simple to

B-2

allow easy manipulation of the data for graphics capabilities available at a user's site. FLEX includes graphics options to plot time histories, create undeformed and deformed mesh plots, and display elemental field quantities, such as stress and strain, in color.

Table B-1. FLEX Code Features (U).

The contents of this table are unclassified.

3-D Elements	Isoparametric hexahedron, quadrilateral shell with transverse shear deformations; quadrilateral membrane; beam element with transverse shear deformations; bar element; nonlinear springs; nonlinear dashpots.
2-D Elements	Axisymmetric shell; axisymmetric quadrilateral; beam, membrane; spring, dashpot.
Time Integration	Explicit central difference with subcycling; static solutions using dynamic relaxation or conjugate gradient method.
Special elements	Slip and debond elements; 3-D contact and slide-line interfaces with nonlinear contact and sliding models based upon both the penalty and pinball approaches.
Special boundaries	Soil island, Structure Media Interaction boundary; transmitting boundary.
Material Models	Two invariant cap model for soils and rock. Three invariant cap model for concrete, soils, rock, and pressure-dependent materials. Viscoplastic, three invariant cap model with rate dependence and isotropic softening for concrete, soils, rock, and geologic materials available in hex, beam, and shell elements. Von Mises nonlinear hardening model with ductile fracture for metals. Rate-dependent nonlinear von Mises hardening with ductile fracture for metals. Anisotropic and uneven Hoffman, Tsai-Wu, and Hill criteria included for fiber-reinforced composite failure with fracture. Capability for selecting principal tensile strain or effective plastic strain element failure criteria. Element erosion based upon selected strain and fracture failure criteria.
Large Deformations	Updated Lagrangian with Jaumann stress rate.
Source Model	FUSE module coupled to code; FUSE is a total Lagrangian code, with a new large deformation formulation; high pressure equation of state (EOS) and JWL libraries for explosive materials including TNT, Tritonal, etc.

B.3.1 FLEX Software Verification, Validation, and Benchmark Activities (U)

(U) Verifying a code involves comparing the results of a series of computations that have specific phenomenology and physics of interest with exact theoretical solutions, other numerical techniques, and other computer codes. Experience in DTRA programs has shown that this approach is a useful tool for verifying that what was theoretically intended is coded. This is especially true with regard to constitutive models, detection of "elusive numerics bugs," and understanding of differences in results among various calculators using different (or even the same) codes. For the simulations of reinforced concrete structural response and failure, few, if any, "exact" solutions exist. Validation of codes involving comparison with laboratory and small-scale experiments is sometimes included in the benchmarking exercises.

(U) Verification and validation activities for WAI's FLEX code for the blast and shock analysis of hardened structures were conducted (Table B-2) under DTRA's Silo Test Program (STP), Missile System Vulnerability (MSV) program, the Underground Technology Program (UTP), the Conventional Weapons Effects (CWE) program, and the High Value Fixed Target (HVFT) program. It was also validated in test programs conducted for the Minuteman III and B-52H Weapons System Safety Assessment Programs. For these programs, pretest predictions for H-1224A container drop tests (Wong et al., 1996; Harding et al., 1994), C-141B fuselage impact tests (Wong et al., 1996; Uncapher et al., 1994a,b) and TF-30 engine impact tests (Lawver et al., 2002; Tennant et al., 1996) into soil covered and bare reinforced concrete walls were successfully compared with the test data. Examples of comparisons with the C-141B longitudinal fuselage impact test and the TF-30 engine impact test are shown in Figure B-2 and Figure B-3. FLEX was extensively benchmarked against other nonlinear codes, such as DYNA-3D, as well as precision test programs conducted by DTRA, and large-scale silo and component test programs conducted by the Ballistic Missile Organization (BMO) and the U.S. Army Corps of Engineers Waterways Experiment Station (WES).

Table B-2. Benchmark and Validation Comparisons (U).

The contents of this table are unclassified.

Silo Test Program (STP) Program: Misty Port and Mineral Find Precision Tests: Failure of Buried Steel Cylinders Under Air blast and Ground Shock loading (Levine et al., 1991; Levine and Tennant, 1991).
Missile System Vulnerability (MSV) Program: Scale-model reinforced concrete silos under airblast and ground shock loading with internal subsystems (Tennant and Levine, 1994; Tennant and Levine 1991).
High Value Fixed Target Program: Code Benchmark Program: Constitutive model comparisons along selected stress paths with other calculators; Code Validation Program: DEINT 1/6 scale weapon tests on walls and floors, LTS structures full scale internal detonation weapons tests, DE-21, DE-51 full scale tests, Precision Wall Test (PWT) series of airblast only quarter-scale wall tests, PWTS series of half-scale air blast and fragment wall tests, DE-146, DE-142/150; Static Slab Predictions (Tennant and Levine 1997; Tennant et al., 1997).
Underground Technology Program (UTP) Tunnel Calculations: UTP Code Benchmark program; Mighty North 1 slide-line and constitutive benchmark comparisons with other calculators. UTP Code Validation; Mighty North 1 Test (Wong et al., 1991; Wong et al., 1995; Nikodym et al, 1997).
DTRA Minuteman III and B-52H WSSA Programs: Full-Scale C-141 airplane Impact Tests; TF-30 Engine Impact tests into Bermed and Bare Reinforced Concrete Walls (Tennant et al., 1996; Lawver et al., 2002) and H-1224A container Impact Tests (Harding et al., 1994).
CTS 1 Validation Test: Prediction of full scale test structure to blast loading. Prediction of column response to blast loading. Predicted that even if column removed there would be no collapse of even one bay. Prediction confirmed after column removed when test was complete (Tennant et al., 1999).

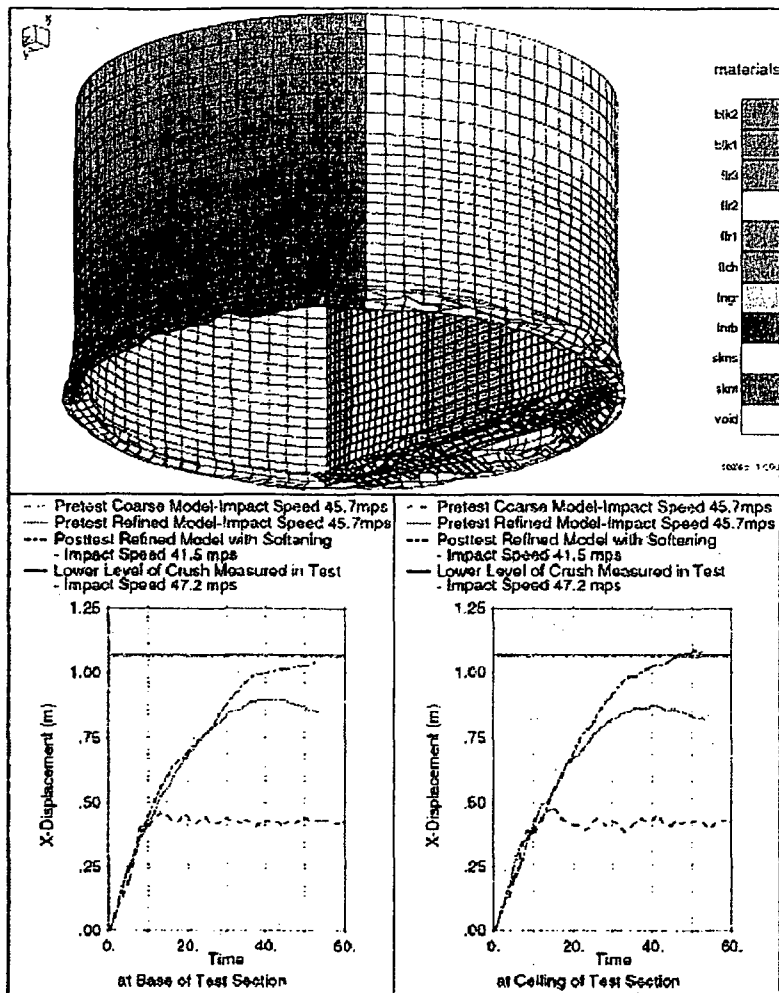


Figure B-2. Predicted Axial Shortening of Test Section at Two Locations vs. Measured Crush; C-141B Longitudinal Impact Test, 43 m/s (96 mph) (1 m = 3.28 ft; 1 mps = 2.24 mph) (U).

The contents of this figure are unclassified

(U) Figure B-4 shows a comparison of blind pretest predictions for air blast loading of buried steel cylinders in sand and clay conducted under DTRA's Silo Test Program. The deformation modes in each geology were accurately predicted (Levine et al., 1991) and the responses clearly show the effect of different types of soil on structural response. Figure B-5 shows a comparison of predicted and observed damage for a reinforced concrete wall subjected to combined air blast and fragment loads. Again, the predicted damage and deformations closely agreed with the test data (Tennant et al., 1997).

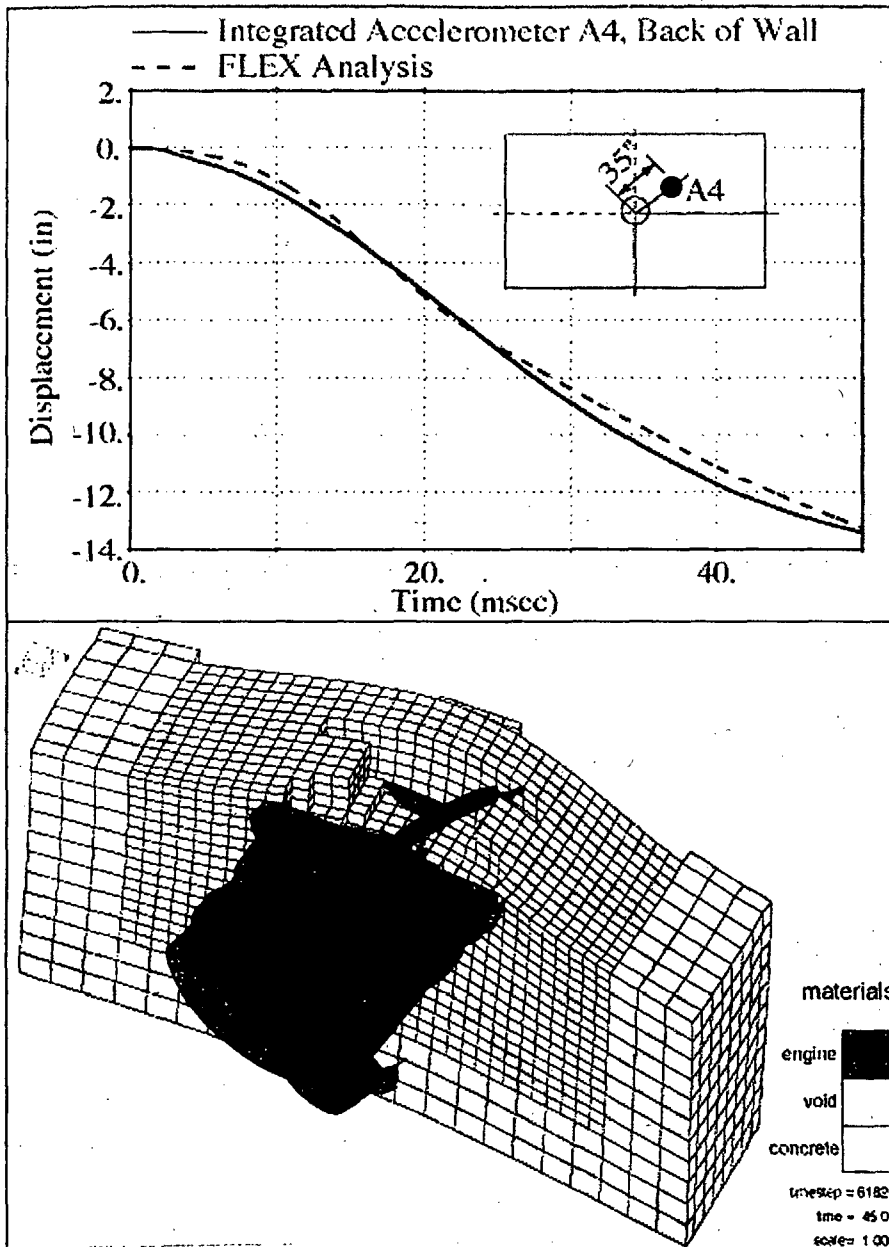


Figure B-3. Comparison of Predicted and Measured Reinforced Concrete Wall Response for a TF-30 Engine Impacting at 350 f/s (107 m/s) (1 in = 2.54 cm) (U).

The contents of this figure are unclassified.

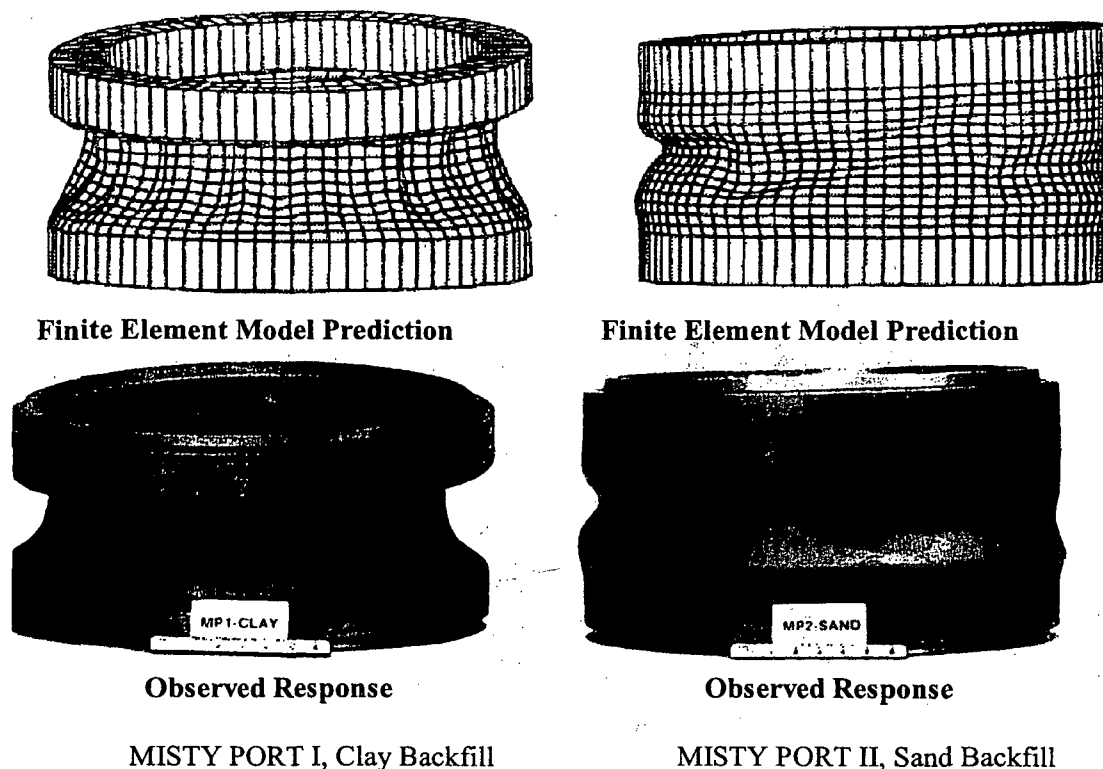


Figure B-4. Comparison of Predicted and Observed Deformations for Surface Flush Buried Steel Cylinders Subjected to Airblast and Ground Shock Loading (U).

The contents of this figure are unclassified.

B.3.2 Material Models (U)

B.3.2.1 Metal Model (U)

(U) The model used in the calculations is a Von Mises isotropic, elasto-plastic, strain-hardening model with a typical trilinear hardening representation of steel behavior, as illustrated in Figure B-6. The constitutive model representations for failure of metals are based upon an isotropic ductile fracture model. After reaching ultimate strain, localized behavior is assumed to occur at each integration point. Softening values are chosen based upon stress-strain behavior of a specimen. With this model, severely distorted elements can be eroded when the effective plastic strain exceeds a value at which they could have fragmented. Beam and shell elements are eroded when the average of all integration points exceeds a user-specified threshold. The element is no longer processed, but the nodal mass is retained. Rate enhancement is explicitly included in the ductile fracture model used in the computations through a Duvaut-Lions viscoplastic formulation. These rate effects decay with ductile fracture so that the residual strength at finite strain rate is zero when softening is complete.

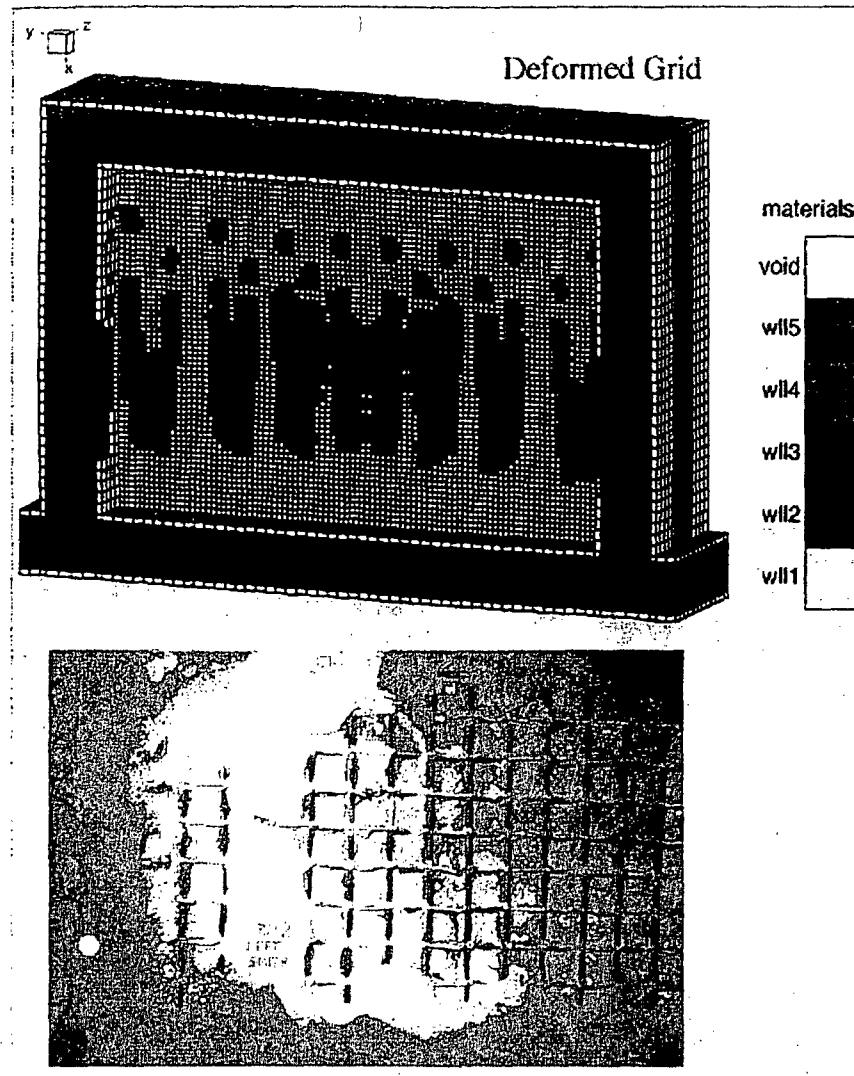


Figure B-5. Predicted and Observed Wall Damage for Air-Blast and Fragment Loaded Reinforced Concrete Wall (U).

The contents of this figure are unclassified.

(U) The softening function used is:

$$\sigma_1 = \sigma_{ult} \left[\frac{\epsilon^{psft}}{\epsilon^p} (1-a) + a \exp \left(-b \left(\epsilon^p - \epsilon^{psft} \right) \right) \right]$$

where

$$\epsilon^{psft} = \epsilon^{sft} - \frac{\sigma_{ult}}{E}$$

The equivalent plastic strain ϵ^p is defined as the accumulation of $d\bar{\epsilon}$, where

$$d\bar{\epsilon} = \sqrt{\frac{2de_{ij}^p de_{ij}^p}{3}}$$

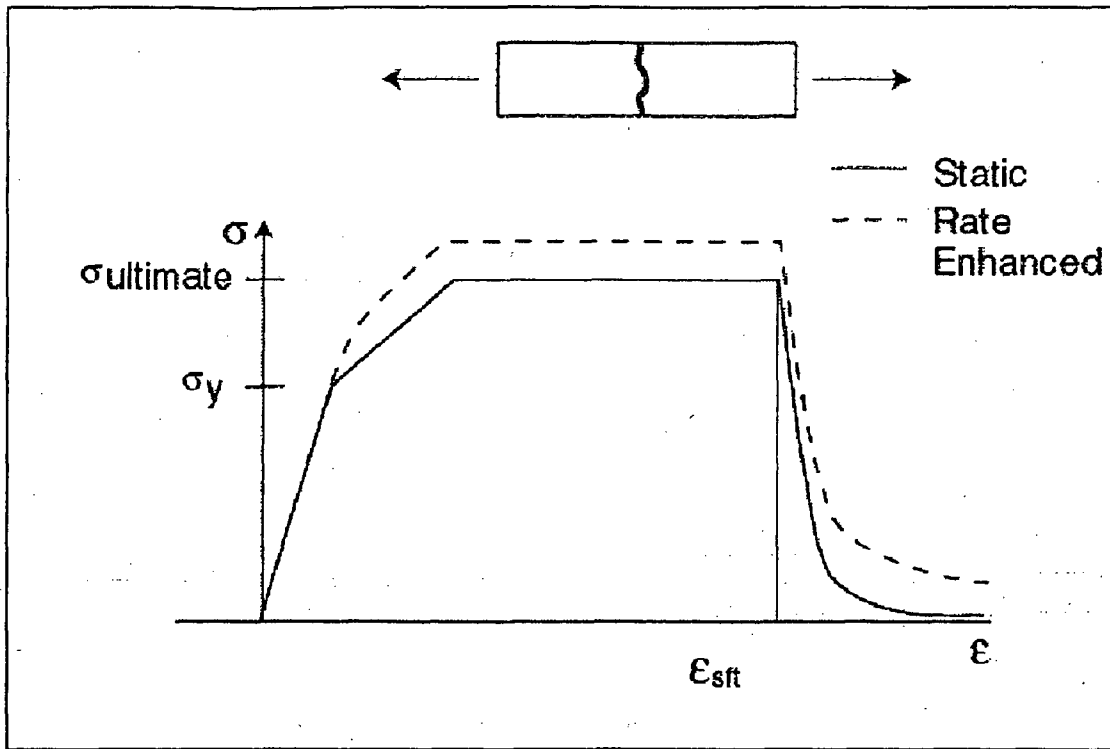


Figure B-6. Metal Model (U).

The contents of this figure are unclassified.

B.3.2.2 Concrete Model (U)

(U) The viscoplastic concrete model, SFT1 (Mould and Levine, 1994) was used to model the concrete. The model consists of a perfectly plastic three-invariant failure surface, a three-invariant strain hardening cap, and a J_1 (first stress invariant: $J_1 = \sigma_x + \sigma_y + \sigma_z$) tension limit, invoking Koiter's rule at corners (Figure B-7a). Elastic behavior is assumed to be linear and isotropic. This baseline inviscid response is regularized via a Duvaut-Lions type viscoplasticity with piecewise linear overstress. Triaxial compression tests in which concrete specimens were loaded to different stress points show that significant damage is only observed for stress states near the failure surface. Large compressive strains do not induce appreciable damage. Motivated by this data and by residual failure surface data, softening is implemented by shifting the failure surface and J_1 limit towards zero along the J_1 axis as a function of expansive volumetric plastic strain (Figure B-7b).

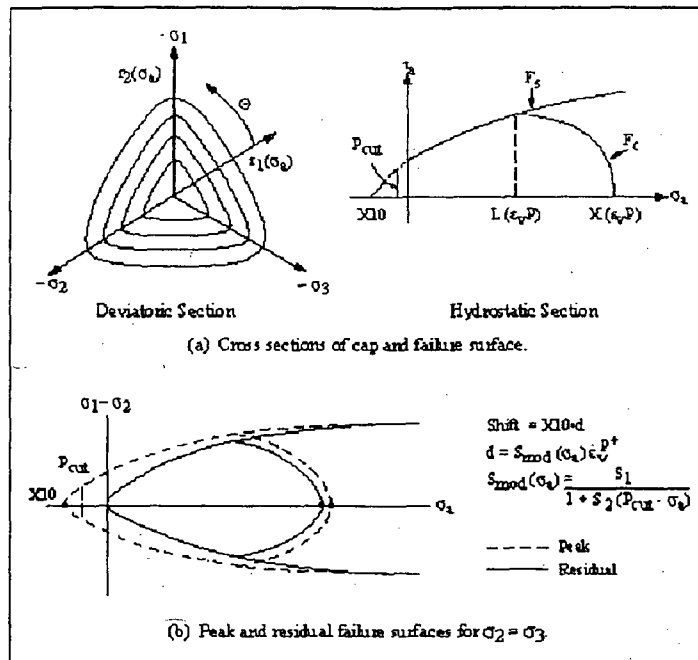


Figure B-7. Three-Invariant Viscoplastic Softening Model (U).

The contents of this figure are unclassified.

(U) Because plastic strain increments on the cap are equivoluminal or compressive, no softening occurs when the stress state is on the cap. To account for the increased ductility observed in compression relative to that observed in tension, a pressure-dependent relation was introduced for failure surface shifting. "Shift" moves the yield surface towards the origin to implement the kinematic softening approach (Figure B-1b). The amount of failure surface translation is controlled by an isotropic softening parameter. The evolution of the softening parameter is a function of the positive volumetric plastic strain. In a deviatoric slice, the cap transitions from geometrically similar to the failure surface at $\sigma_a = L$, to circular at $\sigma_a = X$. The cap has a horizontal tangent at its intersection with the failure surface. Cap motion is governed by the volumetric component of the viscoplastic strain. It moves outward with compressive increments, but does not contract with expansive increments.

(U) Based upon data (Hurlbut, 1985), the measured plastic strain directions lie somewhere between the associated and Mises potential values. No discernible trend with increasing pressure is evident. Significantly, numerical experiments have indicated that controlling this dilation is a crucial aspect of capturing shear failures. Therefore, a constant was introduced that modifies the volumetric component of the flow rule. The associativity in the Rendulic plane may vary from fully associated flow to a flow rule that is normal to the pressure axis in the Levy-Mises sense, which develops no component of volumetric plastic strain. The associativity in the Rendulic plane can vary from 1.0 (fully associated flow) to zero (Levy-Mises flow rule) depending upon the user's specifications. Currently, a constant associativity of 0.5 is used, although the capability of varying the associativity as a function of the softening parameter is available. Non-associated flow was also introduced in the π -plane, purely for algorithmic convenience. A radial return of the deviatoric stresses is done that allows far simpler and more efficient algorithms than a rigorous associated return. It is emphasized that the use of viscoplasticity removes the

uniqueness problems that result from invoking a nonassociated flow rule in a rate-independent model.

(U) If one examines the localization length base implicitly inherent in the viscoplastic formulation, convergence cannot be insured unless the element sizes are on the order of several millimeters. For realistic problems, this leads to excessively large numbers of elements. In these instances and for static problems where the viscoplastic effects are minimal, regularization is achieved by adjusting the fracture energy based upon element size used in the problem and simulation of triaxial tests using these element sizes.

(U) The use of viscoplastic softening results in a residual unconfined tensile or compressive strength after dynamic enhancement and softening. This residual strength is approximately equal to the strength enhancement. Since this is not realistic, the viscoplastic function is "damaged" using the softening parameter and reduced by the factor $(1-d)^n$. Here, n is an empirically chosen parameter that is usually 3.0. This allows the strength to be reduced to the residual surface strength values.

B.4 Finite Element Models (U)

Ex 2 p.B-11a

Ex 3 p.B-11b

(U) The metals were represented with the metal model described in Section B.3.2.1. Parameter values are summarized in Table B-3. Refer to Figure B-7 for the meaning of the parameters. No parameters are listed for model simplifications, e.g., an elastic perfectly plastic material has no values for ultimate stress or strain rate dependence.

B.4.2 HI-STORM Cask (U)

(U) Figures B-10 through B-17 show the finite element representation of the HI-STORM/HI-STAR system. The model includes 12 beam elements (for the top bolts), 95,424 shell elements, 99,976 continuum elements, and an additional 8295 shell elements to represent the rigid surface supporting the cask.

(U) The concrete was modeled with the SFT1 material model described in Section B.3.2.2.

Ex # 3
p.B-11c

Figure B-8.

The contents of this figure are unclassified.

Ex #2
p.B.12a

Figure B-9.

The contents of this figure are unclassified.

Ex #2
p.B-12b

The contents of this table are unclassified.

Ex 2 p.B-13a

Ex 3 p.B-13b

Table B-4.

The contents of this table are unclassified.

Ex 2 PB-13c

Ex 3 PB-13d

(U) Bolt responses are reported in local coordinates. Each element's local y-axis is collinear with a radial line from the cask's central axis through the element's vertical axis (local x-axis). The local z axis is in the direction given by the vector product $\underline{x} \times \underline{y}$. The bolt integration point locations in local coordinates are given in Table B-5.

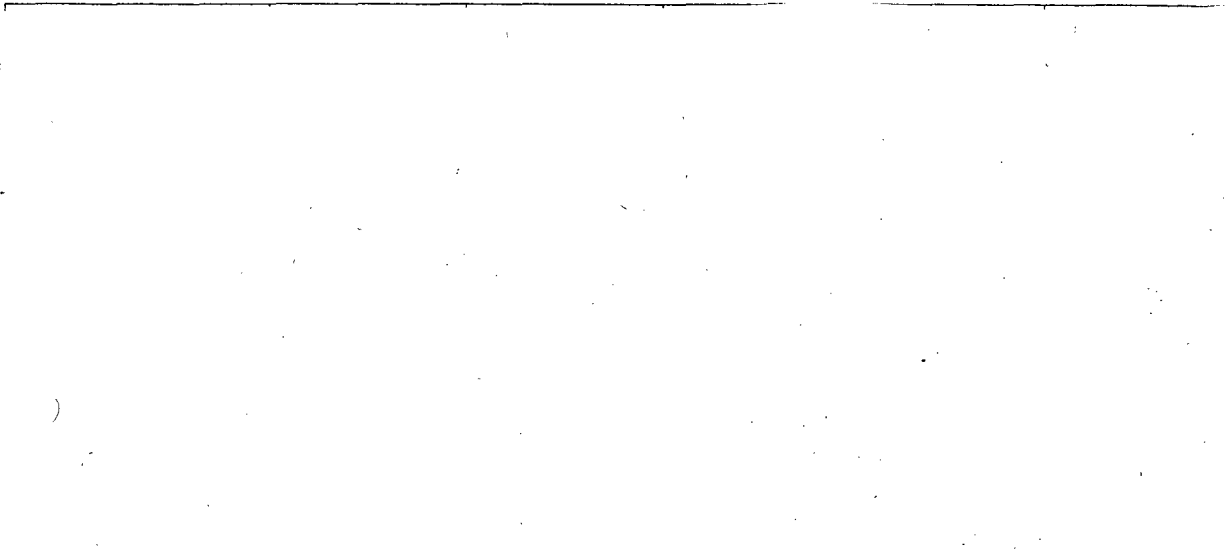
Table B-5. Bolt Integration Points in Local Coordinates (r=bolt radius) (U).

The contents of this table are unclassified.

Ex 2
PB-13e

Table B-6. Material Parameters for Cask Model (U).

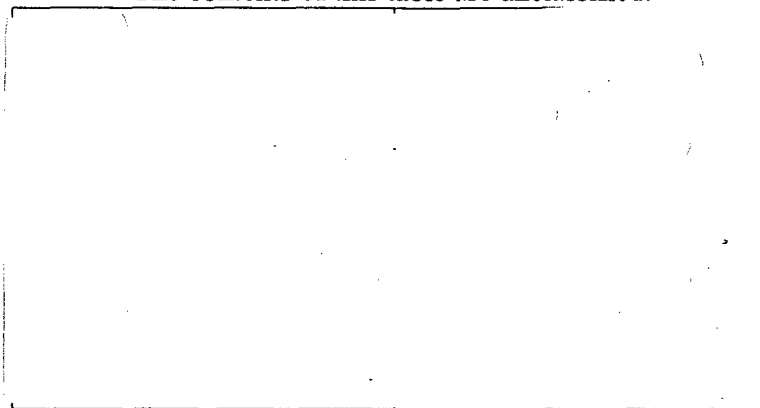
The contents of this table are unclassified.



Ex 2
p.B-14a

Table B-7. Rate Curve B for Cask Materials (U).

The contents of this table are unclassified.



Ex 2 p.B-14b

Table B-8 - Rate Curve C for Cask Materials (U).

The contents of this table are unclassified.

Ex 2 p.B-14c

Table B-8 - Rate Curve C for Cask Materials (Continued) (U).

The contents of this table are unclassified.

Ex 2 p.B-15a

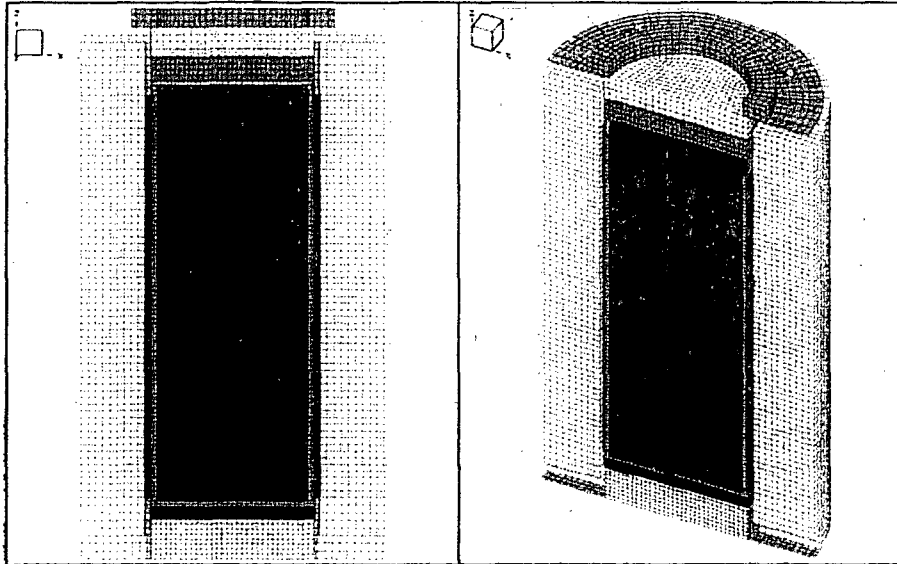


Figure B-10. Cut-Away View of HI-STORM/Hi-STAR Model Grid (U).

The contents of this figure are unclassified.

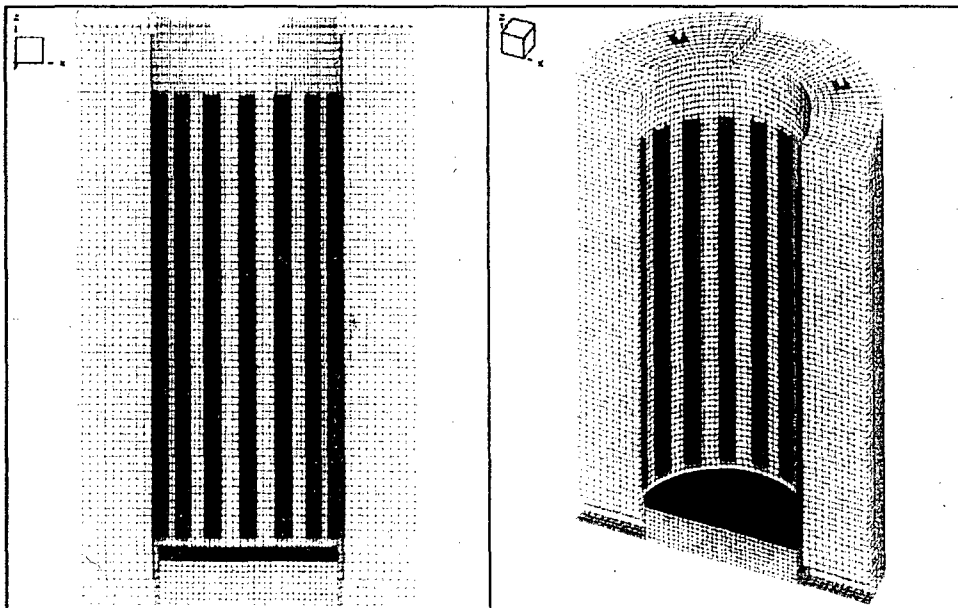


Figure B-11. Cut-Away View of Storage Cask Grid Radial Shield and Pedestal (U).

The contents of this figure are unclassified.

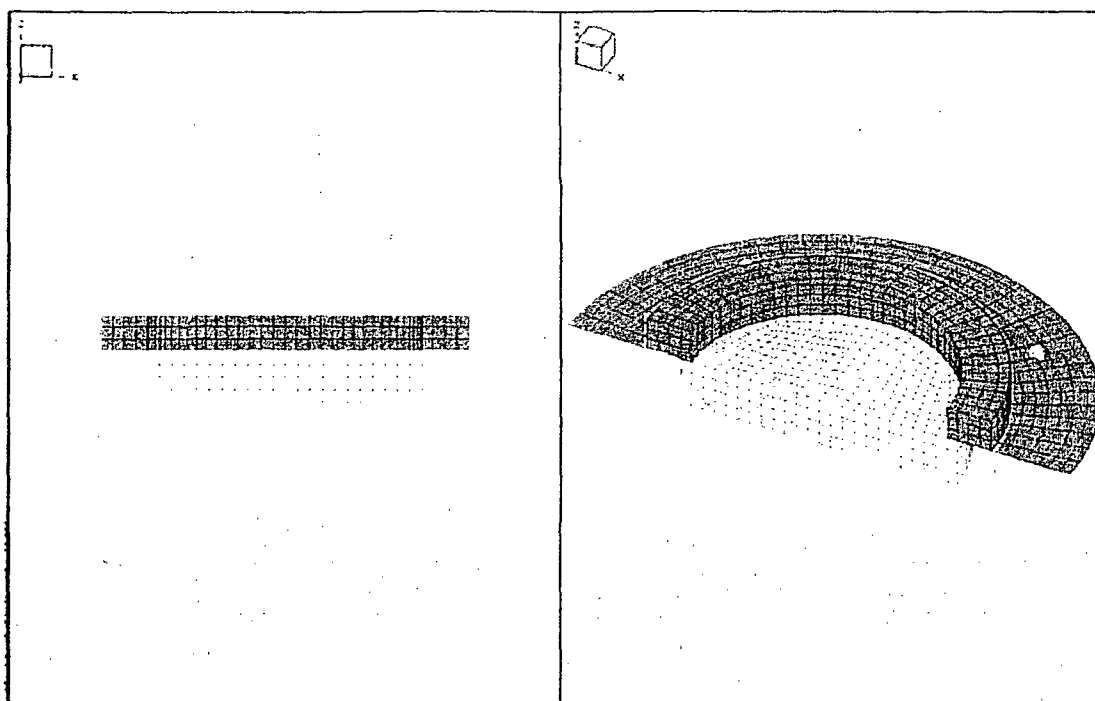


Figure B-12. Cut-Away View of Storage Cask Grid Lid Shield, Top Plate, and Shield Block (U).

The contents of this figure are unclassified.

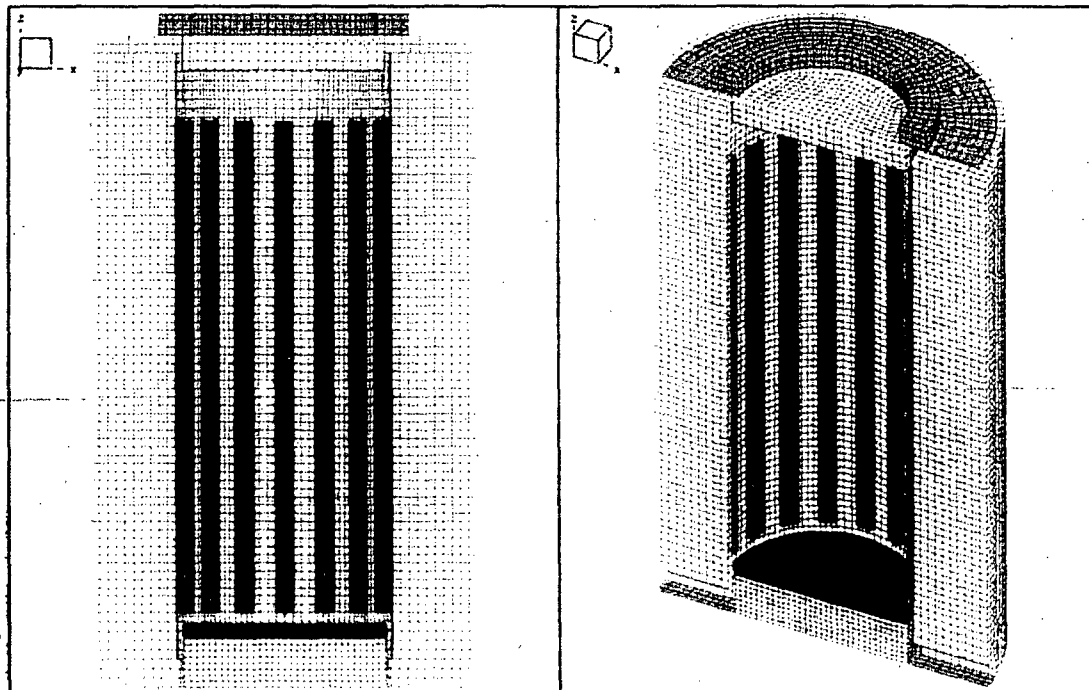


Figure B-13. Cut-Away View of Storage Cask Grid (U).

The contents of this figure are unclassified.

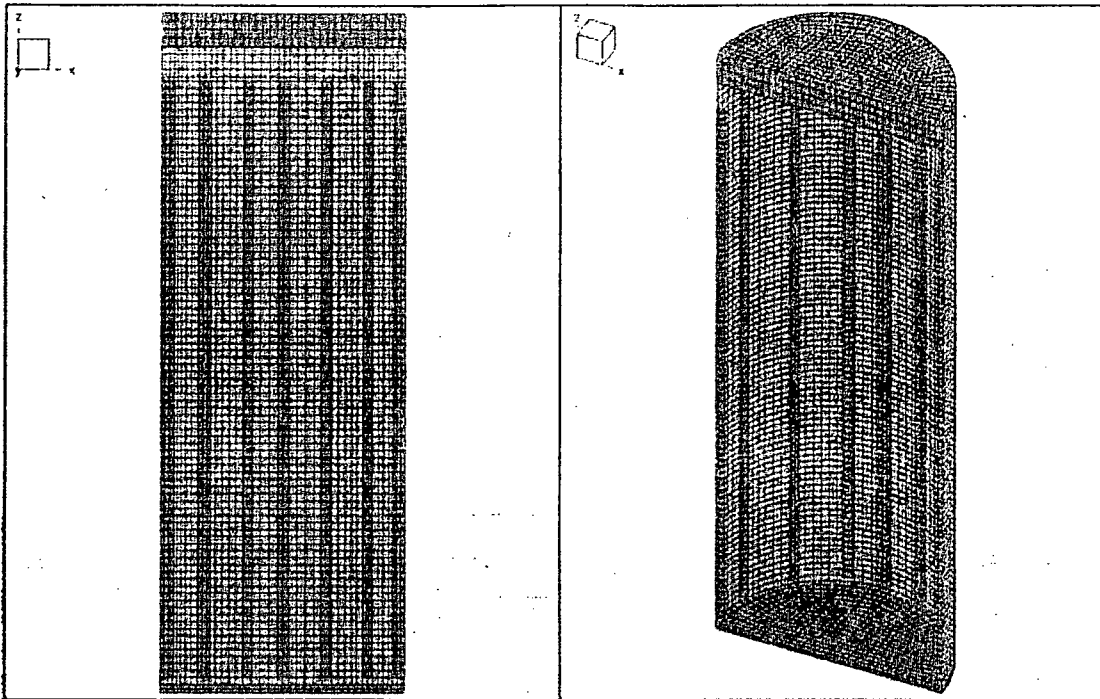


Figure B-14. Cut-Away View of MPC Grid Canister Only (U).

The contents of this figure are unclassified.

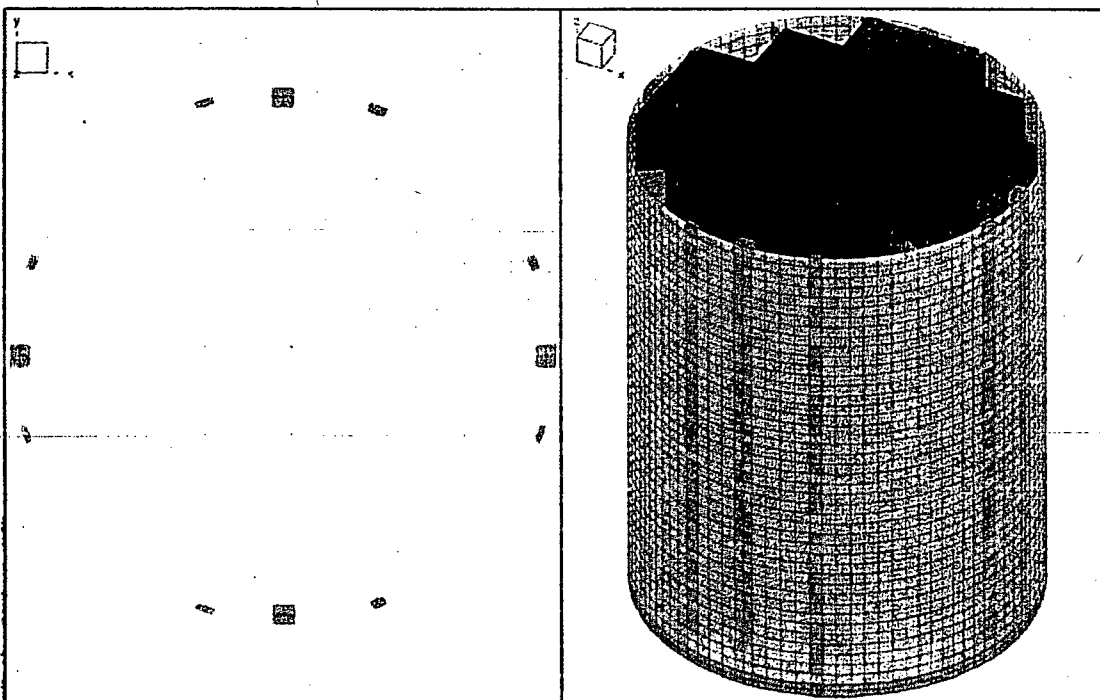


Figure B-15. Cut-Away View of MPC Grid (U).

The contents of this figure are unclassified.

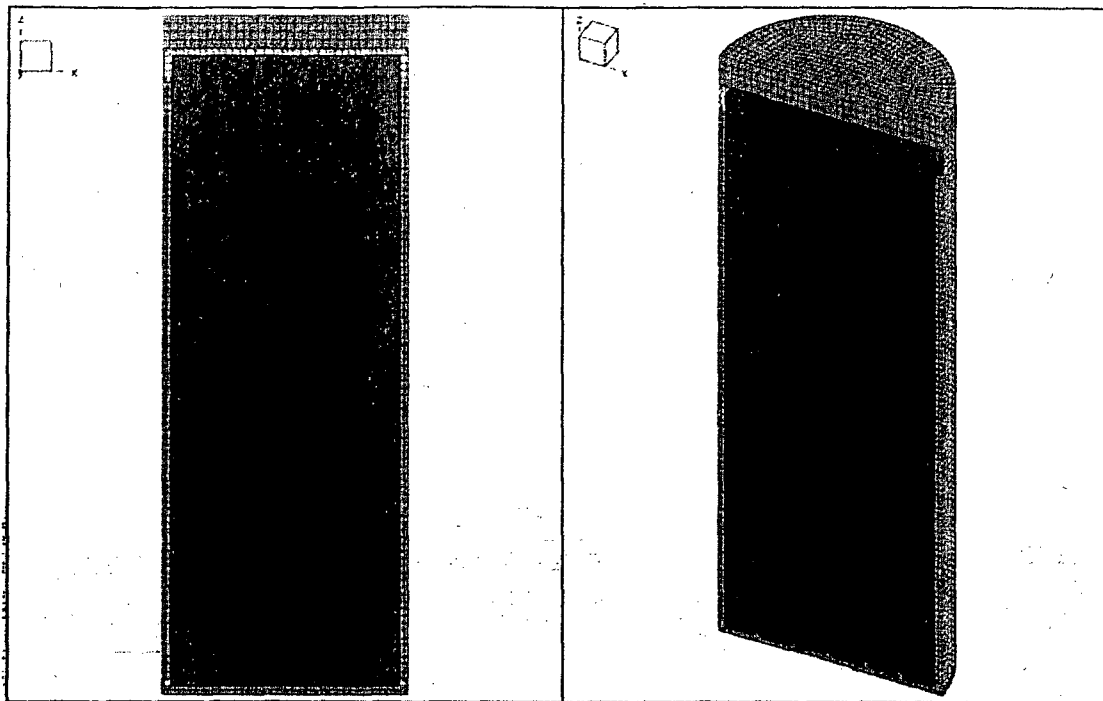


Figure B-16. Cut-Away View of MPC Grid Canister and Basket (U).
The contents of this figure are unclassified.

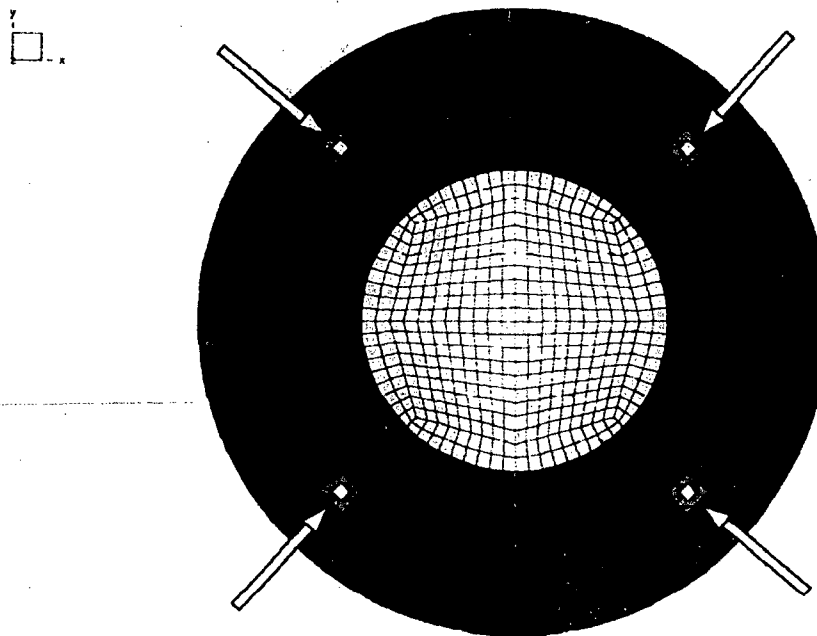


Figure B-17. Bolt Locations (Top View) (U).
The contents of this figure are unclassified.

B.5 Results (U)

Ex 3
p. B-19a

For metals, the equivalent plastic strain and principal tensile strain are displayed. Refer to Figure B-17 and Table B-5 for bolt locations and quantities, respectively.

Ex 3 p. B-19b

Figure B-18.

The contents of this figure are unclassified.

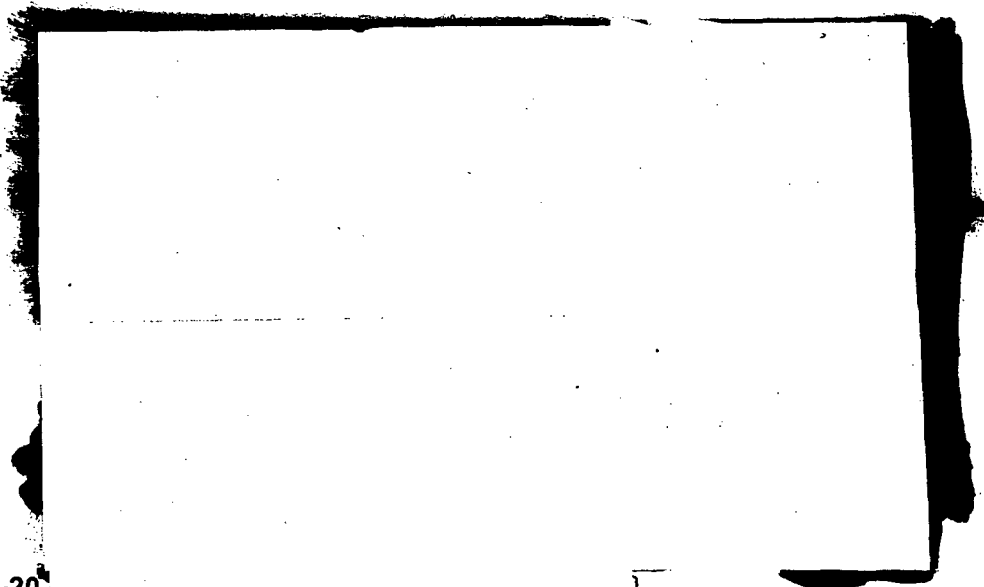
Ex 2
p. B-19c

Ex 3
p. B-20a

Figure B-19.

The contents of this figure are unclassified.

Ex 2
p. B-20b



Ex 1
p. B-20c

Figure B-20.

The contents of this figure are classified C.

Ex 2
p. B-20d

Ex 1
p. B-21a

The contents of this figure are classified C. Ex 2 p. B-21b

Ex 1
p. B-21c

The contents of this figure are classified C. Ex 2 p. B-21d

Ex 1
p. B-22a

The contents of this figure are classified C.

Ex 2
p. B-22b

Ex 1
p. B-22c

The contents of this figure are unclassified C.

Ex
p. B-22d

PB-23-a
Ex # 3

Figure B-25.

The contents of this figure are unclassified.

Ex # 3

PB-23-b

Figure B-26.

The contents of this figure are unclassified.

PB-24-a
Ex 3

Figure B-27.

The contents of this figure are unclassified.

PB-24-b
Ex 3

Figure B-28.

The contents of this figure are unclassified.

Ex 1
p.B-25a

Ex 3
p.B-25b

Ex 2
p.B-25c

EX3
p.B-25d

Ex 2
p.B-25e

Ex 3
p.B-25f

Figure B-29.

The contents of this figure are classified C.

B.5.2

equivalent plastic strain and principal tensile strain are displayed. Refer to Figure B-17 and Table B-5 for bolt quantity locations.

For metals, the

B.5.3

equivalent plastic strain and principal tensile strain are displayed. Refer to Figure B-17 and Table B-5 for bolt quantity locations.

For metals, the

P-B-26-a
Ex #3

The contents of this figure are unclassified.

P-B-26-b
Ex #3

The contents of this figure are unclassified.

P-B-27-a
Ex #3

Figure B-32.

The contents of this figure are unclassified.

EX 1
P-B-27-b

Figure B-33.

The contents of this figure are classified C.

P-B-27-c
Ex #3

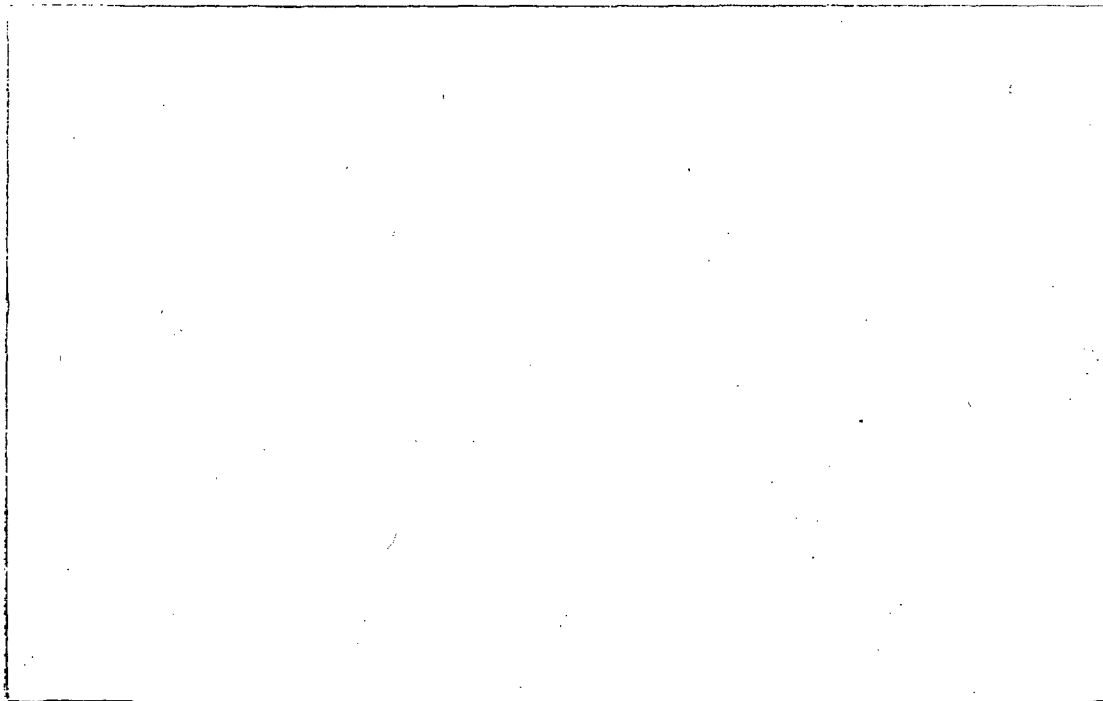


Figure B-34.

The contents of this figure are classified C.

Ex 1
P-B-28-a

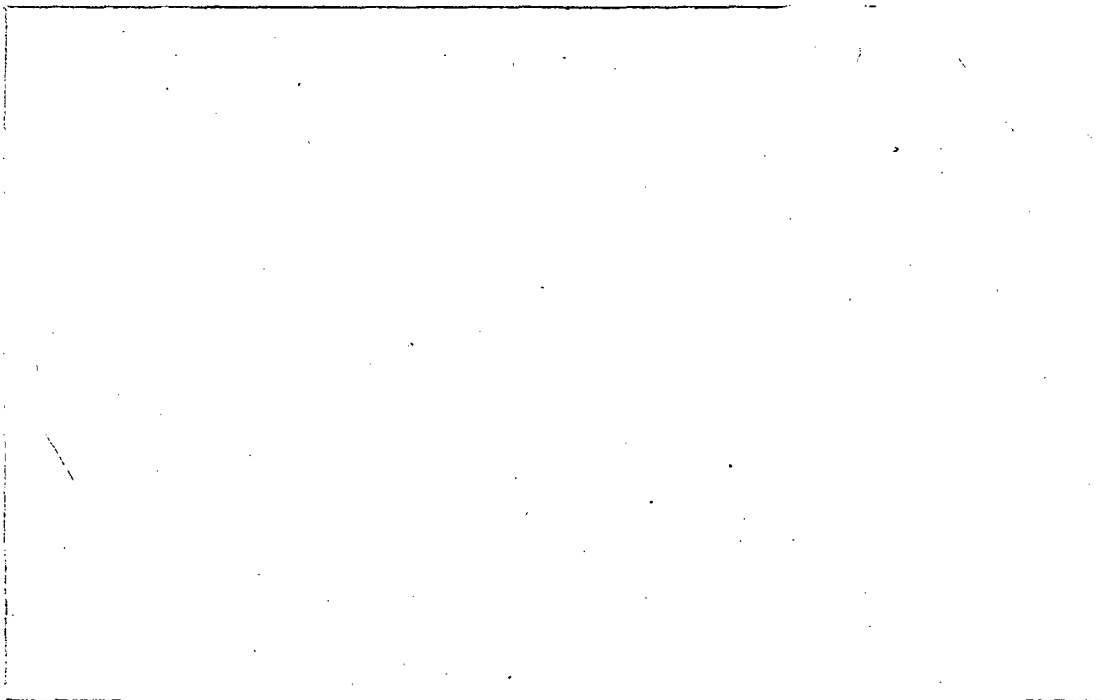


Figure B-35.

The contents of this figure are classified C.

P-B-28-b
Ex # 3

Ex 1
P-B-28-c

P-B-28-d
Ex # 3

Ex 1
P.B. 29a

Figure B-36.

The contents of this figure are classified C.

P.B. 29-b
Ex 3

Ex 1
P.B. 29-c

Figure B-37.

The contents of this figure are classified C.

Ex 3
P.B. 29-d

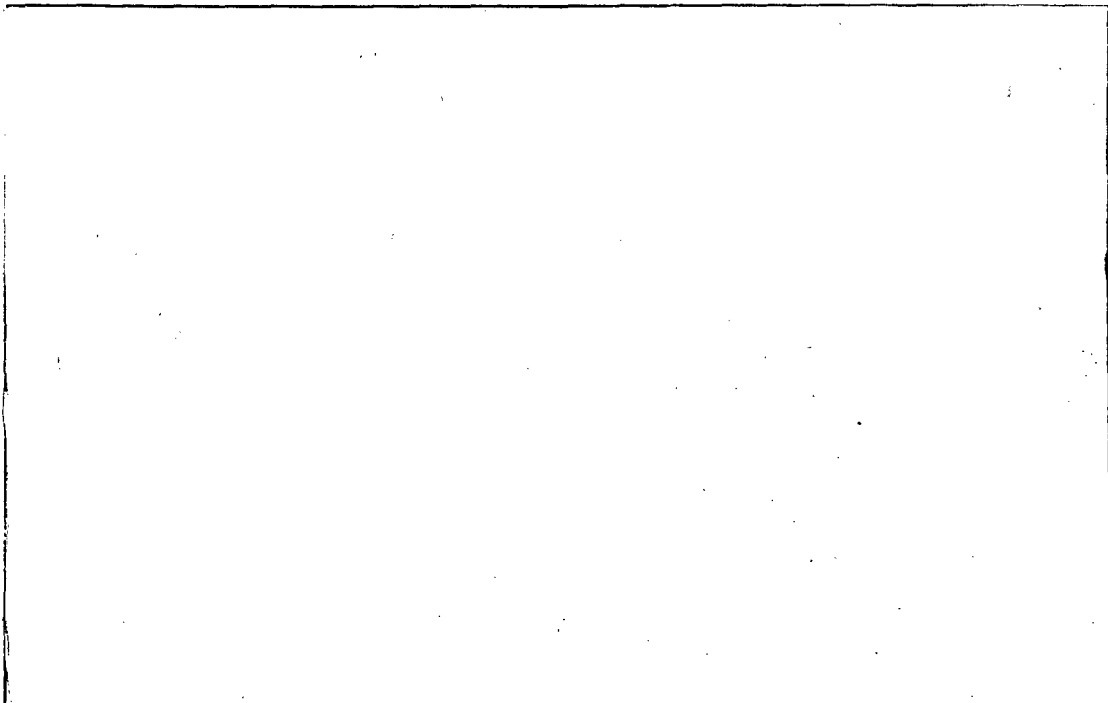


Figure R-38

The contents of this figure are classified C.

Ex 1
P-B-30-a

Ex 3
P-B-30-b

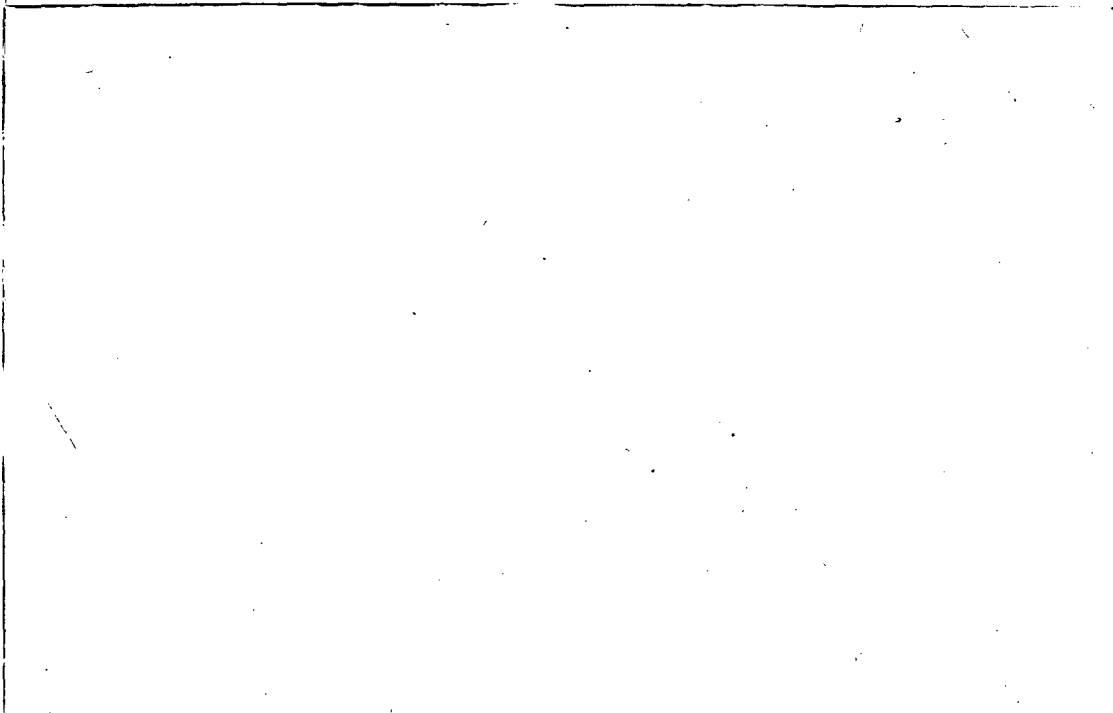


Figure B-39

The contents of this figure are classified C.

B-30

Ex 1
P-B-30-c

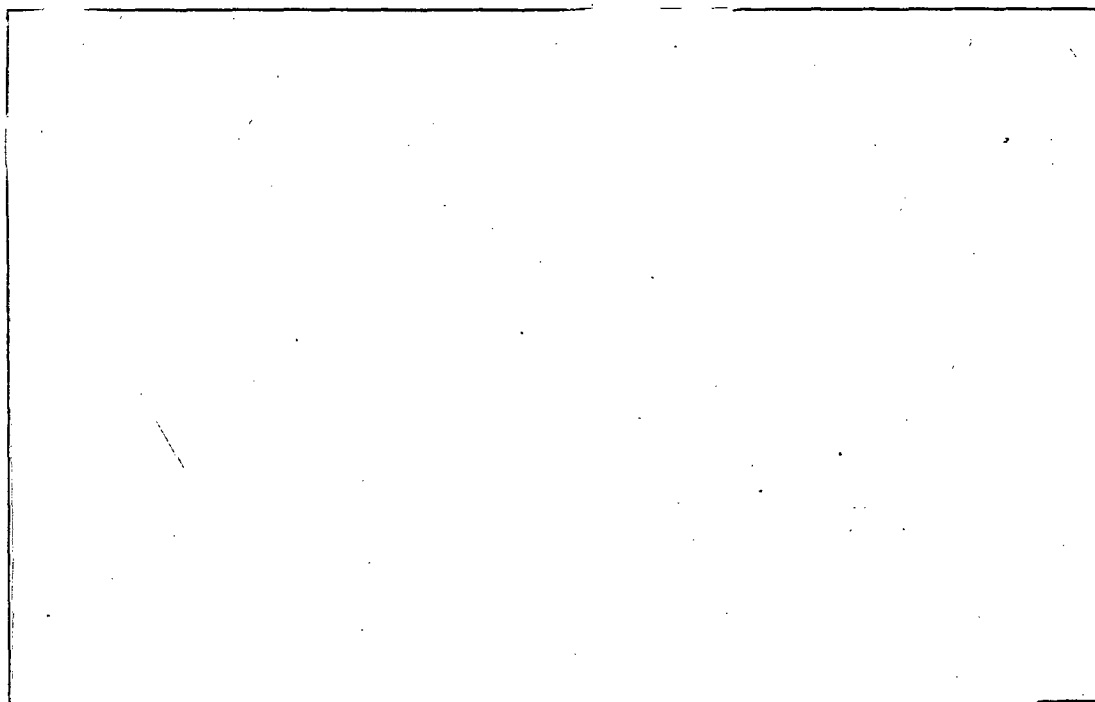
Ex 3
P-B-30-d

Ex # 3

P-B-31-a

Figure B-40.

The contents of this figure are unclassified.



Ex - 1

P-B-31-b

Figure B-41.

The contents of this figure are classified C.

B-31

Ex # 3

P-B-31-c

Ex # 3

P-B-32-c

Figure B-42.

The contents of this figure are unclassified.

Ex # 3

P-B-32-b

Figure B-43.

The contents of this figure are unclassified.

Ex 3
P-0.33 - a

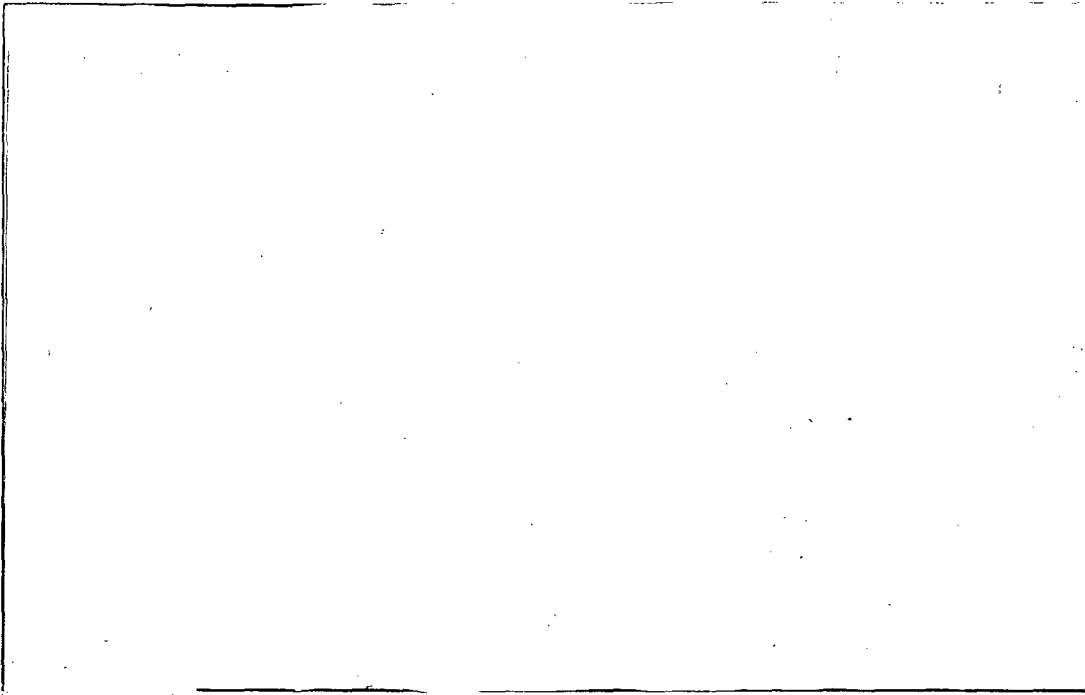
Figure B-44.

The contents of this figure are unclassified.

Ex 3
P-0.33 - b

Figure B-45.

The contents of this figure are unclassified.



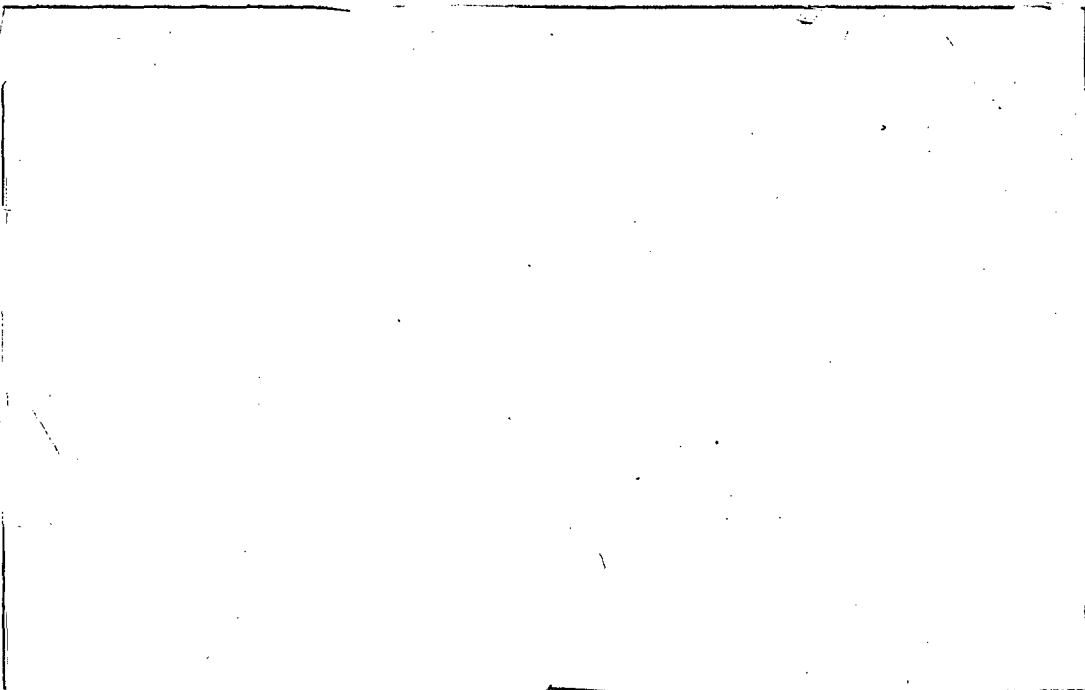
Ex 1
P.B-34-a

Ex #3

Figure 46.

The contents of this figure are classified C.

P.B-34-b



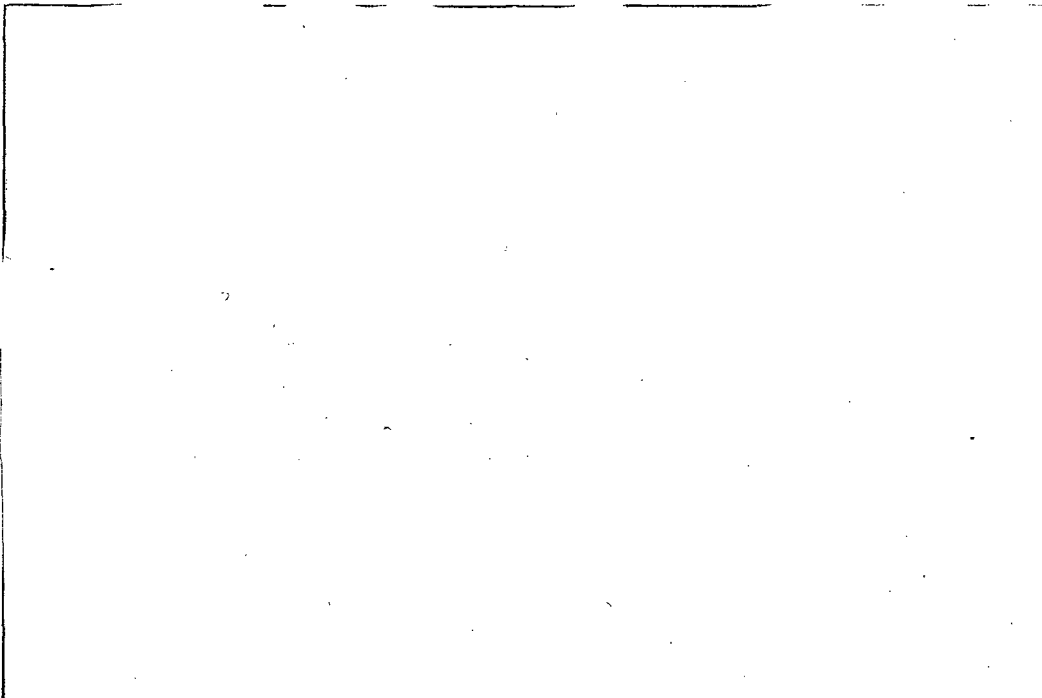
Ex 1
P.B-34-c

Figure B-47.

The contents of this figure are classified C.

B-34

Ex #3
P.B-34-d

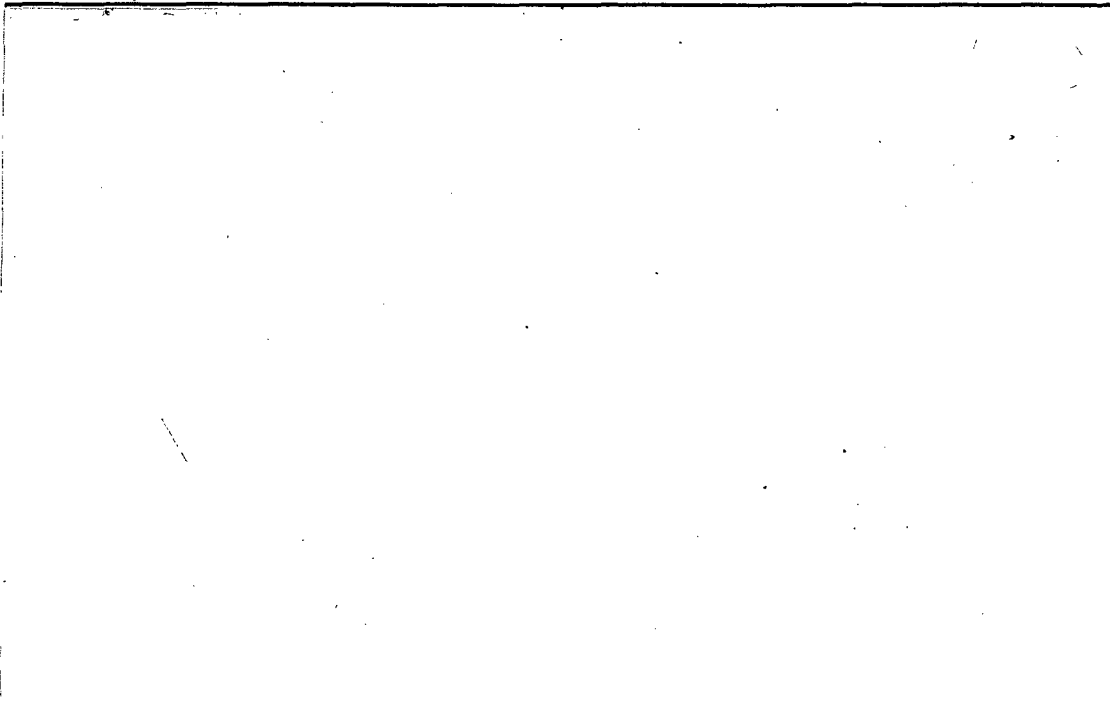


Ex 1
P.B-35a

Figure B-48.

The contents of this figure are classified C.

Ex 3
P.B-35-b

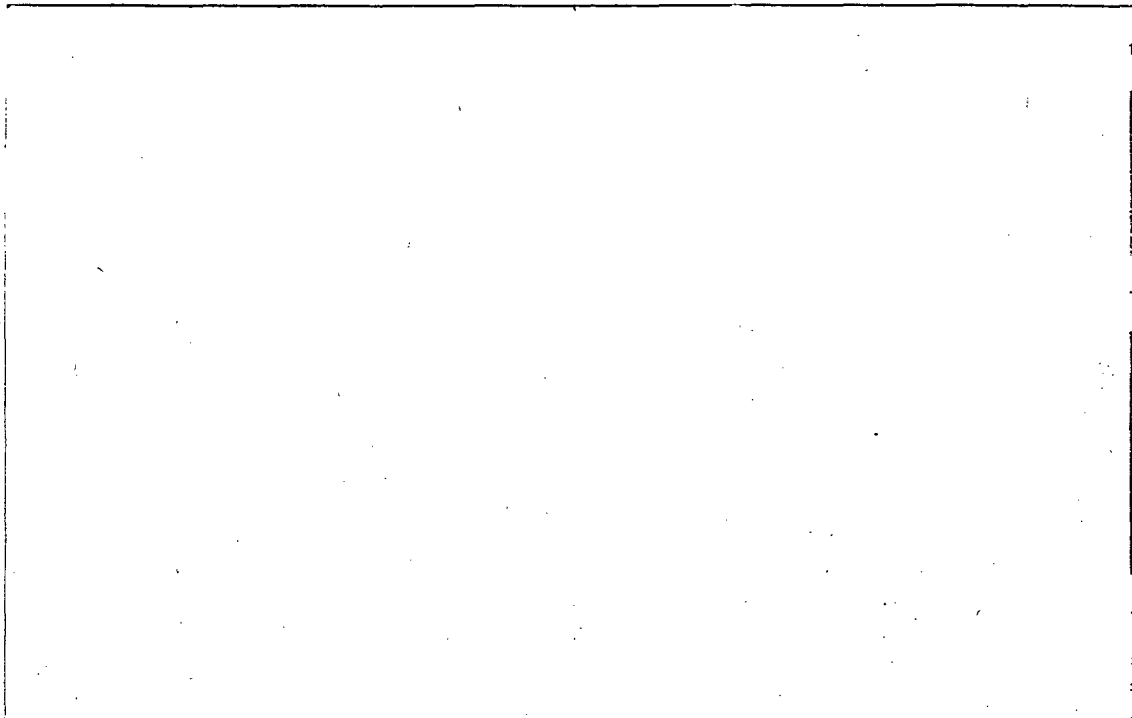


Ex 1
P.B-35-c

Figure B-49.

The contents of this figure are classified C.

Ex 3
P.B-35-d

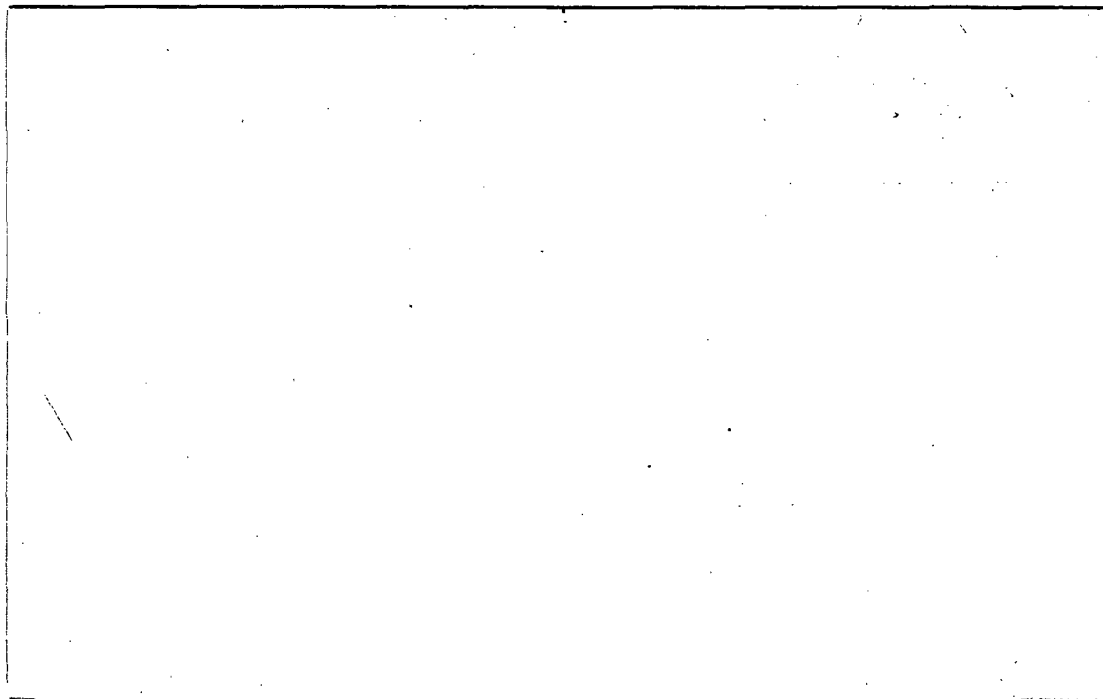


Ex 1
P-B-36-a

Figure B-50.

The contents of this figure are classified C.

Ex 3
P-B-36-b



Ex 1
P-B-36-c

Figure B-51.

The contents of this figure are classified C.

B-36

Ex 3
P-B-36-d

Ex 3
p.B-37a

Figure B-52.
(U).

The contents of this figure are unclassified.

Ex3
p-B-37-d

Figure B-53.
(U).

The contents of this figure are unclassified.

B-37

EX 3
P-B-38-a

Figure B-54.
(U).

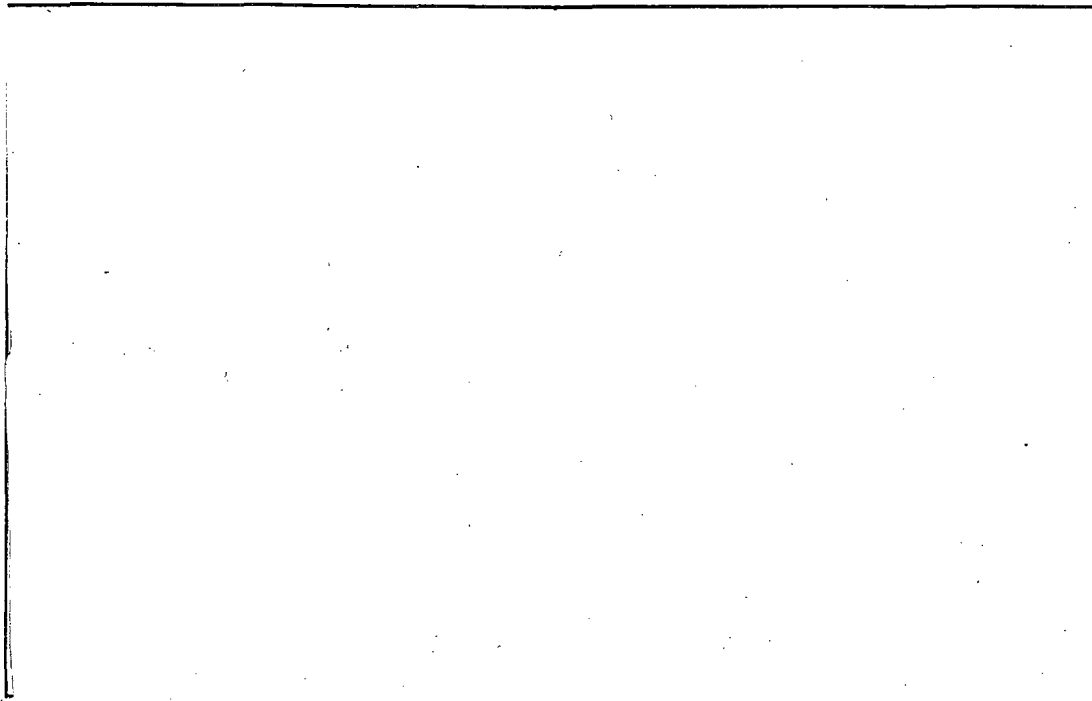
The contents of this figure are unclassified.

EX #3
P-B-38-b

Figure B-55.
(U).

The contents of this figure are unclassified.

B-38



Ex 1
P-B-39-a

Figure B-56.

The contents of this figure are classified C.

Ex 3
P-B-39-b

B.1 Summary and Conclusions (U)

(U)

P-B-39-c

Ex 2

EX 3 P-B-39d

EX 2
P-B-39-e

(U)

EX 3
PB-39f

References (U)

(U) DiMaggio, F. L. and Sandler, I.S. 1971. "Material Models for Granular Soils," J. Eng. Mech. Div, ASCE V 97, No. EM3, June 1971.

(U) Harding, D. C., et al. 1994. *Impact Testing of the H1224A Shipping/Storage Container*, SAND94-0308, Sandia National Laboratories, Albuquerque, NM, May 1994.

(U) Hurlbut, B.J., 1995. "Experimental and Computational Investigation of Strain-Softening in Concrete," Structural Research Series 8508, Univ. of Colorado, Boulder Co., 1985.

(U) Levine, H. S., 1982. "A Two-Surface Plastic and Micro-Cracking Model for Plain Concrete," *Nonlinear Numerical Analysis of Reinforced Concrete, Proc. Winter Annual Meeting, ASME, Phoenix, AZ, Nov. 1982.*

(U) Levine, H. S., D. Tennant and F. Wong. 1991. "Response of Buried Vertical Steel Cylinders to High Intensity Air Blast Loadings," *Proc. 1991 ASME-PVP Conference, Symposium on Structural Dynamics Produced by Extreme Loading Conditions, San Diego, CA, June 23-27, 1991.*

(U) Levine, H. S. and D. Tennant. 1991. "Dynamic Buckling of Buried Steel Cylinders," *Proc. 1991 ASME Winter Annual Meeting, Symposium on Dynamic Response of Structures to High Energy Excitations, AMD Vol. 127/PVP-Vol. 225, Atlanta, GA, Dec. 1-6, 1991.*

(U) Mould, J., H. Levine and D. Tennant. 1994. "Evaluation of a Rate-Dependent Three Invariant Softening Model for Concrete," *Fracture and Damage in Quasi-Brittle Structures*, edited by Z.P. Bazant et al., Chapman and Hall, London, UK, 1994, pp. 231.

(U) Mould, J. C., Jr. and H. S. Levine. 1993. "A Rate-Dependent Three Invariant Softening Model for Concrete," published in *Studies in Applied Mech., Mech. and Materials and Structures*, Ed. by G. Voyiadjis, L. Bank and L. Jacobs, Elsevier.

(U) Mould, J. and H. S. Levine. 1987. "A Three-Invariant Viscoplastic Concrete Model," *Constitutive Laws for Eng. Materials: Theory and Applications, Volume I*, ed. C. S. Desai, et al., Elsevier Pub. Co., Jan. 5-8, 1987, pp. 707.

PB-40a
Ex 2

P. B-40b
Ex 2

(U) Nikodym, L., M. Xie, F. Wong and H. Levine. 1997. "Validation of Jointed Rock Models for Dynamic Response of Tunnels," presented at Joint ASME, ASCE, SES Summer Annual Meeting, Northwestern University, June 29 - July 2, 1997.

(U) Tennant, D. W. and H. S. Levine. 1991. "Response and Failure of Internal Structural Subsystems Under Blast and Shock Loading," *ASME J. Pressure Vessel Technology*, Vol. 116, No. 4, Nov. 1994.

(U) Tennant, D. and H. Levine. 1991. "Response Predictions of Reinforced Concrete Structures Subjected to Combined Air Blast and Fragment Loadings," *Proceedings of the 68th Shock and Vibration Symposium, Hunts Valley, MD, November 3-6, 1997*.

(U) Tennant, D. and H. Levine. 1994. "Response of Embedded Cylindrical and Articulated Structures to Air blast and Ground Shock Loads," *Proc. 62nd Shock and Vibration Symposium, Springfield, VA, October 29-31, 1991*.

(U) Tennant D., H. S. Levine, and J. C. Mould, Jr. 1997. "Prediction of Static and Dynamic Response of Reinforced Concrete Slabs using a Rate-Dependent Three Invariant Softening Model for Concrete," *Proceedings of the 8th International Symposium on the Interaction of the Effects of Munitions with Structures, April 22-25, 1997*.

(U) Tennant, D., H. Levine, D. Lawver and R. Smilowitz. 1999. "Analysis of a Multi-Story Flat Slab Building Subjected to an External Detonation Using a First Principles Finite Element Code," *Proceedings, 70th Shock and Vibration Symposium, Albuquerque, NM November 15-19, 1999*.

(U) Tennant, D.W., J. S. Mould, Jr., H.S. Levine, and D. K. Vaughan. 1996. "Comparison of Crash Computations Using Different Constitutive Relations for Validation of Aircraft Crash Models," *Proceedings 1996 Pressure Vessels and Piping Conference, PVP Vol. 325, Structures Under Extreme Loading*.

(U) Uncapher, W. L., et al. 1994a. *Axial Impact Testing of a C-141B Aircraft Fuselage Section with Shipping Containers*, Sandia National Laboratories Report SAND94-2739, TT1360.

(U) Uncapher, W.L., et al. 1994b. *Lateral Impact Testing of a C-141B Aircraft Fuselage Section*, Sandia National Laboratories Report SAND94-2602, TT1353.

(U) Vaughan, D.K. and J. Mould. *Flex User's Manual*, Version 1-J.6, Weidlinger Associates, 2000.

(U) Wong, F., et al. 1991. *Tunnel Size Effects*, DSWA-TR-91-19.

(U) Wong, F., et al. 1995. *Analytical Support to Underground Technology Program (UTP) and Lethality Assessment of Buried Structures Program*, DSWA-TR-94-189.

~~CONFIDENTIAL-NSI~~

Final Draft

(U) Wong, F., et al. 1996. *Nuclear Weapons System Safety Assessment System Response Modeling for Minuteman III W78/87; C-141 Transportation Study*, DNA TR-94-188, January 1996.

~~CONFIDENTIAL-NSI~~

Appendix C: Effect of Pool Fires on a Dry Storage Cask (U)

C.1 Introduction (U)

(U) The experiences of the September 11th attacks and previous studies suggest that the pooling of fuel after a high-speed jetliner attack onto a field of storage casks is very unlikely.

Ex. 2
p. C-1a

However, to better understand the performance of the studied cask when exposed fires, simulations of different fire scenarios were performed.

Ex. 2
p. C-1b

(U) Several fire configurations were simulated using computational fluid dynamics (CFD) fire codes. The results from the fire simulations determined the flow of hot gases through the vented annular space around the internal spent fuel canister. The transient response of the canister and the spent fuel due to this flow of hot gases was then calculated using a simple heat conduction code and a three-dimensional (3D) finite element analyses (FEA) code. Finally, the thermo-mechanical response of the canister to the increasing temperature and pressure of the canister gas atmosphere was also analyzed using the FEA technique.

(U) To determine the heat fluxes imposed on the storage cask by pool fires, fire simulations were performed using the VULCAN fire code and CAFE-P/Thermal coupled fire and heat transfer code. All fire simulations were run long enough to reach fully developed flow conditions and steady-state heat fluxes.

(U) VULCAN was used to develop fire temperatures for each of the different fire configurations analyzed (fully engulfing or partially engulfing fires without wind, and a bent-over, wind-driven, partially engulfing fire).

When these internal flow conditions were calculated using VULCAN, they were input to a simplified 1D heat transfer model to calculate the heat transfer response of the canister when loaded with spent fuel.

Ex. 2
p. C-1c

(U) Even when engulfed by fire, heat transfer into the canister will not be exactly uniform because the HI-STORM cask is vented and the cask is not radially symmetric. While the 1D heat transfer analysis provided a reasonable upper bound estimate of the canister temperature inside the overpack, modifications to the CAFE code allowed for the simulation of this problem in 3D. Therefore, it was decided to examine the difference between the predictions from a 3D analysis that coupled the fire simulation to the heat transfer response of the HI-STORM cask,

and the results obtained from 1D heat transfer correlations that used the output from the VULCAN fire simulations as input.

(U) When the fire was modeled using a coupled CAFE-P/Thermal code, the flow conditions were automatically passed from CAFE, which modeled the fire, to P/Thermal, which calculates the heat transfer response of the canister. The heat transfer response was then compared to the thermo-mechanical failure analysis of the canister in order to estimate whether canister failure would occur. Each heat transfer calculation assumed that the fire lasted for 30 minutes.

Ex 2
p.c. 24

C.2 Fire Duration (U) →

(U) A jetliner crash usually produces a large fireball on impact that may be followed by a fire whose duration is a function of many parameters. For high-speed impacts, the majority of the available fuel in the airplane will be consumed in this initial fireball.

Ex #2
p.c. 26

Instead, all of the fire and heat transfer analyses presented in this appendix examined the cask system's response to the thermal transient associated with any post-crash jet fuel pool fire. Although a thermal event is not part of the selected scenario, these analyses were performed to develop an understanding of the thermal responses of both the canister and the overpack.

(U) A review of historical plane accidents provides a basis for selecting fire durations for these analyses. After the evaluation of available airplane crash fire data (Fisher et al., 1990), it was concluded that fire duration is inversely proportional to crash speeds, suggesting that the high-speed jetliner attack considered in this study will result in a relatively short-duration, post-crash fire. The commercial airplane accident database compiled by Kimura (2003) shows that there have been high-speed (≥ 134 m/s (300 mph)) airplane crashes that resulted in long-duration fires. However, these fires involved cargo and/or natural gas from a broken gas line or occurred in a deep vegetation region or housing area.

#2
Ex
p.c. 20

The temperatures of the fires analyzed were calculated by the CFD fire codes used; therefore, a fire temperature was not an input parameter for these calculations.

C.3 Jet Fuel Fire Analysis of the HI-STORM (U)

(U)

The pool fire was modeled using both VULCAN and CAFE fire codes. Heat transfer to the cask overpack and to the cask canister was modeled in two ways: using 1D heat transfer correlations and using the 3D P/Thermal heat transfer code, which is part of the CAFE-P/Thermal code system. Finally, the thermo-mechanical response of the canister to the heat loads was modeled using the ABAQUS finite element code.

(U) Three fire scenarios involving the storage cask system were considered. [

The VULCAN fire code was used to model all three scenarios. The coupled CAFE-P/Thermal code was used to model the first and third scenarios.

C.3.1 VULCAN Fire Simulations and One-Dimensional Heat Transfer Analyses (U)

(U) Fire simulations were performed with the VULCAN fire code to study the impact of fire scenarios on the storage cask system. VULCAN is a CFD code designed to solve turbulent reactive flow problems. The code handles gas dispersion and fire development scenarios that have a variety of geometric constraints and boundary conditions. VULCAN uses a Cartesian mesh to form geometries in the fire simulation domain. The code solves the Favre-average transport equations using the finite control volume approach. The standard k-e model is used to close the turbulent terms introduced in the transport equations by the Favre averaging approach. VULCAN uses Magnussen's EDC combustion model (Ertesvag and Magnussen, 2000) to obtain the mass generation source term in the species equation and the Boltzmann radiative transport equation to obtain the radiative source term in the energy equation. Benchmark cases for VULCAN can be found in Holen and Vembe (1998).

(U) The geometry of the storage cask system was approximated in VULCAN. The storage cask overpack is approximately 6.1 m high and 3.35 m in diameter. [

FN
Et
p.C-3a

FN
Et p.C-3b
FN
Et p.C-3c

FN
Et
p.C-3d

(U) In the VULCAN model, the jet fuel pool forms on the ground.

Although most of the calculations assumed that the wind conditions were quiescent, one calculation examined a wind-driven fire located just upwind of the cask system.

Ex. 2
P.C-4a

Ex. 2
P.C-4b

Ex. 2
P.C-4c

C.3.1.1 Quiescent Engulfing Fire, Upright Storage Cask (U)

(U) Two models were created for the standing storage cask system; a quarter symmetry model to simulate the cask standing upright in a fully engulfing fire, and a half symmetry model to simulate the upright cask when exposed to a partially engulfing fire on one side of the cask. The domain for the quarter symmetry model extended 25m in the x, y, and z directions. The domain for the half-symmetry model was approximately twice the size of the quarter symmetry domain in the x direction.

(U) For the quarter symmetry model, a coarser mesh and a finer mesh were created to study the dependence of results on mesh size. The coarser mesh had 377 thousand nodes and the finer mesh, shown in Figure C-1, had 475 thousand nodes. A Courant number (CN) of 7 was used for the coarser mesh runs. For the finer mesh runs, two different CNs, 2 and 7, were used. The CN value was varied because larger CNs reduce simulation run times. In both meshes, the fuel pool extended outward approximately 5m from the edge of the storage cask overpack. Finally, these simulations were run for a short period of time (90-180 seconds).

Ex. 2
P.C-4d

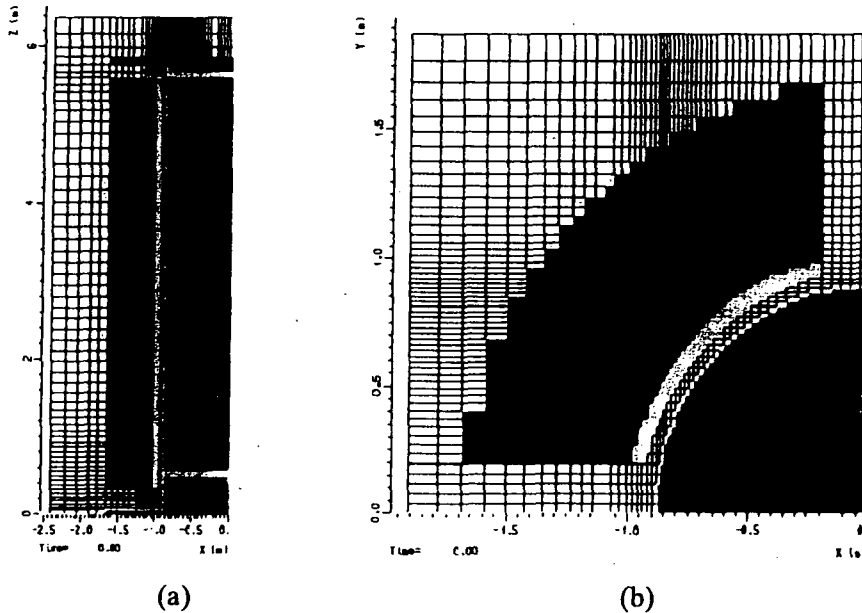


Figure C-1 Mesh Used in Simulation of the Storage Cask System (475,000 nodes):

(a) Front view section at $y = 0.2$ m

(b) Top view section approximately 5.8 m from the ground (U).

The contents of this figure are unclassified.

(U) Because each simulation modeled a fully engulfing quiescent fire, the simulation results showed a fire that was evenly distributed around the storage cask system.

of the finer mesh were also compared against the coarser mesh results.

Temperature contours lines above the container were also closer together for the finer mesh calculations. Differences in results between the meshes were due to high turbulence regions, such as at the entrance of the vent and above the storage cask, finer time and spatial resolution are required to better capture combustion effects. In annular space next to the canister, no significant differences in temperature were observed between the finer and coarser mesh runs or between the finer mesh runs with different CNs.

(U) The large mass and slow heat-up rate of the overpack means that temperature differences in the flame envelope near the overpack are unimportant. Because the annular space between the overpack and the canister is heated principally by the gases passing through this space, not by conduction through the overpack, the gas temperatures at the lower vent inlets to this space determine the heating rate of the canister. Therefore, since the coarser and finer meshes with CNs of 7 yielded about the same gas temperatures at the lower vent inlets, the coarser mesh size

Results
Ex #2
p. C-5a
Ex #2
p. C-5b

~~CONFIDENTIAL - NSI~~

Final Draft

was chosen for all subsequent calculations.

#2
Ex
p. C-6a

Ex 1
p. C-6b

Figure C-2 1 nperature (K) Contours Showing Differences in Results Due to Mesh Size and CN (U).

The contents of this figure are classified C.

Ex 1
p. C-6c

~~CONFIDENTIAL - NSI~~

Ex #2
p. C-7a

]

Ex 1
p. C-7b

Figure C-3. Temperature (K) Contours Showing Results of Pool Size Study (U).
The contents of this figure are classified C.

Ex 1
p. C-7c

(C)
p.c-8a

C.3.1.2 Wind-driven Partially Engulfing Fire, Upright Storage Cask (U)

(U) Experiments have shown that wind-driven fires have higher flame temperatures than quiescent fires because the wind increases the rate of oxygen supplied to the flame envelope (Gritzo et al., 1995b). Thus, wind-driven fires that engulf the cask could decrease cask heat-up times. Given the large mass and low conductivity of the cask overpack's concrete layer, the higher temperatures of a wind-driven fire will not cause the temperature of the inner wall of the overpack to increase rapidly. <

#2
Ex
p.c-8b

(U)

For this scenario, a computational grid was generated from that used for the fully-engulfed, standing cask scenario. The quarter-cask model used in the earlier scenario was extended to a half-cask model, which had a single symmetry plane that bisected both the cask and the fuel pool. The wind is blowing along the plane of symmetry. The resulting grid contains nearly 844,000 cells. In this model, the ribs in the annular gap were not modeled and the material properties were the same as those for the quarter-cask model.]

11 Ex #2
p.c-8c11 Ex 2
p.c-8d

(U) Some specifics of the computational mesh are shown in Figures C-4 and C-5. Figure C-4 shows a top view of the computational mesh, the jet fuel pool (the black area in the figure), and a horizontal section through the cask near ground level (the magenta and olive green object) showing the vent locations. Figure C-5 shows the mesh in the annular gap. The

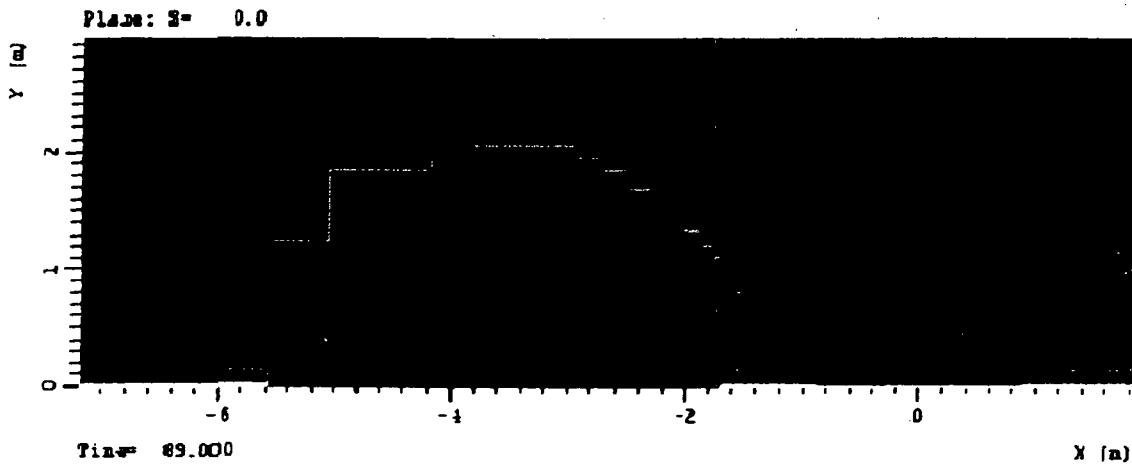


Figure C-4. Computational Mesh, Jet Fuel Pool, and Storage Cask Model (U).

The contents of this figure are unclassified.

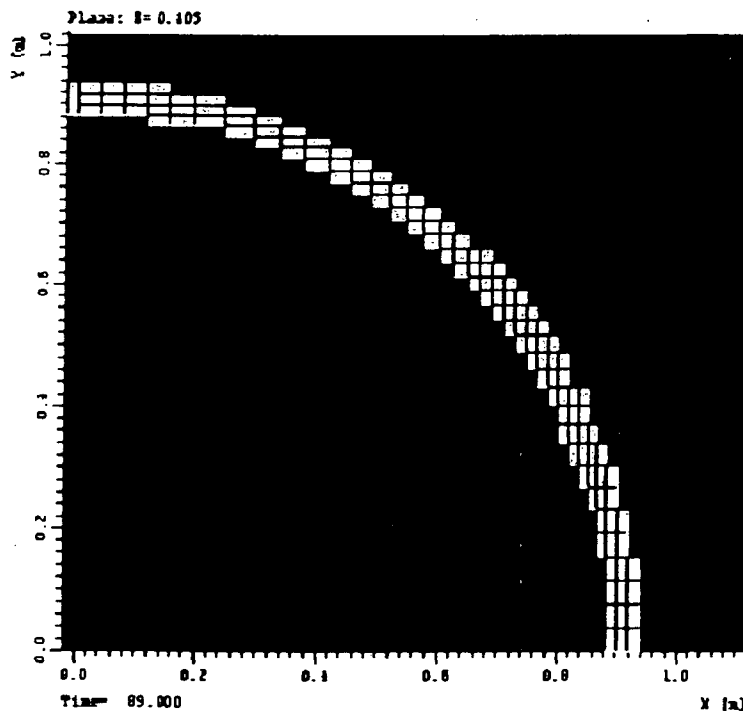


Figure C-5. Grid in the Gap (Horizontal Section) (U).

The contents of this figure are unclassified.

computational domain extended from -25 m to 19 m along the x-axis, from 0 m to 15 m along the y-axis, and from 0 m to 19 m along the z-axis. The cask centerline coincides with the z-axis and the $y = 0$ plane is the symmetry plane. Figure C-4 shows that the upwind edge of the fuel pool is coarsely modeled compared to the downwind pool edge, which is modeled with many more cells.

(U) Figures C-6 through C-10 present the results of this wind-driven fire scenario.

Figure C-8 presents gas temperatures on the symmetry plane. Figures C-6 and C-7 show that as elevation increases the flame envelope separates from the cask. Figure C-8 shows that along the symmetry plane the flame envelope separates from the cask because the wind tips the flame envelope over so that it extends outward behind the cask.

Figure C-6

The contents of this figure are classified C.

C-10

Ex 1
p. C-11a

#2
Ex
p. C-11b

Ex 1
p. C-11c

#2
Ex
p. C-11d

Figure C-7

The contents of this figure are classified C.

Figure C-8

The contents of this figure are classified C.

C-11

Figure C-9:

The contents of this figure are unclassified.

(U) ✓
occurs.

The high temperature regions in this plot show where combustion

The high temperature regions (streamers) in Figure C-10 show where combustion is occurring in the gap. VULCAN calculates the heat transfer rate from these combustion regions to the inner surface of the gap, which is the outer surface of the canister.

The full VULCAN computational output shows that the streamers wave back and forth a bit. If the ribs in the annular gap were modeled, the streamers might have fluctuated less, but this would not significantly change the overall heat transfer to the canister.

Ex1
pC-12a

Ex
pC-12b

Ex
pC-12c

Ex
pC-12d

Ex
pC-12e

Ex 1
p.C-13a

Figure C-10

The contents of this figure are classified C.

Ex #2
p.C-13b

C.3.1.3 Quiescent, Fully or Partly Engulfing Fire, Tipped-Over Storage Cask (U)

Ex #2
p.C-13c

(U) All of these calculations used the coarser mesh discussed in Section C.3.1.1 and a CN of 5. Some details of the computational fire mesh and the size and position of the fuel pool used in the four simulations are shown in Figures C-11 and C-12. 11 Ex #2
p.c. 14b

The vents are arranged in an "X" configuration. The origin of the axis system is at the center of the casks' base plane when standing upright, with the z-axis oriented vertically, the y-axis along the (now horizontal) centerline of the cask system, and the x-axis radially outward in the horizontal direction. Figure C-11 shows the X-configuration of the vents and the x-z computational mesh in the region near the vent system. The mesh coarsens significantly as distance from the cask increases. The four trapezoidal blue-gray objects in this figure denote the cask overpack. The spaces between these objects are the overpack vent channels, and the circular blue-gray object is the cask canister.

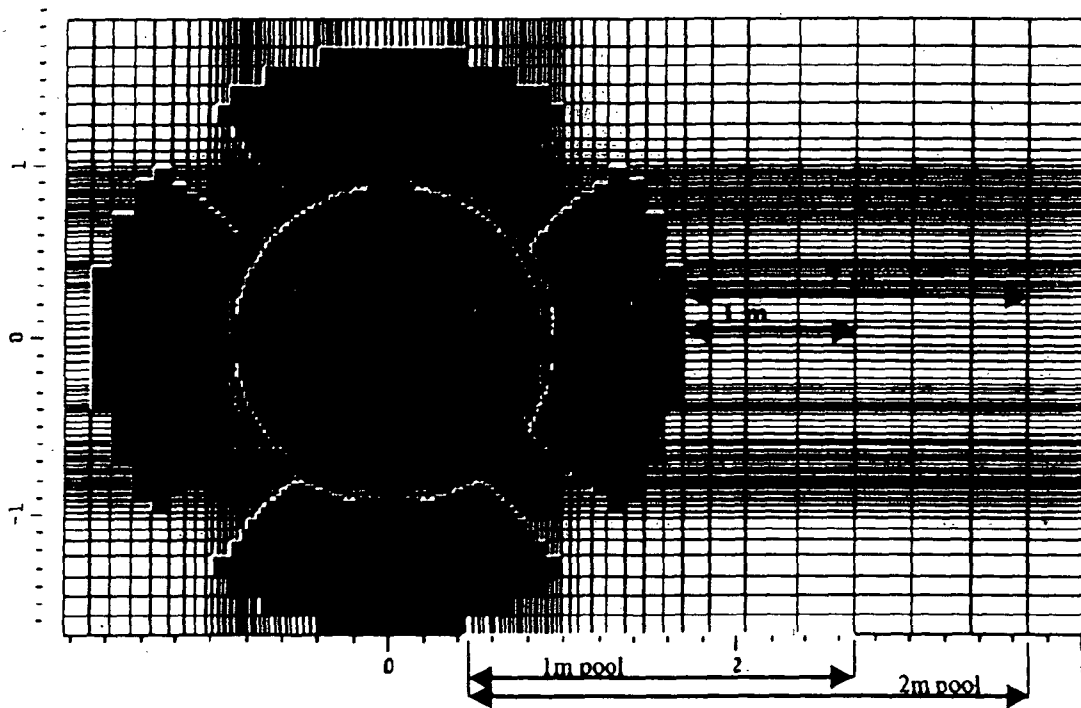


Figure C-11 Vertical Cross-Section Through the Base Vents (Showing Part of the Computational Grid and Fuel Pool Dimension) (U).

The contents of this figure are unclassified.

(U) Figure C-12 shows a horizontal cross-section through the centerline of the cask system and the computational mesh in the x-y plane. Four regions of the fuel pool are shown in this figure.

The pool size for Scenario 1 is represented by the sum of all four pool regions. The pool for Scenario 2 is represented by Regions 2, 3, and 4. For both scenarios, the cask is located in the center of the pool. Regions 3 and 4 represent the pool for Scenario 3. For

Ex #2
p.C-15a

Ex #2
p.C-15b

Figure C-12 Horizontal Cross-Section Plane Through the Cask Centerline (showing the Computational Grid and Pool Boundaries) (U).

The contents of this figure are unclassified.

this scenario, the cask is half in the fuel pool. And only Region 4 is used to represent the pool for Scenario 4. For this scenario, only one quarter of the projection of the tipped over cask is in the fuel pool.

(U) Scenario 1 examines a fuel pool that completely surrounds the tipped-over cask system and extends 2 m beyond the outer perimeter of the system. Because the cask is lying on its side, when

the extent of the surface under and inside the cask perimeter is considered, the full surface of the fuel pool is larger than 2 m. The pool for this simulation includes all four pool regions shown in Figure C-12. Because in this simulation there is a geometric plane of symmetry and no wind, the problem has a computational plane of symmetry, which passes through the axial centerline of the cask system and lies in the x-z direction. Thus, for this simulation, only the computational mesh on the positive x side of the symmetry plane was modeled (i.e., the region of $x < 0$ in Figures C-11 and C-12 was eliminated from the computational domain). With this configuration, the problem was modeled with over 500,000 computational cells.

Thus, in this simulation, only pool Regions 2, 3, and 4 in Figure C-12 were used.

(U) For both Scenarios 1 and 2, fuel vapors entered the four overpack vents positioned just above the fuel surface.

(U)

Scenarios 3 and 4 examine this situation.

specifies the fuel pool.

resulted in a computational model with over 1,000,000 cells.

(U)

Plots of the temperature in this annular space are shown in Figures C-13 through C-16 for Scenarios 1 through 4, respectively. In these four figures, the cylindrical surface that passes through the center of the annular gap was unrolled and the half of that surface on the side of the cask engulfed by the fire is displayed in each plot. For Scenarios 1 and 2, which examine fully engulfing fires, the temperature plot for the other half of the cylindrical surface would be essentially identical to the plots displayed in Figures C-13 and C-14. Lastly, in each of these figures, the y-axis scale presents circumferential distance around the half cylinder, with the zero distance located where the half cylinder intersects the horizontal centerline plane through the cask system.

Ex. 2
p. C-16a

Ex. 2
p. C-16b

Ex. 2
p. C-16c

Ex. 2
p. C-16d

For Scenario 4, region 4

This
Ex. 2
p. C-16e

Ex. 2
p. C-16f

Ex 1
p. C-17a

Figure C-13 Temperature (K) in Annular Gap Adjacent to the Canister for Scenario 1 (U).
The contents of this figure are classified C.

Ex 1
p. C-17b

Figure C-14 Temperature (K) in Annular Gap Adjacent to the Canister for Scenario 2 (U).
The contents of this figure are classified C.

Ex 1
p. C-18a

Figure C-15 Temperature (K) in Annular Gap Adjacent to the Canister for Scenario 3 (U).
The contents of this figure are classified C.

Ex 1
p. C-18b

Figure C-16 Temperature in Annular Gap Adjacent to the Canister for Scenario 4 (U).
The contents of this figure are classified C.

Ex #2
p. C-19a

(U) In addition to temperatures, parameters that can estimate the energy released in the gap are the net fuel vapor and net oxygen into the gap around the canister.

Ex #2
p. C-19b

(U) As mentioned earlier, the ribs in the gap were omitted for these calculations.

Ex #2
p. C-19c

(U) It could be argued that some of the pool (in the "shadow" of the cask) would not receive a high enough heat flux to evaporate fuel at that rate.

SGI Ex3
p. C-19dEx #2
p. C-19eEx #2
p. C-19f

C.3.1.4 One-Dimensional Heat Transfer Analyses of the Canister (U)

C.3.1.4.1 Thermal Response of Cask Canister when Inside Cask Overpack (U)

(U) Four mechanisms for heat input to the spent fuel canister of the storage cask from the jet fuel fire are considered in this section. First, the heat may conduct through the steel-concrete-steel cask overpack. Second, the fire may interrupt the natural cooling of the canister causing a radioactive decay heat load to raise the canister temperature. Third, the canister may be heated by hot gases from the fire that are then convected into the annular space between the overpack and the canister. Finally, the canister may be directly heated by combustion in the annular space of unreacted fuel and air, if they are both convected there.

C-19

Ex #2
p. C-19g

Ex #2
p.C-20a

(U) The second mechanism is radioactive decay heat. The storage cask maximum thermal load is 22 kW, and the thermal capacitance of the canister and its contents is 3.774 MJ/K (6440 BTU/°F) (Holtec International, 2000, p. 11.2-15).

Ex #2
p.C-20b

(U) The third mechanism considered for raising the temperature of the canister and its contents is convection of hot combustion gasses into the annular space between the steel-concrete-steel overpack and the canister. This annular space is included in the cask system design to allow removal of decay heat from the canister by the buoyancy-driven upward flow of cooling air inside this annulus. Here, the heating rate of the canister caused by a flow of hot gasses through the annular space was investigated.

(U) Heat transfer through the contents (fuel rods, fuel assembly structures, canister basket) of the spent fuel canister was simulated by modeling these structures as a uniform material of constant heat capacitance and thermal conductivity. These internal canister structures are surrounded by the 1.27-cm thick steel shell of the canister. The heat capacitance of the homogenized fuel structures was taken from the HI-STORM Safety Analysis Report (SAR), and its effective conductivity was determined from steady-state temperature profiles provided in the SAR. The effective conductivity can be estimated from the radial temperature difference across the homogenized fuel structures and the following relation:

$$k_{eff} = \frac{P}{4\pi H \Delta T}, \quad (C-1)$$

where P is the decay heat power of the fuel (watts), H is the internal height of the canister (meters), and ΔT is the temperature difference between the centerline and the edge of the fuel region (K or °C). An estimate for ΔT is available in Figure 4.2.20 of NAC International (2002). This resulted in an effective conductivity for the fuel region of 1.4 W/m-K.

(U) The maximum gas flow rates induced in the annular space that surrounded the canister were estimated from the results of VULCAN fire simulations (see Sections C.3.1.1 - C.3.1.3).

Ex #2
p.C-20c

Ex #2
p.c-2/a

(U) The energy added to the canister by the flow of hot combustion gases through the annular space can be estimated by the following equation:

Ex #2
p.c-2/b

Figure C-17 provides the centerline and surface (edge) temperature transients for the fuel region due to the 30-minute fire.

Ex #2
p.c-2/c

(U) The fourth mechanism for heating up the canister and its contents is combustion inside the annular space surrounding the canister of any unburned fuel and oxygen convected there. A VULCAN computer model was constructed to examine this scenario (see Section C.3.1.3).

Ex #2
p.c-2/d

Ex. 1
p. C-22a

Figure C-17

Ex. 2
p. C-22b

The contents of this figure are classified C.

Ex. 1
p. C-22c

(U)

Ex. 2
p. C-22d

The results from this calculation are presented in Figure C-18.

Ex. 1
p. C-23a

Figure C-18

Ex. 2
p. C-23b

The contents of this figure are classified C.

Ex. 1
p. C-23c

C.3.1.4.2 Thermal Response of the Bare Cask Canister (U)

Ex. 1
p. C-23d

Ex-1
p.c-24a

Figure C-19

Ex-1
p.c-24b

The contents of this figure are classified C.

(U) Lastly, the 1D computer code used in the analysis presented in this and the previous subsection was verified by comparison to another calculation. This verification is presented in Section C.3.2.

C.3.2 Three-Dimensional CAFE-P/Thermal Fire and Heat Transfer Simulations of a No-Wind and a Wind-Driven Pool Fire for an Upright Storage Cask and a Bare Canister (U)

(U) Even when engulfed by fire, heat transfer into the cask will not be exactly uniform and should be modeled as a 3D problem because the HI-STORM cask is vented and is not radially symmetric. Because of the 3D nature of this problem, it was decided to examine the difference between the predictions of a 3D analysis that coupled the fire simulation to the heat transfer response of the HI-STORM cask, and the results obtained from 1D heat transfer correlations (Section 3.1.4) that used the output from the fire simulations (Sections C.3.1.1 - C.3.1.3) as input. This 3D analysis was performed using the CAFE-P/Thermal code system. CAFE-P/Thermal was also used to model the highly 3D problem presented by the offset, wind-driven fire case.

(U) The CAFE code is a CFD fire model that includes all the dominant physics present in fires. MSC PATRAN/Thermal is a commercially available FEA thermal code usually referred to as P/Thermal. The CAFE fire code is coupled with the P/Thermal FEA code. CAFE is a CFD code that calculates the fire field and passes boundary condition information to the P/Thermal FEA code, which calculates the heat transfer response of the object exposed to the fire modeled by CAFE. These two codes interact throughout the fire simulation, making a fully-coupled CFD-FEA analysis tool. Therefore, a coupled fire-heat transfer analyses of the upright cask standing in the middle of the fuel pool and the upright cask standing next to the fuel pool were carried out

using the CAFE-3D code. To perform these calculations, the CAFE code was modified so that flow through the small annular gap in the HI- STORM cask could be modeled.

(U) The HI-STORM overpack was modeled in CAFE to properly capture the thermal radiation shield provided by the overpack to the MPC and to restrict the convective heating provided by the hot gases that enter the cask through the cooling vents. The MPC was modeled in P/Thermal to properly capture the 3D heat transfer response to the flow of hot gases near/over its external surface. Figure C-20 shows the CAFE mesh of the HI-STORM overpack and Figure C-21 shows the P/Thermal mesh of the canister.

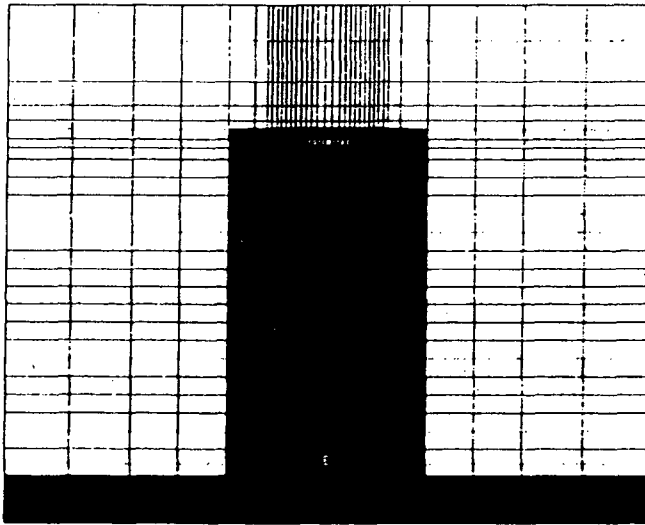


Figure C-20. CAFE-3D Mesh of the HI-STORM Overpack (U).

The contents of this figure are unclassified.

(U) The CAFE model consists of a 40 m x 10 m x 20 m domain discretized as $45 \times 27 \times 25 = 30,375$ 3D CFD cells. What is shown in Figure C-20 shows a section of this computational domain, where the white background is the plane of symmetry and the gray at the bottom represents the ground as it extends outward from this plane.)

Ex. 2
p. C-25a

(U) The P/Thermal model consisted of nearly 42,000 3D finite elements.

The thermophysical properties for the homogenized internals were obtained from NAC International (2002). These properties are presented in Table C-1. The initial condition of the MPC for the transient fire simulations was obtained from the steady-state solution shown in Figure C-22. This steady-state solution is in good agreement with the results presented in NAC International (2002).

Ex. 2
p. C-25b
p. C-25c

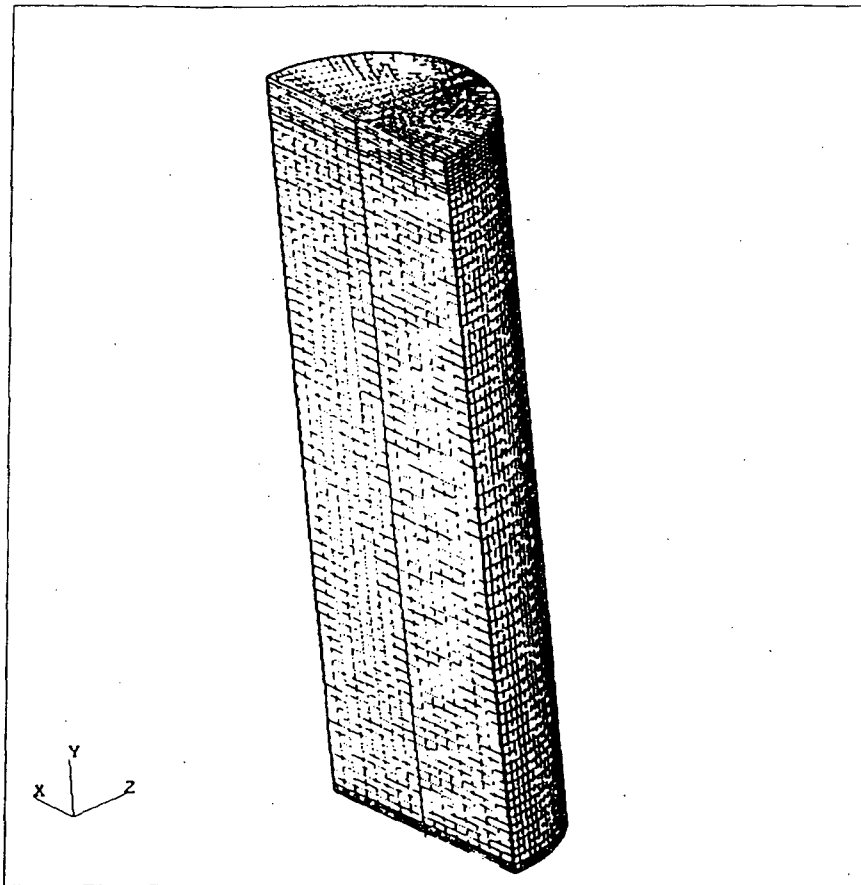


Figure C-21. P/Thermal Mesh of the Multipurpose Canister (MPC) (U).
The contents of this figure are unclassified.

Table C-1. Effective Thermophysical Properties of Homogenized MPC Internals (U)
The contents of this table are unclassified.

Homogenized MPC Internals	@ 366 K	@ 505 K	@ 644 K
Thermal Conductivity (W/m-K)	1.246	1.681	2.198
Density (kg/m ³)	2204.21	2204.21	2204.21
Specific Heat (J/kg-K)	352.81	352.81	352.81

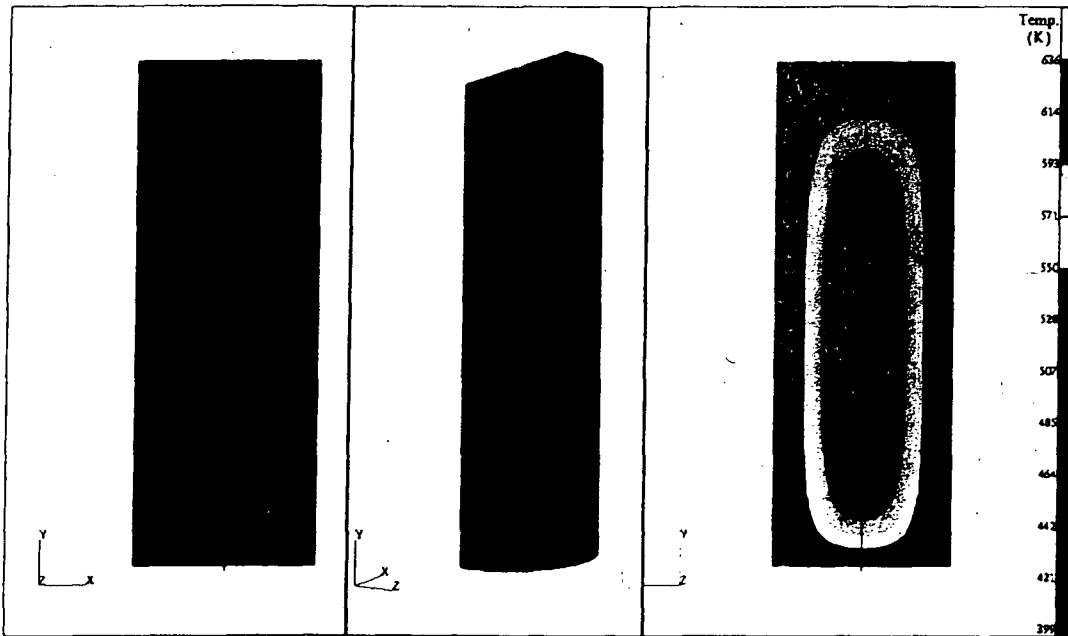


Figure C-22. Steady-State Temperature Distribution of the MPC – Normal Condition (U).
The contents of this figure are unclassified.

C.3.2.1 CAFE-P/Thermal Results for the Fully-Engulfing, No-Wind Case (U)

(U) The results from the simulations in which the HI-STORM cask was upright and centered with the fuel pool and no wind are presented in Figures C-23 through C-25.

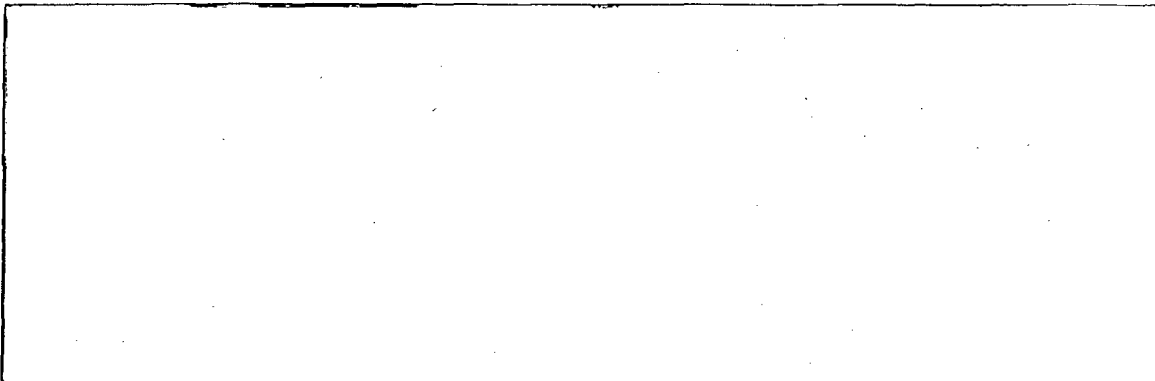


Figure C-23. Results of the CAFE Simulation for a Fully Engulfing, Quiescent Fire. The figure on the left shows the fire as viewed from outside while the right shows the temperature gases at the symmetry plane. All temperatures are in K (U).

The contents of this figure are classified C.

(U) Figures C-24 and C-25 present three views of the HI-STORM canister's thermal response. The first two views in each figure present canister surface temperatures. In the second view, the canister has been tilted slightly and rotated counter-clockwise about 45 degrees from its position in the first view. The third view presents internal canister temperatures on the symmetry plane that bisects the fire and the cask.

Ex 1
p. C-28a

Figure C-24. Temperature Distribution of the HI-STORM Canister after 15 Minutes for the No-Wind Case (U).

The contents of this figure are classified C.

Ex 1
p. C-28b

Figure C-25. Temperature Distribution of the HI-STORM Canister after 30 Minutes for the No-Wind Case (U).

The contents of this figure are classified C.

(U)

The localized maximum temperature presented in Figure C-25 is higher because of the nonuniform, 3D heat flux applied over the canister wall by the CAFE fire code, which is more realistic than the 1D uniform heat flux applied to the canister in the previous section. On the other hand, the two solutions are more similar when looking at the temperature of the region about $\frac{3}{4}$ of the canister's height in the 3D results presented in Figure C-25.

This is because hot combustion gases entering the annular space between the canister and the overpack lose thermal energy as they flow up the annulus and cool before they exit through the top vents of the overpack. The CAFE-P/Thermal results presented above are more realistic and therefore will be considered for further thermo-mechanical analyses of the canister.

C.3.2.2 CAFE-P/Thermal Results for the Wind-Driven Adjacent Fire Case (U)

(U)

Figure C-26 presents two views of the fire. The first view on the left shows that the wind tips the flame envelope of the fire so that it partially engulfs the cask. The second view shows the temperature of gases at the symmetry plane through the center of the fire and the cask. This view shows that hot gases enter the overpack bottom vent next to the burning fuel pool; that these hot gases continue to burn as they enter the annular gap; and that they also burn as they exit the overpack from the vent at the top of the cask.

Figure C-26

All Temperatures are in K (U).

The contents of this figure are classified C.

(U) Figures C-27 and C-28 show the thermal response of the HI-STORM canister for the wind-driven fire case at 15 and 30 minutes, respectively. The three views in each figure are the same as those presented in Figures C-24 and C-25. This figure shows that the thermal response of the

C-29

Ex #2
p. C-29aEx #2
p. C-29bEx #2
p. C-29cEx 1
p. C-29dEx #2
p. C-29e

~~CONFIDENTIAL - NSI~~

Final Draft

Ex 1
p. C-30a

Figure C-27.

The contents of this figure are classified C.

Ex #2
p. C-30b

Ex 1
p. C-30c

Figure C-28.

The contents of this figure are classified C.

Ex #2
p. C-30d

C-30

~~CONFIDENTIAL - NSI~~

canister is highly asymmetric and thus can only be properly analyzed using a 3D heat transfer code like P/Thermal.

Ex. 1
p. C-31a

C.3.2.3 CAFE-P/Thermal Simulation of the Bare Canister (U)

(U) CAFE-P/Thermal was also used to evaluate the 3D response of the bare canister while exposed to a fully engulfing fire. The fuel canister was assumed to lie on the ground after coming out of its storage overpack during a severe airplane impact. The canister model is the same one used for all the previous CAFE-P/Thermal calculations. The initial temperature distribution of the canister and its contents was calculated assuming normal storage conditions for which results are presented in Figure C-22.

Ex. 2
p. C-31b

Ex. 1
p. C-31c

Ex 1
p. C-32c

Figure C-29.

(U).
The contents of this figure are classified C.

Ex. 2
p. C-32 b

Ex 1
p. C-32c

Figure C-30.

(U).
The contents of this figure are classified C.
C-32

Ex. 2
p. C-32d

Ex 1
p. C-33a

Figure C-31{

(U).

The contents of this figure are classified C.

Ex 2
p. C-33b

C.3.3 Thermo-Mechanical Response of the Cask Canister (U)

(U) This section discusses the thermo-mechanical response of the HI-STORM storage cask MPC when exposed to high temperatures. The results from this section are combined with the temperature history results from Sections C.3.1 and C.3.2 to determine this canister's response to fire environments.

(U) A series of static, thermo-mechanical analyses of the storage cask canister were conducted using the finite element code ABAQUS (Hibbit et al., 1998). The canister is subjected to the internal pressure resulting from an increase in the temperature of the canister gas atmosphere. The canister was modeled in three different positions; inside the overpack, partially outside the overpack, and completely outside the overpack. For each analysis performed, Table C-2 lists the cask position and the temperature to which the canister gases were assumed to be heated.

Table C-2. ABAQUS Analysis of the Canister (U)
The contents of this table are unclassified.

--	--

Ex #2
pC34a

(U) In each analysis, the canister's shell is assumed to be at the specified gas temperature. The pressure inside the canister is increased slowly as predicted by linearly ramping up the temperature of the canister gas atmosphere. The linear ramping of the temperature is done to account for the path dependency of the canister's plastic deformation. The maximum pressure reached corresponds to the assumed maximum temperature and the final canister volume produced by the canister bulging as it plastically deforms. To perform this calculation, ABAQUS requires the specific volume of the canister as input.

Ex #2
pC34b

C.3.3.1 The ABAQUS canister model (U)

(U) Figure C-32 presents important features of the HI-STORM canister. The ABAQUS FE model of the canister is shown in Figure C-33. Because the canister has a plane of symmetry, the canister model is axisymmetric. The model contains 1599, CAX4R, four-node bilinear axisymmetric quadrilateral elements. There are eight elements through the canister shell thickness and 150 along its length. The space inside of the canister occupied by the fuel rods and the assembly and basket structures are combined into a single (lumped) volume. The inside surface of the canister and the outside surface of this single "lumped" volume is lined with two node hydrostatic elements. Given an initial reference pressure and temperature and using the ideal gas law, the hydrostatic elements apply a pressure load along the canister's inner surface. The code calculates the current pressure given the temperature and canister volume. Since there is some elastic and plastic deformation of the canister, the final pressure is always lower than predicted by the ideal gas law for the increase in temperature at constant volume.

(U) The basic configuration of the MPC canister is presented in Figure C-32

Ex #2
pC34c

Ex #2

PC 35a

Figure C-32. Canister Configuration (U).
The contents of this figure are unclassified.

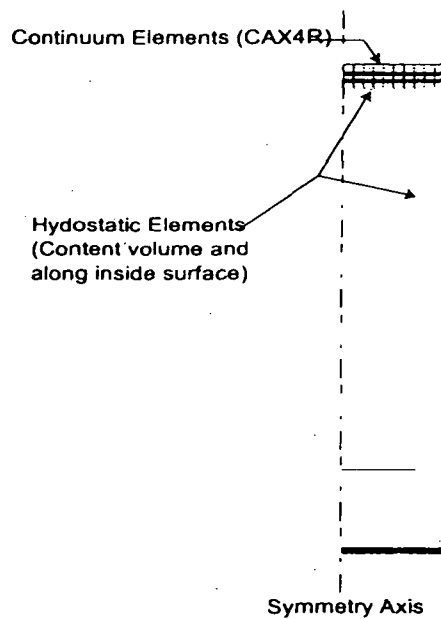


Figure C-33. Canister FE Model (U).
The contents of this figure are unclassified.

Ex #2
PC 35b

]

Ex #2
p. C-36a

Chavez et al. (1994) conducted high-temperature and short-time creep experiments on type 304 stainless steel.

Ex #2
p. C-36b

English units are used in the Larson-Miller equation to maintain the values of the material constants and to be consistent with historical data.

(U)

Ex #2
p. C-36c

This quantity, called the principal facet stress, is defined as follows:

$$\sigma_f = 2.24\sigma_1 - 0.62(\sigma_2 + \sigma_3) \quad (C-5)$$

where $\sigma_1 > \sigma_2 > \sigma_3$ are the principal stresses. All stresses presented in this analysis are principal facet stresses.

Ex #2
p. C-36d

Ex #2
P.C-37a

Ex #1
P.C-37b

Figure C-34. Plot of LMP vs. Stress Using the Data Developed by Chavez et al. (1994)
(1 psi = 6.895 KPa) (U).

The contents of this figure are classified C.

C.3.3.2 Thermo-Mechanical Analysis Results (U)

Ex 1
P.C-37c

~~CONFIDENTIAL - NSI~~

Final Draft

Ex 1
p. 1-38

C-38

~~CONFIDENTIAL - NSI~~

Ex. 1
p.C-39a

FigureC-35

The contents of this figure are classified C.

Ex. 2
p.C-39b

Ex. 1
p. C-39c

Figure C-36

The contents of this figure are classified C.

Ex. 2
p. C-39d

Ex. 1
P.C-400

Figure C-37

The contents of this figure are classified C.

Ex 2
P.C-400b

Ex. 1
P.C-400c

C.3.3.3

P.C-400d
Ex 2

The instantaneous increase in the canister wall temperature is assumed because of the short time it takes for the canister wall to heat up when directly exposed to an engulfing fire. The time varying internal pressure is a result of the slower response of the internal gas and fuel assemblies to the external heating.

Ex 1
p C-41a

Figure C-38. Stress in the Canister Bottom and

The contents of this figure are classified C.

Ex #2
p C-41b

Ex 1
p C-41c

Figure C-39.

The contents of this figure are classified C.

Ex #2
p C-41d

Table C-3

The contents of this table are classified C.

Ex 2

p.c-42a

Ex 1

p.c-42b

Figure C-40.

The contents of this figure are classified C.

Ex # 2

p.c-42c

Ex 1

p.c-42

Ex 1
p.C-43a

Figure C-41.

The contents of this figure are classified C.

Ex #2
p.C-43b

Ex 1
p.C-43c

Figure C-42. Canister Stress at Two Locations Plotted as a Function of the Internal Gas Temperature. (U)

The contents of this figure are classified C.

C.4 Discussion (U)

Ex 1
pC-44a

C.5 References (U)

- (U) Blanchat, T.K. and L. Manning. 2002. *Mock B52 Bomb Bay Fire Experiment Data and Analysis for Model Validation and Development*, SAND2002-0145
- (U) Chavez, S.A., Korth, G.E., Harper, D.M. and Walker, T.J. 1994. "High-Temperature Tensile and Creep Data for Inconel 600, 304 Stainless Steel and SA106B Carbon Steel," *Nuclear Eng. And Design*, 148, pp. 351-363.
- (U) Ertesvag, I.S. and B.F. Magnussen. 2000. "The Eddy Dissipation Turbulence Energy Cascade Model," *Combust. Sci. and Tech.*, Vol. 159, pp. 213-235.
- (U) Fisher L.E., J.H. VanSant, and C.K. Chou. 1990. *Draft Criteria for Controlled Tests for Air Transport Packages*, UCRL-ID-103684, Lawrence Livermore National Laboratory.
- (U) Gritzo, L.A., et al. 1995a. *Heat Transfer to the Fuel Surface in Large Pool Fires, in Transport Phenomena in Combustion*, edited by S.H. Chan.
- (U) Gritzo, L.A., V.F. Nicolette, J.L. Moya, R.D. Skocypec, and D. Murray. 1995b. *Wind-Induced Interaction of a Large Cylindrical Calorimeter and an Engulfing JP8 Pool Fire*, SAND95-1635C.
- (U) Gritzo, L.A., Y.R. Yudaya, and W. Gill. 1997. *Transient Measurements of Radiative Properties, Soot Volume Fraction and Soot Temperature in a Large Pool Fire*, SAND97-2062J.
- (U) Hibbit, Karlsson and Sorensen. 1998. *ABAQUS/Standard User's Manual* (Hibbit, Karlsson and Sorensen, Inc., HKS, 1080 Main Street Pawtucket, RI, 02860-4847) version 5.8 edition.
- (U) Holen, J.K. and B.E. Vembe. 1998. *Benchmark Cases Calculated with VULCAN 97*, Internal Report, SINTEF Energy, 1998. Can be obtained from Victor Figueroa, (505) 844-0631.
- (U) Holtec International. 2000. *HI-STORM Topical Safety Analysis Report*, Revision 10, Holtec International Report Number HI-951312, Holtec International, Marlton, NJ (available from NRC document room).
- (U) Kimura, C. 2003. *Historical Commercial Airplane Crash Database*, submitted to Sandia National Laboratories. . Can be obtained from Carlos Lopez, (505) 845-9545.
- (U) Koski, J.A. 2000. "Measurement of Temperature Distributions in Large Pool Fires with the use of Directional Flame Thermometers," PPVP- Vol. 408, *Transportation, Storage, and Disposal of Radioactive Material*, ASME-2000. pp. 111-115.
- (U) Martinez, M.J. and P.L. Hopkins. 2000. *Modeling Subsurface Multiphase Transport of JP8 During a Fuel Spill Fire*, SAND2000-2462.

(U) Nicolette, V.F. and L.A. Gritzo. 1993. *Comparison of the Kameleon Fire Model to Large-Scale Open Pool Fire Data*, SAND93-2416C.

Ex. 2
p. C-46a

(U) Tieszen, S.R. 1995. *Fuel Dispersal Modeling for -Runway Impact Scenarios*, SAND95-2529.

(U) Tieszen, S.R., and S.W. Attaway. 1996. *Fuel Dispersal in High-Speed Aircraft/Soil Impact Scenarios*, SAND96-0105.